BUBBLES AND CRYSTALS:
TIME-RESOLVED SONOLUMINESCENCE, SONOCRYSTALLIZATION, AND SONOFRAGMENTATION

BY

BRADLEY WESTON ZEIGER

DISSERTATION

Submitted in partial fulfillment of the requirements
for the degree of Doctor of Philosophy in Chemistry
in the Graduate College of the
University of Illinois at Urbana-Champaign, 2012

Urbana, Illinois

Doctoral Committee:

Professor Kenneth S. Suslick, Chair
Professor Richard D. Braatz
Professor Gregory S. Girolami
Professor Benjamin J. McCall

Abstract

The application of high-intensity ultrasound on liquids induces acoustic cavitation: the formation, growth, and implosive collapse of bubbles. In a standing wave a single bubble can be trapped. The conditions formed inside such a bubble during collapse are extreme, reaching temperatures on the order of 15,000 K and pressures of over a thousand atmospheres. These conditions are extreme enough to excite gas molecules in the bubble, resulting in light emission (single-bubble sonoluminescence, or SBSL). To extract information about conditions during cavitation, both atomic emission lines (usually from noble gases) and the underlying broad continuum present in SBSL have been used as spectroscopic thermometers. Unfortunately, these experiments divulge only time-averaged information, whereas the evolution of the conditions created during the collapse of a single bubble has been largely unexplored and the few reports concerning the time evolution of collapsing bubbles are conflicting and problematic.

The extremely bright SBSL achievable in sulfuric acid (hundreds to thousands of times more intense than in water) and long emission lifetimes (typically several nanoseconds at low ultrasonic frequencies, compared to as short as 50 picoseconds in water) permitted the acquisition of high-quality time-resolved spectra for this dissertation.

Time-resolved spectra are consistent with a compressionally-heated bubble and blackbody emission from an opaque plasma. The temperature profile ranges from ~8,000 to 14,000 K with approximate temporal symmetry (the emission during bubble rebound is slightly longer than during collapse) and peak conditions only modestly higher than time-averaged temperatures.

High-intensity ultrasound is also employed in the preparation of molecular crystals, although the field remains in its infancy. The effects of high-intensity ultrasound on the preparation of pharmaceutical compounds are explored here, with emphasis on the breakage of particles post-crystallization. A model compound, aspirin, was crystallized under ultrasonic irradiation and particle morphology and crystal size distributions were compared with other crystallization methods.

Particle breakage during sonication of liquid/aspirin slurries was investigated, establishing relationships between particle size and sonication time or sonication intensity. Particle size distributions were modeled using a population-balance method assuming simple binary breakage events. The importance of liquid viscosity and vapor pressure was also established, with the former strongly influencing breakage rates and the latter being negligible.

The mechanism of particle breakage during sonication was shown to be direct interactions between shockwaves and crystals rather than interparticle collisions, a surprising contrast with superficially similar systems. Decoupling and kinetics experiments were performed to rule out particle-particle collisions, particle-horn collisions, or particle-cell collisions as significant contributors.

Acknowledgments

This thesis would not exist without the assistance of a large number of people. The technical staff, faculty, and fellow graduate students at the University of Illinois have always proved generous with their time and resources, and have on occasion expedited my research as a result. I will, therefore, acknowledge (and in some cases, commensurate) their efforts with a line in the appropriate place: the forefront of my thesis.

Several faculty members have opened their labs and equipment to me. Professor Nick Glumac and Drew Coverdill in the Department of Mechanical Engineering assisted me with high speed photography. Professor Zukoski and Ryan Kramb allowed me to make use of their rheometer for viscosity measurements. Professor Zukoski additionally gave me free access to his dynamic light scattering instrument, with the assistance of So Youn Kim. Professor William O'Brien and Michael Kurowski in the Beckman Institute were invaluable in helping me calibrate my hydrophone, providing necessary equipment and freely offering advice.

The School of Chemical Sciences shops have always offered friendly and personal service. I would especially like to thank Ben Fisher (now retired) in the electronics shop. Kyle Webb in the electromechanical shop also worked very hard to assist me on one particularly vexing project. The glass shop was always willing to try to make whatever exotic piece of glassware I had concocted; I would particularly like to thank Donny, who does excellent work, and Dave, who provides copious conversation. The ladies in the IMP office, especially Beth, Connie, and Theresa, have been consistently friendly and helpful during my tenure time here.

In the course of my graduate career I have been involved in several collaborations. I am grateful to Professor Richard Braatz and Michael Rasche for working with me on population-balance modeling of sonofragmentation. The time-resolved sonoluminescence in Chapter 3 could not have been performed without the equipment and expertise provided by Professor Dana Dlott and Rusty Conner.

The Suslick group, past and present, has naturally had a huge impact on my graduate experience. Several Suslick group members were happy to talk to me and help me with my research and job search in spite of having never overlapped with me. David Flannigan was always prompt and helpful in e-mail communication and even took time from his busy schedule to come in person and help teach me the art of sonoluminescence. Steve Hopkins was also a friendly contact who abetted me in my career search. There are too many students who shared time with me in lab for to me to do justice to our individual interactions. I am grateful for the support, aid, and camaraderie of Scott Dunkle, Brandon Ito, Jonathan Kemling, Howard Kim, Eva Agha, John Overcash, Liang Feng, Hangxun Xu, Maryam Sayyah, Jinrui Guo, Sizhu You, Jin Ho Bang, Maria Fortunato, Rich Helmich, Chris Musto, Sung Lim, Hengwei Lin, Wei Jang, Nathan Eddingsaas, Rachel Campbell, Ming Fang, Min Jang, and Yagang Zhang. Also the various undergrads and first year students. Nasrin Gahvari has been a great help on any number of tasks, a wonderful friend, and a refreshing pillar of sanity amidst my graduate student ilk.

My family has always been supportive of me, if perhaps unappreciative of my choice to pursue graduate studies 2/3 of the way across the country. I would not be here if it were not for the stellar education and the exposure to science that my parents gave me in my formative years.

Finally, I would like to express my gratitude to my advisor, Professor Ken Suslick, who has supported me and tolerated my foibles and antics over the course of these long years. I consider myself extremely fortunate to have had an advisor with a sense of humor compatible with my own without compromising on scientific rigor. I have had opportunity to explore science broadly, dabbling in chemistry, physics, and chemical engineering. I am appreciative of the breadth of experience I have gotten and the latitude I have been given to explore my own interests and ideas, while still receiving direction when needed. There were many long, dark days in the sonoluminescence project, and while at the time I would have preferred to have abandoned it, Ken gave me the time I needed to get it working, and this thesis is better for it.

Table of Contents

Chapter 1: Introduction 1

1.1 Acoustic cavitation and single-bubble sonoluminescence.....................................1

    1.1.1 Introduction to acoustic cavitation..1

    1.1.2 Mechanics of SBSL 2

    1.1.3 A brief history of SBSL 6

    1.1.4 Conditions during SBSL...7

    1.1.5 Mechanisms of light emission 9

    1.1.6 Recent advances in SBSL 14

    1.1.7 Comparison of multibubble and single bubble systems 19

    1.1.8 Conclusion 20

1.2 Sonochemical synthesis of materials 20

    1.2.1 Introduction...20

    1.2.2 Chemical effects of ultrasound for nanomaterials preparation......................24

    1.2.3 Physical effects of ultrasound for nanomaterials synthesis 33

    1.2.4 Combined chemical and physical effects for synthesis of nanomaterials......40

    1.2.5 Conclusions...43

1.3 Sonocrystallization...43

    1.3.1 Introduction...43

    1.3.2 Applications and effects of sonocrystallization 44

    1.3.3 Mechanism of action..52

    1.3.4 Conclusion 56

1.4 References..56

Chapter 2: Materials and Methods 67

2.1 Ultrasonic equipment for preparation, modification, and characterization of molecular crystals 67

2.1.1 Comments on ultrasonic horns 67

2.1.2 Tapped ultrasonic horns 71

2.1.3 Calibrating the ultrasonic horn...74

2.1.4 Set-up for crystallization experiments 76

2.1.5 Analysis of microcrystals...79

2.2 Equipment and methods for production and observation of single-bubble sonoluminescence (SBSL) 80

2.2.1 Generating single bubble sonoluminescence 80

2.2.2 Preparing solutions for SBSL 84

2.2.3 Measuring acoustic pressure 89

2.2.4 The quality factor (Q) 93

2.2.5 Time-resolved spectroscopy of SBSL 95

2.2.6 Data processing and corrections 99

2.3 References...104

Chapter 3: Time-resolved single-bubble sonoluminescence in sulfuric acid 106

3.1 Introduction...106

3.2 Experimental notes..110

3.3 Resonator construction and design 111

3.3.1 Metrics for evaluating SBSL quality 112

  3.3.2 Preparation of solutions for SBSL 113
  3.3.3 Q measurements 116
  3.3.4 Choice and attachment of piezoelectric ceramics 117
  3.3.5 Choice of waveform 120
  3.3.6 Resonator geometry 122
3.4 Applying the streak camera technique to SBSL 125
3.5 Time-resolved SBSL 130
3.6 Concluding remarks 137
3.7 References 139

Chapter 4: Sonocrystallization 142
4.1 Introduction 142
4.2 Experimental notes 147
4.3 Cooling crystallization of aspirin 148
4.4 Spray sonocrystallization 154
  4.4.1 Spray sonocrystallization of aspirin 154
  4.4.2 Spray sonocrystallization of other materials 160
4.5 Concluding remarks 163
4.6 References 164

Chapter 5: Sonofragmentation of Aspirin 167
5.1 Introduction 167
5.2 Experimental 168
5.3 Results and discussion 169
  5.3.1 Sonication of aspirin in aqueous media 170

5.3.2 Sonication of aspirin in hydrocarbons 173
5.3.3 Sonication of aspirin in silicone oils 177
5.3.4 Ultrasonic dosimetry in viscous media 181
5.3.5 Population-balance modeling 186
5.4 Conclusions 193
5.5 References 193

Chapter 6: Mechanisms of Sonofragmentation 199
6.1 Introduction 199
6.2 Experimental 202
6.3 Discussion 204
6.3.1 Particle-horn decoupling 205
6.3.2 Particle-wall decoupling 209
6.3.3 Effect of reactor size 211
6.3.4 Particle-particle versus shockwave-particle interactions 213
6.4 Conclusions and caveats 217
6.5 References 218

Chapter 1

Introduction

The introduction is divided into three parts. Section 1.1 discusses the basic phenomenon of acoustic cavitation and the extreme conditions that can occur when a liquid is irradiated with high-intensity ultrasound. The phenomenon of single-bubble sonoluminescence is discussed as a probe for understanding what goes on during cavitation. Section 1.2 gives an overview of the application of high-intensity ultrasound to the synthesis of materials, with an emphasis on nanomaterials. Section 1.3 highlights the use of ultrasound for the nucleation and processing of pharmaceutically active ingredients (sonocrystallization).

1.1 Acoustic cavitation and single-bubble sonoluminescence

1.1.1 Introduction to acoustic cavitation

High intensity ultrasound has found many important applications in organic synthesis, materials and organometallic chemistry, and industrial manufacturing processes.[1-9] Sonochemistry originates from the extreme transient conditions induced by ultrasound, which produces unique hot spots that can achieve temperatures above 5,000 K, pressures exceeding 1,000 atmospheres, and heating and cooling rates in excess of 10^{13} K/sec.[4, 10]

The speed of sound in a typical liquid is 1,000 to 1,500 m/sec, and ultrasonic wavelengths will vary from roughly a millimeter to ten centimeters over a frequency range of 20 kHz to 15 MHz, much larger than the molecular size scale. The chemical and physical effects of ultrasound therefore arise not from a direct interaction between chemical species and sound waves, but rather from the physical phenomenon of acoustic cavitation: the formation, growth, and implosive collapse of bubbles.[11-13] When sound waves with sufficient amplitude propagate through a liquid, the liquid is under dynamic tensile stress and the density changes with alternating expansive and compressive waves. Bubbles will be generated from pre-existing impurities (e.g., gas-filled crevices in dust motes) and oscillate with the applied sound field.

There are two basic ways to apply an ultrasonic field: as a progressive wave or as a standing wave. The former requires higher intensity from the signal source in order to induce cavitation, and creates a more chaotic system with many bubbles. A standing wave permits the production and stabilization of a single bubble. A multi-bubble system is a practical necessity for any preparative sonochemistry – yields from a single bubble are prohibitively low – while a single bubble system is more conducive to fundamental investigation. Differences between the two will be discussed at the end of Section 1.1 before the presentation of practical applications of sonochemistry. The remainder of Section 1.1 will be devoted to a discussion of the phenomenon of light emitted from a single cavitating bubble levitated in a standing ultrasonic wave, called single bubble sonoluminescence (SBSL).

SBSL is a powerful tool for observing the conditions created during acoustic cavitation. The spectroscopic characterization of light emitted from the acoustically-driven bubble permits a quantitative description of the temperatures and pressures achieved. The phenomenon of SBSL has been reviewed at great length in other theses[14-16] and academic reviews.[10, 17] This thesis will therefore only give an overview of the field and relevant principles and will focus on the most recent and most important developments.

1.1.2 Mechanics of SBSL

In order to acoustically nucleate a bubble in a pure liquid a negative pressure of sufficient magnitude to overcome the tensile strength of the liquid must be applied.[13] In theory this pressure should be enormous; the tensile strength of water at room temperature is expected to require over 1,000 bar of pressure to overcome.[18] In practice it requires only ~1 bar of pressure to induce nucleation due to the presence of nucleation sites, either tiny gas bubbles already present in solution or gas pockets in crevices in particulate impurities. Efforts to rigorously degas and purify liquids can dramatically increase the measured tensile strength.[13, 19] In practice a bubble for SBSL is often introduced by other means, most commonly injection by pipette, laser-induced cavitation, or local boiling by passing a current through nichrome wire (the heating element from a toaster).[20]

Once a bubble is nucleated it will oscillate with the applied acoustic field. At low acoustic powers the bubble will oscillate almost linearly, meaning that the phase of the bubble cycle matches the phase of the driving acoustic pressure. The bubble collapses with the same velocity and radius profile as it grows with (except inverted). As the acoustic pressure increases the bubble's inertia perturbs this symmetry. The bubble's growth will continue into the positive pressure phase of the acoustic cycle, followed by a rapid collapse. Figure 1.1 shows the increasing non-linearity of bubble behavior as the applied acoustic pressure increases.[21]

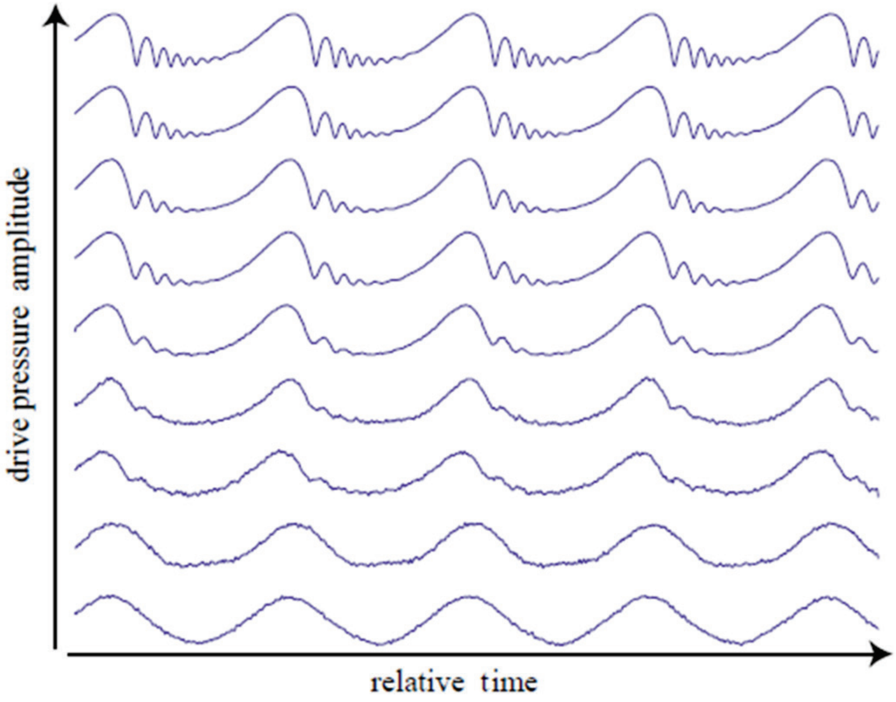

Figure 1.1 Nonlinear bubble oscillation. Bubble dynamics as detected by laser scattering off a bubble driven at different acoustic pressures.[21]

The forced oscillation of a bubble can be described by the Rayleigh-Plesset equation. Various forms of this equation exist, depending on the degree of rigor required. It is commonly formulated as

$$R\ddot{R} + \frac{3}{2}\dot{R}^2 = \frac{1}{\rho}\left[\left(P_o + \frac{2\sigma}{R_o} - P_v\right)\left(\frac{R_o}{R}\right)^{3\gamma} - P_o - P(t) - 4\eta\frac{\dot{R}}{R} - \frac{2\sigma}{R}\right]$$

where R is the bubble radius, ρ is the liquid density, P_o is the ambient pressure, σ is the surface tension, R_o is the ambient bubble radius, P_v is the liquid's vapor pressure, γ is the polytropic ratio, $P(t)$ is the driving pressure, and η is the shear viscosity. Overdots indicate the first (for one dot) or second (for two dots) derivative with respect to time (i.e., velocity and acceleration).[22-24] Measuring bubble dynamics by scattering laser light off of the bubble and fitting to a Rayleigh-Plesset model is one common way to estimate the acoustic pressure in an SBSL system.[25] The equation ceases to be valid near maximum bubble implosion when the bubble wall is moving faster than the speed of sound in the liquid, limiting its application to some fundamental questions in SBSL.[26-27]

All important consequences of acoustic cavitation are direct results of this nonlinear motion. The rapid collapse of the bubble causes intense compressional heating of gasses inside the bubble. The nonlinear motion is also necessary for acoustic levitation of bubbles and rectified diffusion. Acoustic levitation, or bubble trapping, is the result of the primary Bjerknes force.[28] The Bjerknes force pushes bubbles towards the pressure antinode of an acoustic wave when the antinode is at low pressure and away from the antinode when it is at high pressure (Figure 1.2).

The force arises from a pressure gradient across the bubble because the bubble size is significant compared to the acoustic wavelength. On balance the net force is towards the antinode because the bubble is bigger on average during the low pressure phase of the acoustic cycle. As a result the pressure gradient across the bubble is smaller and the pressure is applied over a smaller cross-sectional area. If the Bjerknes force is greater than the buoyant force the bubble will be trapped at the antinode. At low acoustic pressures the bubble motion is linear and the bubble will not be trapped. At high acoustic pressures the bubble will grow inertially into the positive-pressure phase, increasing the average bubble size during the high pressure phase of the acoustic field, and the bubble will move away from the center due to buoyancy.

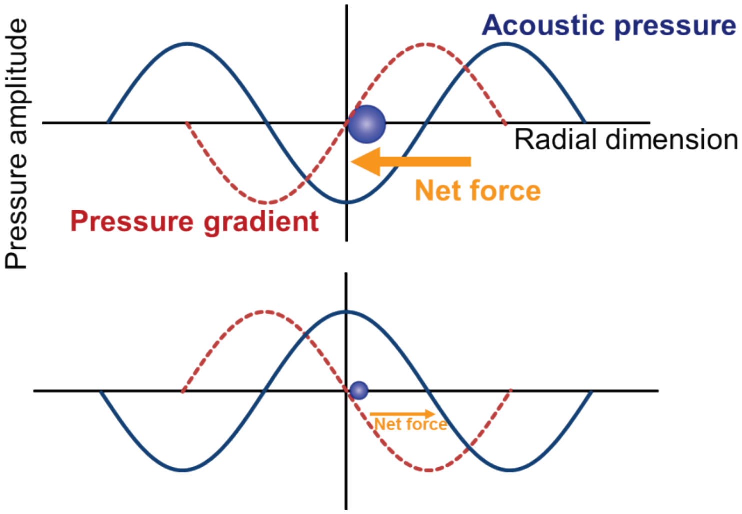

Figure 1.2 Bubble levitation. The primary Bjerknes force is a consequence of pressure gradients across the bubble pushing it towards the antinode during negative pressure (top) and away from the antinode during positive pressure (bottom). The bubble is bigger under negative pressure and the net force is consequently towards the antinode.[21]

Rectified diffusion is a bubble growth mechanism, again as a consequence of the nonlinear motion of an acoustically-forced bubble. During bubble expansion the gas inside the bubble is rarefied, resulting in diffusion of gas molecules into the bubble from the host liquid. These gas molecules come from gasses dissolved in the liquid and vapor from solvent evaporation. During bubble compression the reverse process occurs and gas molecules diffuse out of the bubble. The rate of diffusion is related to surface area, and the bubble is on average larger during the rarefaction step, leading to a net influx of gas and slow bubble growth over many acoustic cycles. There is a second, concurrent mechanism necessary to fully explain rectified diffusion, called the shell effect. Diffusion rates also depend on concentration gradients. During bubble expansion the liquid around it is compressed to make room and creates a relatively larger concentration gradient. During bubble collapse the shell expands, the concentration gradient is smaller, and diffusion is slower.[29]

A highly-forced acoustic bubble will grow due to rectified diffusion until it is lost to buoyancy or shatters into smaller bubbles. A bubble in the absence of an acoustic field or in a weak acoustic field will dissolve due to surface tension. There is a very narrow window of acoustic pressure where no there is net mass exchange and stable, reliably repeating SBSL can occur (Figure 1.3).[30] The gas content of the host liquid also determines whether SBSL can occur stably, and simple gas diffusion is inadequate to explain the range of conditions under which SBSL is observed.[31] Excess air is sonochemically converted to soluble species (mostly NO_x) and leave the bubble (dissolve in the host liquid), serendipitously leaving behind a useable concentration of argon.[21, 32]

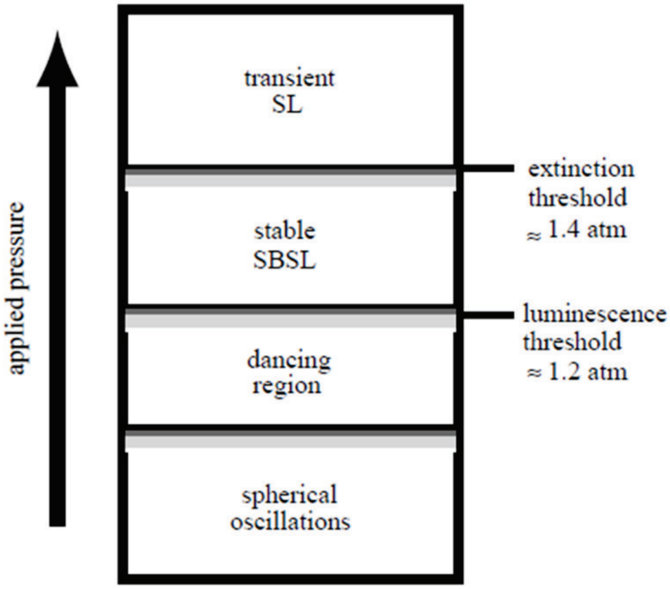

Figure 1.3 SBSL thresholds. At low acoustic pressures the bubble will oscillate linearly and eventually dissolve. At moderate acoustic pressures the bubble will be trapped approximately in the center. Sonoluminescence will occur in a very narrow window of 1.2 to 1.4 atm of acoustic driving pressure (in water). At high acoustic pressure rectified diffusion limits the lifetime of the bubble and luminescence is transient.[21]

1.1.3 A brief history of SBSL

Multibubble sonoluminescence has been known since at least 1934, but failed to attract the interest of even the researchers who discovered it.[33] Work at Northwestern in 1966 showed that the sonoluminescence flash duration was under a nanosecond, making it the fastest manmade light source at the time.[34] The cavitation establishment was dismissive, asserting that these results were an obvious consequence of what was known about bubble motion.[35] The discovery of SBSL was greeted with a similarly cool reception. The earliest report of single-bubble sonoluminescence was by Yosioko and Omura in 1962.[36] Their work, which was published exclusively in Japanese, received little notice in the scientific community. A few other researchers briefly rediscovered the phenomenon, but it remained ignored by the community at large.[37] It was not until Felipe Gaitan, working with Lawrence Crum, that the field began to get traction. Gaitan's work attracted the attention of Seth Putterman at UCLA that SBSL began to gain prominence.[38-39] Since those seminal publications SBSL has blossomed into an exciting and competitive field.

1.1.4 Conditions during SBSL

The conditions achieved inside the collapsing bubble are characterized spectroscopically, in much the same way that stellar temperatures are measured. In fact, many sonoluminaries are fond of calling the bubble a "star in a jar"[35] Figure 1.4 shows some emission spectra from argon in 85 wt% sulfuric acid.

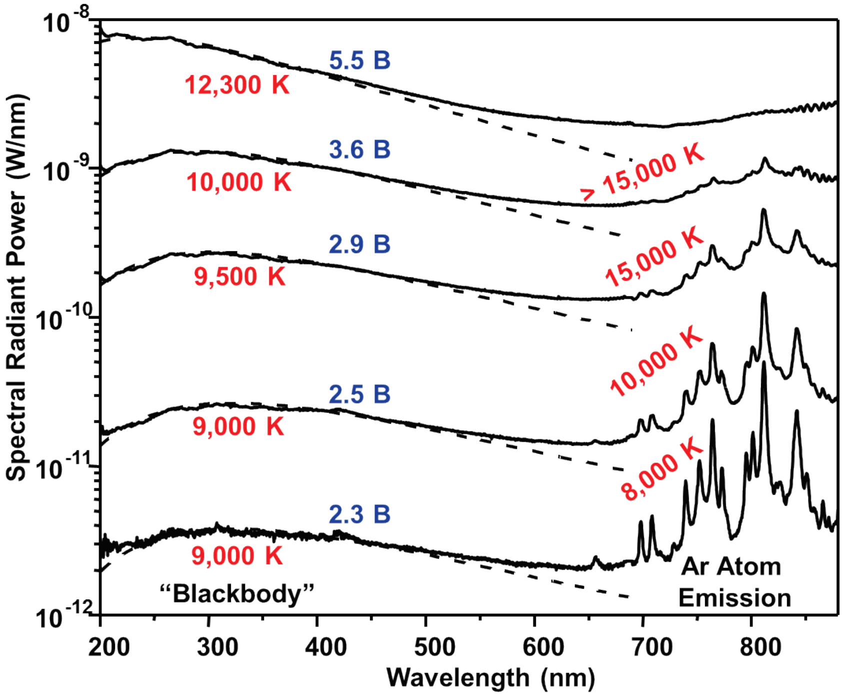

Figure 1.4 SBSL spectra. Emission from 85 wt% sulfuric acid regassed with 400 Torr Ar. Temperatures on the left are calculated from fitting the continuum to a blackbody and temperatures on the right come from fitting atomic emission lines to a Boltzmann distribution.[40]

There are two distinct spectral regions in evidence: a broad continuum peaked in the UV, and atomic emission lines in the near IR. The observation of atomic emission lines is almost exclusively limited to sulfuric acid. In water only a broad continuum is observed.[17] Sulfuric acid is a very attractive medium to study, partly because of the inclusion of atomic lines, but also because emission is dramatically brighter in concentrated H_2SO_4 than in water and the range of acoustic pressures that will support stable SBSL is much larger.[40] The increased emission intensity is due to the low vapor pressure of sulfuric acid (~40 mTorr[41]), which results in very few polyatomic molecules in the vapor phase. A great deal of energy is consumed by bond vibrations and dissociations, so limiting the number of polyatomics in the gas phase dramatically increases the conditions achievable inside the bubble.[42] It is similarly known that decreasing the temperature of water to decrease its vapor pressure will increase SBSL output.[43] Water, sulfuric acid, and (to a lesser extent) phosphoric acid have all been experimental systems of intense study in the field of SBSL. Research on sulfuric acid SBSL systems will be discussed preferentially in this introduction because it is most relevant to the experimental work presented later in the thesis.

There are several surprising features in the spectra in Figure 1.4. The most obvious mystery is that the match between temperatures derived from the blackbody region and the atomic region are not very impressive. This may be because the two spectral pieces come from a different space in the bubble or a different time during collapse (still an open question), or because the blackbody region is not really a blackbody (discussed in Section 1.1.5). Another astonishing feature is that Ar^+ lines can be observed in the spectrum, a species 37 eV above the ground state, while a measured temperature of ~15,000 K corresponds to only ~1.3 eV.[44] This was initially believed to imply a much hotter, optically-opaque plasma core with a relatively cool emitting surface.[40] More recent work, discussed in Section 1.1.6, suggests that this may not be a complete explanation of the phenomenon.

The pressures reached inside the bubble can also be probed via the atomic emission lines. Pressure broadening (lifetime broadening) and Stark broadening of these lines are common plasma diagnostics for measuring effective pressures. Various pressure measurement techniques estimate pressures well in excess of 1,000 bar.[44] Figure 1.5 shows line broadening and peak shifts used to calculate pressure.

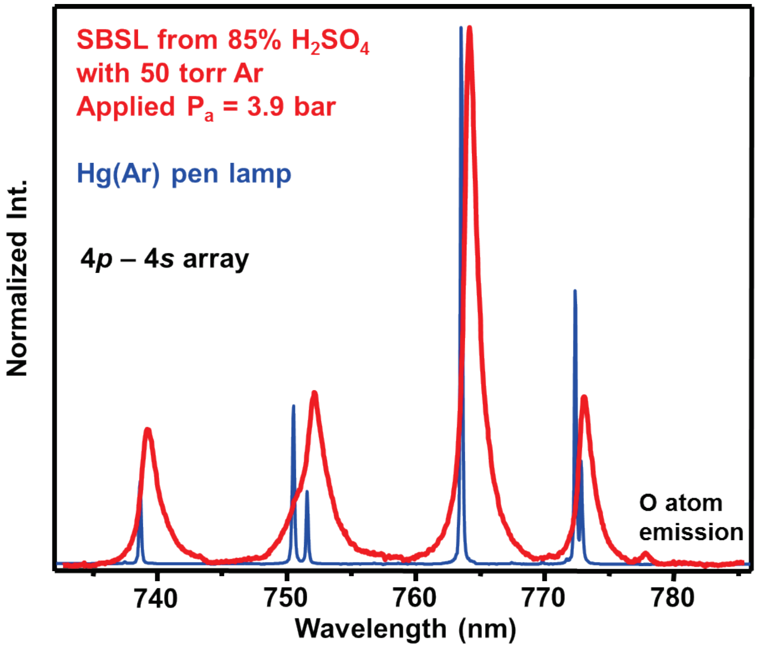

Figure 1.5 Pressure estimation. Comparison of SBSL lines to atomic lines from a standard lamp. Line widths can be used to estimate pressures during SBSL based on Stark broadening and pressure broadening. Natural line widths and Doppler broadening are trivial, but instrumental broadening must be accounted for.[44]

1.1.5 Mechanisms of light emission

The broad continuum emission present in all SBSL has historically been a subject of considerable debate. The two widely-considered and hotly-contested mechanisms will be discussed here: Bremsstrahlung radiation and blackbody radiation.

Bremsstrahlung radiation, or braking radiation, is light emitted by an accelerating charge. Typically the charge is specifically an electron interacting with another charged particle or applied Coulombic force. The radiation intensity depends inversely on the square of the particle mass, so electron Bremsstrahlung will dominate any system that also contains other accelerating charges. Bremsstrahlung arises from changes in kinetic energy of a moving particle, and a free electron can have any value for kinetic energy. As a result Bremsstrahlung can produce a continuous emission spectrum, necessary for consistency with SBSL. A number of theoretical papers have suggested that Bremsstrahlung is responsible, at least in part, for the SBSL continuum.[45-54] Figure 1.6 schematically illustrates Bremsstrahlung radiation.

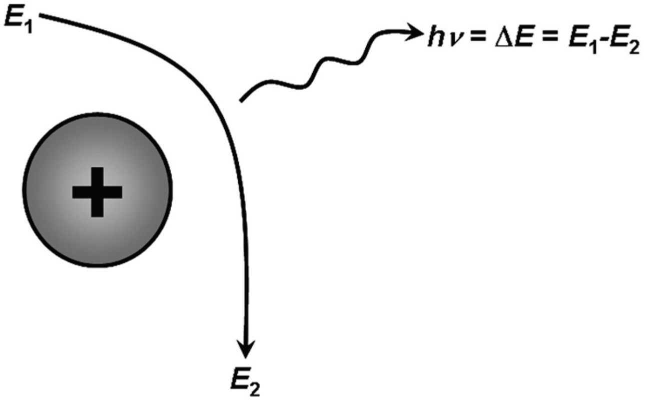

Figure 1.6 Bremsstrahlung radiation. A free electron interacts with either ionic or neutral species to produce broadband light as the electron is forced to decelerate.

The Bremsstrahlung spectrum is a function of temperature and degree of ionization, and the power at each wavelength can be expressed as

$$P(\lambda, T, \alpha) = \frac{128\pi}{9}\left(\frac{2\pi}{3k_BTm_e}\right)^{\frac{1}{2}} \frac{(n_c\alpha)^2e^6}{m_ec\lambda^2} {R_e}^3\Delta\tau_{SL}exp^{-\frac{hc}{\lambda k_BT}}$$

where *e* is the charge of an electron, *α* is the degree of ionization, *T* is the temperature, *λ* is the emission wavelength, n_c is the gas density, R_e is the radius of emission, *Δτ* is the emission time, and m_e is the mass of an electron. This model is relatively difficult to fit to sonoluminescence spectra because it requires some assumptions about the degree of ionization, which is not a trivial task. The Saha equation as formulated below predicts the ionization level of a plasma where only single ionization events are accessible:

$$\frac{N_eN_+}{N_a} = 2\frac{g_+}{g_a}\left(\frac{2\pi m_ek_BT}{h^2}\right)^{\frac{3}{2}} exp^{\frac{-I_{m+1}}{k_BT}}$$

Here, N_e is the number of free electrons, N_+ is the number of ions, N_a is the number of neutral atoms, g is the partition function, m_e is the electron mass, k_B is Boltzmann's constant, h is Planck's constant, T is the temperature, and I is the ionization potent[55]ial of the m+1 state. A simplistic estimation of the degree of ionization using the Saha equation at measurable SBSL temperatures gives temperatures too low to account for the emission intensity of SBSL if it were the result of Bremsstrahlung emission.[56-60]

Blackbody radiation comes from a plasma where photons and matter are in equilibrium with one another, implying many photon – particle collisions before the photon escapes (i.e., an optically dense plasma). The shape of the emission spectrum depends only on the temperature of the emitting plasma and is government by Planck's law, which dictates that the output power (B) of a blackbody at a given wavelength (λ) is

$$B_\lambda(T) = \frac{2\pi hc^2 {R_e}^2 \Delta\tau_{SL}}{\lambda^5}\left(e^{\frac{hc}{\lambda\, \mathrm{k}_B \mathrm{T}}} - 1\right)^{-1}$$

where $\Delta\tau$ is the emission time, and R_e is the emission radius. Other symbols are constants with the same assignation as in the Saha equation. There are several specific consequences of Planck's law. One is that the peak of the blackbody spectrum corresponds to a specific emitter temperature according to Wien's displacement law:

$$\lambda_{max} = \frac{2{,}897{,}768.5\ \mathrm{nm} \cdot \mathrm{K}}{T}$$

The other consequence relevant to this thesis is the Stefan-Boltzmann law, which dictates that the total emission intensity of a blackbody emitter is directly proportional to the fourth power of the emitter temperature. Figure 1.7 illustrates the properties of a blackbody emitter.

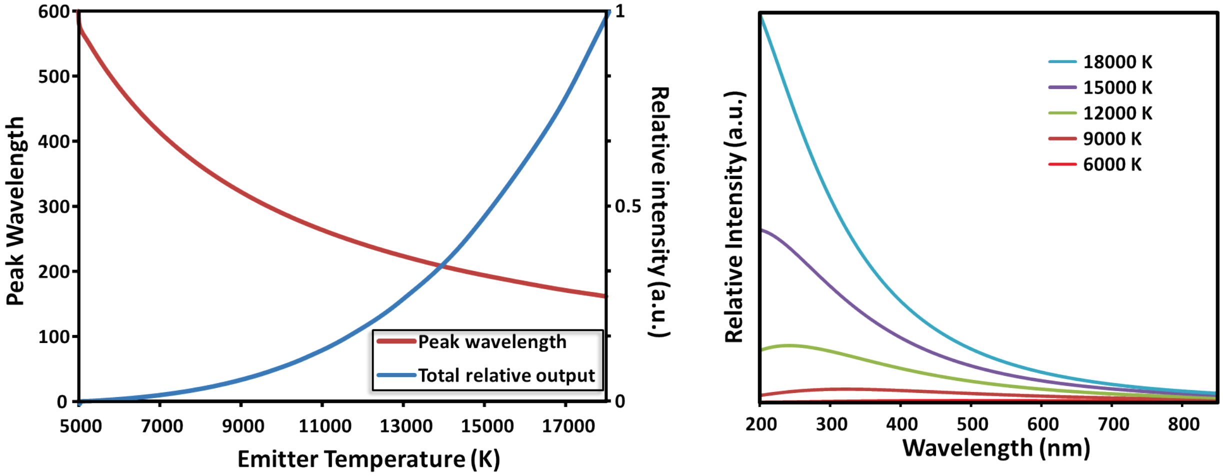

Figure 1.7 Blackbody radiation. Left: spectral properties of a blackbody emitter as predicted by Wien's displacement law and the Stefan-Boltzmann law. Right: spectra for a blackbody at various temperatures. Only relative intensities are given because absolute intensity depends on emitter area and emission time.

Blackbody emission generally describes the SBSL continuum emission with respectable fidelity. Figure 1.8 compares a blackbody fit to a Bremsstrahlung fit for a typical SBSL spectrum in water. The blackbody fits are able to reproduce the experimental spectrum well. There is some danger, however, that many broad, slow changing functions can be modeled reasonably well by a blackbody distribution.

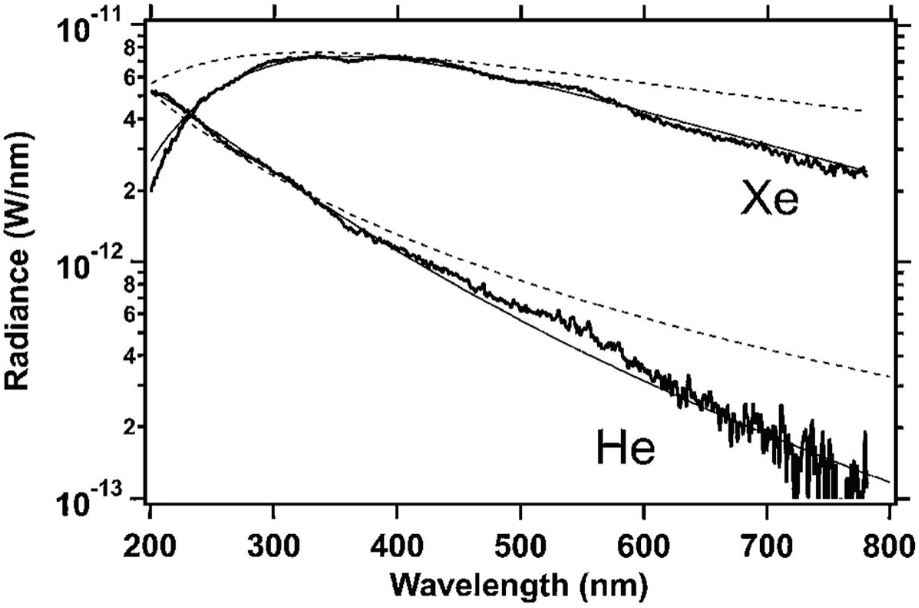

Figure 1.8 SBSL Spectra from Water with Xe and He. The solid lines are blackbody fits (8,000 K for Xe and 20,400 for He). The dashed lines are Bremsstrahlung fits (21,500 K for Xe, and infinite temperature for He).[61]

There are two significant objections to explaining the SBSL continuum as a blackbody. The first is that a blackbody emitter heating from ambient temperature to peak SBSL temperatures and cooling back down should not emit UV light during early heating and late cooling stages (i.e., low temperature emitters have no short wavelength component to their spectrum). Experiments have shown, however, that the duration of emission for UV wavelengths and red wavelengths is identical.[62-63] Figure 1.9 shows the SBSL pulse width for two different spectral regions measured by time-correlated single photon counting.

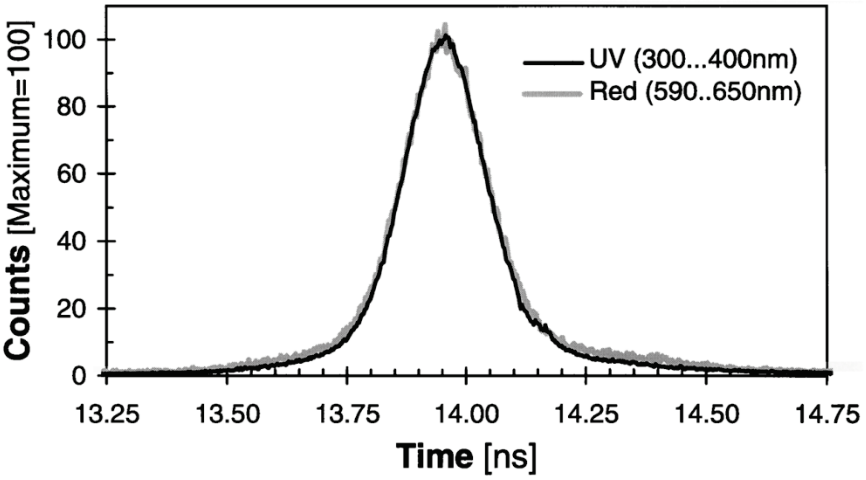

Figure 1.9 Pulse width comparison. The pulse widths in the UV and the red are identical, casting doubt on blackbody emission as the sole explanation for SBSL continuum emission.

The other major criticism of blackbody emission is that measured SBSL temperatures are much too low to create an opaque plasma, which is necessary for photon-particle equilibrium. As an example, the mean-free path of photons produced inside an 18,000 K xenon bubble is expected to be several hundred microns, which is much larger than the bubble itself.[64] One possible reconciliation is that the plasma has a relatively cool surface surrounding a hotter opaque plasma core (at least ~35,000 K).[64-65] Other recent work has provided additional strong experimental evidence for an opaque plasma forming during SBSL and is discussed in section 1.1.6.

It is noteworthy that decreasing the bubble size by increasing the frequency will change the emission spectrum. SBSL at 1 MHz produces a spectrum that fits better to Bremsstrahlung emission than to blackbody emission. This is consistent with SBSL being dominated by blackbody emission until the plasma radius is reduced to the point that the mean free path of photons is relatively large. Figure 1.10 shows the emission of the 1 MHz bubble and various efforts to fit the curve.[66]

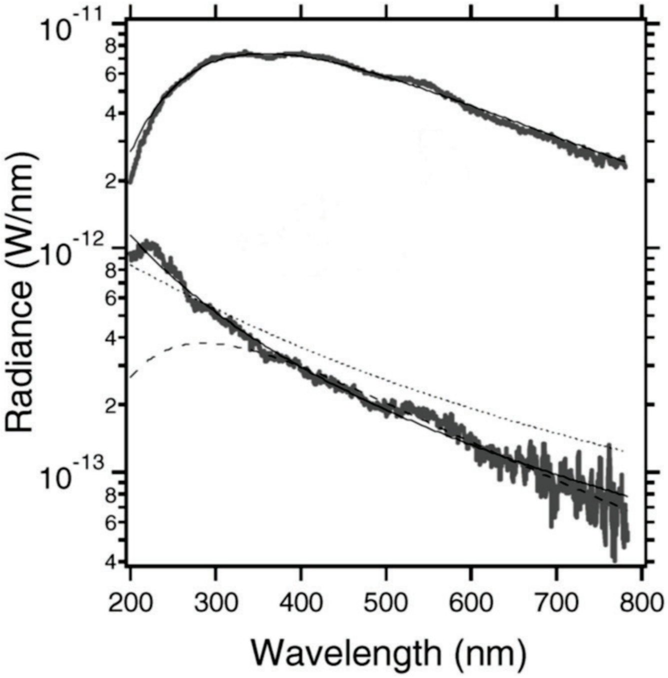

Figure 1.10 SBSL at 1 MHz. The top spectrum is SBSL emission from a bubble in water regassed with 3 Torr Xe and driven at 42 kHz. The spectrum is fit to an ideal blackbody at 8,000 K. The bottom spectrum is from a bubble driven at 1 MHz in water regassed with 600 Torr Xe. The spectrum is best fit by a Bremsstrahlung spectrum at 10^6 K (solid line). The other models shown are for Bremsstrahlung at 65,000 K (dotted line) and an ideal blackbody at 10,000 K (dashed line).[66]

1.1.6 Recent advances in SBSL

Recent work in the field of single-bubble sonoluminescence has provided a compelling, although perhaps not definitive, narrative of SBSL. The Putterman group has provided conclusive evidence of an opaque plasma in a sonoluminescing bubble and gives experimental evidence that would help explain why the emission time of SBSL has no wavelength dependence,[67] and creates the beginnings of a theoretical framework to explain how opacity can be achieved in such a small volume under SBSL conditions.

Unfortunately these experiments are performed at infrasonic or low audible frequencies, which produce very bright and long-lived bubbles,[68] but it is not certain that these lessons translate to the ultrasonic regime where most SBSL work and practical applications occur (recall that SBSL at 1 MHz behaves much differently than at a few tens of kHz).[66]

A novel sonoluminescence apparatus demonstrates the power of using low frequency. The acoustic pressure necessary for sonoluminescence is provided simply by dropping a stainless steel tube full of degassed phosphoric acid. Figure 1.11 shows the experimental apparatus and the application of pressure.

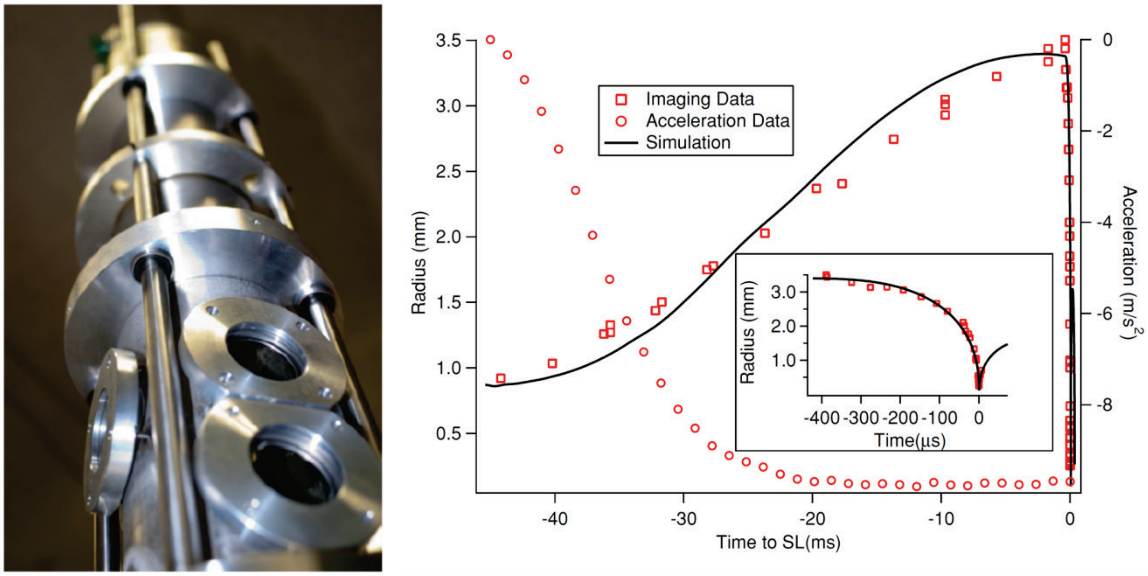

Figure 1.11 Drop tube SBSL. A bubble is introduced into a stainless steel tube with viewing ports (left), allowed to rise until it is in the desired location (detected by laser scattering), and then the magnetically-levitated tube is dropped. The tube enters free fall until it is abruptly stopped by impact. The tube acceleration is shown by the red circles; the magnet takes ~35 ms to shut off completely. The bubble grows during free fall (red squares). A 2.5 atmosphere pressure pulse travels through the liquid, rapidly collapses the bubble (inset), and induces SBSL.[68]

The bubble is very large at its maximum, larger than 3 mm in radius, and the impinging pressure front is large (in pressure amplitude). These two effects combine to produce an extremely bright (100 W) and long-lived (~150 ns!) luminescent event. The application of the acoustic pressure is non-uniform (the pressure front is traveling from bottom to top) and the bubble collapse is highly asymmetric (Figure 1.12).

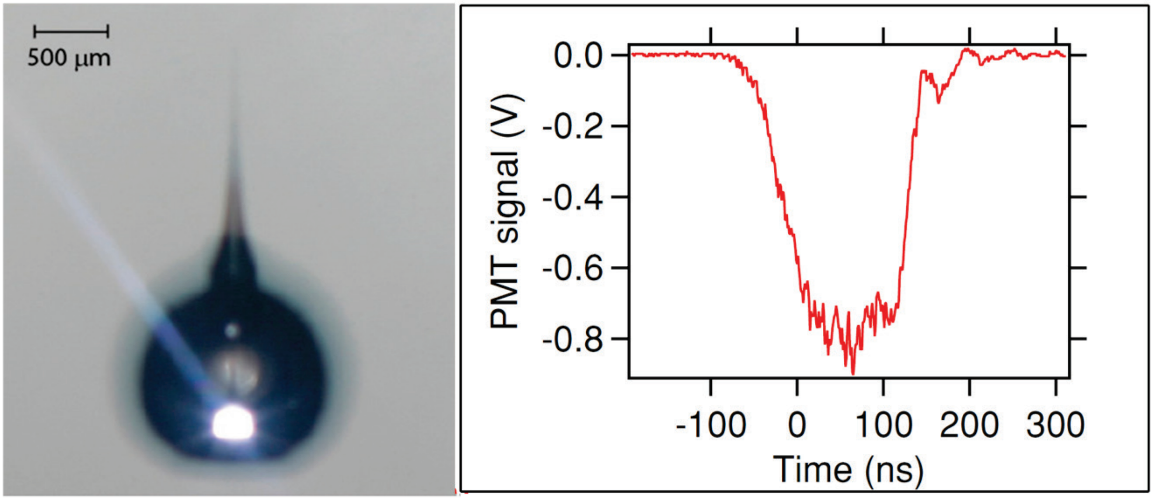

Figure 1.12 Drop tube SBSL. Left: image of backlight bubble exposed for 50 µs. The bright spot in the bottom is the sonoluminescence. Right: PMT signal from a typical experiment showing the long emission time.[68]

The conditions reached inside the bubble (10,200 K, measured by fitting the spectrum to Planck's law) are considerably less extreme as a result of the asymmetric collapse, but it is interesting that it was demonstrated that SBSL can still occur in a nonspherically collapsing bubble. It is also noteworthy that the plasma emission radius calculated from the blackbody fit and the bubble size (~100 µm) at its minimum match one another, indicating that a blackbody plasma fully fills the bubble. Dropping the tube from heights greater than 0.7 cm resulted in weaker sonoluminescence. This is presumably because shape instabilities limit the sonoluminescence, supporting the generally accepted notion that spherical collapse leads to higher energy concentration.

Other work in low-frequency SBSL systems (this time in a 40 Hz hammer tube) provides evidence that Bremsstrahlung and blackbody emission both contribute to SBSL emission.[67] Streak camera measurements suggested the formation of a dilute plasma, transitioning fully to an optically opaque, blackbody emitter, and back to a dilute plasma. The Bremsstrahlung radiation at the beginning and end of the SBSL emission could explain the lack of wavelength dependence on pulse width discussed earlier.

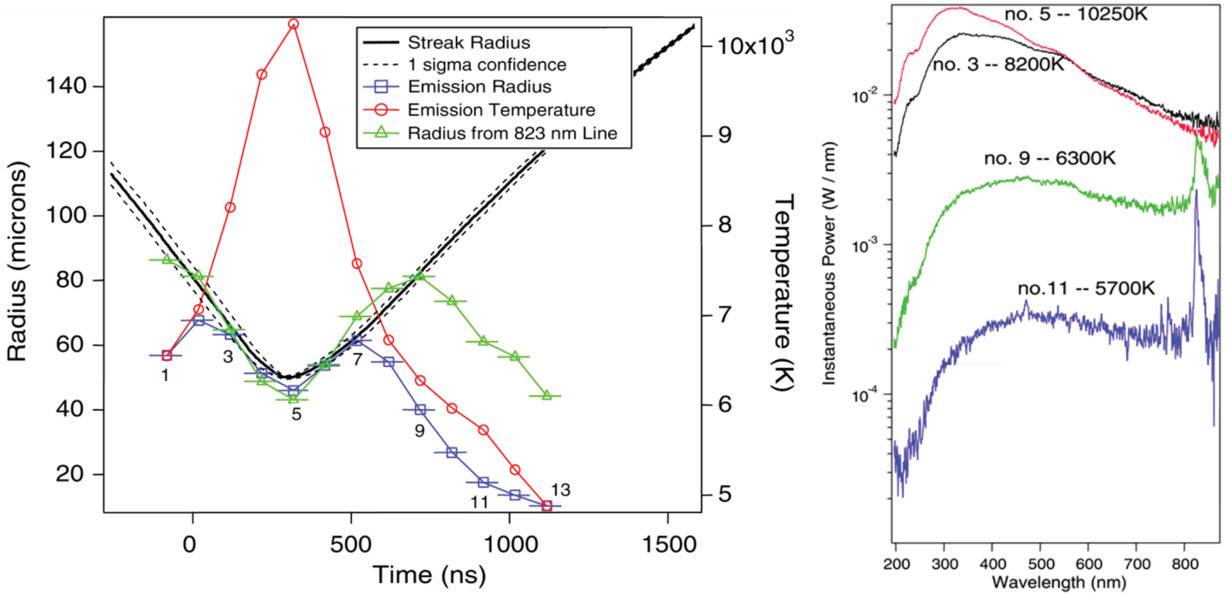

Figure 1.13 Time-resolved SBSL. Time-resolved spectra for a sonoluminescing xenon bubble in phosphoric acid at 40 Hz. Each spectrum on the right is separated by 100 ns and spectrum no. 5 coincides with the minimum radius, 500 ns into the emission. The spectra consist of a thermal continuum and an atomic line at 823 nm. The quality of the blackbody fit to the thermal portion of the spectrum is equally good for the data near the minimum radius as the data where the 823 line is prominent.[67]

The appearance and disappearance of the atomic emission line, coupled with the blackbody emission radius matching the measured bubble radius (by laser scattering) at minimum radius but diverging earlier and later, indicates the coexistence of an opaque blackbody and a dilute, weakly-ionized plasma when atomic emission is apparent and only an opaque blackbody when it is absent. The peak temperature of 10,250 K is still too low to explain the optical opacity with a traditional application of the Saha equation. It was proposed, therefore, that particle densities are too high to use the dilute plasma models that historically dominated the field. Instead, Debye shielding significantly decrease the effective ionization potential, leading to optical opacity at much lower temperatures than otherwise predicted. The proposed modified ionization potential (χ) is given as

$$\chi \approx \chi_0\left(1-2\gamma\alpha_B n_0^{\frac{1}{3}}\right)-\frac{e^2}{\delta_D}$$

where χ_0 is the unshielded ionization potential, γ is the polytropic ratio, α_B is the Bohr radius, n_0 is the number of atoms, e is the fundamental unit of charge, and δ_D is the distance an electron must move to be liberated: $\sqrt{kT/8\pi n_e e^2}$, where n_e is the number of free electrons. The number of free electrons is determined by the Saha equation, which in turn depends on the ionization potential. Determining self-consistent solutions to the problem yields two solutions. One is a stable, weakly ionized plasma, the other is unstable towards further ionization and in this model will proceed to complete ionization. While this does account for an opaque plasma, it is not physically viable and the theory still lacks a mechanism to stabilize the ionization.[67]

The mean free path of a photon under these conditions is calculated to be ~60 mm using the dilute gas model, roughly 1,000 times the emission radius.[69] There is little doubt, however, that the plasma is actually opaque and therefore highly ionized, supporting the Debye shielding model. The opacity of the SBSL plasma was demonstrated by the application of a laser to a large, bright bubble. The plasma absorbed the incident light and correspondingly grew brighter where the laser hit (Figure 1.14). Notably, this was not necessarily the case for a dimly luminescing bubble.[69]

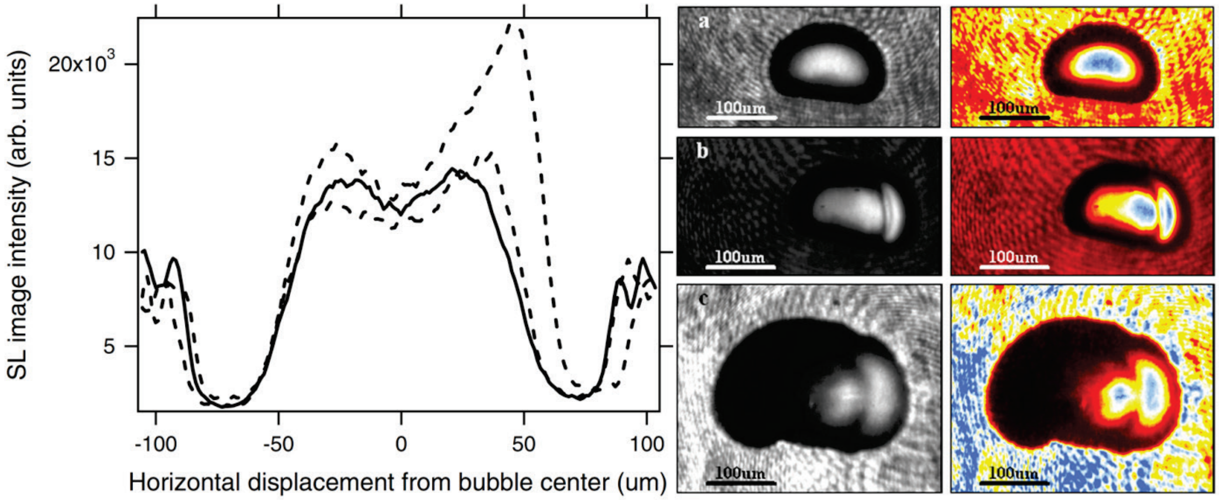

Figure 1.14 Optical opacity of SBSL. A large, bright bubble is struck with a laser. Left: Comparison of the horizontal profiles of laser heated bright bubbles. The solid curve is a bright bubble with no laser. The dashed curves are bubbles heated by low energy laser pulses of 1.2 mJ (upper) and 1.0 mJ (lower). The laser impinges from the right (positive displacement values). Right: Images and false color versions of the bubble with exposure before laser heating (a), 60 ns after laser heating (b), and 360 ns after laser heating (c). Laser is incoming from the right side.[69]

1.1.7 Comparison of multibubble and single bubble systems

While a single bubble is an attractive medium to study, it is not practical for preparative work. Multibubble sonoluminescence and sonochemistry is usually done using an ultrasonic horn (typically at around 20 or 40 kHz). These horns deliver much higher power in the form of progressive wave, inducing a huge number of nucleation events. At this high acoustic driving pressure rectified diffusion dominates and bubbles grow over their lifetimes. Eventually the bubble will become too large and grow inertially well into the high pressure phase of the acoustic field. At some point the applied positive pressure will overcome inertia and the bubble will collapse catastrophically, leading to intense compressional heating. Figure 1.15 compares SBSL bubble dynamics to multibubble dynamics.

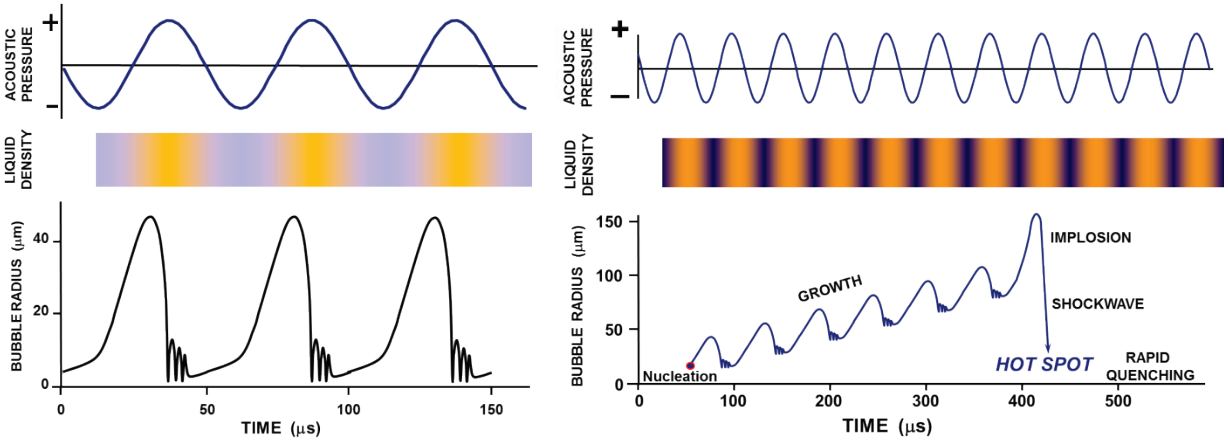

Figure 1.15 Multibubble versus single bubble. A bubble in SBSL is stable and collapses identically over millions of cycles. Bubbles in a multibubble system grow over time through rectified diffusion before final, catastrophic collapse.

The bubbles in multibubble sonochemistry interact strongly with each other through secondary Bjerknes forces. They also experience significant translational motion due to acoustic streaming, and they can interact with reactor walls. In general, the bubble collapse in a multibubble system is much less spherical than in a single bubble system and energy concentration is consequently much lower. Nonetheless, conditions in multibubble sonochemistry are still extreme enough to produce luminescence and initiate chemistry. Conditions measured by multibubble sonoluminescence indicate temperatures of several thousand Kelvin and pressures of hundreds of atmospheres.[70-72] The bubble core during multibubble sonoluminescence is still an opaque plasma.[73]

1.1.8 Conclusion

SBSL is a powerful technique for understanding the conditions during sonochemistry. The field is rapidly maturing, but fundamental questions remain. Agreement has still not been reached on the mechanism of light emission responsible for the continuum in SBSL. The evolution of the bubble spectrum over time with high resolution and at ultrasonic frequencies remains to be explored. Whether the lessons of low frequency SBSL apply to ultrasonic SBSL is also an important question that needs to be addressed.

1.2 Sonochemical synthesis of materials

1.2.1 Introduction

The extreme conditions achieved during sonochemistry are distinct from other conventional synthetic techniques such as photochemistry, wet chemistry, hydrothermal synthesis, or flame pyrolysis (Figure 1.16).[2-4, 11]

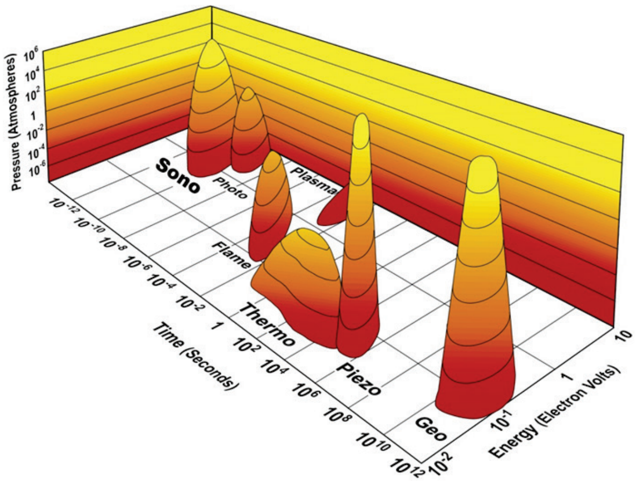

Figure 1.16 Islands of chemistry as a function of time, pressure, and energy. Sonochemistry occupies a unique short-time, high-energy, and high-pressure space.

The extreme, transient conditions produced during acoustic cavitation allow for the formation of unique materials and also permit syntheses on the benchtop in a room-temperature liquid that would otherwise require high temperatures, high pressures, or long reaction times. When a liquid is irradiated by high intensity ultrasound, high-energy chemical reactions occur. Sonochemistry can be employed in the synthesis of materials from volatile or nonvolatile precursors, but generally through different mechanisms (Figure 1.17). In the former case, the volatile precursor (e.g., a volatile organometallic compound) will produce free metal atoms generated by bond dissociation due to the high temperatures created during bubble collapse. These atoms can be injected into the liquid phase and nucleate to form nanoparticles or other nanostructured materials if appropriate templates or stabilizers are present in the solution. Nonvolatile precursors may still undergo sonochemical reactions, even outside of the collapsing bubbles by undergoing reactions with radicals or other high energy species produced from the sonolysis of vapor molecules inside the collapsing bubbles that then diffuse into the liquid phase to initiate a series of reactions (e.g., reduction of metal cations).

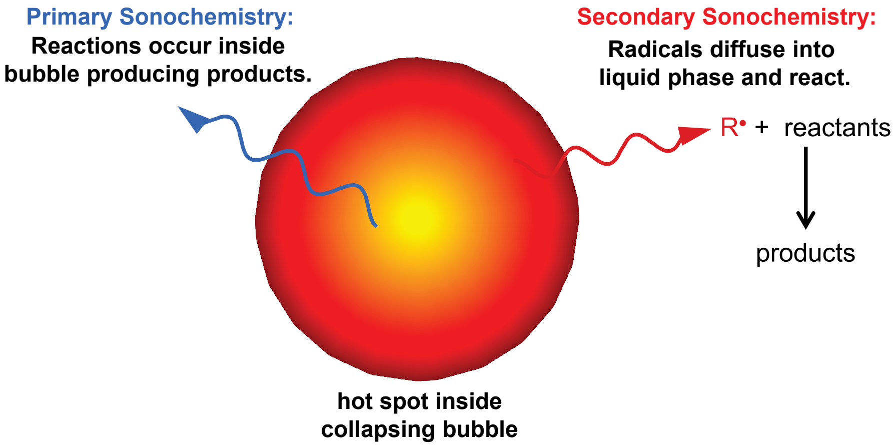

Figure 1.17 Primary sonochemistry and secondary sonochemistry for preparation of nanomaterials. An example of primary sonochemistry is the generation of metal atoms from sonolysis of weak metal-carbon bonds from volatile organometallic compounds inside the collapsing bubble that then diffuse into the bulk liquid to form functional nanomaterials. Secondary sonochemical products may arise from chemically active species (e.g., organic radicals from sonolysis of vapor) that are formed inside the bubble, but then diffuse into the liquid phase and subsequently react with solution precursors to form a variety of nanostructured materials.

The physical effects induced by high intensity ultrasound are also often accompanied by chemical consequences and find increasingly frequent use in materials synthesis. A trivial example is the simple heating of the bulk liquid: typical laboratory scale ultrasonic horns deliver roughly 10 to 100 watts of acoustic energy into the liquid during sonication. This ultrasonic power output must be calibrated, most commonly by calorimetry, in order to accurately report experimental conditions, but unfortunately many researchers overlook this critical parameter.

The most important physical phenomena for the preparation or modification of nanomaterials are microjets and shock waves. Microjets occur when bubbles collapse near an extended surface (i.e., surfaces several times larger than the bubble radius).[74] The inhomogeneity of the bubble's surroundings induces an asphericity into the bubble, which self-reinforces during collapse; this is similar to a shaped-charge explosive. These high speed microjets impact the surface and can cause pitting and erosion of surfaces leading to modification of surfaces and generation of surface nanostructures.

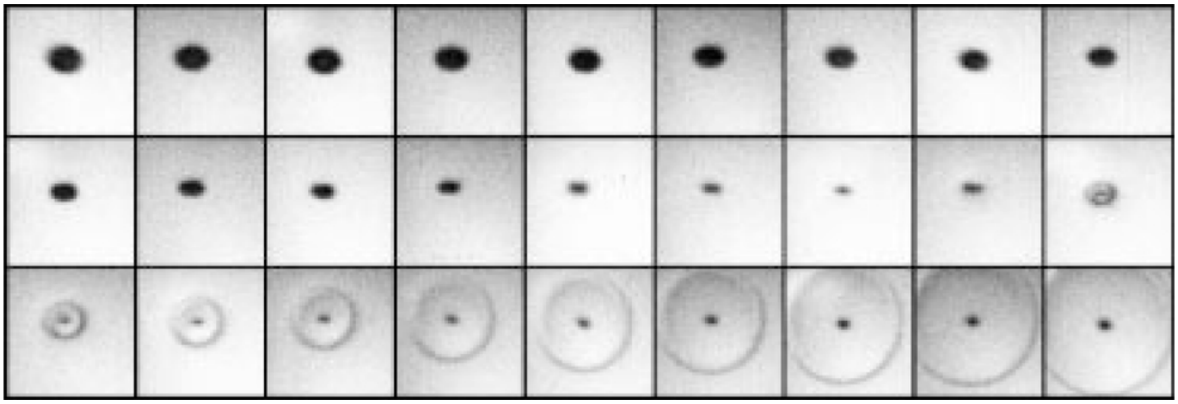

Figure 1.18 A spherical shock wave launched from a laser-induced collapsing bubble. The shock wave can reach 60 kbar with velocities of 4 km/s. Images were acquired at a shutter speed of 20.8 million frames per second, frame size was 1.5 x 1.8 mm^2, and the exposure time was 5 ns.

If the bubble is unperturbed by a surface, then the rapid rebound from its minimum radius is spherical. The compression of the surrounding liquid propagates outward as a shock wave from the rebounding bubble. A shock wave generated from a laser-induced collapsing bubble is shown in Figure 1.18.[75] Such shocks can reach pressures of 60 kbar and velocities of 4 km/sec in water. These shock waves can induce several different physical effects with chemical consequences, including enhanced mass transport due to strong turbulent mixing and acoustic streaming. In addition, shock waves can accelerate solid particles suspended in the liquid. Interparticle collisions can reach velocities of hundreds of meters per second, causing changes in particle size distributions, particle morphologies, and surface compositions.[76-77] Particle agglomeration (for malleable materials), particle fragmentation (for brittle materials) and exfoliation of layered materials into 2D layers have all been observed.[2-3, 9]

The applications of high intensity ultrasound to materials chemistry are diverse and rapidly increasing. Figure 1.19 gives a broad organizational schema for sonomaterials research to date. In this section, a sampling of the most important and most recent results of sonochemical applications to nanomaterials synthesis and preparation is presented. These applications are organized based on the chemical or physical effect of ultrasound exploited for the formation of nanomaterials: (1) primary sonochemistry employing volatile precursors, (2) secondary sonochemistry using non-volatile precursors, (3) materials created or modified through the physical effects of ultrasound (i.e., shock waves), and (4) materials where both chemical and physical effects of ultrasound have a synergistic impact.

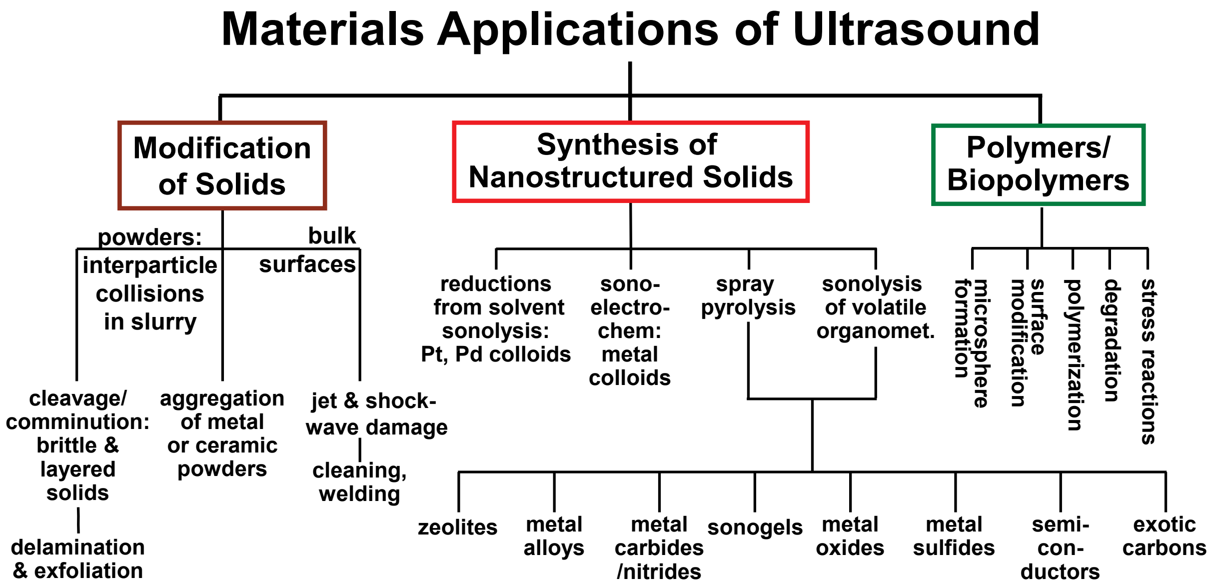

Fig 1.19 Materials applications of sonochemistry.

1.2.2 Chemical effects of ultrasound for nanomaterials preparation

A. Nanomaterials prepared from volatile precursors

Ultrasonic irradiation of volatile organometallic compounds such as $Fe(CO)_5$ or $Cr(CO)_6$ in a nonvolatile solvent (e.g., silicone oil or long-chain hydrocarbons) results in dissociation of the metal-carbonyl bonds and release of individual elemental metal atoms.[78] These atoms will be thermally excited to the point that they emit visible light analogous to emission from flame excitation and their atomic emission lines have been used to characterize the bubble conditions.[70] Nonvolatile solvents are necessary because additional vapor, especially of polyatomics, absorbs the available energy in the collapsing bubble (via rotational and vibrational molecular modes, ionization, and competing bond dissociation) and the conditions achieved are much less extreme. A variety of metallic nanomaterials can be produced in this way depending on the presence of surfactants, supports, or other reactants (Figure 1.20).[2]

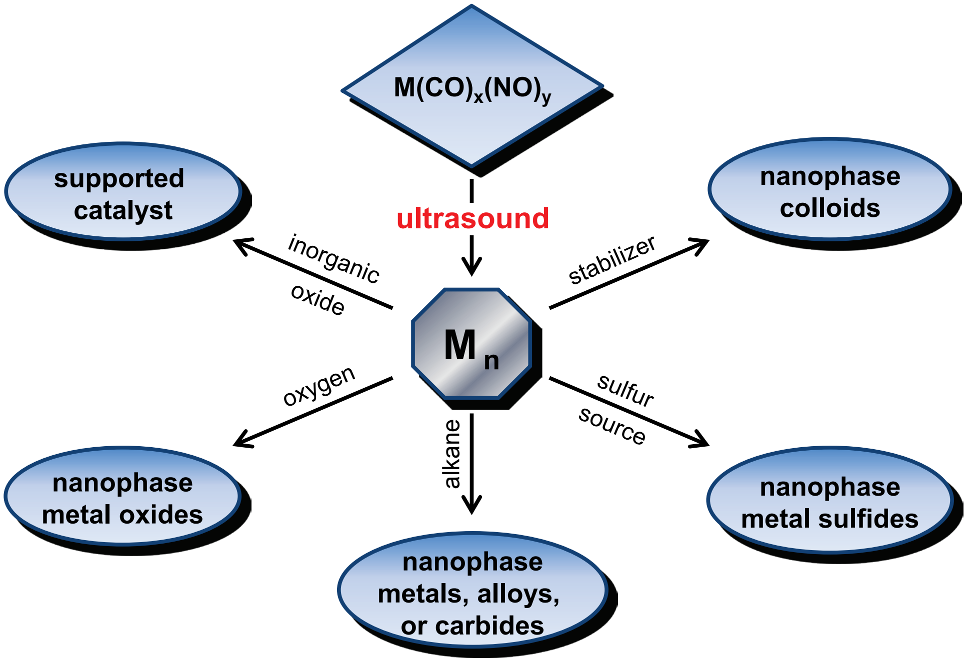

Figure 1.20 Sonochemical routes to nanostructured materials from volatile organometallic precursors.

Nanostructured metal particles were the first demonstration of the application of chemical effects of high intensity ultrasound for the preparation of nanomaterials.[79] Ultrasonic irradiation of solutions containing volatile organometallic compounds such as $Fe(CO)_5$, $Ni(CO)_4$, and $Co(CO)_3NO$ produced porous, coral-like aggregates of amorphous metal nanoparticles.[79-80] A classic example of this is the sonication of $Fe(CO)_5$ in decane at 0 °C under Ar, which yielded a black powder. The material was >96% iron, with a small amount of residual carbon and oxygen present from the solvent and CO ligands. SEM images revealed that the powder was an agglomerate of 20 nm iron particles. If surfactants such as oleic acid or polyvinylpyrrolidone were present in the solvent to stabilize the particles then individual iron nanoparticles were produced.[81] These iron nanoparticles had a diameter of ~8 nm and were amorphous (measured by electron diffraction). Magnetic studies indicated that these iron nanoparticles were superparamagnetic. Bimetallic alloy particles have also been prepared in this way. For example, sonication of $Fe(CO)_5$ and $Co(CO)_3NO$ led to the formation of Fe-Co alloy particles.[82-83] The composition was controllable by varying the ratio of the precursors in the solution. Alloy nanoparticles typically exhibit superior catalytic properties compared to monometallic nanoparticles.

The metal atoms decomposed from organometallic compounds during sonication are highly reactive and can react with other chemical substances in the solvent to form new materials. Nanostructured MoS_2, for example, was synthesized by the sonication of $Mo(CO)_6$ with elemental sulfur in 1,2,3,5-tetramethylbenzene under Ar.[84] MoS_2 prepared sonochemically differs dramatically in morphology from conventional MoS_2: conventional MoS_2 is a layered, platelike material, while sonochemically synthesized MoS_2 exhibited a spherical morphology with an average diameter of 15 nm. TEM examination revealed that sonochemically prepared MoS_2 contained more defects and showed many more edges, although both MoS_2 materials had the same interlayer distance of 0.62 ± 0.01 nm. MoS_2 has been frequently used as a hydrodesulfurization catalyst in the petroleum industry to remove sulfur from crude oil before combustion. Sonochemically prepared MoS_2 exhibited substantially higher catalytic activity than conventional MoS_2 for the hydrodesulfurization of thiophene. The increase in catalytic activity was attributed to the higher surface area and more edges and defects found in the sonochemically prepared MoS_2 (Figure 1.21).

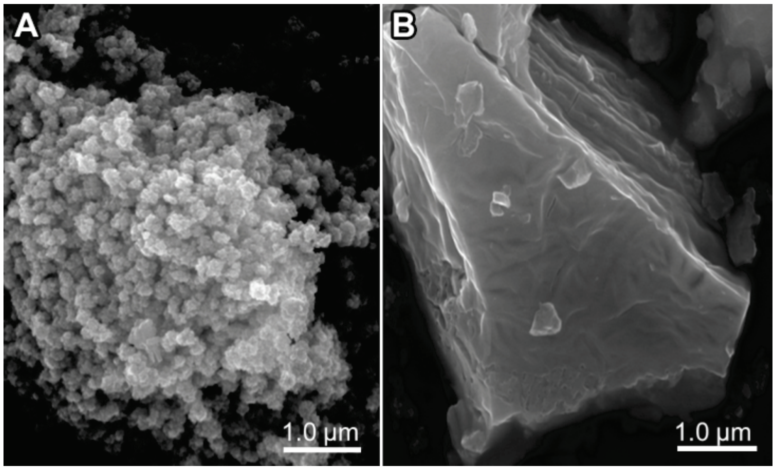

Figure 1.21 MoS_2. SEM images of (A) sonochemically synthesized MoS_2 and (B) conventional MoS_2.[84]

The preparation of refractory nanomaterials remains problematic because most high temperature routes lead to agglomeration of precursors or intermediate states during the synthesis. Sonochemical routes, however, produce the needed high temperatures on the nanoscale in the localized hot spots of the collapsing bubble. As a specific example, sonochemistry provides a convenient approach to prepare nanostructured metal carbides that exhibit excellent catalytic activity.[85-86] Mo_2C and W_2C are particularly interesting catalysts because they show catalytic activity similar to platinum group metals, but their syntheses are challenging because of the refractory nature of metal carbides. The sonication of $Mo(CO)_6$ or $W(CO)_6$ in hexadecane leads to the formation of amorphous metal oxycarbides. Removing oxygen by heating under 1:1 CH_4/H_2 leads to the formation of nanostructured Mo_2C or W_2C as porous aggregates of small nanoparticles with surface areas of 130 m^2/g and 60 m^2/g for Mo_2C and W_2C, respectively. They exhibit activities and selectivities similar to platinum for dehydrogenation reactions.[85] In addition, these nanostructured metal carbides show superior activity, selectivity, and stability for the hydrodehalogenation of organic pollutants.[86] Metal nitrides can also be prepared by the sonication of metal carbonyl compounds under a reductive gas mixture of NH_3 and H_2 at 0 °C.[87]

When a sacrificial template (e.g., microspheres of silica or carbon) is present in the sonicated solution, the free metal atoms produced by ultrasonic irradiation of volatile organometallic compounds can deposit onto the template to form different structured materials. For example, ultrasonic irradiation of $Mo(CO)_6$, sulfur, and silica nanoparticles in isodurene under Ar forms MoS_2–coated silica nanoparticles.[88] Replacing Ar with air and removing sulfur from the system yields MoO_3–coated silica nanoparticles. Etching of the silica component by HF leaves hollow MoS_2 or MoO_3. These hollow MoS_2 nanoparticles had better catalytic activity toward the hydrodesulfurization of thiophene than even sonochemically prepared MoS_2 nanoparticles due to the significantly increased number of edge defects and improved accessibility to both inner and outer surfaces of the hollow structures. Amusingly, the hollow MoO_3 spheres, which are initially amorphous, upon heating crystallize into hollow single crystals.[88]

Ultrasonic irradiation of $Fe(CO)_5$ in the presence of carbon nanoparticles provided a facile method for the preparation of hollow hematite.[89] Carbon nanoparticles were used as a template that spontaneously removes itself through combustion induced by the rapid oxidation of the outer Fe shell upon exposure to air. Porous Co_3O_4 was produced in a similar fashion when carbon nanotubes were used as the template and $Co_4(CO)_{12}$ as the precursor.[90] Co_3O_4 prepared in this way was found to be an excellent electrode material for lithium-ion batteries.

A sonochemical method has also been used to synthesize single-walled carbon nanotubes via ultrasonic irradiation of a solution containing silica powder, ferrocene, and *p*-xylene (Figure 1.22).[91] In this synthesis, ferrocene was used as the precursor for the Fe catalyst, *p*-xylene was used as a carbon precursor, and silica powder provided nucleation sites for the growth of carbon nanotubes. Ferrocene was sonochemically decomposed to form small Fe clusters and *p*-xylene was pyrolyzed to carbon atoms and carbon moieties. This approach provides a convenient synthetic route for the preparation of carbon nanotubes under ambient conditions. In addition, no extra purification steps were needed in this process, which opens up the possibility for large-scale ultrasonic synthesis of high-purity, single-walled carbon nanotubes.

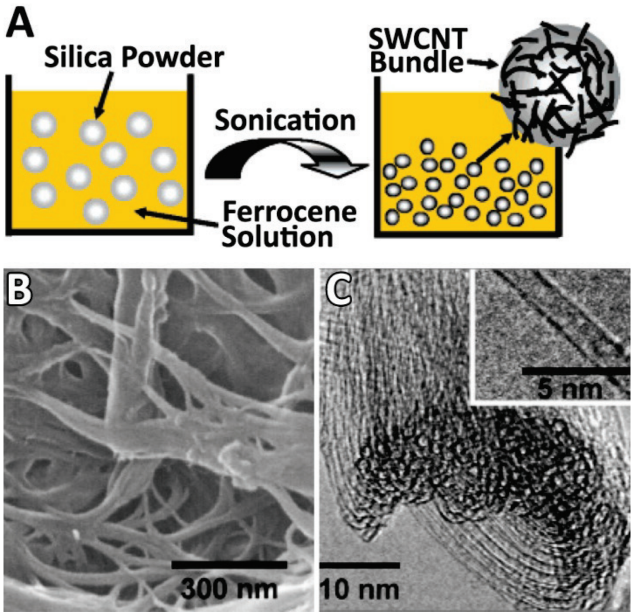

Figure 1.22 Carbon nanotubes. (A) Schematic illustration of the sonochemical preparation of single-walled carbon nanotubes on silica powders. (B) SEM image of carbon nanotube bundles on polycarbonate filter membrane. (C) HRTEM images of single-walled carbon nanotubes within the bundles.[91]

Ultrasonic irradiation of common organic solvents such as $CHCl_3$, CH_2Cl_2, and CH_3I with HF-etched Si nanowires yielded hydrocarbon materials with diverse structures (e.g., nanotubes and nano-onions).[92] The nanostructured SiH_x on the Si nanowires served as a template for the nucleation of carbon species formed from the pyrolysis of volatile organics inside the collapsing bubbles.

B. Nanomaterials prepared from nonvolatile precursors

Sonochemistry is also commonly used to prepare nanostructured noble metals when nonvolatile precursors are dissolved in a volatile solvent (usually water or alcohols). In these cases, sonolysis of the solvent vapor produces strong reductants that have a number of advantages over traditional reduction techniques: no additional reducing agents are required, the reduction rate is generally very fast, and very small nanoclusters can be made in this way when suitable stabilizers are present.

Ultrasonic irradiation of water generates highly reactive H• and OH• radicals which are responsible for redox chemistry. These reactive radicals can further react with organic additives (e.g., 2-propanol or ethanol) in the solution to generate secondary radicals (R•) which can dramatically promote the reduction rate. Overall, the process (including competing reactions) can be summarized as follows:

$$H_2O \rightarrow H\bullet + OH\bullet \quad (1)$$

$$H\bullet + H\bullet \rightarrow H_2 \quad (2)$$

$$H\bullet + OH\bullet \rightarrow H_2O \quad (3)$$

$$OH\bullet + OH\bullet \rightarrow H_2O_2 \quad (4)$$

$$RH + OH\bullet \text{ (or } H\bullet) \rightarrow R\bullet + H_2O \text{ (or } H_2) \quad (5)$$

$$M^{n+} + nR\bullet \text{ (or } H\bullet) \rightarrow M^0 \quad (6)$$

$$mM^0 \rightarrow M_m \ \text{ (M = noble metal)} \quad (7)$$

Unlike metallic particles prepared from the sonication of volatile organometallic compounds, which are typically amorphous, materials produced from nonvolatile compounds are usually well crystallized.

Nanostructured noble metals (e.g., Au, Ag, Pt, and Pd) can be prepared by a large number of synthetic routes, including controlled chemical reduction, solvothermal synthesis, photochemical reduction, and radiolytic reduction. Sonochemical preparation also provides a facile approach for the production of spherical metal nanoparticles.[93-99] A systematic study carried out by Grieser *et al.* on the effect of ultrasound on the synthesis of noble metal nanoparticles has shown that the particle size is largely determined by solvent/surfactant properties: particle size is inversely related to alcohol concentration and alkyl chain length.[93] This observation led to the conclusion that alcohol molecules adsorbed to the surface of nuclei can limit the growth of small nanoparticles. The other possible explanation for this result is that more secondary radicals can form at higher alcohol concentrations which leads to faster reduction rates which in turn results in smaller and possibly more uniform particles.

Sequential sonochemical reduction of two different metallic ions will result in bimetallic core-shell nanoparticles. For example, the sonochemical reduction of a solution containing both Au(III) and Pd(II) ions led to the formation of nanoparticles with a Pd shell over an Au core.[94] The core-shell structure is a result of the difference in reduction potential between Pd(II) and Au(III) ions. When Au and Pd nanoparticles are formed simultaneously, excess Au(III) ions will oxidize Pd nanoparticles to form Au and Pd(II) ions. The Pd shell can only form once the gold ions have all been reduced into nanoparticles. A similar approach can be used to sonochemically prepare Au/Ag and Pt/Ru core-shell particles.[95-96]

Sonochemical methods have also been developed to prepare nonspherical nanoparticles. For example, gold nanorods have been synthesized by the sonochemical reduction of $HAuCl_4$ in the presence of $AgNO_3$, CTAB, and ascorbic acid.[97] The solution pH influences the aspect ratio of the gold nanorods: as the pH of the solution increases, the average aspect ratio of the gold nanorods decreases. Ultrasound-induced reduction of $HAuCl_4$ onto pre-synthesized gold seeds using polyvinylpyrrolidone (PVP) as a stabilizing polymer leads to the formation of monodispersed gold nanodecahedra.[98] This sonochemical method can significantly increase the yield and reproducibility. Ag nanoplates have also been synthesized by a similar ultrasound-assisted Ostwald ripening process using Ag nanoparticles as seeds.[99] These platelike nanostructures served as templates to fabricate ringlike metal structures via a simple displacement reaction under ultrasonic irradiation. Ag nanowires and nanorods have also been prepared by sonicating suitable Ag precursors.

Polymers or small molecules can act as structure directing agents as well as stabilizers. Ultrasonic irradiation of a $HAuCl_4$ solution containing α-D-glucose produced gold nanobelts with a width of 30~50 nm and a length of several micrometers.[100] These gold nanobelts are formed through 3 steps: (1) formation of gold nanoparticles via sonochemical reduction, (2) aggregation and room-temperature temperature sintering of gold nanoparticles directed by α-D-glucose, and (3) further growth along the Au[111] direction with recrystallization finally yielding the isolated single-crystalline gold nanobelts.

Highly fluorescent, stable, and water-soluble Ag nanoclusters (diameter less than 2 nm) have been successfully prepared by the sonication of aqueous $AgNO_3$ solutions with dissolved polymethylacrylic acid (PMAA) (Figure 1.23).[101] The charged carboxylate groups of PMAA can stabilize clusters of Ag atoms in solution and prevent further growth of nanoclusters to form large nanoparticles. The optical and fluorescence properties of these Ag nanoclusters can be controlled by varying synthetic conditions, e.g., sonication time, stoichiometry of the carboxylate groups relative to Ag^+, and the polymer molecular weight. Ag nanoclusters, as a new kind of nanoparticle fluorophore, are likely to find widespread applications in bioimaging, chemical and biosensing and single-molecule studies.

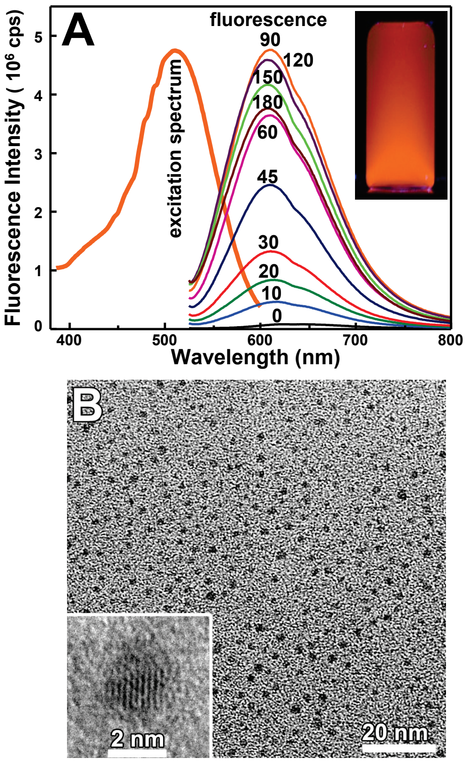

Figure 1.23 Silver nanoclusters. (A) fluorescence emission spectra of Ag nanoclusters prepared by a sonochemical method (inset: vial containing a solution of the Ag nanoclusters illuminated by a 365 nm UV lamp). (B) TEM images of as-prepared Ag nanoclusters after 90 min sonication (inset shows a single magnified Ag nanocluster).[101]

The sonochemical reduction of nonvolatile precursors in solution is not limited to noble metals. For example, trigonal Se nanowires were prepared by the sonication of amorphous Se colloids in alcohol solvents without templates or surfactants (Figure 1.24).[102] Nanocrystals of trigonal Se were nucleated sonochemically and acted as seeds for the growth of Se nanowires through a solid-solution-solid transformation mechanism driven thermodynamically: amorphous Se has a higher free energy than trigonal Se.

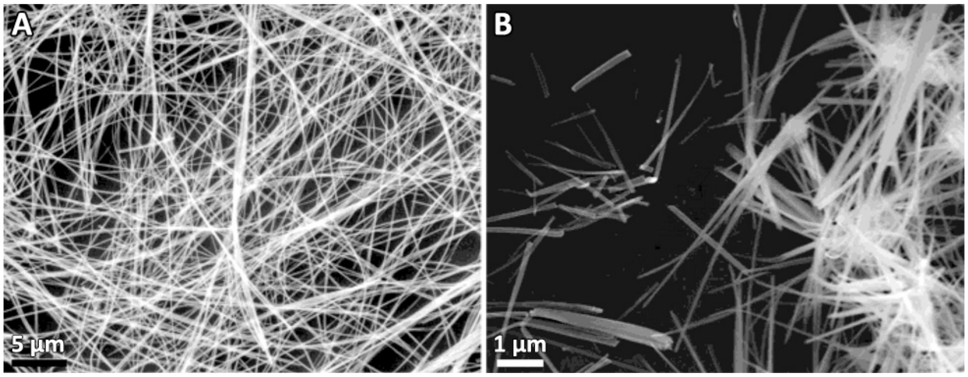

Figure 1.24 Se nanowires. SEM images of (A) typical trigonal Se nanowires synthesized by sonication of amorphous selenium grown in ethanol at room temperature and (B) grown from amorphous Se colloids in ethanol without sonication.[102]

Various metal oxides and metal chalcogenides have also been prepared by sonochemical methods with nonvolatile precursors. A typical synthesis of these types of materials involves the sonication of a solution containing a metal salt and an oxygen or chalcogen source (e.g., air for oxygen, thiorea for sulfur, selenourea for selenium, or sometimes, a sulfate or selenate). Reactive species such as reactive radicals or atoms (O• or S•) can react with metal ions in the solution to form metal oxides or metal chalcogenides. If proper structure directing agents are used, different nanostructured materials (e.g., hollow spheres, nanorods, nanowires, or nanocubes) can be obtained. For example, ultrasonic irradiation of $CdCl_2$, $NaSeSO_3$, and ammonia leads to the formation of hollow CdSe spheres.[103] $CdCl_2$ was hydrolyzed under the basic conditions to form $Cd(OH)_2$ which acted as an in situ template for the sonochemical formation of hollow structures. This process can be written as follows:

$$H_2O \rightarrow H\bullet + OH\bullet \qquad (8)$$

$$2H\bullet + SeSO_3^{2-} \rightarrow Se^{2-} + 2H^+ + SO_3^{2-} \qquad (9)$$

$$Cd(OH)_2 + Se_2– \rightarrow CdSe + 2OH^- \qquad (10)$$

$$nCdSe \rightarrow (CdSe)_n \qquad (11)$$

Hetero-structured materials such as core/shell SnO_2/CdS and ZnO/CdS have also been prepared via sonochemical deposition of metal sulfide onto metal oxides.[104] In a similar fashion, by exploiting the hydrogen radicals formed from sonolysis of water vapor inside the collapsing bubbles, copper hydride (CuH) can be produced via ultrasonic irradiation of a copper (II) aqueous solution.

As a synthetic tool, sonochemistry can deposit nanoparticles formed in situ onto pre-existing substrates (e.g., polystyrene spheres, silica particles, carbon nanotubes, or a polymer matrix).[105-107] Graphene has emerged as a new 2D material with unique electrical, thermal, and mechanical properties. Catalyst assemblies of nanostructured materials with exfoliated, single-layer graphene (often prepared sonochemically, as discussed later) have shown great promise for a wide range of applications including sensors, fuel cells, lithium-ion batteries, photocatalysts, and fuel cells. Ultrasonic irradiation of graphene oxide with $HAuCl_4$ in water produced well-dispersed reduced graphene oxide/Au composites by simultaneous or sequential reduction procedures.[108] The formation of reactive OH• and H• radicals via sonolysis of water vapor inside collapsing bubbles is responsible for the formation of reduced graphene oxides and the reduction of Au(III) to Au nanoparticles.

Aligned nanostructures can be achieved with the help of ultrasound. For example, vertically aligned ZnO nanorods were prepared on substrates such as Zn sheets, Si wafers, glass, and polycarbonate membranes by sonicating a precursor solution containing Zn^{2+}.[109] Ultrasonic irradiation rapidly induces the anisotropic growth of ZnO along the (0001) direction on the substrate. The alignment is presumed to be due in part to the relative depletion of Zn^{2+} concentration at the base of the growing rods relative the tops of the rods. Oxygen atoms, hydroxyl radicals or hydroperoxyl (HO_2) radicals formed by the sonication of water in air are thought to be responsible for the formation of these ZnO rods. Compared to a conventional hydrothermal process, the growth rate of ZnO is increased by 10 fold, with an average growth rate of ~500 nm/h.

1.2.3 Physical effects of ultrasound for nanomaterials synthesis

The most important physical effects of high intensity ultrasound arise from the high-speed jets and intense shock waves induced by cavitation. They have been frequently used to prepare emulsions, agglomerate malleable materials, break down friable materials, modify solid surfaces, and exfoliate layered materials. Enhanced mass transfer as a consequence of acoustic streaming and bulk thermal heating are other physical effects of high intensity ultrasound.

A good example of exploiting the physical effects of ultrasound is the enhancement of intercalation of guest substances into layered materials first developed by Green, Suslick and coworkers.[110] In more recent work, graphite, with its layered planar structure, can accommodate in between each graphene layer guest molecules or atoms to form graphite intercalation compounds, but the formation of intercalation compounds is usually a very slow process. Ultrasonic irradiation, however, can dramatically increase the reaction rate.[111] For example, potassium intercalated compounds (KC_8) can be prepared by the sonication of graphite with potassium under an Ar atmosphere in 3 minutes while normal preparation methods require 1~8 hours via a solid state reaction at high temperature under an inert atmosphere. H_2PtCl_6 can also be intercalated into graphite layers to prepare Pt nanoparticles intercalated in graphite after exposure to an H_2 gas stream.[112] The sonication of potassium intercalated graphite in ethanol can generate carbon nanoscrolls (Figure 1.25).[113] The conversion efficiency is very high, up to ~80%, compared to a reaction in the absence of ultrasound, which results in very few nanoscrolls. The reason for the formation of carbon nanoscrolls is not fully understood, but ultrasound provides the necessary mechanical energy to overcome the van der Waals force between each graphene layer. The individual exfoliated graphene layers can then fold via intralayer interactions to reach a stable structure in the solvent.

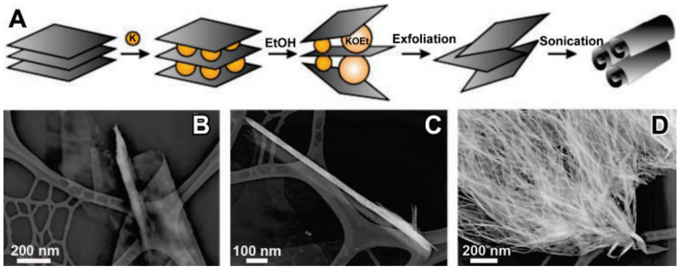

Figure 1.25 carbon nanoscrolls. (A) Schematic illustration of the intercalation and exfoliation process to prepare carbon scrolls. TEM images of (B) a thin layer of graphite sheets in the process of scrolling, (C) an isolated carbon nanoscrolls with open ends, and (D) a bundle of scrolled carbon nanosheets.

Ultrasound has become a formidable tool for the chemical preparation of single and few layer graphene. In a typical synthesis of graphene oxide, pristine graphite is oxidized by Hammer's method to form graphite oxide, which has an increased interlayer distance relative to graphite and the van der Waals force is consequently weaker. After mild sonication (bath sonication is sufficient), single-layered graphene oxides can be produced which can then be chemically reduced to graphene. A more straightforward method for the preparation of graphene is the direct liquid-phase exfoliation of graphite by sonication. To obtain high yields of exfoliated graphenes from graphite, the surface energy of the solvent must match the surface energy of graphite, 40~50 mJ/m^2. Sonication of graphite in suitable solvents (e.g. N-methyl-pyrrolidone (NMP)) can lead to the formation of single layer and few-layer graphenes.[114] Ultrasound is also frequently used to disentangle single-walled carbon nanotubes, which usually form bundles due to van der Waals forces.

This approach can be generalized to other layered materials such as $MoSe_2$, $MoTe_2$, MoS_2, WS_2, $TaSe_2$, $NbSe_2$, $NiTe_2$, BN, and Bi_2Te_3, all of which can be exfoliated in the liquid phase to prepare single-layered nanosheets (Figure 1.26).[115] Ultrasound is a broadly useful tool for overcoming the attractive forces between individual layers to break 3*D* layer-structured materials down to 2*D* planar structures.

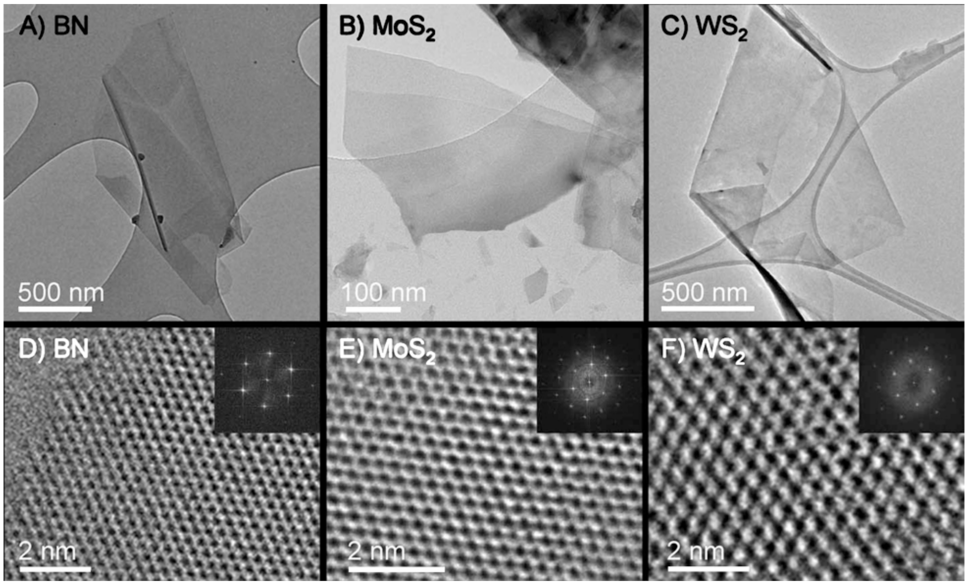

Figure 1.26 TEM images of individual nanosheets. (A to C) Low-resolution TEM images of flakes of BN, MoS_2, and WS_2, respectively. (D to F) High-resolution TEM images of BN, MoS_2, and WS_2 monolayer (Insets) Fast Fourier transforms of the images.

The impact of ultrasonic shock waves on pre-existing particles in a liquid is also an interesting use of the physical effects of ultrasound. For instance, high intensity ultrasound can drive metal microparticles suspended in liquid slurries into one another at high speeds (hundreds of meters/sec) to induce local melting at the point of collision and consequent agglomeration (Figure 1.27).[76-77]

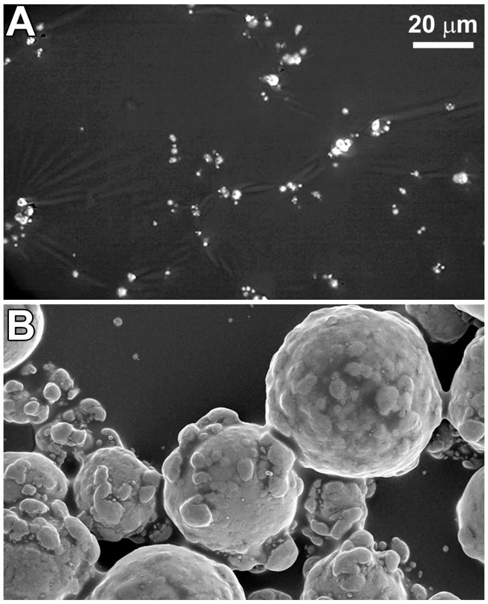

Figure 1.27 Interparticle collisions. Effects of ultrasonic irradiation on slurries of fine Zn powder (5 μm diameter, roughly spherical). (A) SEM before ultrasonic irradiation. (B) Dense agglomeration after 90 min sonication of 2% w/w decane slurry at 20 kHz, 50 W/cm2, 283 K, where agglomerates are made from ~1000 of the initial particles and loadings up to 50% w/w show similar results. The same magnification is used in both images.[77]

This can only happen with metals with relatively low melting point (e.g., Sn, Zn, Cr, and barely Mo). If the melting point of the metal is higher than ~3000 K, no melting at the point of impact occurs. Furthermore, agglomeration of metal particles occurs only over a fairly narrow range of radius in the regime of a few microns. Neither particles too large nor too small will be accelerated to a sufficient velocity to induce local melting and consequent agglomeration (Figure 1.28).

Such interparticle collisions during ultrasonic irradiation of slurries of high temperature superconductors can significantly improve their properties.[116-117] For example, the superconducting properties of $Bi_2Sr_2CaCu_2O_{8+x}$ are significantly improved after sonication as a slurry in decane due to the enhancement of intergrain coupling resulting from interparticle collisions.[116] Intergrain coupling controls the critical magnetic field (Jc) that limits the fields that can be formed with $Bi_2Sr_2CaCu_2O_{8+x}$ superconductors.

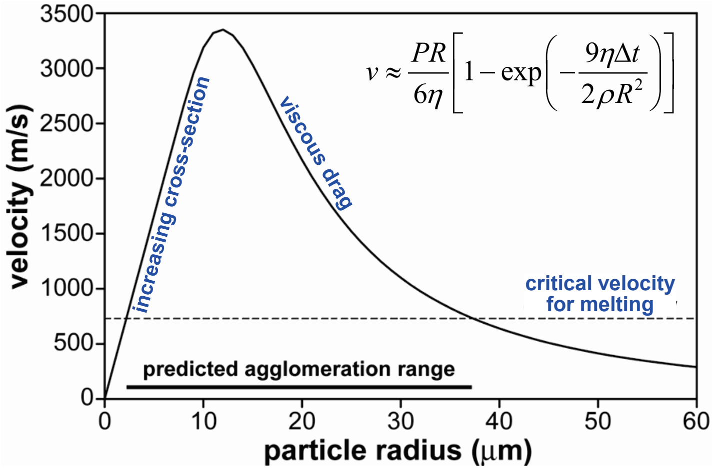

Figure 1.28 Threshold behavior. Calculated velocities of interparticle collisions of Zn powder during ultrasonic shock waves as a function of particle radius. The critical velocity necessary for collisional agglomeration determines the particle size range over which agglomeration will occur.

Ultrasound can also be used to promote the diffusion of dopant ions into spherical nanoparticles. For example, high intensity ultrasound is used to prepare Mg^{2+} doped ZnO nanoparticles with tunable photoluminescence (from yellow to blue, Figure 1.29).[118] The quantum yield of these Mg^{2+} doped ZnO nanoparticles is very high, >60% under optimal conditions. XRD and HRTEM results indicate that no MgO phase exists in the ZnO nanoparticles. Ultrasonic irradiation of a slurry containing Au colloids and TiO_2 particles can lead to the formation of Au nanoparticles intercalated into a mesoporous TiO_2 structure which shows enhanced photocatalytic properties.[119]

The microjets and shock waves produced by high intensity ultrasound near solid surfaces can also cause physical changes on the surfaces of particles and substrates. For instance, high intensity ultrasound has been applied to improve anticorrosion surface coatings. Generally, even pure aluminum metal is coated by a few nm thick oxide layer. This layer is not able to protect fully against corrosion agents and is often not strongly adhered to the underlying metal. The corrosion protection and adhesion properties, however, can be improved via ultrasonic treatment.[120] After ultrasonic irradiation, the existing oxide layer is removed and a newly active oxide layer forms that has been shown to exhibit superior resistance to corrosion.

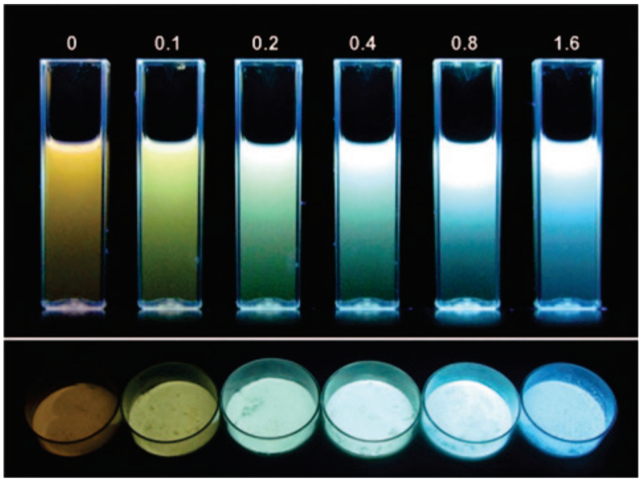

Figure 1.29 Photographs (under UV light) of ethanol solutions (upper) and dry powders (lower) of Mg/ZnO nanoparticles prepared by ultrasonic irradiation of ZnO with Mg^{2+} with different Mg/Zn ratios.[118]

Ultrasonic irradiation can also improve sol-gel syntheses, a versatile technique for the preparation of nanostructured metal oxides. Application of ultrasound during a sol-gel process can accelerate the hydrolysis process and create metal oxides with narrower size distributions, higher surface area, and improved phase purity. For example, TiO_2, ZnO, CeO_2, MoO_3, V_2O_5, and In_2O_3 have all been prepared by the ultrasonic irradiation of their respective precursor solutions.[121-122] TiO_2 nanoparticles prepared by ultrasonic irradiation of the precursor solution are more photocatalytically active than commercial TiO_2 nanoparticles.[121] The increase in photocatalytic activity is attributed to the improved crystallinity of TiO_2 which is achieved due to accelerated hydrolysis under sonication. Ultrasound can also induce the formation of unique morphologies during the synthesis of nanostructured metal oxides in the presence of soft templates. For example, hollow $PbWO_4$ spindles were prepared from the sonication of a solution of $Pb(CH_3COO)_2$, $NaWO_4$, and P123 (a Pluronic block copolymer, $EO_{20}PO_{70}EO_{20}$, M_{avg}=5800).[123] In the absence of ultrasound, however, only solid particles were obtained. It was argued that ultrasound played an important role in the transformation of P123 micelles into hollow micelle aggregates which led to the formation of the hollow spindle structure.

The power of the physical effects of high intensity ultrasound is further illustrated by mechanochemical reactions of polymers, which include force-induced scission of covalent bonds. It has been well known since the 1950s that ultrasonic irradiation of solutions of high molecular weight polymers (both biomolecular and synthetic) results in chain scission and macroradical production.[124] More recently, the incorporation of mechanically sensitive chemical groups ("mechanophores") into a polymer chain makes it possible to illustrate the mechanical forces present during exposure to ultrasound.[125] Sonication accelerates rearrangement reactions with a bias towards reaction pathways that yield molecules not necessarily obtained from purely thermal or light-induced reactions.[125] For example, when 1,2-disubstituted benzocyclobutene is incorporated into a polymer chain and undergoes an ultrasonically-triggered electrocyclic ring opening process the same products are formed regardless of whether the original molecule was *cis* or *trans* (Figure 1.30). If the reaction were initiated by light or heat alone, different products would form depending on the initial isomer. Thus, the mechanical force induced by ultrasound can alter the shape of the potential energy surfaces so that otherwise disfavored reactions can proceed under mild conditions. Ultrasound offers a way to access reaction pathways that may differ dramatically from those achieved by simply changing chemical or physical parameters. If stress-sensitive and cleavable groups are integrated in the polymer chain, sonication can result in the precise scission of the polymer chains. Some weak covalent bonds such as peroxide and azo bonds, strained rings, and weak coordinative bonds (e.g., palladium-phosphorus bonds) can be cleaved by ultrasound,[126-129] and even the click reaction can be unclicked within a polymer chain.[130]

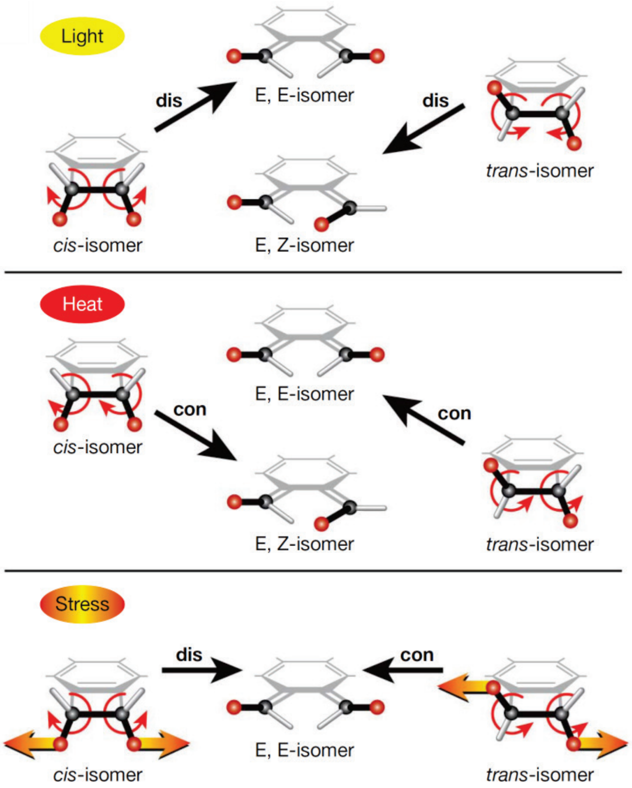

Figure 1.30 Predicted intermediates of benzocyclobutene based on different activation mechanisms. Top: light activation induces only disrotary (dis) ring opening. Middle: heat activation induces only contrarotary (con) ring opening. Bottom: stress (ultrasound) causes dis or con ring opening depending on initial isomer.[125]

1.2.4 Combined chemical and physical effects for synthesis of nanomaterials

Under certain conditions, both the chemical and physical effects of high intensity ultrasound can play a synergistic role in the synthesis of nanomaterials. The application of the physical effects of ultrasound on the preparation of graphene was described in above, but the chemical effects of ultrasound can also be exploited to aid in the preparation of functionalized graphenes. Recent work has shown that the use of a reactive solvent, such as styrene, that can be sonochemically activated allows for the relatively facile production of polymer functionalized single and few-layer graphenes in a single step.[131] During ultrasonic irradiation of graphite in styrene, polystyrene radicals will form and attack the surface of the exfoliated graphenes to form functionalized graphenes. Alternatively, the surface of graphite may first be functionalized by the radicals followed by exfoliation and further functionalization of the newly exposed graphene face will occur (Figure 1.31). TEM images of graphenes prepared in this way are shown in

Figure 1.32. Sonication of a solution containing poly(vinyl alcohol) and graphite also led to the formation of polymer functionalized graphenes.[132] The functionalization was achieved via sonochemical degradation of poly(vinyl alcohol) to form macroradicals which then grafted onto graphene surfaces.

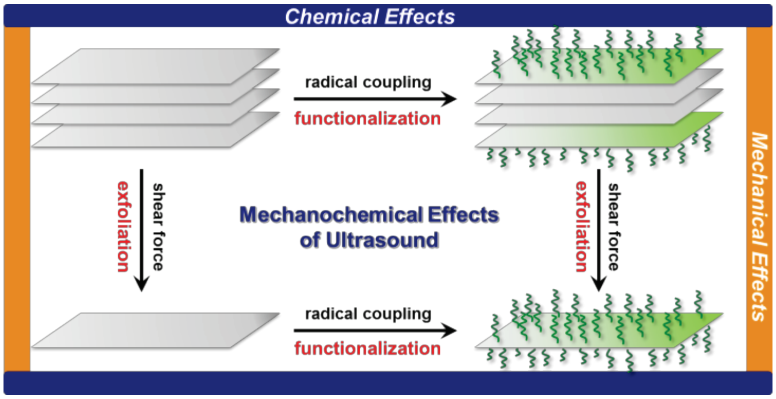

Figure 1.31 Sonochemical preparation of graphenes. Schematic illustration of the mechanochemical effects of ultrasound for the synthesis of polymer functionalized graphenes.

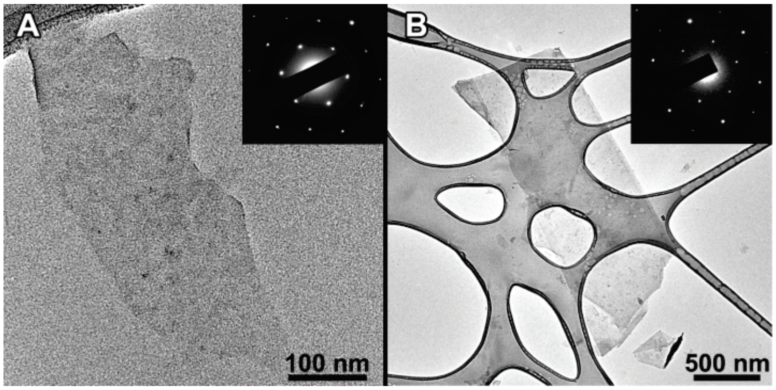

Figure 1.32 Graphene. TEM images of (A) single-layer graphene and (B) trilayer graphene with SAED insets confirming single-layer and few-layer graphenes, respectively.[131]

Another notable example of the application of both chemical and physical effects of high intensity ultrasound in materials synthesis is the preparation of protein microspheres. Sonication of a protein solution (e.g., serum albumins) led to the formation of microcapsules which can contain gas or nonaqueous liquid and whose surfaces are easily modified (Figure 1.33).[133-135] The mechanism responsible for the formation of protein microspheres involves two acoustic phenomena: emulsification (a physical effect) and cavitation (and the subsequent chemical effects). Sonication creates an emulsion with proteins in the interface of two liquid phases. However, emulsification alone is not enough to prepare stable protein microspheres. Radicals (e.g., $HO_2\bullet$) produced via the sonolysis of water induce the cross-linking of the disulfide bonds between cysteine amino acid residues. The protein microspheres can also be modified after sonochemical preparation, for example with conjugation of cancer-cell selective ligands (e.g., folate, monoclonal antibodies, RGD peptides) to their surface.[135]

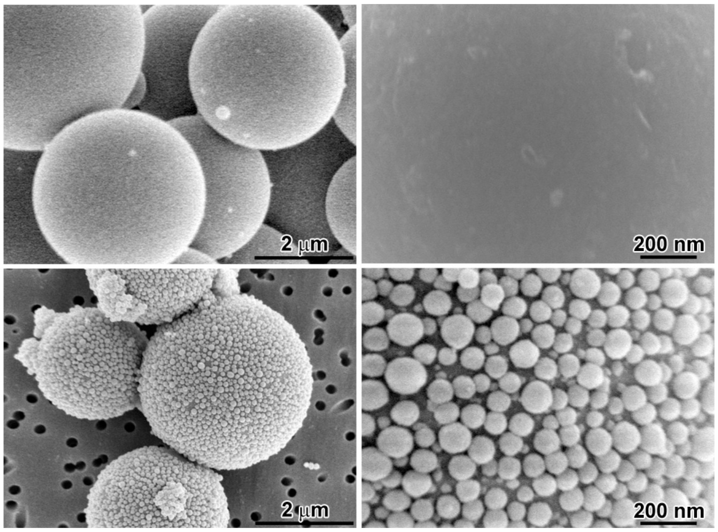

Figure 1.33 Protein microspheres. SEM images of sonochemically prepared protein microspheres before and after nanoparticle functionalization by layer-by-layer adhesion. Top left: native microspheres as prepared by sonication of bovine serum albumin. Top right: close-up of the surface. Bottom left: silica-coated microspheres using an RGD polylysine peptide to reverse surface charge. Bottom right: close-up of its surface.[135]

These protein microspheres have a wide range of clinical applications. Their use as echo contrast agents for improved sonography (e.g., echocardiography) has become standard.[136] Protein microspheres have also been developed as ^{19}F-MRI contrast agents,[137] as in vivo MRI temperature probes, as optical coherence tomography contrast agents,[138] and as multifunctional, multimodal cancer imaging contrast agents.[139]

The combination of chemical and physical effects of ultrasound can also be applied to prepare organic latex beads in a one-pot fashion. Through intense turbulence, ultrasound will create an emulsion of organic monomer in an aqueous medium. The radicals formed by sonolysis of water can diffuse into the organic phase to initiate the polymerization process. No additional initiators are required in this approach. In this method, fluorescent or magnetic substances can be incorporated into the latex particles to prepare functional latex beads.[140-141] For example, magnetic latex beads with a high content of magnetic nanoparticles have been prepared by ultrasonic irradiation of an emulsion of magnetite nanoparticles, surfactants, water and a reactive monomer.[141] Short sonication of this solution results in the formation of an emulsion of monomer loaded with magnetite nanoparticles stabilized by surfactants in the aqueous phase. Continuous sonication initiates the polymerization of the monomers to form latex particles.

1.2.5 Conclusions

High intensity ultrasound is responsible for a number of physical and chemical effects that are conducive to the preparation or modification of nanomaterials. The diverse mechanisms of action make it a powerful tool relevant to a large number of topics of current interest, including graphene, polymers, metal and metal oxide catalysts, crystallization, and anisotropic materials. With simple variations of reaction conditions and precursor compositions, myriad nanostructured materials with controlled morphologies, structures, and compositions have been successfully prepared by the application of high intensity ultrasound.

1.3 Sonocrystallization

1.3.1 Introduction

The ability of ultrasound to nucleate molecular crystals was first reported by Alfred Loomis in 1927 as part of a survey of the chemical effects of high intensity ultrasound.[22] He reported that supersaturated or supercooled liquids were “little affected” by the application of ultrasound, or gave no consistent results (perhaps because of his very high frequency of 100 to 500 kHz). The last 40 or so years has seen significant interest in the field and a considerable body of work empirically investigating sonocrystallization.[142] The mechanism of action, however, remains unsolved. The primary driver of the field has been the pharmaceutical industry, which has tremendous interest in facile and reproducible crystallization of pure active pharmaceutical ingredients with specific particle size distributions. Many major pharmaceutical companies hold at least one patent employing ultrasound for the induction of crystallization.[143] This section will give a sampling of the use of ultrasound for various pharmaceutical applications and progress towards understanding the mechanism of action will be discussed.

1.3.2 Applications and effects of sonocrystallization

One notable effect of ultrasound is a decrease in induction time and metastable zone width. These concepts are illustrated in Figure 1.34. When a drug solution is cooled below its solubility limit (or otherwise supersaturated) it forms a metastable solution. The induction time is the time between the creation of an unstable state and the onset of nucleation and it will vary depending on temperature and degree of supersaturation. The metastable zone is considered to be the area between the solubility curve and the point at which crystals precipitate spontaneously.

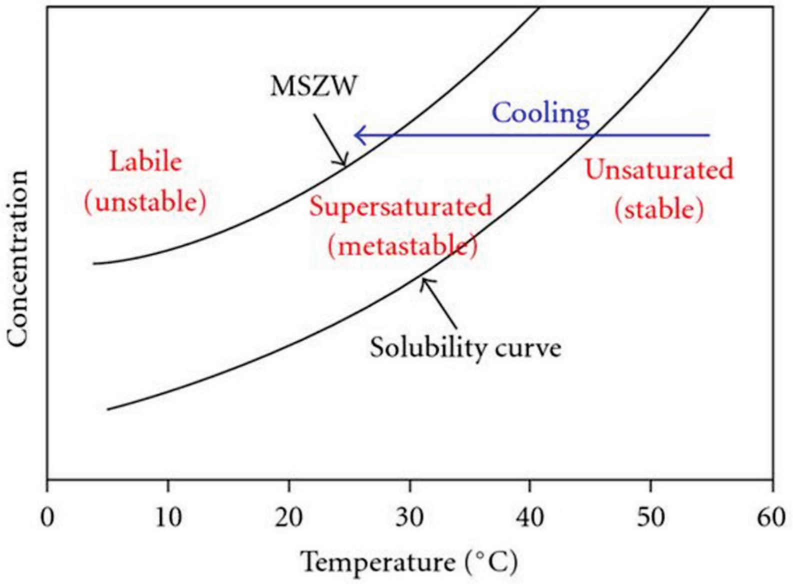

Figure 1.34 Illustration of the metastable zone width (MSZW).

The effects of ultrasound on induction time and metastable zone width are illustrated in Figure 1.35. Roxithromycin dissolved in acetone is supersaturated by the addition of water as an antisolvent.

Crystallization was performed at 25 °C at various levels of supersaturation, where supersaturation (S) is defined as the ratio between the mass of solute dissolved and the thermodynamic solubility limit. Ultrasound also had a significant effect on crystal morphology (Figure 1.36).[144]

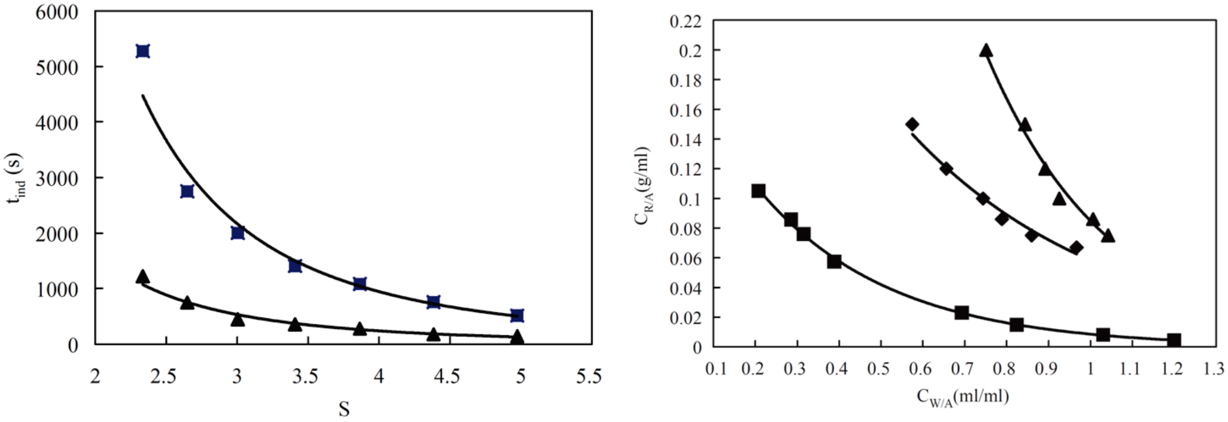

Figure 1.35 Effect of ultrasound on induction time and metastable zone width. Left: induction time for roxithromycin at different supersaturations in the presence (triangles) and absence (squares) of ultrasound. Right: metastable zone width (ratio of water to acetone, $C_{W/A}$ required to induce nucleation) at different concentrations ($C_{R/A}$) in the presence (diamonds) and absence (triangles) of ultrasound. Black squares represent the solubility curve.[144]

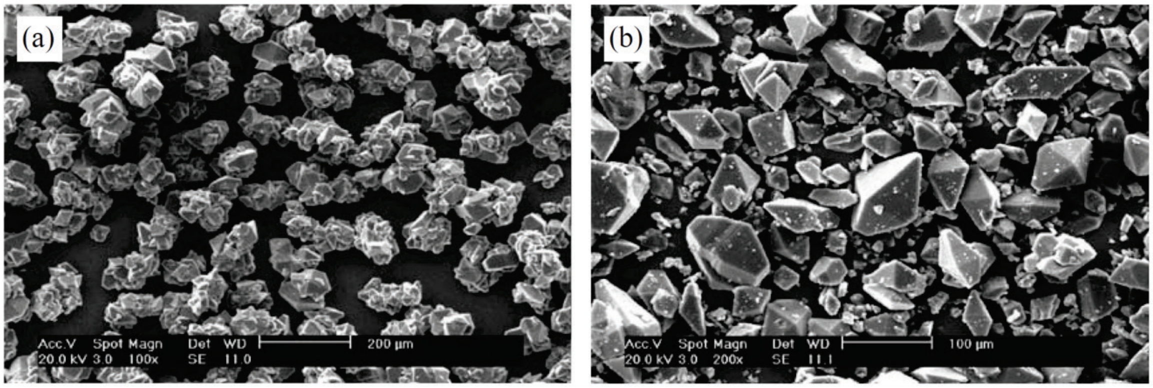

Figure 1.36 Sonocrystallization of roxithromycin. Crystals grown without ultrasound (a) and with ultrasound (b).[144]

Ultrasound is also known to be useful for controlling average particle sizes. If crystals in a closed-system experiment are allowed to precipitate until equilibrium is achieved (no remaining supersaturation) the average particle size will be determined by the number of crystals as the mass of drug available to come out of solution is fixed. This assumes that ripening processes do not change the number of crystals. The particle size can be controlled, therefore, by changing the number of nucleation events. The tightness of the particle size distribution is related, in part, to the length of the nucleation period (i.e., disparity in ripening times). Changing ultrasonic power and sonication time can both influence particle size.[142, 145-146] Although this is well-accepted and frequently exploited, the literature showing this systematically is remarkably poor.

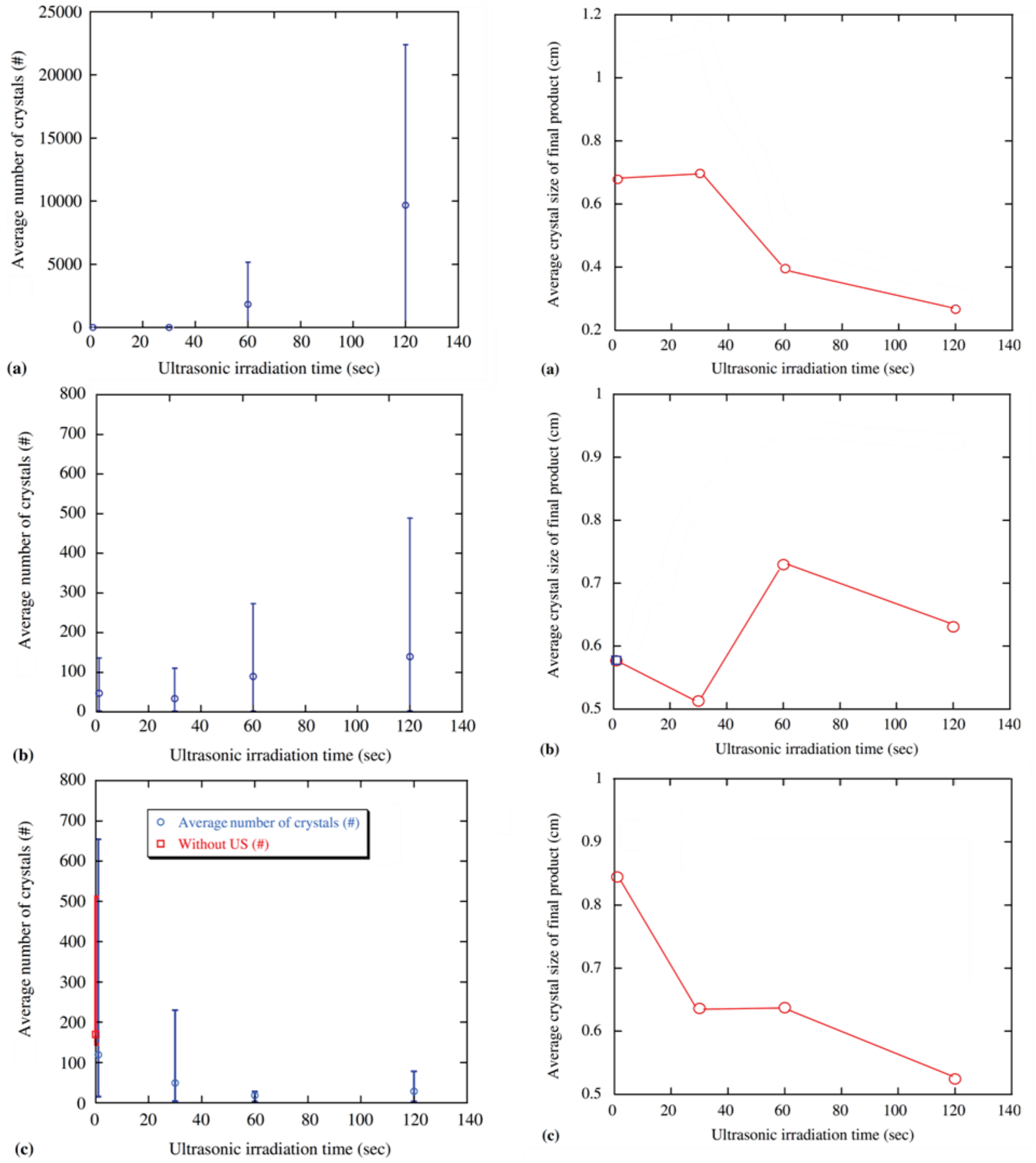

Figure 1.37 Sonocrystallization of acetylsalicylic acid. Left: number of crystals formed as a function of sonication time at 4.5 W (a), 4.0 W (b), and 2.5 W (c). Right: average particle size as a function of sonication time at 4.5 W (a), 2.5 W (b), and 4.0 W (c).[147]

The best demonstration of these effects is a paper by Miyasaka which uses very low power to influence the size of very large aspirin crystals (Figure 1.37).[147] Due to the low power, low range of power, the small number of points, and the massive error bars, it is difficult to make strong statements based on this work. In a follow-up paper[148] they went so far as to suggest that there was a regime where ultrasound inhibits nucleation based on the total ultrasonic energy input, which seems unlikely. It suggests, rather, that the powers they were operating at were so low that the comingling of error bars between their sonocrystallization experiments and their control experiments rendered their results suspect.

Although most sonocrystallization results in micron-scale particles, ultrasound has been used to prepare nanostructured organic crystals. One example of the application of ultrasound to the formation of nanocrystals is the preparation of cocrystals of 2(resorcinol)•2(4,4′-bpe), which can produce nanocrystalline cocrystals that exhibit single-crystal-to-single-crystal reactivity.[149] Compared with conventional reprecipitation methods, crystals obtained via sonochemistry were smaller and more uniform in size. Figure 1.38 shows some nanococrystals prepared by an antisolvent sonocrystallization.[150] Nanosized organic crystals of a self-assembled hexamer have also been prepared via an ultrasound-induced crystallization process. Nanosized hollow rhombic-dodecahedral crystals of the C-methylcalix[4]resorcinarene hexamer were achieved with rapid nucleation of a crystalline phase.[151] The mechanism for the formation of the hollow organic crystals is attributed to a reversed crystal growth mechanism heretofore described only in the synthesis of inorganic-based materials.

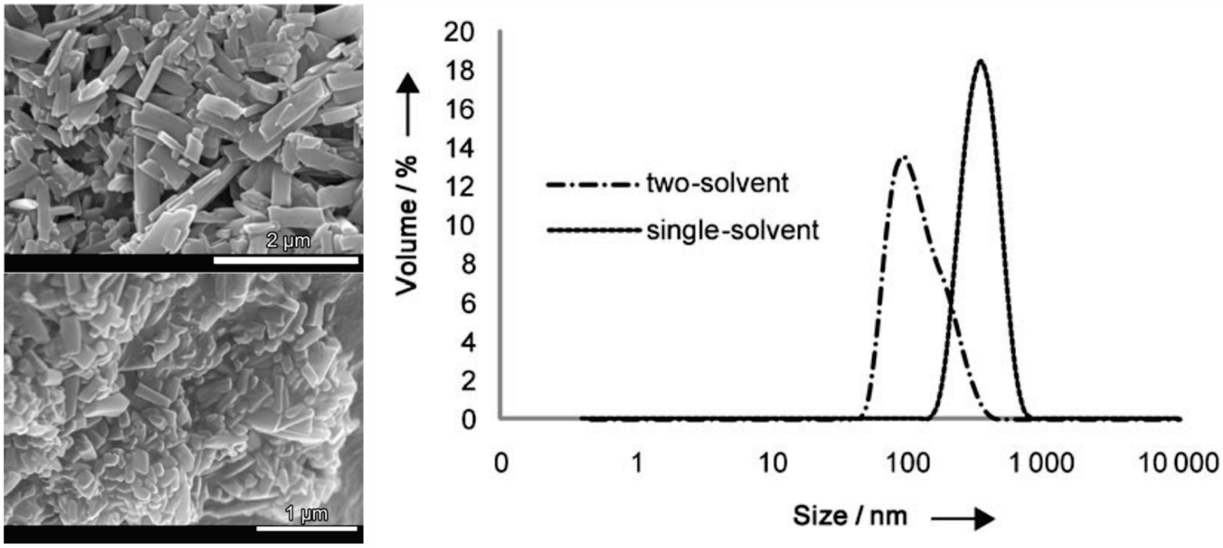

Figure 1.38 Antisolvent sonocrystallization of caffeine/2,4-dihydroxybenzene cocrystals. Top left: both components dissolved in one solvent. Bottom left: each component dissolved in separate solvent. Right: crystal size distributions.[150]

Sonocrystallization can be employed in efforts to control polymorphism. This is perhaps best illustrated by a discussion of the sonocrystallization of calcium carbonate, which is likely the most heavily studied molecule in the field of sonocrystallization (followed closely by adipic acid).[152-158] Calcium carbonate has three important polymorphs: calcite (stable under ambient conditions), aragonite (favored at high pressures and temperatures), and vaterite (thermodynamically unstable).[155] Figure 1.39 shows that both calcite and vaterite are obtainable using ultrasound. It appears that vaterite is kinetically favored under initial crystallization parameters, but extended sonication will promote the ground state polymorph through enhanced mass transport and local heating.[142]

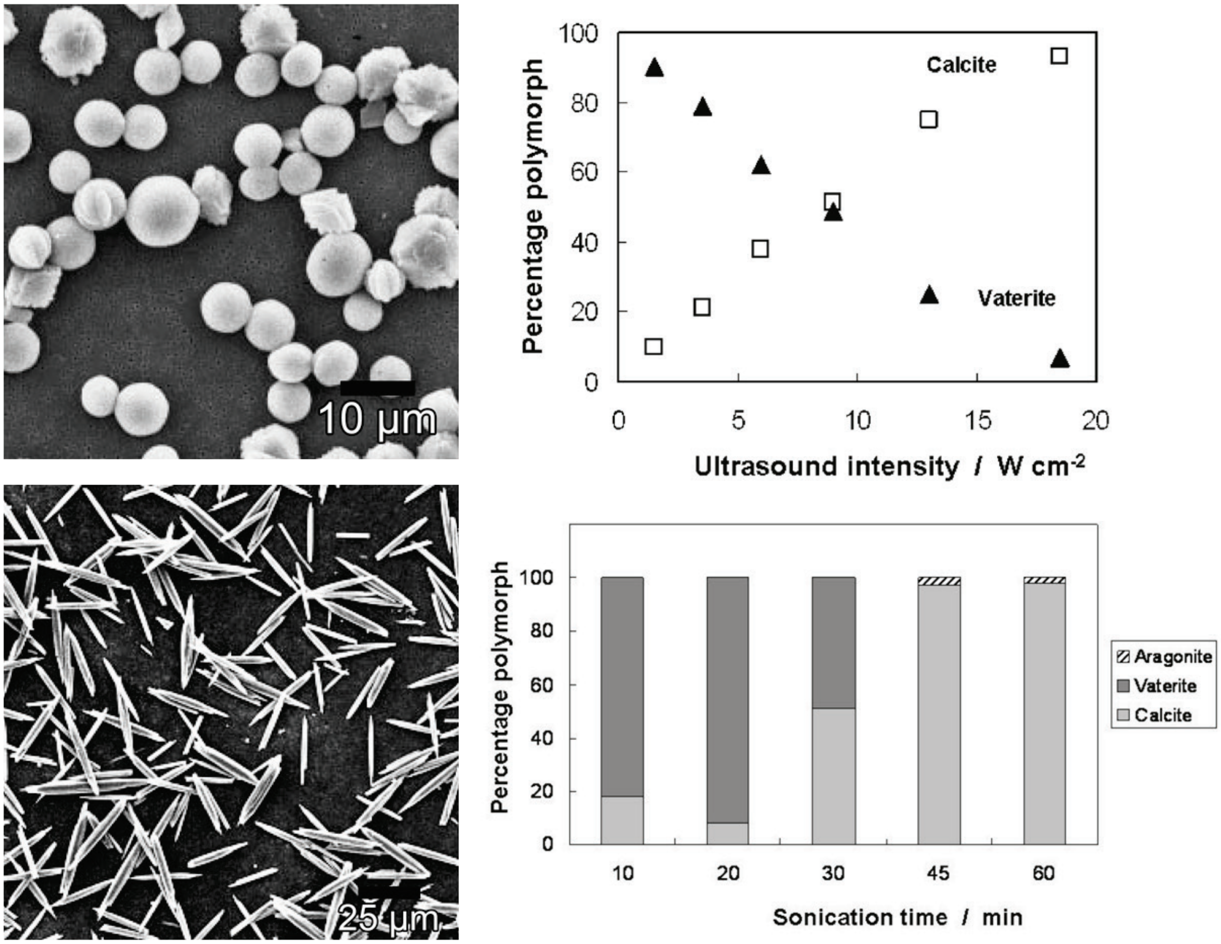

Figure 1.39 Polymorph control of calcium carbonate. Top left: calcite crystals prepared ultrasonically. Bottom left: Vaterite crystals prepared by sonocrystallization.[157] Top right: effect of ultrasonic intensity on polymorph obtained (after sonication for 30 minutes). Bottom right: effect of sonication time on polymorph (at 13 W/cm^2).[155]

Sonocrystallization is industrially scalable, although as a relative newcomer to the field scaling is sometimes a factor limiting or slowing industrial adoption. The biggest fundamental challenge is that radiative dilution and viscous absorption of the ultrasonic wave confounds the achievement of high power densities on the large scale. Figure 1.40 shows two example schemes for overcoming these difficulties. The first is an array of 50 W transducers produced by C^3 Technology that allows for high intensity sonication of a 20-L volume. The sonication vessel permits continuous flow processing so that a large volume can be subjected to high-intensity ultrasound by sonicating only a small fraction of it at any given time.[159] The second is invented by DuPont for the production of adipic acid, which is a precursor to nylon-

6,6. About 2.5 billion tons of adipic acid are produced each year.[160] This apparatus is also continuous flow, with concentrated solution flowing into a large vessel under vacuum. The vacuum removes solvent which concentrates and cools the solution to maintain supersaturation. The solution flows past ultrasonic transducers to induce nucleation and then the resultant mixture leaves through an outlet. Other schemes involve combining ultrasound with older techniques. GlaxoSmithKline, for example, has a patent wherein they use ultrasound to produce seed crystals which are then used to induce further nucleation in a secondary crystallization bath.[161]

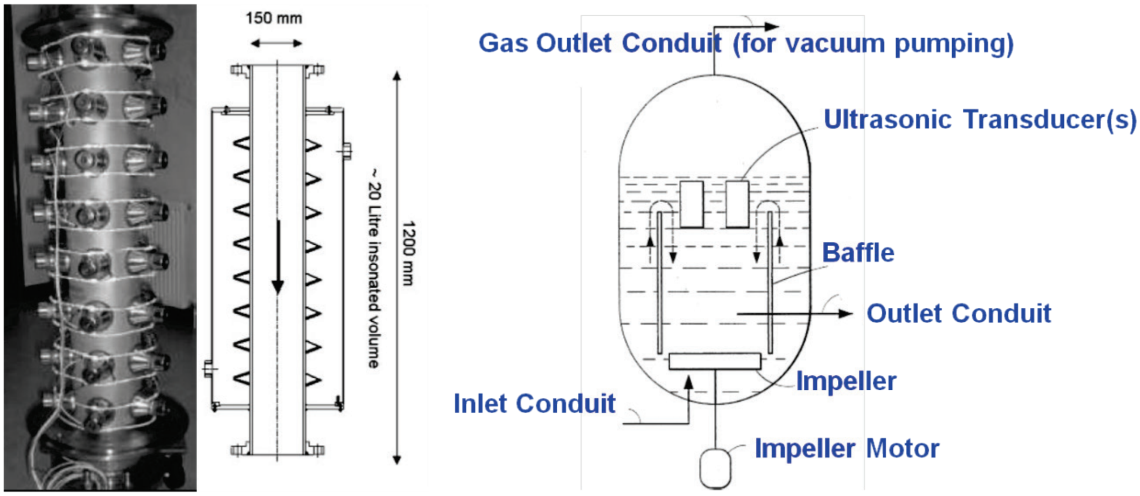

Figure 1.40 Industrial scaling. Left: photograph and scheme of continuous flow sonocrystallization apparatus from C^3 Technology, designed for the production of alumina.[159] Right: crystallizer for adipic acid developed by DuPont, ostensibly capable of handling several thousand gallons.[160]

The pharmaceutical industry is deeply concerned with product purity. One concern with the use of ultrasound is that erosion of the sonotrode can introduce titanium contamination. This is indeed the case, but titanium is an extremely robust material. The levels of titanium typically produced during sonocrystallization and insonation of molecular crystals is under 1 ppm, well below acceptable limits for most applications.[162] Figure 1.41 indicates the rate of titanium erosion in deionized water. Note, however, that sonicating coarse materials (essentially sandblasting the horn) can dramatically increase the rate at which the horn sheds titanium.

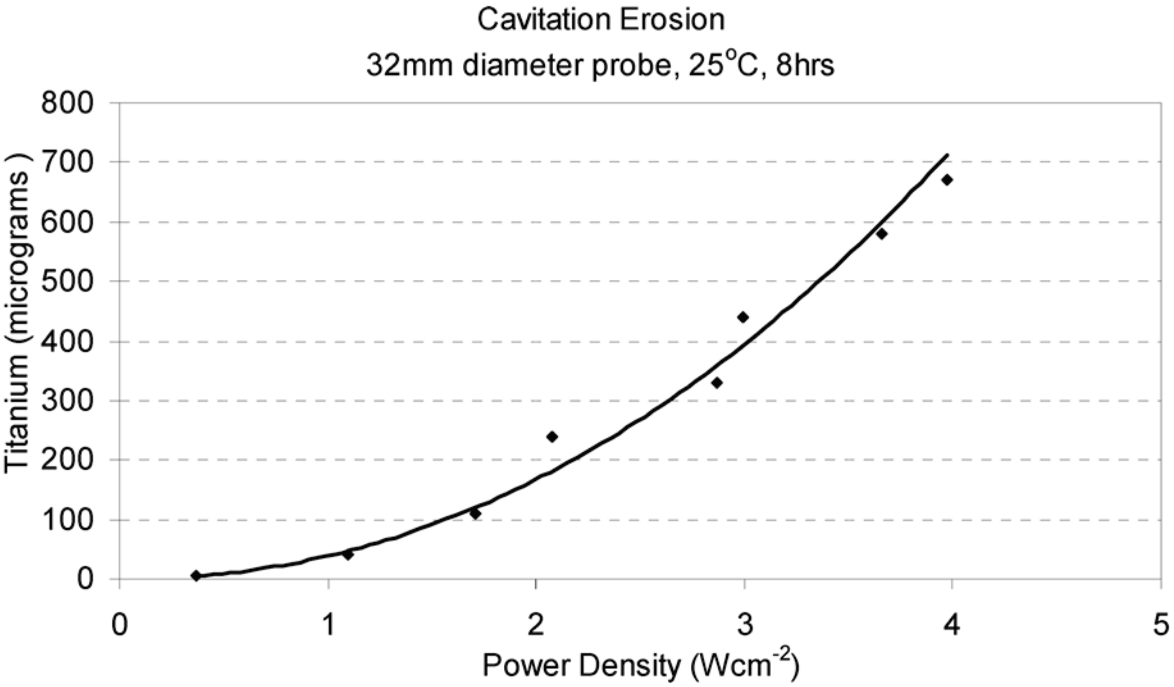

Figure 1.41Titanium shedding. Concentration of titanium in deionized water after 8 hours of sonication at different power settings as measured by ICP.

There are more sophisticated sonocrystallization techniques that will perhaps never achieve industrial scale. One of the more involved applications of ultrasound is a method called Solution Atomization and Crystallization by Sonication, creatively abbreviated as SAXS.[163] In this method, a drug solution is electrosprayed into air. The solvent evaporates while the droplets are in the air, resulting in high levels of supersaturation. These droplets are collected in a 35-40 kHz ultrasonic bath containing antisolvent, which induces nucleation (Figure 1.42). This method has extremely low throughput, 0.5 to 25 ml/hour. Throughput can be dramatically improved by using an air pressure atomizer instead of an electro-spray apparatus, but the resultant particles are not as attractive (the goal was to produce aerosolizeable particles, ~0.5 to 5 μm in diameter).

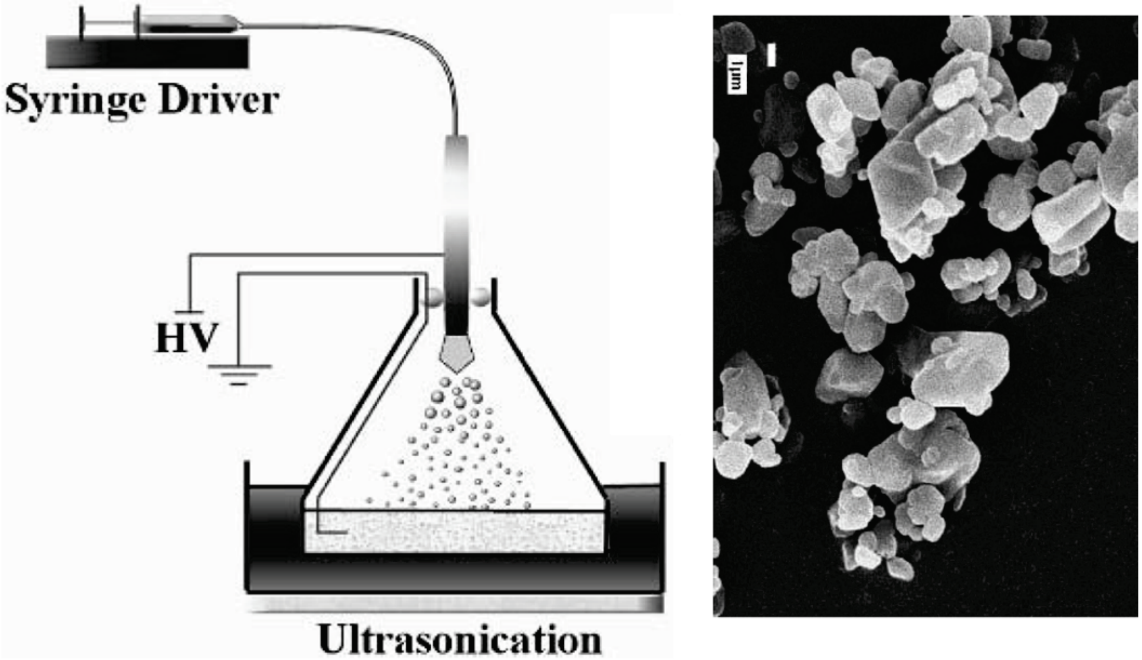

Figure 1.42 SAXS. Left: schematic of SAXS apparatus. Right: paracetamol (acetaminophen) prepared in this way.[163]

1.3.3 Mechanism of action

In spite of the reasonably advanced body of work empirically investigating sonocrystallization, the mechanism of action remains a subject of dispute. Numerous mechanisms have been proposed, and experimental evidence sometimes conflicts. It is possible that no single mechanism is responsible in all cases, as several seem viable and have experimental support.

Nucleation occurs in a thermodynamically unstable solution, either supercooled or supersaturated. The solution is metastable as a consequence of surface energy effects. The molecule-molecule interactions are energetically favorable relative to those molecules remaining solvated (otherwise the solution would not be unstable towards nucleation). The surface-solvent interaction, however, is unfavorable. The volume component grows with the cube of the particle radius while the interfacial energy grows with the square of the radius. As a result, small crystallites are unstable and will dissolve even in a supersaturated solution. In order to form stable crystals a critical nucleus is required (Figure 1.43).

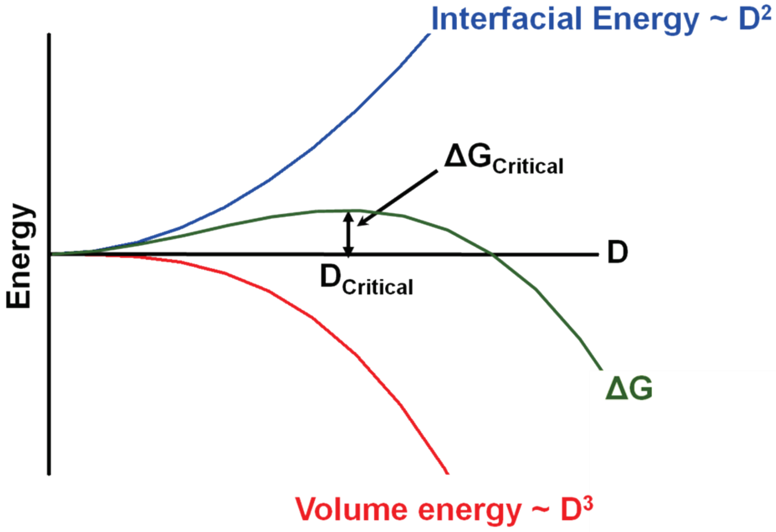

Figure 1.43 Crystallization kinetics. In a supersaturated or supercooled solution the energy of a group of molecules surrounded completely by other like molecules is energetically favored relative to the same number of molecules in solution (volume energy, red line). Surface molecules are disfavored (blue line). The sum of these is the total energy of a crystal (green line). A critical nucleus with size dimension D must be achieved in order to form a stable crystal.

The induction of nucleation can be achieved in two ways: decreasing the interfacial energy (stabilizing the surface) or decreasing the volume energy (increasing the supersaturation). Decreasing the interfacial tension is typically done by introducing a nucleation site. If the crystal-nucleation site interaction is favored over the alternative (solvent-nucleation site and solvent-crystal interactions) then the surface energy will be lessened and the $\Delta G_{Critical}$ will decrease and the nucleation rate will correspondingly increase. Increasing the supersaturation can be done many different ways, including changing temperature (this can be tricky however; lowering the temperature will increase the level of supersaturation, but it will also slow the reaction), increasing the solute concentration, exploiting the common ion effect, adding additional antisolvent, and changing the pressure. Many of these effects have been offered as an explanation for sonocrystallization.

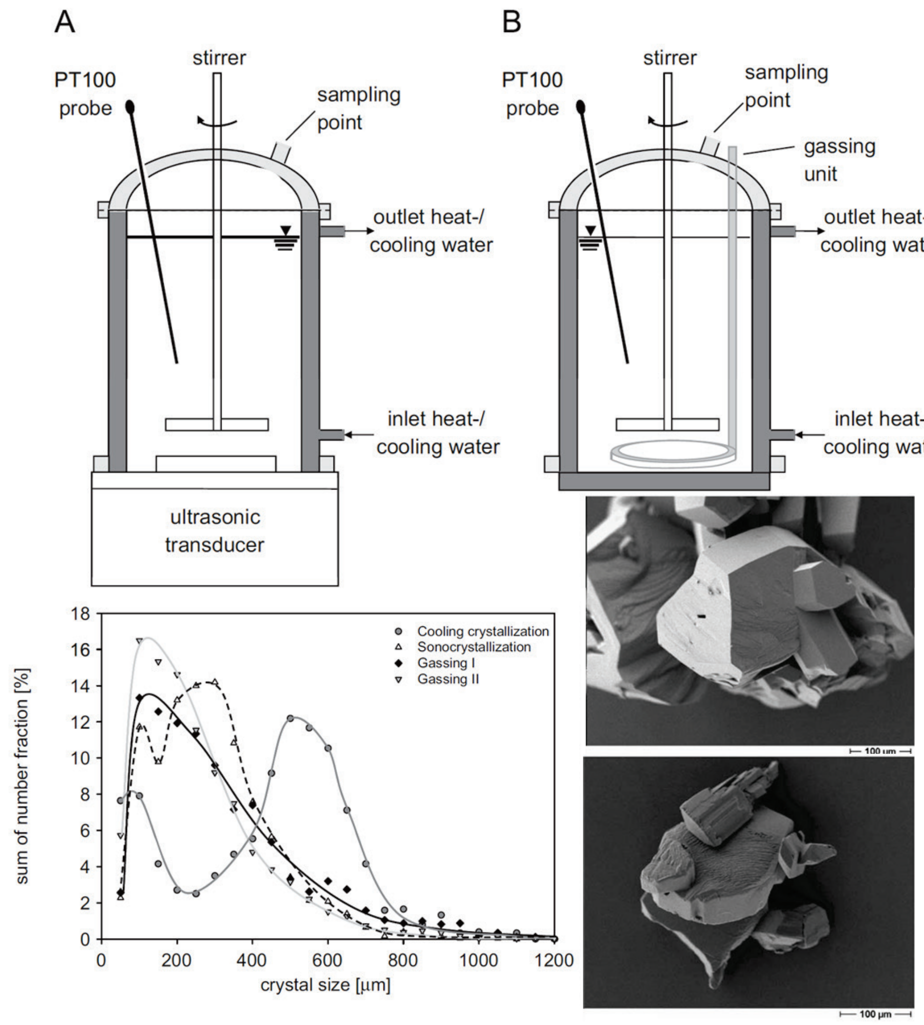

Figure 1.44 Bubble-induced nucleation. Cooling crystallization of adipic acid from acetonitrile. Nucleation was induced by sonication at 355.5 kHz at a nominal 200 W (A) or by the introduction of synthetic air bubbles using a stainless steel ring with holes in it (B). Crystal size distributions and micrographs (upper: sonocrystallized, lower: gassing crystallized) are compared.[164]

Bubbles can act as nucleation sites, and the number and manner in which they are introduced can be used to alter crystal size distributions. Figure 1.44 compares sonocrystallization of adipic acid to nucleation by bubbles. The authors concluded from these data that it was likely that heterogeneous nucleation was the mechanism of action in the case of sonocrystallization, which is a bold step. The effects of ultrasound and the effects of gassing in Figure 1.44 are obviously different, although both reduce average particle size relative to the control and it is possible that under the right experimental conditions the two techniques could produce the same result (assuming equivalent mixing). The strongest statement that should be taken from this work, however, is that bubbles are able to act as nucleation sites.

There is evidence, however, that heterogeneous nucleation is not the mechanism of sonocrystallization. Work at Bell Labs indicated that nucleation occurs during bubble collapse.[165] One might expect that heterogeneous nucleation would occur preferentially when bubbles are largest, as there is greater surface available. This is not conclusive, however, as the higher curvature of small bubbles and consequently higher surface energy may make them better nucleation sites. The observation of nucleation only during cavity collapse also casts doubt on other proposed mechanisms. It had been suggested, for example, that the bubble growth increases the local supersaturation, either by cooling or by evaporation of solvent.[166] Calculations have additionally suggested that the cooling explanation is unrealistic.[165]

Perhaps the most interesting investigation of sonocrystallization was high-speed photograph of the single-bubble sonocrystallization of ice. These experiments were performed in supercooled water and showed that crystallization did not occur in the presence of a bubble in a quiescent liquid or under the application of ultrasound in the absence of cavitation.[167] Other work additionally stated that a single bubble trapped in an ultrasonic field would also not induce nucleation unless it were emitting high pressure pulses.[168]

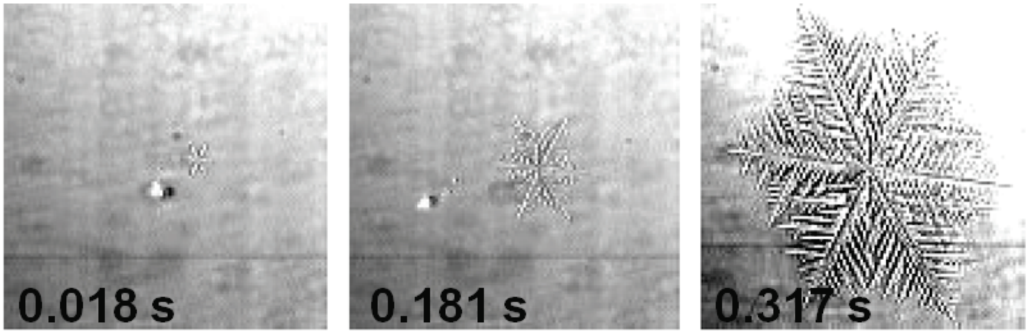

Figure 1.45 Single-bubble sonocrystallization of ice. High speed imaging of an ice crystal nucleated by a single, acoustically-driven bubble.[167]

The lack of nucleation in the absence of a shockwave suggests that sonocrystallization (at least in this instance) is caused by high pressure favoring the denser phase per the Clausius-Clapeyron relation. Water is a curious case, as ice I is less dense than liquid water. In this case the pressure change, asserted to be greater than 1 GPa,[169] was proposed to be sufficient to favor a high pressure phase of ice, probably ice V, which then phase transitioned to ice I after the high pressure front had passed. It could be that in cases where the solid is favored at milder pressures that nucleation would occur more readily.

1.3.4 Conclusion

Sonocrystallization is an exciting field with considerable potential application. Although the phenomenon has been known for more than 80 years the field remains surprisingly undeveloped. Investigations tend to be purely empirical and highly focused. Basic understandings of the mechanism of action and how to fully exploit ultrasound to finely tailor crystal characteristics are yet to be established.

1.4 References

1. Suslick, K. S., *Ultrasound : Its Chemical, Physical, and Biological Effects* VCH Publishers: New York, N.Y., 1988.

2. Suslick, K. S.; Price, G. J., "Applications of ultrasound to materials chemistry." *Annual Review of Materials Science* **1999,** *29* (1), 295.

3. Bang, J. H.; Suslick, K. S., "Applications of ultrasound to the synthesis of nanostructured materials." *Advanced materials* **2010,** *22* (10), 1039.

4. Suslick, K. S., "Sonochemistry." *Science* **1990,** *247* (4949), 1439-1445.

5. Luche, J. L., *Synthetic Organic Chemistry*. Plenum: New York, 1998.

6. Mason, T. J.; Lorimer, J. P., *Applied Sonochemistry: The Uses of Power Ultrasound in Chemistry and Processing*. Wiley-VCH: Weinheim, 2002.

7. Chen, D.; Sharma, S. K.; Mudhoo, A., *Handbook on Applications of Ultrasound: Sonochemisty for Sustainability*. CRC Press: 2011.

8. Pankaj; Ashokkumar, M., *Theoretical and Experimental Sonochemistry Involving Inorganic Systems*. Springer: 2010.

9. Shchukin, D. G.; Radziuk, D.; Möhwald, H., "Ultrasonic Fabrication of Metallic Nanomaterials and Nanoalloys." *Annual Review of Materials Research* **2010,** *40* (1), 345-362.

10. Suslick, K. S.; Flannigan, D. J., "Inside a collapsing bubble: sonoluminescence and the conditions during cavitation." *Annual review of physical chemistry* **2008,** *59* (December), 659-683.

11. Suslick, K. S., "The chemical effects of ultrasound." *Sci. A.* **1989,** *260* (80), 62.

12. Brenner, C. R., *Cavitation and Bubble Dynamics*. Oxford University Press: Oxford, 1995.

13. Leighton, T. G., *The Acoustic Bubble*. Academic Press: London, 1994.

14. Flannigan, D. J. Physical conditions and chemical processes during single-bubble sonoluminescence. University of Illinois at Urbana-Champaign, 2006.

15. Hopkins, S. Exploring the limits of cavitation. University of Illinois at Urbana-Champaign, 2006.

16. Eddingsaas, N. C. Mechanoluminescence and sonoluminescence from acoustic cavitation. University of Illinois at Urbana-Champaign, 2008.

17. Barber, B. P.; Hiller, R. A.; Löfstedt, R.; Putterman, S. J.; Weninger, K. R., "Defining the unknowns of sonoluminescence." *Physics Reports* **1997,** *281* (2), 65-143.

18. Ho-Young, K.; Panton, R. L., "Tensile strength of simple liquids predicted by a model of molecular interactions." *Journal of Physics D: Applied Physics* **1985,** *18* (4), 647.

19. Briggs, L. J., "Limiting Negative Pressure of Water." *Journal of Applied Physics* **1950,** *21* (7), 721-722.

20. Hiller, R.; Weninger, K.; Putterman, S. J.; Barber, B. P., "Effect of noble gas doping in single-bubble sonoluminescence." *Science* **1994,** *266* (5183), 248-248.

21. Matula, T. J., "Inertial cavitation and single-bubble sonoluminescence." *Philosophical Transactions of the Royal Society A: Mathematical, Physical and Engineering Sciences* **1999,** *357* (1751), 225-249.

22. Richards, W. T.; Loomis, A. L., "The chemical effects of high frequency sound waves I. A preliminary survey." *Journal of the American Chemical Society* **1927,** *49* (12), 3086-3100.

23. Noltingk, B. E.; Neppiras, E. A., "Cavitation produced by Ultrasonics." *Proceedings of the Physical Society. Section B* **1950,** *63* (9), 674.

24. Neppiras, E. A.; Noltingk, B. E., "Cavitation Produced by Ultrasonics: Theoretical Conditions for the Onset of Cavitation." *Proceedings of the Physical Society. Section B* **1951,** *64* (12), 1032.

25. Barber, B., "Sonoluminescence." *Philosophical Transactions of the Royal Society of London. Series A: Physical and Engineering Sciences* **1997,** *355* (1724), 641.

26. Loefstedt, R.; Barber, B. P.; Putterman, S. J., "Toward a hydrodynamic theory of sonoluminescence." *Journal Name: Physics of Fluids A; (United States); Journal Volume: 5:11* **1993**, Medium: X; Size: Pages: 2911-2928.

27. Putterman, S.; Evans, P. G.; Vazquez, G.; Weninger, K., "Cavitation science: Is there a simple theory of sonoluminescence?" *Nature* **2001,** *409* (6822), 782-783.

28. Leighton, T. G.; Walton, A. J.; Pickworth, M. J. W., "Primary Bjerknes forces." *European Journal of Physics* **1990,** *11* (1), 47.

29. Young, R. F., *Sonoluminescence*. CRC Press: 2005.

30. Löfstedt, R.; Weninger, K.; Putterman, S.; Barber, B. P., "Sonoluminescing bubbles and mass diffusion." *Physical Review E* **1995,** *51* (5), 4400-4410.

31. Holt, R. G.; Gaitan, D. F., "Observation of Stability Boundaries in the Parameter Space of Single Bubble Sonoluminescence." *Physical review letters* **1996,** *77* (18), 3791-3794.

32. Lohse, D.; Brenner, M.; Dupont, T.; Hilgenfeldt, S.; Johnston, B., "Sonoluminescing Air Bubbles Rectify Argon." *Physical review letters* **1997,** *78* (7), 1359-1362.

33. H., F.; H., S., " Luminescenz im ultraschallbeschickten Wasser." *Z. Phys. Chem. B* **1934,** (27), 421–24.

34. Peterson, F. B.; Anderson, T. P., "Light Emission from Hydrodynamic Cavitation." *Physics of Fluids* **1967,** *10* (4), 874-879.

35. Putterman, S. J., "Sonoluminescence: The Star in a Jar." *Physics World* **1998,** *11* (5), 38-42.

36. Yosioka, K.; Omura, A., "The light emisssion from a single bubble driven by ultrasound and the spectra of acoustic oscillations." *Proceedings of the Annual Meeting of the Acoustical Society of Japan* **1962**, 125-126.

37. Putterman, S. J., "Sonoluminescence - The plot thickens." *Physics World* **1999,** *12*, 18.

38. Barber, B. P.; Putterman, S. J., "Observation of synchronous picosecond sonoluminescence." *Nature* **1991,** *352* (6333), 318-320.

39. Gaitan, D. F.; Crum, L. A.; Church, C. C.; Roy, R. A., "Sonoluminescence and bubble dynamics for a single, stable, cavitation bubble." *The Journal of the Acoustical Society of America* **1992,** *91* (6), 3166-3183.

40. Flannigan, D. J.; Suslick, K. S., "Plasma formation and temperature measurement during single-bubble cavitation." *Nature* **2005,** *434* (March), 52-55.

41. Greenewalt, C. H., "Partial Pressure of Water Out of Aqueous Solutions of Sulfuric Acid." *Industrial & Engineering Chemistry* **1925,** *17* (5), 522-523.

42. Didenko, Y. T.; Suslick, K. S., "The energy efficiency of formation of photons, radicals and ions during single-bubble cavitation." *Nature* **2002,** *418* (6896), 394-397.

43. Barber, B. P.; Wu, C. C.; Löfstedt, R.; Roberts, P. H.; Putterman, S. J., "Sensitivity of sonoluminescence to experimental parameters." *Physical review letters* **1994,** *72* (9), 1380-1383.

44. Flannigan, D. J.; Hopkins, S. D.; Camara, C. G., "Measurement of pressure and density inside a single sonoluminescing bubble." *Physical review letters* **2006,** *96* (20), 204301-204301.

45. Hilgenfeldt, S.; Grossmann, S.; Lohse, D., "A simple explanation of light emission in sonoluminescence." *Nature* **1999,** *398* (April), 402-405.

46. Yasui, K., "Mechanism of single-bubble sonoluminescence." *Physical review. E, Statistical physics, plasmas, fluids, and related interdisciplinary topics* **1999,** *60* (2 Pt B), 1754-8.

47. Frommhold, L., "Electron-atom Bremsstrahlung and the Sonoluminescence of Rare Gas Bubbles." *Physical Review E* **1998,** *58* (2), 1899-1905.

48. Frommhold, L., "Radiative collisions and the sonoluminescence continua." *Journal Name: AIP Conference Proceedings; Journal Volume: 467; Journal Issue: 1; Conference: 14. International conference on spectral line shapes, State College, PA (United States), 22-26 Jun 1998; Other Information: DOI: 10.1063/1.58359; (c) 1999 American Institute of Physics; Country of input: International Atomic Energy Agency (IAEA)* **1999**, Medium: X; Size: page(s) 167-178.

49. Hammer, D.; Frommhold, L., "Spectra of Sonoluminescent Rare-gas Bubbles." *Physical Review Letters* **2000,** *85* (6), 1326-1329.

50. Frommhold, L., "Radiative Collisions and the Sonoluminescence Continua." *AIP Conference Proceedings* **1999,** *467*, 167-178.

51. Yasui, K., "Mechanism of Single-bubble Sonoluminescence." *Physical Review E* **1999,** *60* (2), 1754-1758.

52. Hammer, D.; Frommhold, L., "Electron-ion Bremsstrahlung Spectra Calculations for Sonoluminescence." *Physical Review E* **2002,** *66* (5), 056303.

53. Hammer, D.; Frommhold, L., "Light Emission of Sonoluminescent Bubbles Containing a Rare Gas and Water Vapor." *Physical Review E* **2002,** *65* (4), 046309.

54. Xu, N.; Wang, L.; Hu, X. W., "Bremsstrahlung of Nitrogen and Noble Gases in Single-bubble Sonoluminescence." *Physical Review E* **2000,** *61* (3), 2611-2616.

55. Hasin, P.; Wu, Y., "Sonochemical synthesis of copper hydride (CuH)." *Chemical Communications* **2012,** *48* (9), 1302-1304.

56. Putterman, S.; Evans, P. G.; Vazquez, G.; Weninger, K., "Is there a simple theory of sonoluminescence?" *Nature* **2001,** *409* (6822), 782-783.

57. Vazquez, G.; Camara, C.; Putterman, S.; Weninger, K., "Sonoluminescence: Nature's Smallest Blackbody." *Optics Letters* **2001,** *26* (9), 575-577.

58. Vazquez, G.; Camara, C.; Putterman, S. J.; Weninger, K., "Blackbody Spectra for Sonoluminescing Hydrogen Bubbles." *Physical Review Letters* **2002,** *88* (19), 197402.

59. Camara, C.; Putterman, S.; Kirilov, E., "Sonoluminescence from a Single Bubble Driven at 1 Megahertz." *Physical Review Letters* **2004,** *92* (12), 124301.

60. Liu, K. J.; Grinstaff, M. W.; Jiang, J.; Suslick, K. S.; Swartz, H. M.; Wang, W., "In vivo measurement of oxygen concentration using sonochemically synthesized microspheres." *Biophysical Journal* **1994,** *67* (2), 896-901.

61. Vazquez, G.; Camara, C.; Putterman, S.; Weninger, K., "Sonoluminescence: nature's smallest blackbody." *Optics Letters* **2001,** *26* (9), 575-575.

62. Hiller, R. A.; Putterman, S. J.; Weninger, K. R., "Time-Resolved Spectra of Sonoluminescence." *Physical review letters* **1998,** *80* (5), 1090-1093.

63. Gompf, B.; Günther, R.; Nick, G.; Pecha, R.; Eisenmenger, W., "Resolving Sonoluminescence Pulse Width with Time-Correlated Single Photon Counting." *Physical review letters* **1997,** *79* (7), 1405-1408.

64. Hopkins, S. D.; Putterman, S. J.; Kappus, B. A.; Suslick, K. S.; Camara, C. G., "Dynamics of a Sonoluminescing Bubble in Sulfuric Acid." *Phys. Rev. Lett.* **2005,** *95*, 254301.

65. Flannigan, D. J.; Suslick, K. S., "Plasma formation and temperature measurement during single-bubble cavitation." *Nature* **2005,** *434*, 52-55.

66. Camara, C.; Putterman, S.; Kirilov, E., "Sonoluminescence from a Single Bubble Driven at 1 Megahertz." *Physical review letters* **2004,** *92* (12), 124301-124301.

67. Kappus, B.; Khalid, S.; Chakravarty, A.; Putterman, S., "Phase Transition to an Opaque Plasma in a Sonoluminescing Bubble." *Physical review letters* **2011,** *106* (23), 234302-234302.

68. Kappus, B.; Khalid, S.; Putterman, S., "100-Watt Sonoluminescence Generated By 2.5-Atmosphere-Pressure Pulses." *Physical Review E* **2011,** *83* (5), 5-8.

69. Khalid, S.; Kappus, B.; Weninger, K.; Putterman, S., "Opacity and Transport Measurements Reveal That Dilute Plasma Models of Sonoluminescence Are Not Valid." *Physical review letters* **2012,** *108* (10), 104302-104302.

70. McNamara, W. B., III; Didenko, Y. T.; Suslick, K. S., "Sonoluminescence temperatures during multi-bubble cavitation." *Nature* **1999,** *401* (6755), 772-775.

71. McNamara, W. B.; Didenko, Y. T.; Suslick, K. S., "Pressure during Sonoluminescence." *The Journal of Physical Chemistry B* **2003,** *107* (30), 7303-7306.

72. Xu, H.; Eddingsaas, N. C.; Suslick, K. S., "Spatial separation of cavitating bubble populations: the nanodroplet injection model." *Journal of the American Chemical Society* **2009,** *131* (17), 6060-1.

73. Eddingsaas, N. C.; Suslick, K. S., "Evidence for a plasma core during multibubble sonoluminescence in sulfuric acid." *Journal of the American Chemical Society* **2007,** *129* (13), 3838-9.

74. Blake, J. R.; Gibson, D. C., "Cavitation Bubbles Near Boundaries." *Annual Review of Fluid Mechanics* **1987,** *19* (1), 99-123.

75. Ohl, C.-D.; Kurz, T.; Geisler, R.; Lindau, O.; Lauterborn, W., "Bubble dynamics, shock waves and sonoluminescence." *Philosophical Transactions of the Royal Society of London. Series A: Physical and Engineering Sciences* **1999,** *357* (1751), 269.

76. Doktycz, S. J.; Suslick, K. S., "Interparticle collisions driven by ultrasound." *Science* **1990,** *247* (4946), 1067-1069.

77. Prozorov, T.; Prozorov, R.; Suslick, K. S., "High Velocity Interparticle Collisions Driven by Ultrasound." *Journal of the American Chemical Society* **2004,** *126* (43), 13890-13891.

78. Suslick, K. S.; Flint, E. B.; Grinstaff, M. W.; Kemper, K. A., "Sonoluminescence from metal carbonyls." *The Journal of Physical Chemistry* **1993,** *97* (13), 3098-3099.

79. Suslick, K. S.; Choe, S.-B.; Cichowlas, A. A.; Grinstaff, M. W., "Sonochemical synthesis of amorphous iron." *Nature* **1991,** *353* (6343), 414-416.

80. Grinstaff, M. W.; Cichowlas, A. A.; Choe, S. B.; Suslick, K. S., "Effect of cavitation conditions on amorphous metal synthesis." *Ultrasonics* **1992,** *30* (3), 168-172.

81. Suslick, K. S.; Fang, M.; Hyeon, T., "Sonochemical Synthesis of Iron Colloids." *Journal of the American Chemical Society* **1996,** *118* (47), 11960-11961.

82. Bellissent, R.; Galli, G.; Hyeon, T.; Magazu, S.; Majolino, D.; Migliardo, P.; Suslick, K. S., "Structural properties of amorphous bulk Fe, Co and Fe-Co binary alloys." *Physica Scripta* **1995,** *1995* (T57), 79.

83. Suslick, K. S.; Hyeon, T.; Fang, M., "Nanostructured Materials Generated by High-Intensity Ultrasound: Sonochemical Synthesis and Catalytic Studies." *Chemistry of Materials* **1996,** *8* (8), 2172-2179.

84. Mdleleni, M. M.; Hyeon, T.; Suslick, K. S., "Sonochemical Synthesis of Nanostructured Molybdenum Sulfide." *Journal of the American Chemical Society* **1998,** *120* (24), 6189-6190.

85. Hyeon, T.; Fang, M.; Suslick, K. S., "Nanostructured Molybdenum Carbide: Sonochemical Synthesis and Catalytic Properties." *Journal of the American Chemical Society* **1996,** *118* (23), 5492-5493.

86. Oxley, J. D.; Mdleleni, M. M.; Suslick, K. S., "Hydrodehalogenation with sonochemically prepared Mo_2C and W_2C." *Catalysis Today* **2004,** *88* (3–4), 139-151.

87. Koltypin, Y.; Cao, X.; Prozorov, R.; Balogh, J.; Kaptas, D.; Gedanken, A., "Sonochemical synthesis of iron nitride nanoparticles." *Journal of Materials Chemistry* **1997,** *7* (12), 2453-2456.

88. Dhas, N. A.; Suslick, K. S., "Sonochemical Preparation of Hollow Nanospheres and Hollow Nanocrystals." *Journal of the American Chemical Society* **2005,** *127* (8), 2368-2369.

89. Bang, J. H.; Suslick, K. S., "Sonochemical Synthesis of Nanosized Hollow Hematite." *Journal of the American Chemical Society* **2007,** *129* (8), 2242-2243.

90. Du, N.; Zhang, H.; Chen, B.; Wu, J.; Ma, X.; Liu, Z.; Zhang, Y.; Yang, D.; Huang, X.; Tu, J., "Porous Co_3O_4 Nanotubes Derived From $Co_4(CO)_{12}$ Clusters on Carbon Nanotube Templates: A Highly Efficient Material For Li-Battery Applications." *Advanced materials* **2007,** *19* (24), 4505-4509.

91. Jeong, S.-H.; Ko, J.-H.; Park, J.-B.; Park, W., "A Sonochemical Route to Single-Walled Carbon Nanotubes under Ambient Conditions." *Journal of the American Chemical Society* **2004,** *126* (49), 15982-15983.

92. Sun, X.-H.; Li, C.-P.; Wong, N.-B.; Lee, C.-S.; Lee, S.-T.; Teo, B.-K., "Templating Effect of Hydrogen-Passivated Silicon Nanowires in the Production of Hydrocarbon Nanotubes and Nanoonions via Sonochemical Reactions with Common Organic Solvents under Ambient Conditions." *Journal of the American Chemical Society* **2002,** *124* (50), 14856-14857.

93. Caruso, R. A.; Ashokkumar, M.; Grieser, F., "Sonochemical Formation of Gold Sols." *Langmuir* **2002,** *18* (21), 7831-7836.

94. Mizukoshi, Y.; Okitsu, K.; Maeda, Y.; Yamamoto, T. A.; Oshima, R.; Nagata, Y., "Sonochemical Preparation of Bimetallic Nanoparticles of Gold/Palladium in Aqueous Solution." *The Journal of Physical Chemistry B* **1997,** *101* (36), 7033-7037.

95. Anandan, S.; Grieser, F.; Ashokkumar, M., "Sonochemical Synthesis of Au−Ag Core−Shell Bimetallic Nanoparticles." *The Journal of Physical Chemistry C* **2008,** *112* (39), 15102-15105.

96. Vinodgopal, K.; He, Y.; Ashokkumar, M.; Grieser, F., "Sonochemically Prepared Platinum−Ruthenium Bimetallic Nanoparticles." *The Journal of Physical Chemistry B* **2006,** *110* (9), 3849-3852.

97. Okitsu, K.; Sharyo, K.; Nishimura, R., "One-Pot Synthesis of Gold Nanorods by Ultrasonic Irradiation: The Effect of pH on the Shape of the Gold Nanorods and Nanoparticles." *Langmuir* **2009,** *25* (14), 7786-7790.

98. Sánchez-Iglesias, A.; Pastoriza-Santos, I.; Pérez-Juste, J.; Rodríguez-González, B.; García de Abajo, F. J.; Liz-Marzán, L. M., "Synthesis and Optical Properties of Gold Nanodecahedra with Size Control." *Advanced materials* **2006,** *18* (19), 2529-2534.

99. Jiang, L.-P.; Xu, S.; Zhu, J.-M.; Zhang, J.-R.; Zhu, J.-J.; Chen, H.-Y., "Ultrasonic-Assisted Synthesis of Monodisperse Single-Crystalline Silver Nanoplates and Gold Nanorings." *Inorganic Chemistry* **2004,** *43* (19), 5877-5883.

100. Zhang, J.; Du, J.; Han, B.; Liu, Z.; Jiang, T.; Zhang, Z., "Sonochemical Formation of Single-Crystalline Gold Nanobelts." *Angewandte Chemie* **2006,** *118* (7), 1134-1137.

101. Xu, H.; Suslick, K. S., "Sonochemical Synthesis of Highly Fluorescent Ag Nanoclusters." *ACS Nano* **2010,** *4* (6), 3209-3214.

102. Mayers, B. T.; Liu, K.; Sunderland, D.; Xia, Y., "Sonochemical Synthesis of Trigonal Selenium Nanowires." *Chemistry of Materials* **2003,** *15* (20), 3852-3858.

103. Zhu, J. J.; Xu, S.; Wang, H.; Zhu, J. M.; Chen, H. Y., "Sonochemical Synthesis of CdSe Hollow Spherical Assemblies Via an In-Situ Template Route." *Advanced materials* **2003,** *15* (2), 156-159.

104. Gao, T.; Wang, T., "Sonochemical synthesis of SnO_2 nanobelt/CdS nanoparticle core/shell heterostructures." *Chemical Communications* **2004,** (22), 2.

105. Pol, V. G.; Gedanken, A.; Calderon-Moreno, J., "Deposition of Gold Nanoparticles on Silica Spheres: A Sonochemical Approach." *Chemistry of Materials* **2003,** *15* (5), 1111-1118.

106. Pol, V. G.; Grisaru, H.; Gedanken, A., "Coating Noble Metal Nanocrystals (Ag, Au, Pd, and Pt) on Polystyrene Spheres via Ultrasound Irradiation." *Langmuir* **2005,** *21* (8), 3635-3640.

107. Pan, H.-B.; Wai, C. M., "Facile sonochemical synthesis of carbon nanotube-supported bimetallic Pt-Rh nanoparticles for room temperature hydrogenation of arenes." *New Journal of Chemistry* **2011,** *35* (8), 1649-1660.

108. Vinodgopal, K.; Neppolian, B.; Lightcap, I. V.; Grieser, F.; Ashokkumar, M.; Kamat, P. V., "Sonolytic Design of Graphene−Au Nanocomposites. Simultaneous and Sequential Reduction of Graphene Oxide and Au(III)." *The Journal of Physical Chemistry Letters* **2010,** *1* (13), 1987-1993.

109. Jung, S. H.; Oh, E.; Lee, K. H.; Park, W.; Jeong, S. H., "A Sonochemical Method for Fabricating Aligned ZnO Nanorods." *Advanced materials* **2007,** *19* (5), 749-753.

110. Chatakondu, K.; Green, M. L. H.; Thompson, M. E.; Suslick, K. S., "The enhancement of intercalation reactions by ultrasound." *Journal of the Chemical Society, Chemical Communications* **1987,** (12), 900-901.

111. Jones, J. E.; Cheshire, M. C.; Casadonte, D. J.; Phifer, C. C., "Facile Sonochemical Synthesis of Graphite Intercalation Compounds." *Organic Letters* **2004,** *6* (12), 1915-1917.

112. Walter, J.; Nishioka, M.; Hara, S., "Ultrathin Platinum Nanoparticles Encapsulated in a Graphite Lattice Prepared by a Sonochemical Approach." *Chemistry of Materials* **2001,** *13* (5), 1828-1833.

113. Viculis, L. M.; Mack, J. J.; Kaner, R. B., "A Chemical Route to Carbon Nanoscrolls." *Science* **2003,** *299* (5611), 1361.

114. Hernandez, Y.; Nicolosi, V.; Lotya, M.; Blighe, F. M.; Sun, Z.; De, S.; McGovern, I. T.; Holland, B.; Byrne, M.; Gun'Ko, Y. K.; Boland, J. J.; Niraj, P.; Duesberg, G.; Krishnamurthy, S.; Goodhue, R.; Hutchison, J.; Scardaci, V.; Ferrari, A. C.; Coleman, J. N., "High-yield production of graphene by liquid-phase exfoliation of graphite." *Nat Nano* **2008,** *3* (9), 563-568.

115. Coleman, J. N.; Lotya, M.; O'Neill, A.; Bergin, S. D.; King, P. J.; Khan, U.; Young, K.; Gaucher, A.; De, S.; Smith, R. J.; Shvets, I. V.; Arora, S. K.; Stanton, G.; Kim, H.-Y.; Lee, K.; Kim, G. T.; Duesberg, G. S.; Hallam, T.; Boland, J. J.; Wang, J. J.; Donegan, J. F.; Grunlan, J. C.; Moriarty, G.; Shmeliov, A.; Nicholls, R. J.; Perkins, J. M.; Grieveson, E. M.; Theuwissen, K.; McComb, D. W.; Nellist, P. D.; Nicolosi, V., "Two-Dimensional Nanosheets Produced by Liquid Exfoliation of Layered Materials." *Science* **2011,** *331* (6017), 568-571.

116. Prozorov, T.; McCarty, B.; Cai, Z.; Prozorov, R.; Suslick, K. S., "Effects of high-intensity ultrasound on $Bi_2Sr_2CaCu_2O_{8+x}$ superconductor." *Applied Physics Letters* **2004,** *85* (16), 3513.

117. Prozorov, T.; Prozorov, R.; Snezhko, A.; Suslick, K. S., "Sonochemical modification of the superconducting properties of MgB_2." *Applied Physics Letters* **2003,** *83* (10), 2019-2021.

118. Xiong, H.-M.; Shchukin, D. G.; Möhwald, H.; Xu, Y.; Xia, Y.-Y., "Sonochemical Synthesis of Highly Luminescent Zinc Oxide Nanoparticles Doped with Magnesium(II)." *Angewandte Chemie International Edition* **2009,** *48* (15), 2727-2731.

119. Belova, V.; Borodina, T.; Möhwald, H.; Shchukin, D. G., "The effect of high intensity ultrasound on the loading of Au nanoparticles into titanium dioxide." *Ultrasonics Sonochemistry* **2011,** *18* (1), 310-317.

120. Andreeva, D. V.; Fix, D.; Möhwald, H.; Shchukin, D. G., "Self-Healing Anticorrosion Coatings Based on pH-Sensitive Polyelectrolyte/Inhibitor Sandwichlike Nanostructures." *Advanced materials* **2008,** *20* (14), 2789-2794.

121. Yu, J. C.; Yu, J.; Ho, W.; Zhang, L., "Preparation of highly photocatalytic active nano-sized TiO particles ultrasonic irradiation." *Chemical Communications* **2001,** (19), 1942-1943.

122. Qian, D.; Jiang, J. Z.; Lenvig Hansen, P., "Preparation of ZnO nanocrystals via ultrasonic irradiation." *Chemical Communications* **2003,** (9), 1078-1079.

123. Geng, J.; Zhu, J.-J.; Lu, D.-J.; Chen, H.-Y., "Hollow $PbWO_4$ Nanospindles via a Facile Sonochemical Route." *Inorganic Chemistry* **2006,** *45* (20), 8403-8407.

124. Basedow, A.; Ebert, K., Ultrasonic degradation of polymers in solution
Physical Chemistry. Springer Berlin / Heidelberg: 1977; Vol. 22, pp 83-148.

125. Hickenboth, C. R.; Moore, J. S.; White, S. R.; Sottos, N. R.; Baudry, J.; Wilson, S. R., "Biasing reaction pathways with mechanical force." *Nature* **2007,** *446*, 423-427.

126. Paulusse, J. M. J.; Sijbesma, R. P., "Reversible Mechanochemistry of a PdII Coordination Polymer." *Angewandte Chemie International Edition* **2004,** *43* (34), 4460-4462.

127. Kryger, M. J.; Ong, M. T.; Odom, S. A.; Sottos, N. R.; White, S. R.; Martinez, T. J.; Moore, J. S., "Masked Cyanoacrylates Unveiled by Mechanical Force." *Journal of the American Chemical Society* **2010,** *132* (13), 4558-4559.

128. Berkowski, K. L.; Potisek, S. L.; Hickenboth, C. R.; Moore, J. S., "Ultrasound-Induced Site-Specific Cleavage of Azo-Functionalized Poly(ethylene glycol)." *Macromolecules* **2005,** *38* (22), 8975-8978.

129. Wiggins, K. M.; Hudnall, T. W.; Shen, Q.; Kryger, M. J.; Moore, J. S.; Bielawski, C. W., "Mechanical Reconfiguration of Stereoisomers." *Journal of the American Chemical Society* **2010,** *132* (10), 3256-3257.

130. Brantley, J. N.; Wiggins, K. M.; Bielawski, C. W., "Unclicking the Click: Mechanically Facilitated 1,3-Dipolar Cycloreversions." *Science* **2011,** *333* (6049), 1606-1609.

131. Xu, H.; Suslick, K. S., "Sonochemical preparation of functionalized graphenes." *Journal of the American Chemical Society* **2011,** *133* (24), 9148-51.

132. Shen, B.; Zhai, W.; Lu, D.; Wang, J.; Zheng, W., "Ultrasonication-assisted direct functionalization of graphene with macromolecules." *RSC Advances* **2012,** *2* (11), 4713-4719.

133. Suslick, K. S.; Grinstaff, M. W., "Protein microencapsulation of nonaqueous liquids." *Journal of the American Chemical Society* **1990,** *112* (21), 7807-7809.

134. Grinstaff, M. W.; Suslick, K. S., "Air-filled proteinaceous microbubbles: synthesis of an echo-contrast agent." *Proceedings of the National Academy of Sciences* **1991,** *88* (17), 7708-7710.

135. Toublan, F. J.-J.; Boppart, S.; Suslick, K. S., "Tumor Targeting by Surface-Modified Protein Microspheres." *Journal of the American Chemical Society* **2006,** *128* (11), 3472-3473.

136. Shengping, Q.; Charles, F. C.; Katherine, W. F., "Ultrasound contrast microbubbles in imaging and therapy: physical principles and engineering." *Physics in Medicine and Biology* **2009,** *54* (6), R27.

137. Webb, A. G.; Wong, M.; Kolbeck, K. J.; Magin, R. L.; Suslick, K. S., "Sonochemically produced fluorocarbon microspheres: A new class of magnetic resonance imaging agent." *Journal of Magnetic Resonance Imaging* **1996,** *6* (4), 675-683.

138. Boppart, S. A.; Suslick, K. S., *Optical Coherence Tomography in Cardiovascular Research*. CRC Press: 2007.

139. John, R.; Nguyen, F.; Kolbeck, K.; Chaney, E.; Marjanovic, M.; Suslick, K.; Boppart, S., "Targeted Multifunctional Multimodal Protein-Shell Microspheres as Cancer Imaging Contrast Agents." *Molecular Imaging and Biology* **2012,** *14* (1), 17-24.

140. Bradley, M.; Ashokkumar, M.; Grieser, F., "Sonochemical Production of Fluorescent and Phosphorescent Latex Particles." *Journal of the American Chemical Society* **2002,** *125* (2), 525-529.

141. Teo, B. M.; Chen, F.; Hatton, T. A.; Grieser, F.; Ashokkumar, M., "Novel One-Pot Synthesis of Magnetite Latex Nanoparticles by Ultrasound Irradiation." *Langmuir* **2009,** *25* (5), 2593-2595.

142. Luque de Castro, M. D.; Priego-Capote, F., "Ultrasound-assisted crystallization (sonocrystallization)." *Ultrasonics Sonochemistry* **2007,** *14* (6), 717-24.

143. Ruecroft, G.; Hipkiss, D.; Ly, T.; Maxted, N.; Cains, P. W., "Sonocrystallization: The Use of Ultrasound for Improved Industrial Crystallization." *Organic Process Research & Development* **2005,** *9* (6), 923-932.

144. Guo, Z.; Zhang, M.; Li, H.; Wang, J.; Kougoulos, E., "Effect of ultrasound on anti-solvent crystallization process." *Journal of crystal growth* **2005,** *273* (3-4), 555-563.

145. Li, H.; Wang, J.; Bao, Y.; Guo, Z.; Zhang, M., "Rapid sonocrystallization in the salting-out process." *Journal of crystal growth* **2003,** *247* (1–2), 192-198.

146. Abbas, a.; Srour, M.; Tang, P.; Chiou, H.; Chan, H.; Romagnoli, J., "Sonocrystallisation of sodium chloride particles for inhalation." *Chemical Engineering Science* **2007,** *62* (9), 2445-2453.

147. Miyasaka, E.; Kato, Y.; Hagisawa, M.; Hirasawa, I., "Effect of ultrasonic irradiation on the number of acetylsalicylic acid crystals produced under the supersaturated condition and the ability of controlling the final crystal size via primary nucleation." *Journal of crystal growth* **2006,** *289* (1), 324-330.

148. Miyasaka, E.; Ebihara, S.; Hirasawa, I., "Investigation of primary nucleation phenomena of acetylsalicylic acid crystals induced by ultrasonic irradiation—ultrasonic energy needed to activate primary nucleation." *Journal of crystal growth* **2006,** *295* (1), 97-101.

149. Bučar, D.-K.; MacGillivray, L. R., "Preparation and Reactivity of Nanocrystalline Cocrystals Formed via Sonocrystallization." *Journal of the American Chemical Society* **2006,** *129* (1), 32-33.

150. Sander, J. R. G.; Bucar, D.-K.; Henry, R. F.; Zhang, G. G. Z.; MacGillivray, L. R., "Pharmaceutical nano-cocrystals: sonochemical synthesis by solvent selection and use of a surfactant." *Angewandte Chemie (International ed. in English)* **2010,** *49* (40), 7284-8.

151. Sander, J. R. G.; Bučar, D.-K.; Baltrusaitis, J.; MacGillivray, L. R., "Organic Nanocrystals of the Resorcinarene Hexamer via Sonochemistry: Evidence of Reversed Crystal Growth Involving Hollow Morphologies." *Journal of the American Chemical Society* **2012,** *134* (16), 6900-6903.

152. Dalas, E., "The effect of ultrasonic field on calcium carbonate scale formation." *Journal of crystal growth* **2001,** *222* (1-2), 287-292.

153. He, M.; Forssberg, E.; Wang, Y.; Han, Y., Ultrasonication-Assisted Synthesis of Calcium Carbonate Nanoparticles. 2005; Vol. 192, pp 1468-1481.

154. Nishida, I., "Precipitation of calcium carbonate by ultrasonic irradiation." *Ultrasonics Sonochemistry* **2004,** *11* (6), 423-8.

155. Price, G. J.; Mahon, M. F.; Shannon, J.; Cooper, C., "Composition of Calcium Carbonate Polymorphs Precipitated Using Ultrasound." *Crystal Growth & Design* **2011,** *11* (1), 39-44.

156. Stephens, C. J.; Kim, Y.-Y.; Evans, S. D.; Meldrum, F. C.; Christenson, H. K., "Early stages of crystallization of calcium carbonate revealed in picoliter droplets." *Journal of the American Chemical Society* **2011,** *133* (14), 5210-3.

157. Wang, L.; Sondi, I.; Matijevic, E., "Preparation of Uniform Needle-Like Aragonite Particles by Homogeneous Precipitation." *Journal of colloid and interface science* **1999,** *218* (2), 545-553.

158. Zhou, G.-T.; Yu, J. C.; Wang, X.-C.; Zhang, L.-Z., "Sonochemical synthesis of aragonite-type calcium carbonate with different morphologies." *New Journal of Chemistry* **2004,** *28* (8), 1027-1027.

159. Ruecroft, G.; Hipkiss, D.; Ly, T.; Maxted, N.; Cains, P. W., "Sonocrystallization: The Use of Ultrasound for Improved Industrial Crystallization." *Organic Process Research & Development* **2005,** *9* (6), 923-932.

160. Anderson, H. W.; Carberry, J. B.; Staunton, H. F.; Bhagya, S., C. Crystallization of adipic acid. US 5,471,001, 1995.

161. Craig, S. A.; Jones, A. D. Process for the production of paroxetine hydrochloride propan-2-ol solvate. WO 00/32597, 1999.

162. Dennehy, R. D., "Particle Engineering Using Power Ultrasound." *Organic Process Research & Development* **2003,** *7* (6), 1002-1006.

163. Kaerger, J. S.; Price, R., "Processing of spherical crystalline particles via a novel solution atomization and crystallization by sonication (SAXS) technique." *Pharmaceutical research* **2004,** *21* (2), 372-81.

164. Wohlgemuth, K.; Ruether, F.; Schembecker, G., "Sonocrystallization and crystallization with gassing of adipic acid." *Chemical Engineering Science* **2010,** *65* (2), 1016-1027.

165. Hunt, J. D.; Jackson, K. A., "Nucleation of solid in an undercooled liquid by cavitation." *Journal of Applied Physics* **1966**.

166. Hem, S., "The effect of ultrasonic vibrations on crystallization processes." *Ultrasonics* **1967,** *5* (4), 202-207.

167. Chow, R.; Mettin, R.; Lindinger, B.; Kurz, T.; Lauterborn, W., "The importance of acoustic cavitation in the sonocrystallisation of ice-high speed observations of a single acoustic bubble." *Ultrasonics, 2003 IEEE Symposium on Ultrasonics* **2003**, 1447-1450 Vol.2.

168. Ohsaka, K.; Trinh, E. H., "Dynamic nucleation of ice induced by a single stable cavitation bubble." *Applied physics letters* **1998,** *73* (1), 129-129.

169. Hickling, R., "Transient, High-Pressure Solidification Associated with Cavitation in Water." *Physical review letters* **1994,** *73* (21), 2853-2856.

Chapter 2
Materials and Methods

This chapter describes general methods and experimental equipment relevant to the following chapters of the thesis. The focus will be on the introduction of equipment and methods essential to experiments described in this thesis, with emphasis on principles and specifications rather than particulars of their usage. Details of their applications to specific research topics will be presented in the subsequent chapters. This chapter is divided into two broad subsections: Section 2.1 deals with high-intensity ultrasonic horns for crystallization experiments while Section 2.2 introduces equipment necessary for the production and spectroscopic observation of single-bubble sonoluminescence.

2.1 Ultrasonic equipment for preparation, modification, and characterization of molecular crystals

There are two distinct uses for ultrasonic horns in this thesis: sonocrystallization and sonofragmentation. Two different horn schemes were employed for sonocrystallization and only one for sonofragmentation. This section discusses horn design, mechanisms of action, and deployment for each application.

2.1.1 Comments on ultrasonic horns

Crystallization and sonofragmentation experiments in this work were carried out exclusively with 20 kHz ultrasonic horns from Sonics and Materials. The specific model numbers are provided in descriptions of their applications in the appropriate chapters. For most of this work a horn with a removable, 1 cm^2 tip was used. Figure 2.1 diagrams a typical set-up for a sonication experiment. The horn is driven at its resonance frequency by a stack of lead zirconate titanate piezoelectric transducers. The titanium-aluminum alloy horn is designed to be the right size to be at resonance at 20 kHz when connected to the transducer. The exact resonance frequency is found by adjusting the frequency to minimize the applied power necessary to drive the sonotrode at a given amplitude. Some power supplies do this automatically while others require manual tuning. This is sometimes confusing to new users because the nominal 20 kHz frequency is considered to be fixed. The frequency shift to find resonance, however, is small; large changes in the horn size (for example, repeated sanding of the tip) will cause the horn to fail to be able to find resonance.

The length of the horn puts an antinode at the tip of the horn at 20 kHz. Heavy erosion of the tip can cause the horn to lose power as the acoustic interface will no longer reflect cleanly. Liquids penetrating the threading between the removable tip and the horn can also cause the tip to decouple from the rest of the horn and will cause the device to overload and shut down. This is especially a problem with low surface-tension liquids such as organic solvents but can be avoided by ensuring that the tip is screwed tightly in place.

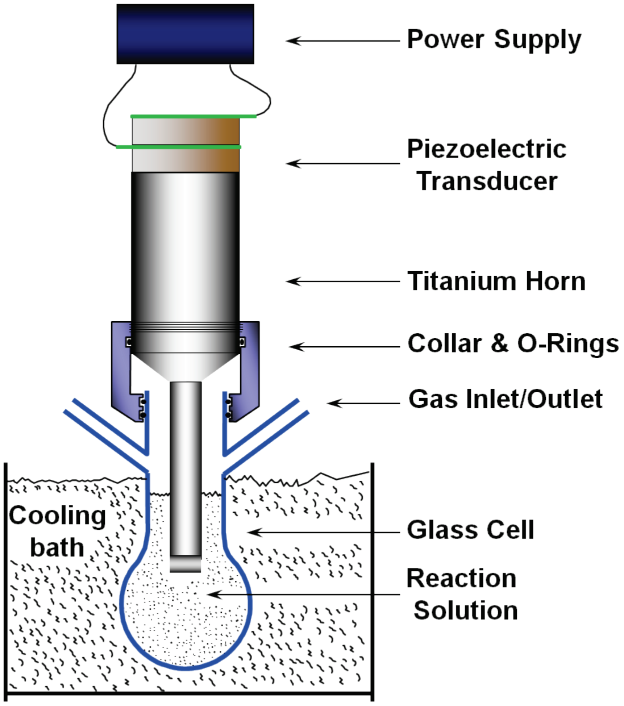

Figure 2.1 Experimental scheme. The lead zirconate titanate piezoelectric transducer is driven by a proprietary power supply at 20 kHz. The delivered power is amplified by tuning to the resonance of the horn and by the tapering of the horn. The horn is immersed in a reaction solution or slurry. In this example the cell (called a Suslick cell by some manufacturers) is held by o-rings on an aluminum collar. The o-rings seal and allow for controlled-atmosphere chemistry. The side-arms can be sealed or gas can be flowed through them. The solution will experience bulk heating; the temperature is modulated with a thermal bath.

The power supply of the horn delivers a voltage to the transducers, alternating phase at 20 kHz. The transducers correspondingly expand and contract according to the piezoelectric effect. This in turn applies pressure to the horn. The horn tapers to amplify the pressure applied at the end of the horn. Figure 2.2 shows some tapering schemes. All horns in this work were exponentially tapered, which is most effective for propagating the ultrasonic field. The other two designs shown are less powerful, but are popular because they are easier to machine.[1]

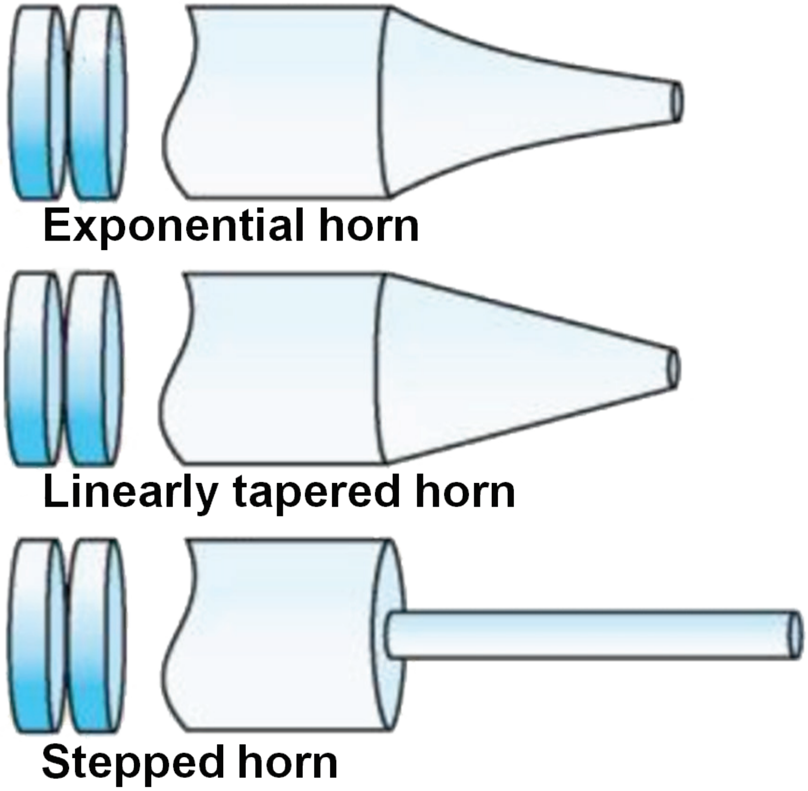

Figure 2.2 Horn designs. Reducing the horn diameter results in an amplification of the pressure delivered. A sharp step causes some of the sound to be reflected, but is relatively easy to manufacture.[1]

Sound propagates through the horn (and elsewhere) as a compression wave, meaning that the horn is alternating between expansion and contraction. Connections among horn parts are made at nodes. There are additionally threads at this point on many horns allowing for the attachment of a collar for holding glassware in place. As the horn tip is both an antinode and the point of maximum tapering (minimum diameter), it is the point of maximum displacement. Figure 2.3 shows calculated strains on the horn over the course of one acoustic cycle.[2] The first and last horn pictures represent the horn at maximum extension and the centermost horn picture is at maximum compression. Between maximum compression and extension the tip of the horn is displaced by roughly 50 μm.

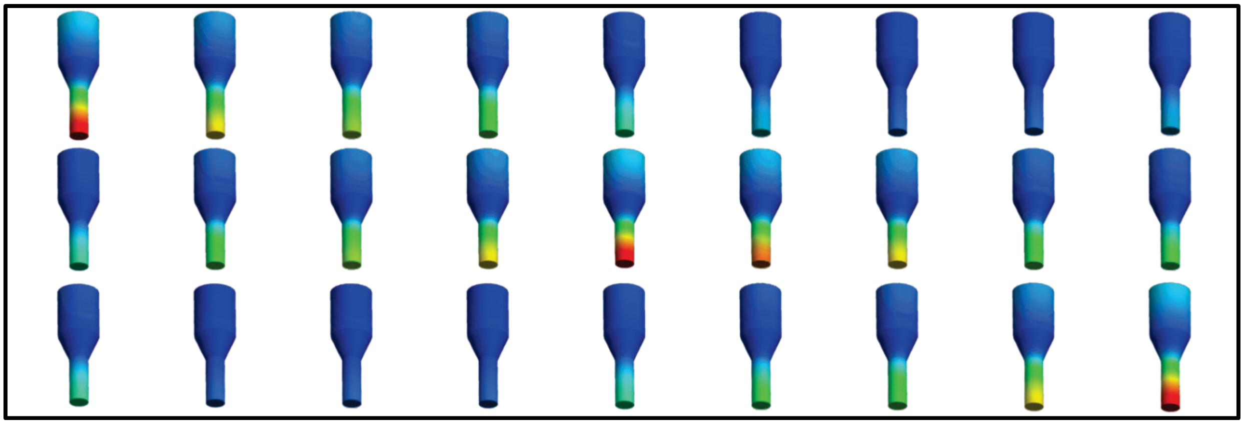

Figure 2.3 One acoustic cycle of an ultrasonic horn. The time spacing is arbitrary and depends on the horn frequency (for a 20 kHz horn one cycle will be 50 milliseconds so each image is separated by 1.85 ms). The horn is at maximum extension in the first and last image and at maximum compression in the center image. The color scheme indicates absolute displacement from rest, with blue corresponding to no displacement and red representing maximum displacement. The horn tip moves approximately 50 μm between maximum extension and maximum compression.[2]

2.1.2 Tapped ultrasonic horns

Another equipment scheme used in this work was a tapped horn. In this case ports have been drilled through the node of the horn and also up through the tip of the horn until the two bores connect. Figure 2.4 illustrates this idea. In this case liquid can flow through the horn and spread out over the surface of the horn. The liquid will be atomized by momentum transfer. Similarly, a liquid can be dispersed in another liquid. A small amount of liquid will flow out of the horn, displacing the liquid that was previously present, and then be dispersed when the high pressure phase of the ultrasonic field occurs. Liquid must either be flowing into the port or the port must be sealed or else ultrasonic pumping will occur. A tapped horn immersed in a liquid with no positive flow will pump liquid up through the tap and out the ports on the side. This is because the point of highest pressure is immediately below the horn. The pressure difference between the point below the horn and the points inside and above the horn causes the liquid to flow upwards and eventually out of the horn if the acoustic pressure is high enough to overcome gravity.

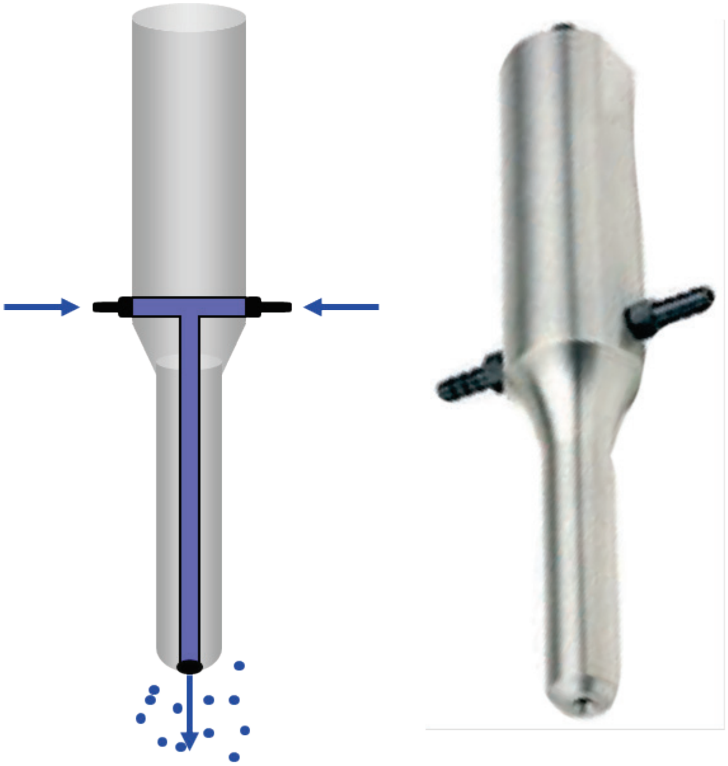

Figure 2.4 Tapped horn. Left: illustration of flow path in tapped horn. Right: image of tapped horn from manufacturer.

For a spray in air this particular horn (Sonics and Materials dual inlet atomizing probe VCX 130 AT) is capable of processing up to 20 L/hr of water with median droplet sizes of 90 μm (per manufacturers specification). If the horn is off then the liquid will just drip or drizzle, depending on flow rate. Figure 2.5 shows what the actual spray looks like in air at different powers. At 20% power (<1 W) there is insufficient momentum transfer to atomize the liquid. By 30% (~5.6 W) power the liquid is entirely converted to a fine mist.

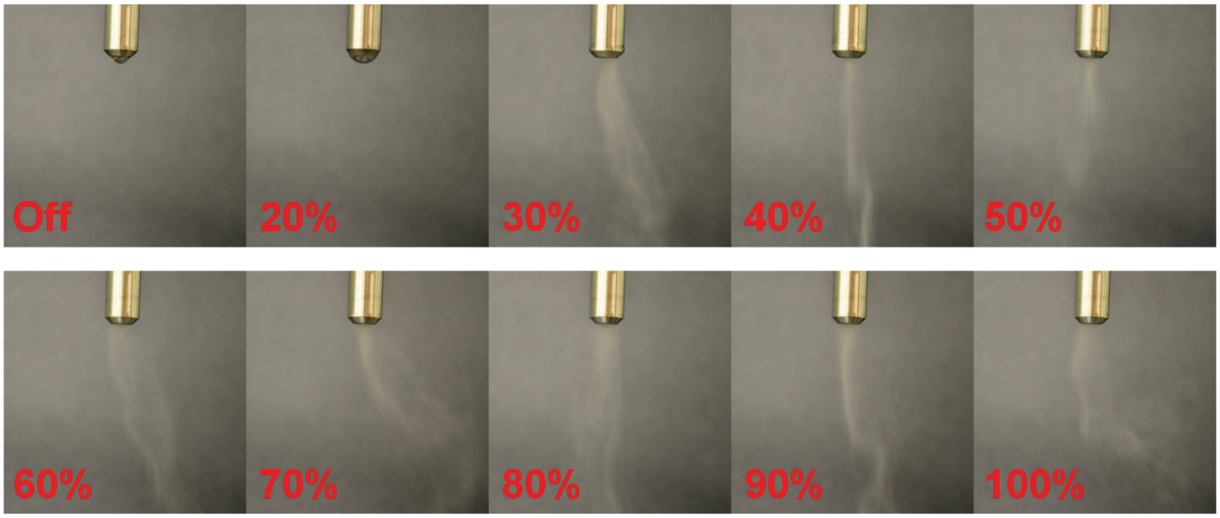

Figure 2.5 Tapped horn spray in air. Sonospray of ethanol passed through tapped 20 kHz ultrasonic horn at a rate of 3.3 ml/min. Horn power varies from off (0%) to ~40 W (100%).

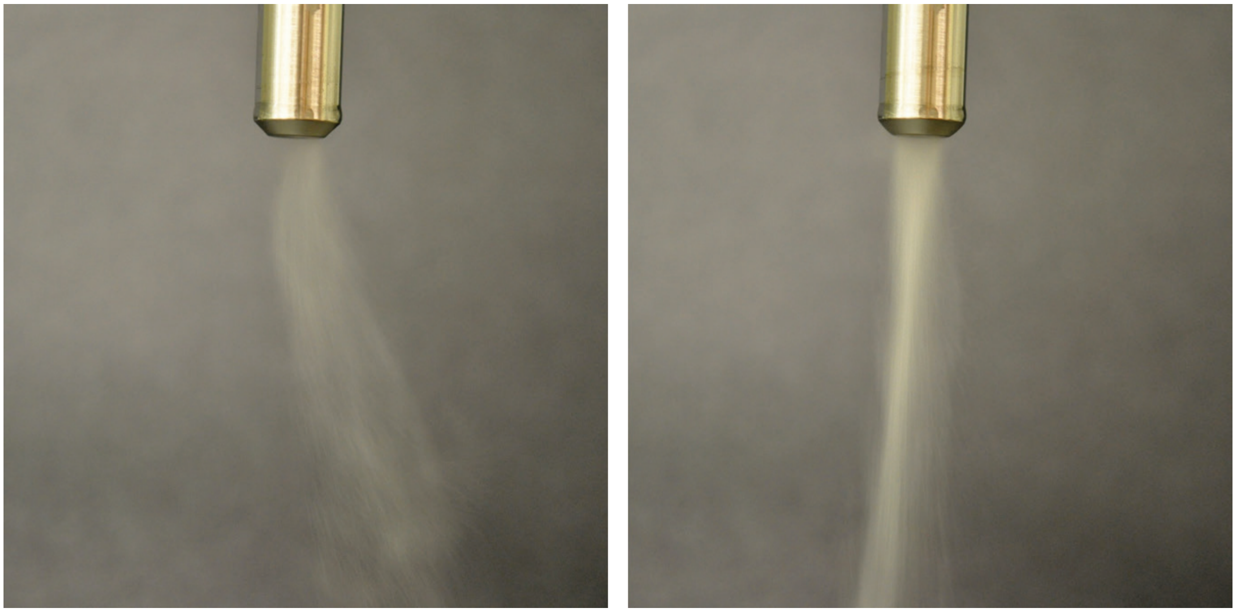

Figure 2.6 Tapped horn spray in air. Sonospray of ethanol passed through tapped 20 kHz ultrasonic horn at 30% power. Left: ethanol flowing at 3.3 ml/min. Right: ethanol flowing at 12.7 ml/min.

Flow rate is also important, of course. Figure 2.6 compares two different flow rates at 30% power. Flow rate is controlled by a peristaltic pump. Low flow rates produce a wispy, diffuse cloud of droplets while higher flow rates produce a more focused stream. At high flow rates and low acoustic power the centermost part of the stream can become a jet of liquid rather than a cloud of droplets.

2.1.3 Calibrating the ultrasonic horn

It is necessary to calibrate any horn in order to accurately report its output power. Horns typically have a nominal input power of 500 or 750 W and the user may vary the output from either 0% or 20% (depending on the transducer and power supply) to 100%. The actual power output cannot be obtained simply by multiplying the input power by the output percentage, as there are other losses in the system. One must instead measure the power output of the horn every time the system is changed (e.g., changing the power supply, changing the replaceable tip, sanding the tip many times).

The power output is most commonly standardized by calorimetry, although chemical dosimetry[3-4] is sometimes reported instead. To estimate the horn output calorimetrically, the horn is immersed in a known mass of water in an insulated container (e.g. 250 g of water in a dewar) and energized. The temperature change of the water is measured over a reasonable time period (every 30 seconds for 3 minutes was used in this work). The power output can be calculated from the temperature change according to the equation

$$Power = m\,C\,\frac{\Delta T}{\Delta \tau}$$

where m is the mass of water used, C is the heat capacity of the water (4.18 J g^{-1} K^{-1}), $\Delta\tau$ is the experiment time, and ΔT is the temperature change. In practice the $\Delta T / \Delta\tau$ relation is obtained by plotting the seven temperature measurements taken versus time, applying a linear fit, and extracting the slope of the line. The power for each power supply setting can then be correlated to the actual power output to generate a calibration curve. An aluminum collar screwed to the antinode of the horn for securing glassware may have a small effect on the delivered power. Conventional wisdom states that if a horn is going to be used with a collar it is preferential to perform the calibration with the collar in place. An example calibration plot for a 20 kHz ultrasonic horn with and without an aluminum collar is shown in Figure 2.7. The collar has a negligible effect in this case. The calibration was fit to a linear function in this case because it fits well ($r^2 > 0.996$ in both cases), but there is no fundamental expectation that this relationship should be linear. More complex relationships may be used to approximate the calibration if the linear fit is poor.

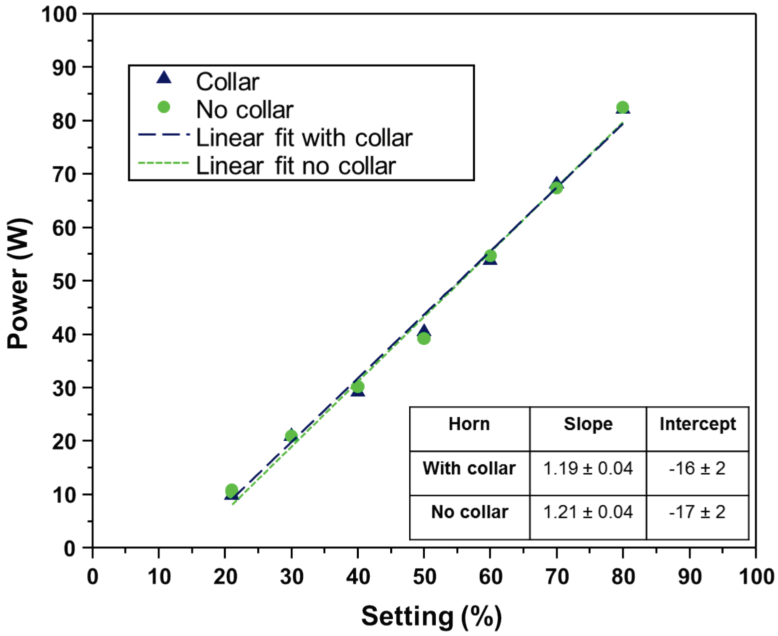

Horn	Slope	Intercept
With collar	1.19 ± 0.04	-16 ± 2
No collar	1.21 ± 0.04	-17 ± 2

Figure 2.7 Calibration curve for a 20 kHz ultrasonic horn. A typical calibration curve is shown here and the power outputs of a horn with an aluminum collar and without are compared. Data are fit well by linear regression fits.

2.1.4 Set-up for crystallization experiments

Crystallization of drug materials was performed using both types of ultrasonic apparatus described above (solid horn with replaceable tip and tapped horn). The general experimental scheme for each method is diagrammed here. Figure 2.8 shows the set-up for crystallization experiments performed with the solid horn.

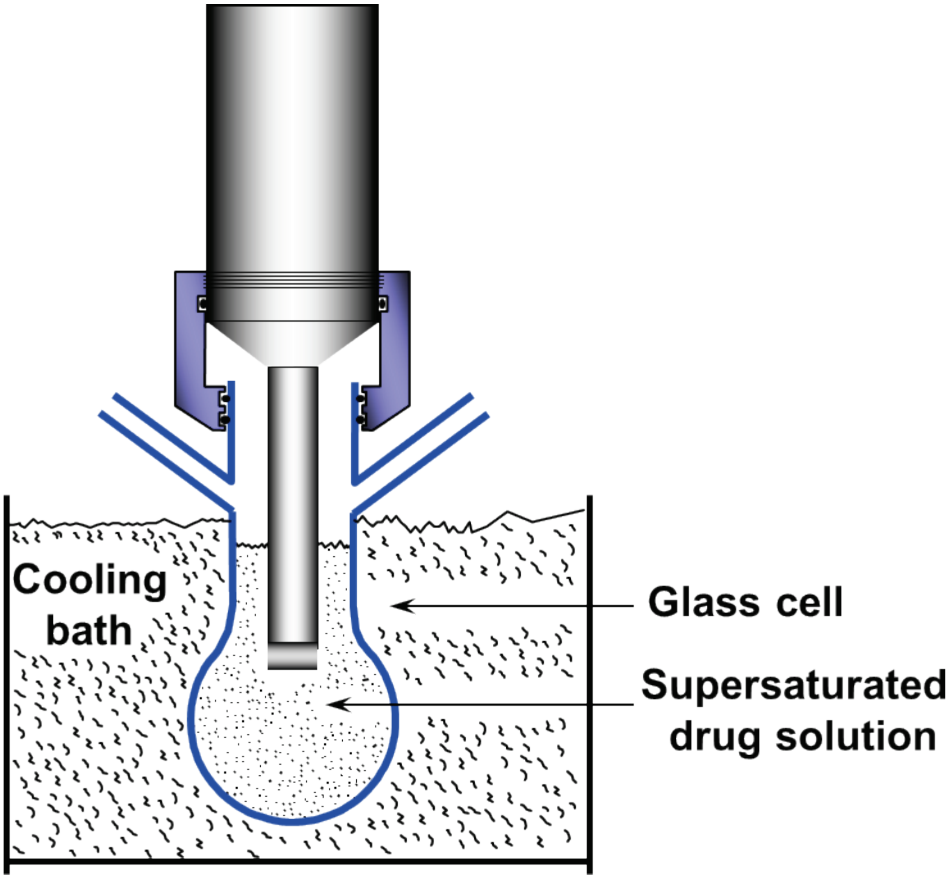

Figure 2.8 Cooling sonocrystallization. Nucleation is induced in a supersaturated drug solution by the application of ultrasound. Supersaturation is achieved by cooling using a thermostatted water bath.

A drug solution is dissolved in a solvent at elevated temperature, cooled to supersaturation, and nucleated via the application of ultrasound. Although a sonication cell which permits a controlled atmosphere, such as that shown in Figure 2.8, may be used, it is not necessary. In fact it was generally preferred to use a beaker, which was larger volume and allowed for rapid and facile insertion of the horn prior to nucleation and immediate removal afterwards. Although the horn can be immersed for the entire supercooling step it is itself a potential nucleation site (e.g., crevices between the removable tip and the horn) and it seemed desirable to minimize its presence prior to the insonation step.

Antisolvent sonocrystallization experiments involved a slightly more sophisticated apparatus, shown in Figure 2.9. A drug solution is pushed through the horn at a controlled rate using a syringe pump. The antisolvent can be a fixed reservoir, or a continuous flow (as in the cartoon) controlled by a peristaltic pump.

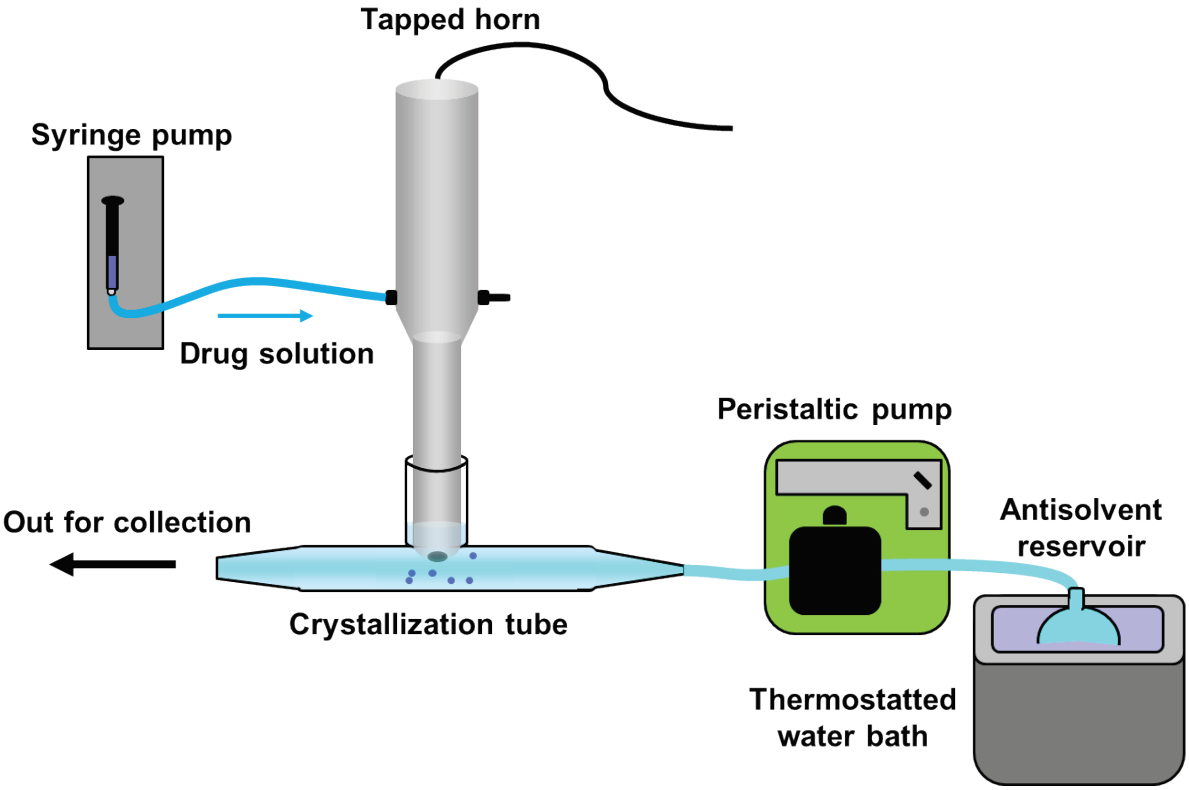

Figure 2.9 Antisolvent sonocrystallization. Droplets of a drug solution are dispersed in an antisolvent by ultrasound.

Presumably the solvent is dispersed in the antisolvent (which it is miscible with) and each droplet can act as an individual nucleation vessel. The solvent-antisolvent mixing and the nucleation are both promoted by the ultrasound. The slurry can be collected directly or diluted in additional antisolvent in the back end to quench ripening from the residual solvent.

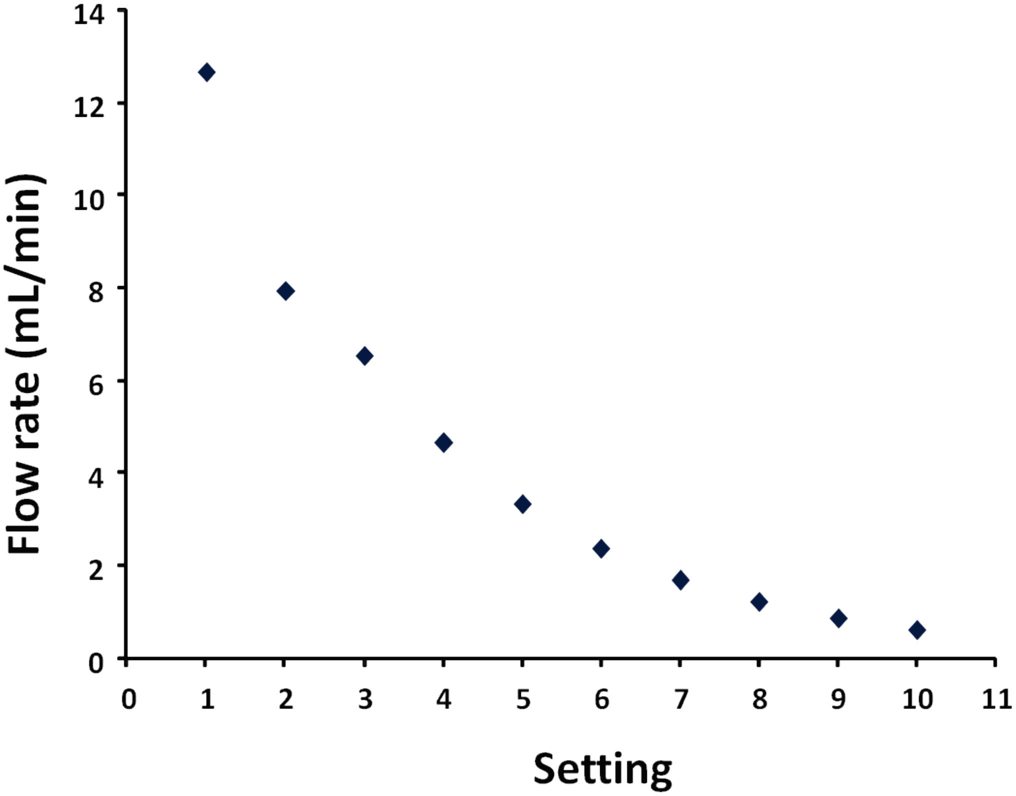

Figure 2.10 Solvent flow rate. The delivery rate of solvent depends on the syringe pump settings and the diameter of the syringe used. These data are for a 10 ml glass syringe.

The antisolvent and solvent flow rates are both variable. Figure 2.10 shows the flow rate of solvent delivered by the syringe pump for the first ten (out of 30) settings on the syringe pump using a 10 ml glass syringe. The peristaltic pump controlling the antisolvent flow rate has less distinct settings ("less distinct" meaning a continuously variable knob as opposed to discrete choices available on the syringe pump). It was preferred to keep it at the maximum setting (~65 ml/min), but could be varied down to 25 ml/min. Lower settings would produce a highly erratic flow.

2.1.5 Analysis of microcrystals

Larger (several microns or larger) crystals were analyzed with optical microscopy and image analysis. Image analysis was performed using ImageJ, a free, open-source software package available through the NIH.[5] Although ImageJ has automated protocols for image analysis they tended to be ineffective for this work. Routines for dealing with overlapping particles (watershedding algorithms) are only effective for slight overlap and even then commonly fail. Only images with well-dispersed particles, which normally occur only when there are few particles, could be analyzed in this way. This presents the dual problems of requiring a large number of images to process and additional judgment in determining whether the images used are representative of the whole.

Images were processed manually in an effort to overcome these challenges. The perimeter of each particle was defined by hand and the program calculated the corresponding area and circularity. Circularity is defined as

$$Circularity = 4\pi \frac{Area}{Perimeter^2}$$

and is a measure of the compactness of the shape. Circularity can vary from 0 to 1, where a circularity value of 1 would correspond to a perfect circle and 0 would be a rectangle with 0 width (an infinite aspect ratio). A perfect square would have a circularity of π/4. In this work crystals typically started as rectangles with aspect ratios of ~4:1 and trended towards a 1:1 aspect ratio under sonication, which was reflected in the circularity. Data acquired using ImageJ were used to compare experiments quantitatively and for population-balance modeling.

2.2 Equipment and methods for production and observation of single-bubble sonoluminescence (SBSL)

Single-bubble sonoluminescence was produced in a variety of resonant cells of different geometries. A general scheme will be presented here and design considerations will be discussed in more depth in Chapter 3. Similarly, the general apparatus, electronics, and procedure for collecting time-resolved spectra will be shown here, but the development of the technique to collect sonoluminescence spectra will be expanded on in Chapter 3.

2.2.1 Generating single bubble sonoluminescence

SBSL is the result of a single bubble trapped in an acoustic field. The basic requirements for this are an appropriate medium (a liquid), something to contain the liquid (the resonator), and something to provide the acoustic field. In this work sulfuric acid was the medium of choice, for reasons discussed in detail in Chapter 1. The acoustic field was applied with a piezoelectric ceramic which was in turn attached to a variety of electronics which will be described in this section.

Figure 2.11 shows an example SBSL resonator configuration. While the picture in the diagram is a round-bottom flask, any number of geometries may be used. Spheres and cylinders are most common in general, but sonoluminescence can be produced in beakers, Erlenmeyer flasks, coca-cola glasses,[6] and even Klein bottles. The resonator is typically held by clamping around its neck. A metal collar with a rubber spacer between the metal and the glass is sometimes used in order to minimize damping from the clamp, but is not a critical component. The clamp is held by an xyz translation stage to allow fine adjustment of the bubble position for collection of the light for spectroscopic evaluation.

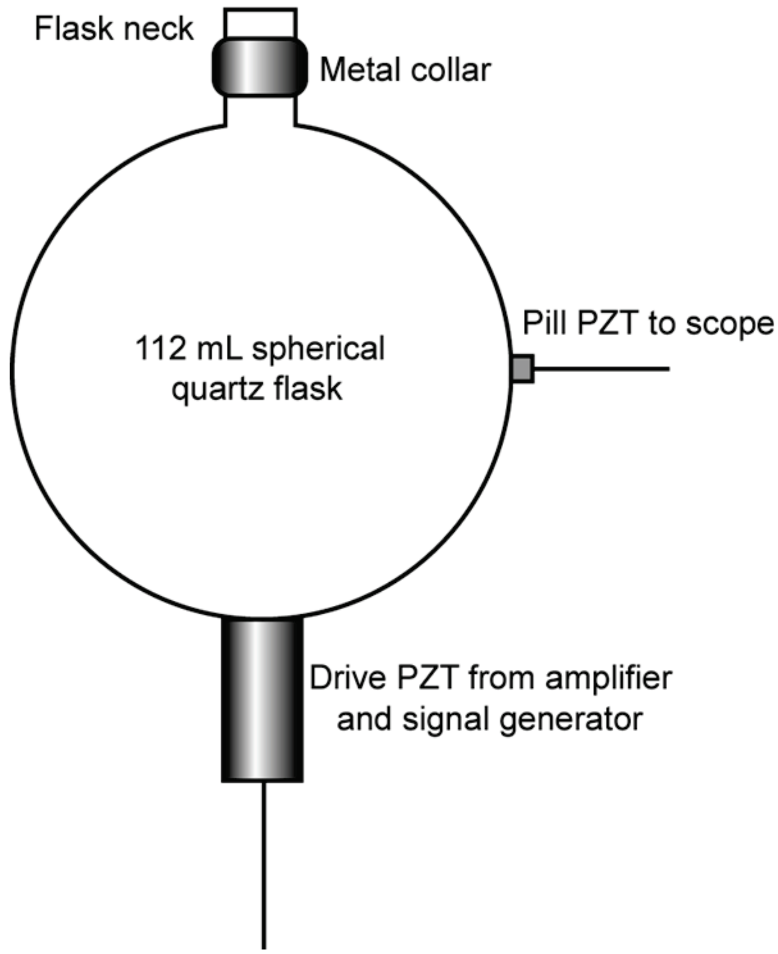

Figure 2.11 SBSL resonator scheme. A glass resonator (not necessarily spherical) is acoustically driven with a lead zirconate titanate (PZT) piezoelectric ceramic. The pill acts as a diagnostic microphone for detection of vibrations and is not strictly needed for the generation of SBSL.

An acoustic field is applied to the resonator by a piezoelectric ceramic, typically a poled cylinder of lead zirconate titanate (PZT). It is common to use a matched set of two ceramics, but it is not clear that there is any advantage to this. The ceramic is affixed with Loctite Quick Set^{TM} epoxy or Lightweld, a UV-cured glue. The former makes a more durable bond but requires several hours at minimum to cure satisfactorily (over a day to cure fully), while the latter can be prepared in a matter of minutes. The epoxy has the advantage of facile removable by either immersion in hot water for ~30 minutes or soaking in methylene chloride for a brief period. Lightweld required extended soaking in methylene chloride to remove the ceramic.

The acoustic field can be observed by an external PZT microphone affixed to the side (also with glue or epoxy) or an immersed needle hydrophone (DAPCO NP10-3), which also employs a piezoelectric protected by a layer of epoxy as the detector. Observation of the output of either of these diagnostics aids in finding resonances of the cell by looking for voltage spikes on the oscilloscope while sweeping the driving frequency. Although convenient, this is not strictly necessary; sulfuric acid tolerates a wide range of acoustic pressures and has very bright bubbles. It is generally effective to simply turn up the driving pressure and sweep the frequency until luminescence is observed or cavitating bubbles are heard (at high pressures the bubbles will slam into the glass and make a sharp sound). The pill or hydrophone is still needed for measuring the quality factor (Q) of resonators, which is discussed in Section 2.2.4.

Finding resonance can sometimes be a challenge and seems to require an intuitive feel for the system. It is helpful to have an idea of the correct frequency range to explore. For simple geometries one may calculate the expected resonance, although in practice luminescence always seems to occur at a frequency several kHz higher than expected. For a liquid-filled sphere spherically-symmetric resonances occur at

$$f_{sphere} = \frac{c\,n}{2r}$$

where c is the speed of sound in the liquid (1,470 m/sec for 85 wt% sulfuric acid[7]), r is the cell radius, and n is the order of the harmonic.[8] For a liquid-filled cylinder resonances can be approximated as[7]

$$f_{cylinder} = \frac{c}{2\,\pi}\sqrt{\left(\frac{n\,\pi}{L_z}\right)^2 + \left(\frac{x_{l,q}}{r}\right)^2}$$

where *c* is again the speed of sound, *n* is the order of the harmonic, and *r* is the cell radius. Additionally, L_z is the length of the cylinder and $x_{l,q}$ is a zero of a cylindrical Bessel function. The zeros of the cylindrical Bessel function for $l = 0$ are

$$k_{r,\theta} r = \begin{cases} x_{0,1} = 2.4048 \\ x_{0,2} = 5.5201 \\ x_{0,3} = 8.6317 \end{cases}$$

Typically, more exotic resonator shapes will have resonances similar enough to those of an equivalent sphere to get in the ballpark, but finding the exact resonance must be found empirically in all cases.

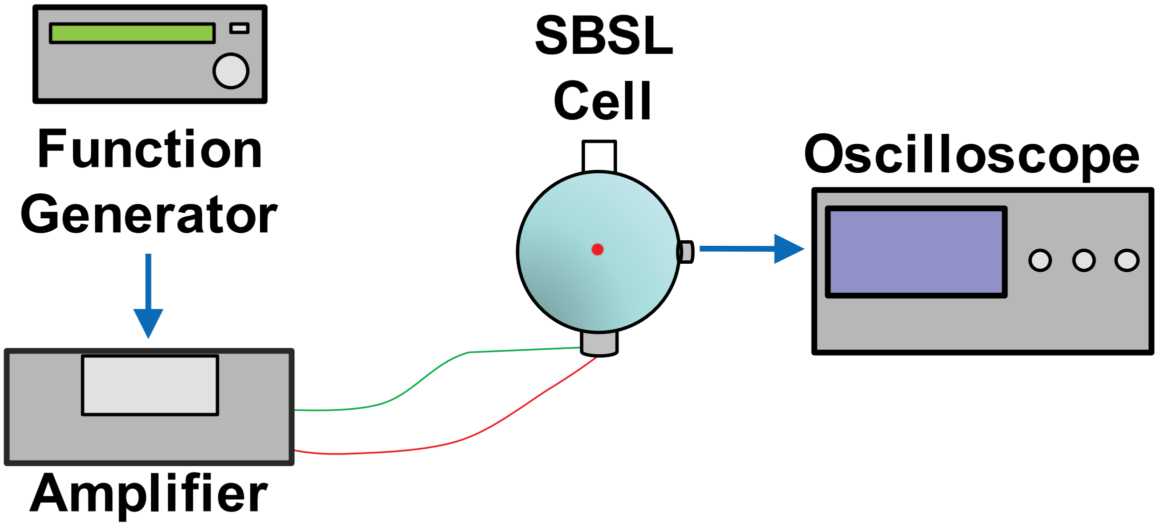

Figure 2.12 SBSL electronics set-up. An electronic waveform is generated by an arbitrary function generator, amplified, and converted to an acoustic wave by a PZT. Vibrations can be detected by a pill PZT or hydrophone and observed via an oscilloscope.

The waveform applied to the PZT – which can be sinusoidal, square, triangular, sawtooth, and perhaps other forms[9] – is generated by an arbitrary function generator (Hewlett-Packard 33120A). This device creates an alternating voltage with a manually-tuned frequency.

This frequency can be swept rapidly when finding the fundamental frequency of the resonator and can be tuned by steps as small as a millionth of a Hertz when optimizing conditions. In practice it is rarely useful to tune by steps smaller than 1 Hz and never smaller than 0.1 Hz. The function generator outputs a maximum of 10 V peak-to-peak, which was insufficient to generate sonoluminescence. For this reason the voltage is amplified before delivery to the PZT.

The PZT ceramic acts as a capacitor with high electronic impedance. The amplifier has variable output impedance (up to 1000 Ω), but cannot match the ceramics. On example ceramic was measured to have an impedance of 3000 Ω. As a result, a high voltage is required to deliver adequate power, which is achieved by routing the function generator output through a 700 watt Amplifier Research 700A-1 amplifier. These connections are made with BNC-terminated coaxial cables.

The amplifier will distort incoming signals above 800 mVPP, so when higher voltages are required it is important to maximize the output impedance and turn up the gain on the amplifier rather than increase the voltage on the function generator beyond the amplifier's limit. The impedance mismatch can be addressed with an inductor circuit, but turning up the gain on the amplifier is effective and there was never any clear improvement with an inductor circuit in place.

2.2.2 Preparing solutions for SBSL

SBSL in this work was generated almost exclusively in 85 wt% sulfuric acid. Emission characteristics and bubble stability both depend on the gas content of the liquid, so it was necessary to carefully control this parameter. A wide variety of techniques have been used to degas sonoluminescence solutions, including sonication, boiling, freeze-pump-thaw, and vacuum pumping. The last was employed in this work. The degassing/regassing apparatus used is diagrammed in Figure 2.13.

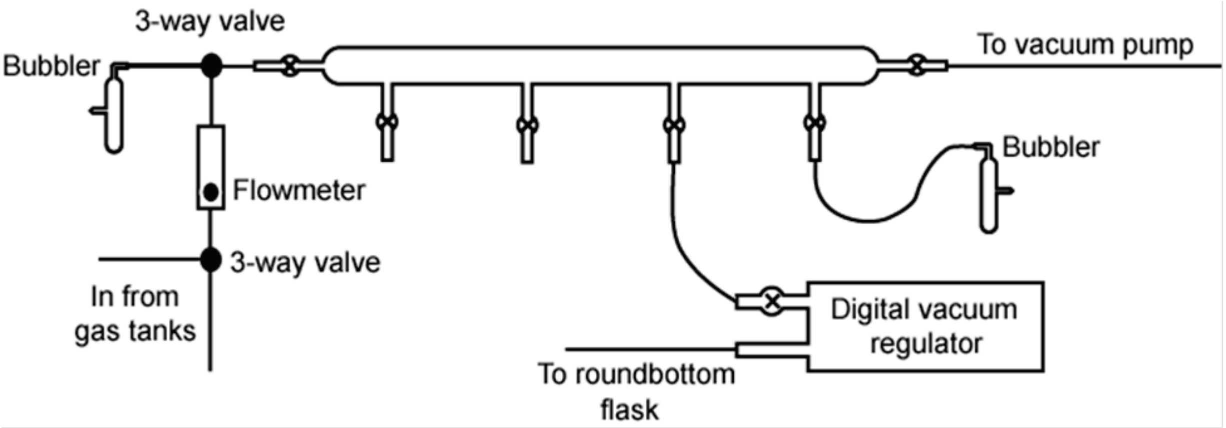

Figure 2.13 Degassing rig for SBSL. A roughing pump is used to degas liquids. Regassing is controlled with a vacuum regulator.

A sufficient volume of sulfuric acid was prepared by the admixture of 98 wt% sulfuric acid and nanopure water (water deionized to >18 MΩ·cm resistance, scrubbed for organics, and passed through a 0.45 µm filter with a Barnstead NANOpure® ultrapure water purification system). The mixing was done in a 500 or 1000 mL roundbottom flask with a sidearm for schlenk work and a 24/40 neck joint. This flask was immersed in ice to counteract the heat of mixing of the two liquids and minimize the water lost to evaporation. The specific volume used depended on the type of resonator used.

A magnetic stir bar was added to the flask and the top was sealed with a Teflon cap or a septum. The flask was immersed in a temperature controlled bath to keep it at room temperature during degassing and allowed to thermally equilibrate before exposure to vacuum. The vacuum was applied through a schlenk line attached to a roughing pump. The line typically pulled a vacuum of 25 mTorr. The solution was gently stirred and allowed to degas overnight. The vapor pressure of concentrated sulfuric acid is extremely low – about 40 mTorr[10] – so it is not necessary to use a LN_2 trap, but it is preferred due to the lower pressures achievable from cryogenic pumping. The long degassing time is needed because of the high viscosity of the mixture.[11] This can be overcome by heating the solution –solutions can be prepared with heating in just a few hours – but water is lost in the process and the actual final concentration must be determined by measuring the volume of water caught in the liquid nitrogen trap or by titration. Figure 2.14 shows some relevant properties of sulfuric acid/water mixtures.

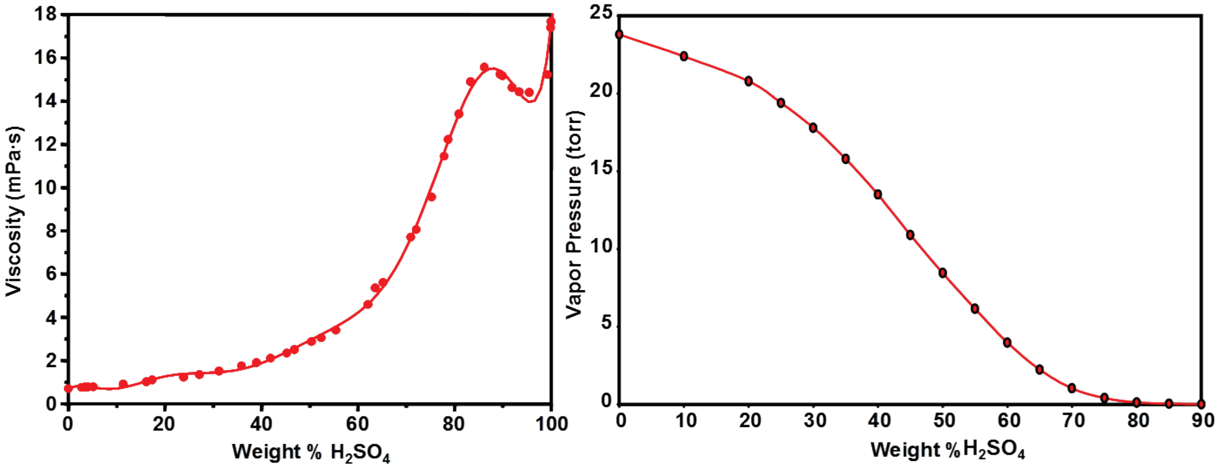

Figure 2.14 Properties of sulfuric acid/water mixtures. Left: viscosity of sulfuric acid/water mixtures as a function of concentration. Adapted from Rhodes, F. H. *et al. Ind. Eng. Chem. Res.* **1923**, *15*, 850. Right: vapor pressure of sulfuric acid/water mixtures as a function of concentration. Adapted from Greenewalt, C. H. *Ind. Eng. Chem. Res.* **1925**, *17*, 522.

After degassing for at least a day solutions were regassed with 50 Torr of noble gas, usually krypton or xenon. Regassing was done with the aid of a J-KEM Scientific digital vacuum regulator, model 200.

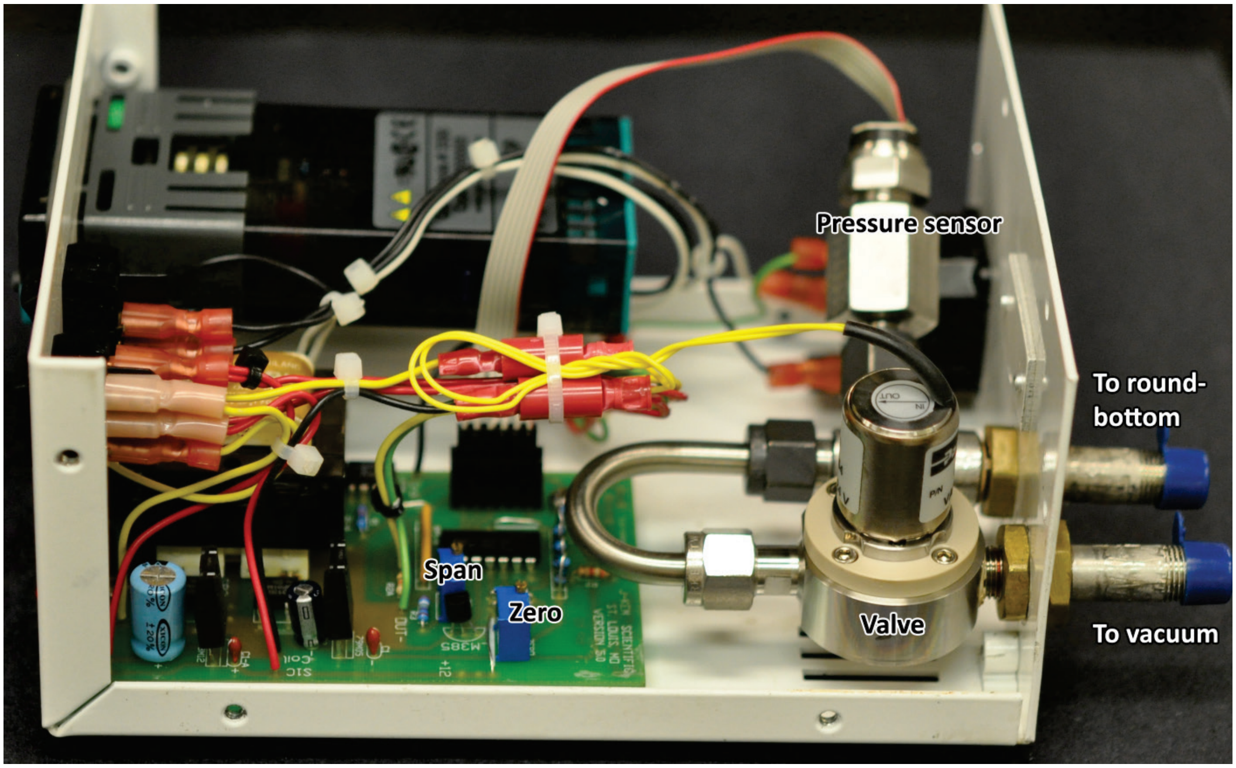

Figure 2.15 Digital vacuum regulator for regassing solutions. Important components of the vacuum regulator.

The vacuum regulator is essentially a stainless steel, U-shaped tube with a pressure sensor (employing a ceramic piezoelectric) and a solenoid valve (Figure 2.15). The "to vacuum" outlet is connected to a needle valve (not shown). The device has a setpoint function that allows the user to target a pressure and the regulator will automatically modulate gas flow to achieve the desired pressure. The pressure is changed by opening or closing the solenoid valve, which regulates a 60 μm pinhole. This setpoint function is optimized for degassing rather than regassing and generally works poorly for preparing SBSL solutions. It is much more precise to disable the setpoint function and control gas flow manually using the needle valve.

The "span" and "zero" labels in Figure 2.15 refer to screws used for calibrating the pressure sensor. The vacuum regulator should be evacuated completely (down to a few mTorr) and the "zero" screw should be turned until the digital display reads "0." A reference gauge is necessary to know when adequate vacuum (significantly below 0.1 Torr) is achieved. The regulator should then be exposed to atmospheric pressure and the “span” screw turned until the display matches the local barometric pressure. Several iterations of this process may be required. The regulator is accurate, at best, to 0.1 Torr.

The 60 μm pinhole makes evacuation of the round-bottom flask through the regulator inefficient. It was found with multiple regulators that vacuum pressures lower than 0.5 Torr could not be achieved when routed through the regulator, even when a second thermocouple gauge hooked into the system immediately before the regulator would read as low as 5 mTorr. Further, the solenoid valve has a tendency to trap small particulate impurities, which can keep the valve from working properly or contaminate solutions during regassing and it is consequently preferred to minimize its time in service. For these reasons degassing was performed without the regulator in place.

When it was time to regas, stirring was stopped and the round-bottom flask was sealed, disconnected from the vacuum line, and connected to the vacuum regulator. The tubing going to the regulator from the vacuum line and to the flask from the regulator was evacuated to below 1 Torr of pressure and then flushed with 760 Torr of the noble gas intended for regassing. The regulator is not designed for positive pressures so care must be taken not to overpressurize during flushing. The line was flushed three times before finally being evacuated, at which point the needle valve on the regulator was closed and the stopcock on the round-bottom flask was opened. Stirring was restarted and 50 Torr of noble gas was slowly bled into the system. The flask was sealed at the stopcock and the solution was allowed to stir for one hour.

Stirring was stopped after 1 hour, the flask was gently vented to atmospheric pressure, and the solution was transferred to the resonator by slowly pouring. Cannula transfer using

Teflon tubing was assayed at times, but there was no discernible improvement in bubble behavior and there were concerns about additional regassing during the transfer process. It was further extremely difficult to get the correct volume by cannula transfer, as it is necessary to fill the resonator to an exact height to get high-quality resonance and good reproducibility. This volume is typically at the neck of the vessel, so a small miscalculation can lead to concentrated sulfuric acid pouring over the side of the flask, degrading the epoxy and silvering on the ceramics, and causing other undesirable effects on local equipment and researchers.

2.2.3 Measuring acoustic pressure

Measurements of acoustic pressure were made with a DAPCO NP10-3 needle hydrophone (Figure 2.16). Measurements were made by immersing the probe into the solution near the bubble and moving it until the highest reproducible pressure measurement was observed. It is important that the hydrophone not touch any glass surfaces or an artificially high reading will be obtained. It is also necessary to eliminate the SBSL bubble and any bubbles introduced by the immersion of the hydrophone, as their cavitation will cause spikes in the signal.

The hydrophone has a stainless steel casing that seems to be adequately resistant to sulfuric acid. The pressure sensor is a PZT in the tip of the hydrophone, protected by an epoxy. The epoxy will survive short immersion in concentrated sulfuric acid, but extended and repeated exposure will eventually induce failure, especially if cavitating bubbles adhere to its surface.

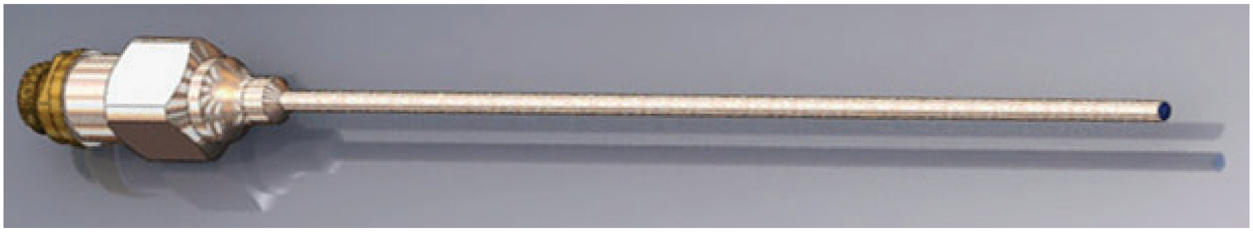

Figure 2.16 Needle hydrophone for measuring acoustic pressure. DAPCO NP10-3 needle hydrophone.

The hydrophone connects to a BNC cable which can be plugged into an oscilloscope to measure the output voltage. This output is proportional to acoustic pressure. The hydrophone will age and should be recalibrated annually for sensitive measurements. Needle hydrophones are the hydrophones of choice in the field of SBSL, in part because many SBSL resonators have small necks and will not permit a large diameter hydrophone, but mainly because the hydrophone is small relative to the wavelength of the acoustic field and will perturb it minimally during measurement. Unfortunately hydrophones of this size are designed to operate at or above 1 MHz. They are functional for SBSL because extremely high pressures are reached in the experiment relative to most hydrophone applications, overcoming their inherently poor sensitivities at low ultrasonic frequencies.[6]

Unfortunately, low sensitivity makes the hydrophone extremely difficult to calibrate. There are two basic calibration schemes: comparison and reciprocity.[12] The reciprocity technique relies on the principle that a hydrophone can also act as a signal source. If one hydrophone has a calibrated output then it can be used to calibrate the receiving hydrophone. This was not possible for the DAPCO needle hydrophone because no available calibrated hydrophone could produce significant signal to be detected. The comparison technique involves measuring the output of an unknown signal source with a calibrated hydrophone, then replacing the hydrophone with the unknown hydrophone. The comparison technique was employed here.

The hydrophone should be in the acoustic free-field for calibration, meaning (in part) that it should not be experiencing reflections from the walls of the calibration chamber. At high frequencies (megahertz range) and short wavelengths this is a relatively simple task: one may simply collect a short burst of signal for calibration before any reflected waves have time to reach the hydrophone. At low ultrasonic frequencies this is not feasible without a huge volume of water. Although there are facilities equipped to do this, they are expensive – a calibration quote from Neptune Sonar Ltd. was considerably pricier than a new (uncalibrated) hydrophone. Instead of using a large volume of water it was necessary to use an anechoic chamber. Professor William D. O'Brien, Jr. in the Beckman Institute generously permitted the use of his lab for this task. A 20 kHz ultrasonic horn was used as the signal source – nothing else readily available produced a strong enough signal. A NIST-traceable NRL hydrophone (also borrowed from the O'Brien group) was used as a reference.

The sensitivity of needle hydrophones is orientation-dependent. This is not a crucial factor when measuring a spherically-symmetric wave (as in SBSL), but when calibrating from a point source it is necessary to point the needle tip directly at the source, necessitating the complete immersion of the hydrophone in water. Silicone caulking protects the electrical connections of the hydrophone, but the connections were additionally wrapped in Teflon tape for greater water resistance.

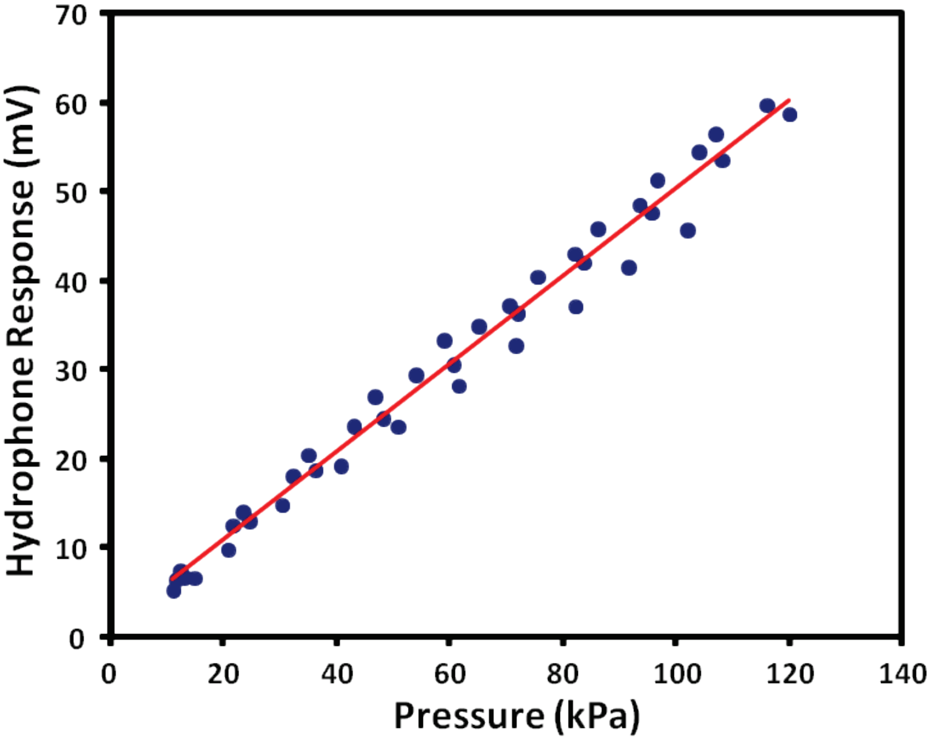

Figure 2.17 Hydrophone calibration curve. Blue dots are measurements representing multiple trials. Red line is linear regression fit.

It is very difficult to place the needle hydrophone in exactly the same place as the sensitive element in the reference hydrophone and the data in Figure 2.17 are consequently noisy (the measurement in the error approaches 20%). The calibration (47.6 mV/atm) was accepted because it was similar to previous calibrations of the same instrument and because it is most valuable as an internal comparison tool, as each lab in the field has their own way of measuring acoustic pressure.

There are special calibration techniques available to the SBSL researcher. One technique is to prepare a water solution regassed with 150 Torr of air. SBSL in this solution will begin at 1.2 atm and become brightest at 1.4 atm (followed by rapid bubble destruction at higher driving pressures). Knowing these two points allows for a rough 2-point check of the hydrophone, but requires some judgment.[13] A more precise way to do this is to stabilize a non-luminescing bubble (below 1.2 atm driving amplitude) and extract the acoustic pressure from solving the Rayleigh-Plesset equation based on laser scattering off the bubble. A calibration may be performed based on the comparison of the hydrophone response to the bubble dynamics.[6]

2.2.4 The quality factor (Q)

Researchers in the field of single-bubble sonoluminescence are apt to discuss it as an art[14] or voodoo.[8] It is difficult to quantitatively describe how well an SBSL system is working, which in turn makes it difficult to optimize. Further, aspects such as room temperature and the age of the epoxy holding the ceramics in place are difficult to control precisely and may have significant effects on bubble behavior. The quality factor, Q, is the primary figure of merit used for describing how well an SBSL system works. Much is made of this number, with 1000 supposedly being a desirable Q for SBSL.[8] Discussion of the merits of Q will occur in Chapter 3. Here, however, we will define Q and describe its measurement.

Q is sometimes described as the "ring time" of the resonator, in analogy with a bell. It is mathematically described as

$$Q = \frac{\omega}{BW}$$

where ω is the resonant frequency and BW is the bandwidth, or full-width half max, of the pressure peak as you change the frequency away from resonance. Figure 2.18 illustrates this idea. One way to estimate the Q values is to measure the acoustic pressure with a hydrophone or pill at a variety of frequencies and generate a plot such as those in Figure 2.18. It was more convenient to measure the ring time of the cell, however. The idea is that the driving force is quelled in order to see how long the resonance is detectable. The number of cycles it takes for the amplitude of the signal to decay to 1/e (~37%) of its original value is equal to Q/π. In practice the time required to decay to 1/e is measured and this is converted to the number of cycles using the resonant frequency.[15]

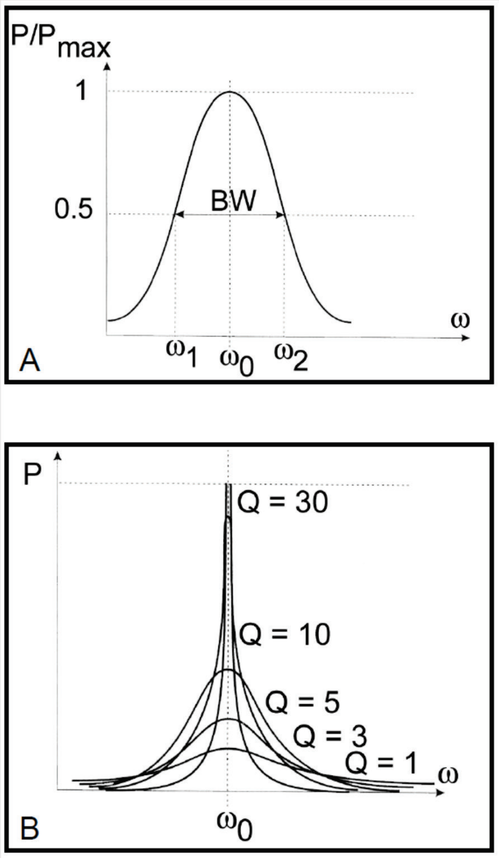

Figure 2.18 Visual representation of Q. A) Illustration of the meaning of BW (bandwidth) for the definition of Q. B) Comparison of relatively high (sharp peak) and low (broad peak) Q values.

The Hewlett-Packard 33120A arbitrary function generator has a burst function, which runs an on and off cycle. For measuring Q values the cell was driven for 5000 cycles to allow the acoustic wave to build up in the resonator. Two of these 5000 cycle bursts were generated every second (a 5000 cycle burst at 2 Hz). The decay after the shutoff of the electronics was observed via a hydrophone or pill connected to an oscilloscope and was highly reproducible unless resonance shifted due to temperature changes. Figure 2.19 shows an example of this decay and represents a Q of 300 at 27.5 kHz.

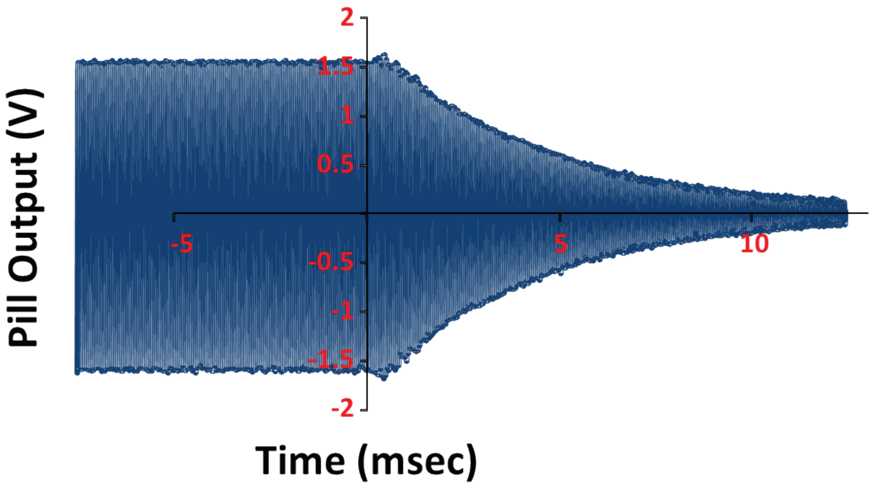

Figure 2.19 Signal decay. Die-off of pill signal after driving electronics are switched off. These data come from a resonator driving at 27.5 kHz and represents a Q of ~300.

The signal is entirely the result of the "ringing" of the resonator. The resonator was disconnected and the same experiment was performed, but monitoring the output directly from the amplifier rather than from the pill to ensure that there is no analogous "ringing" in the electronics. The output reached 0 V within one cycle, indicating that the driving voltage has no contribution to the decay time.

2.2.5 Time-resolved spectroscopy of SBSL

Time-resolved spectra were acquired with a Hamamatsu C4334-01 streak camera detector attached to an Oriel MS-257 spectrograph (Figure 2.20) in the Dlott group. The streak camera was triggered by a delay generator (Stanford Research Systems model DG645), which was in turn triggered by a PMT (Hamamatsu H10720-01 PMT with a C10065 evaluation board) detecting an SBSL pulse. A 250 ml Erlenmeyer flask was used as the resonator and aluminum off-axis mirrors were used to guide and focus the light into the spectrometer.

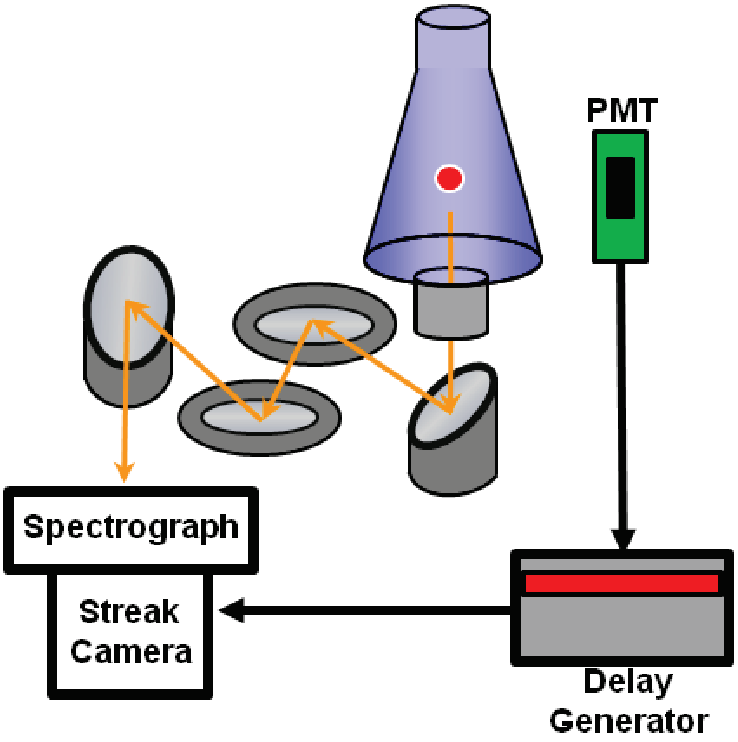

Figure 2.20 Time-resolved SBSL collection apparatus. A single, luminescing bubble is trapped in a 250 mL Erlenmeyer flask with 85 wt% sulfuric acid solution regassed with Kr or Xe. SBSL emission was imaged 1:1 onto the 200 μm slit of the spectrograph using aluminum-coated parabolic off-axis mirrors suitable for the collection of UV light. The streak camera was triggered by a delay generator, which is in turn triggered by the PMT response to the immediately preceding sonoluminescence event.

The streak camera operation is cartooned in Figure 2.21. Incoming light is spectrally resolved by the spectrograph and passes through a 50 μm slit to impinge on a photocathode. The photocathode converts the photons into electrons, which pass through the streak tube. The streak tube is an evacuated chamber with deflection plates on the top and bottom. The deflection plates supply a voltage ramp that deflects the electrons. These electrons are amplified by a microchannel plate, converted back to photons by a phosphor screen, and finally detected by a CCD.

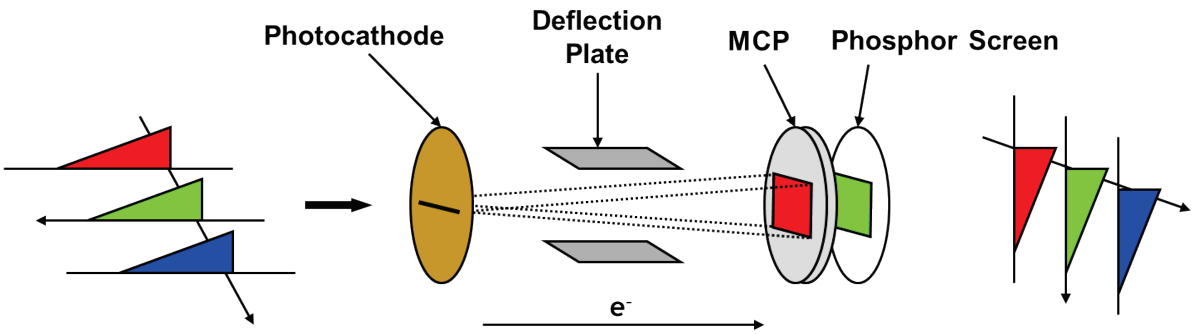

Figure 2.21 Streak camera operation.

The voltage ramp results in electrons being deflected by different amounts depending on when they entered the streak tube. The different deflections result in the final photons hitting the detector CCD in different locations. The voltage ramp is well-defined as a function of time and time information can therefore be extracted from the spatial information collected by the CCD. The CCD is 480 pixels tall by 640 pixels wide and has a resolution of 7 pixels, meaning that there are approximately 68 resolving units available on the chip. The temporal resolution achievable is determined by the rate at which the voltage ramps (the sweep rate). At higher sweep rates higher temporal resolution is achieved, down to 15 ps on this instrument, but a shorter time period can be observed, limited by the height of the CCD chip. At 15 ps resolution the time window is only 1 ns.

SBSL in this work was produced at roughly 21 kHz; each acoustic cycle is therefore ~47 μsec in length while the sonoluminescence event is on the order of 10 ns long. A streak window of 20 ns or 50 ns was used for temporally resolving SBSL in this work. Catching a 10 ns event with a 20 ns window in a 50 μsec space requires precise synchronization of the detection equipment with the sonoluminescence pulse.

The synchronicity of sonoluminescence can be quite good – the time wander between pulses can be as low as 200 ps in water.[16] In sulfuric acid the synchronicity is a few nanoseconds up to several microseconds. The time-resolved SBSL experiment exploits the high synchronicity possible in sulfuric acid, using one SBSL pulse to trigger the delay generator, which creates a delay equal to one acoustic cycle. After one period a second SBSL pulse is expected, and the delay generator triggers the streak camera. The synchronicity must be on the order of 10 ns or better in order to successfully collect a sonoluminescence event with reasonable frequency.

The streak camera can be triggered at the same frequency as the bubble emission, but the CCD detector can only refresh at 20 Hz. The synchronicity of SBSL is imperfect and catching multiple events on a single frame is therefore undesirable. Single frames were captured by including a second delay (a "prescale" function on the delay generator) of approximately 1,000 acoustic cycles between each collection. Figure 2.22 illustrates this idea.

Figure 2.22 Streak camera operation. Triggering scheme for time-resolved collection of SBSL. One SBSL event triggers the streak camera to detect the following event. Roughly 1,000 acoustic cycles are not streaked (truncated in figure) to allow the CCD detector to refresh, and then the collection cycle is repeated.

Spectra were saved as Hamamatsu Image Sequences (.his files), which is the fastest saving protocol available in the streak camera software. This essentially creates a video of events which must subsequently be extracted frame-by-frame for analysis. About 5,000 frames were collected in each file. The system was checked to ensure that it was still on resonance and tuned if necessary between collections.

2.2.6 Data processing and corrections

Single bubble events were captured rather than integrating many shots because imperfect synchronicity would cause the spectra to imperfectly overlap with one another in time. Figure 2.23 shows several sample frames. The handful of photons in one frame is typical; the light emission from a single SBSL event is small, the solid angle collected is small, and there are absorptive and scattering losses in the optical path. Consequently, a large number of frames must be added to produce a spectrum, but in order to do this each frame must be corrected for its temporal jitter.

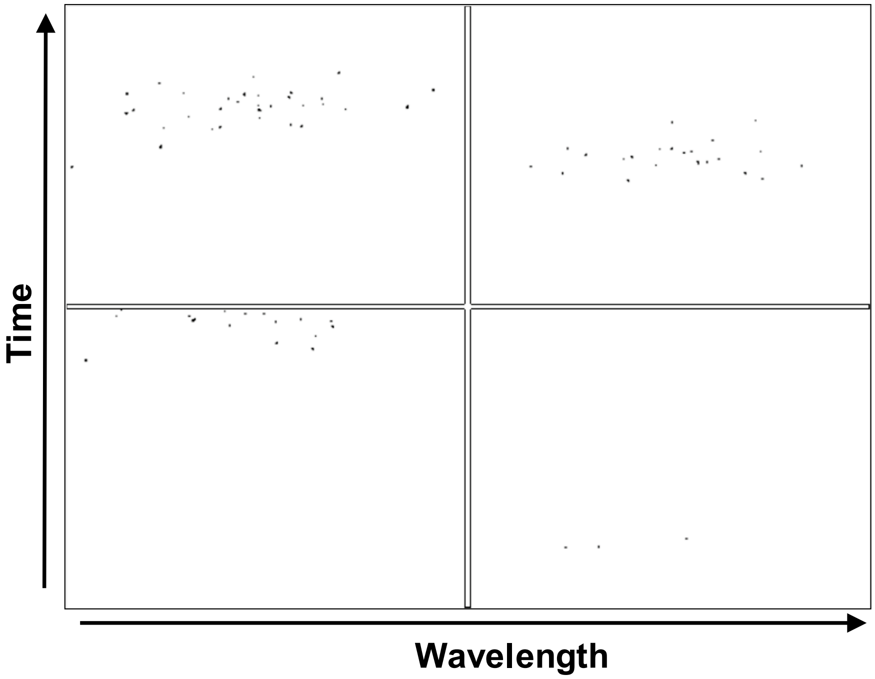

Figure 2.23 Example streak camera data. Top two spectra: SBSL events that fall within collection window but are shifted in time relative to one another. Bottom left: SBSL event partially out of the frame. Bottom right: noise.

Jitter correction was done using a MATLAB script. Each frame is extracted from the .his file as a .dat file, which contains a 480x640 array of tab-delimited numbers corresponding to the response of each CCD pixel. All of these numbers are non-zero due to dark current, but the signal from real photons is about one hundred times higher than the background at the gain settings used in this experiment (gain was set at 14 or 16). The background was subtracted by zeroing all numbers below twice the median pixel value. All frames that had below ~10 photons, for example, the bottom right frame in Figure 2.23, were excluded from further analysis.

The low signal in a given frame means that two photons hitting the same pixel is an insignificantly rare event, which is fortunate because the very high gain settings used in this experiment would make it challenge to distinguish between a one-photon and two-photon event. A low-light technique called single photon counting was employed here, where all signal below a threshold was set to 0 and all signal above the threshold was set to 1 using a MATLAB script.

The temporal center of mass of each frame was calculated by summing each row – creating a 480x1 vector with no wavelength information and finding the center of mass of the vector, calculated as

$$Center\ of\ mass = \frac{1}{J}\sum j_i i$$

where *J* is the total intensity in the entire frame, and *j* is the intensity of a given vector index, *i*. If the center of mass is too close to the top or bottom of the frame (conservatively chosen to be the top and bottom 25%), as in the bottom left of Figure 2.23, the frame is excluded from further analysis. All frames that pass intensity and position criteria are subjected to a flat-field and tilt correction.

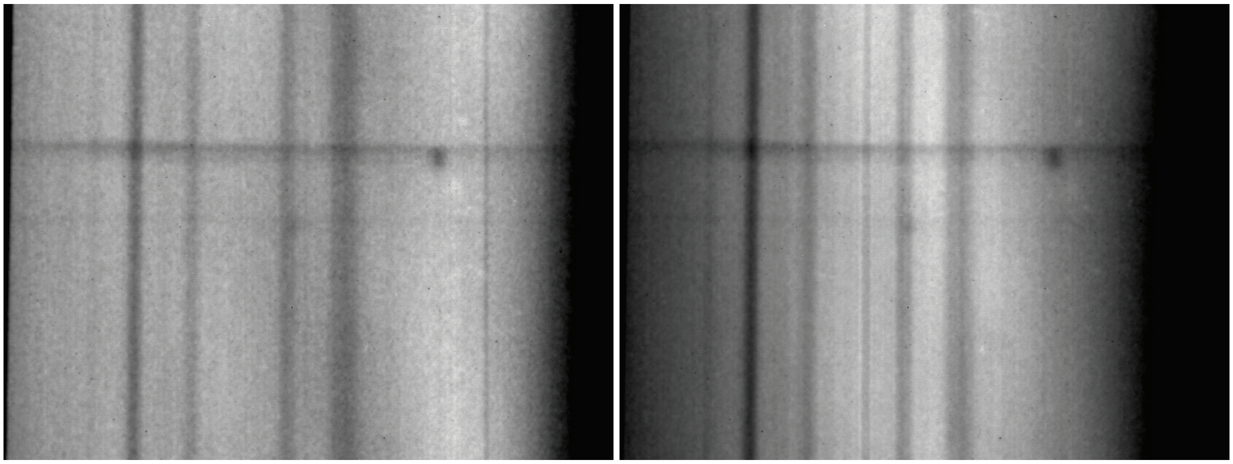

Figure 2.24 CCD response to calibration lamps. Left: CCD response to deuterium calibration lamp. Right: CCD response to tungsten halogen calibration lamp.

Figure 2.24 shows the response of the entire optical pathway (except for the sulfuric acid and resonator), streak camera, and CCD camera to a standardized deuterium lamp and to a standardized quartz tungsten halogen lamp, both NIST traceable. The CCD has regions of low sensitivity due to laser damage, courtesy of previous users. Each spectrum must be corrected for the sensitivity of the CCD pixels that detected it before it can be jitter-corrected, called the flat-field correction. The correction amplifies the signal in low sensitivity regions to acknowledge the fact that there is a lower probability of detection for photons striking that pixel. The expected spectrum is a function of wavelength only (i.e., the intensity should vary in the x dimension but not the y dimension). Figure 2.25 gives the expected spectrum for each lamp, which was used a reference to generate the correction matrix.

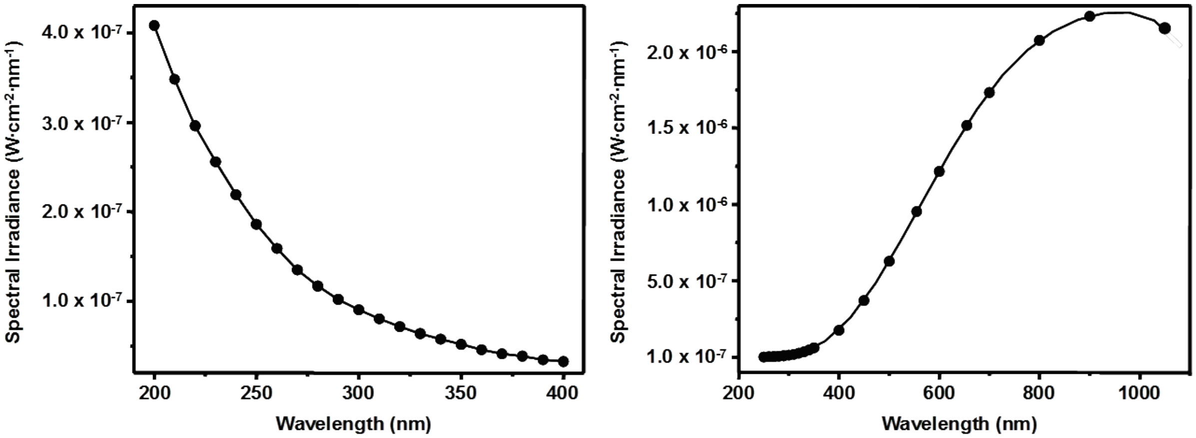

Figure 2.25 Output of standardized lamps. Left: deuterium standard lamp output. Plot and polynomial fit of the true emission spectrum of the OL UV-40 deuterium standard lamp as provided by the manufacturer. Right: quartz tungsten halogen standard lamp output. Plot and polynomial fit of the data of the true emission spectrum of the Eppley Lab EH-164 quartz tungsten halogen standard lamp as provided by the manufacturer.

After intensity corrections the spectrum is corrected for tilt, which is a slight shift in pixel position performed in MATLAB. The photocathode is not perfectly level and incoming white light will consequently not strike a single row of pixels when the camera is not streaking. The tilt causes a variance of 8 pixels across the length of the CCD. This is corrected by applying a counter-slope to the data in MATLAB.

Jitter correction is finally completed after flat-field and tilt corrections. All frames are added about their temporal centers of mass to create a spectrum. Final corrections are performed on the integrated spectra. These corrections are for the absorption of the quartz window on the bottom of the resonator and for the absorption of sulfuric acid. These absorbances are shown in Figure 2.26.

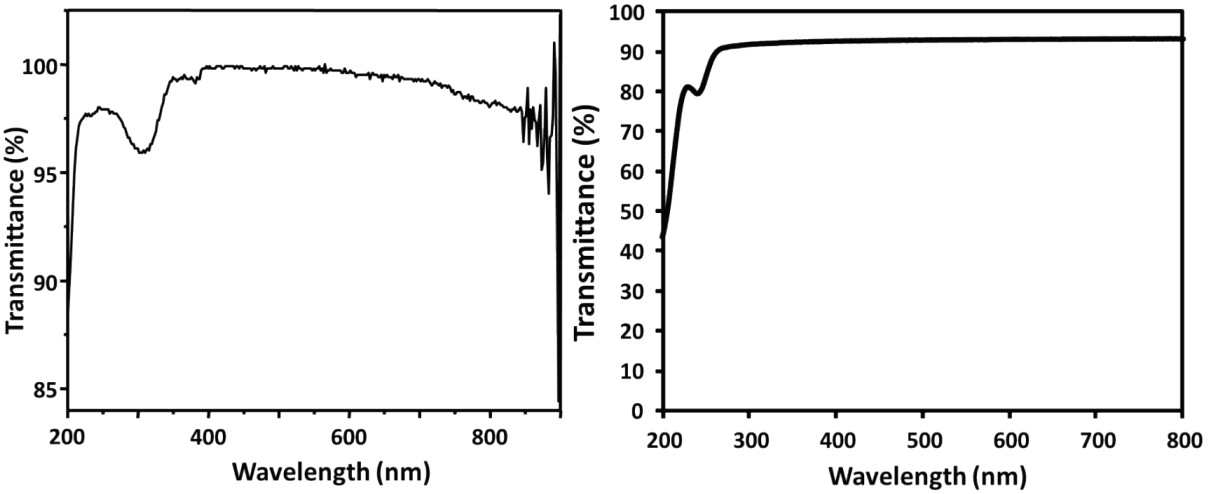

Figure 2.26 Absorbances of optical components. Left: absorbance of quartz window. Right: absorbance of 1 cm 85 wt% sulfuric acid.

The final summed and corrected matrix may be divided into sections consisting of 7 rows each. Each of these columns corresponds to one time block, which is 750 ps for a 50 ns streak or 300 ps for a 20 ns streak, which are the two streak settings relevant to this work. These spectra are plotted and fit to a blackbody distribution. The Planck equation for a blackbody is

$$B_\lambda(T) = \frac{A}{\lambda^5}\left(e^{\frac{hc}{\lambda \, k_B T}} - 1\right)^{-1}$$

where B_λ is the intensity at a given wavelength, T is the temperature of the emitting blackbody, k_B is Boltzmann's constant, h is Planck's constant, c is the speed of light, and A is a prefactor that includes several physical constants, the emissivity of the plasma, the radius of emission, and the collection efficiency of the system. A and T are adjustable parameters for fitting. The value of A was taken as the average A value from high-signal time blocks (roughly ±1 ns about the temporal center of mass) and held constant, making T the only adjustable parameter in the final fitting step.

2.3 References

1. *Piezoelectric Ceramics: Properties and Applications*. APC International, Ltd: Mackeyville, Pennsylvania, 2002; p 111.

2. http://sonomechanics.com/technology/ultrasonic_horn_designs_and_properties/ (accessed June 1).

3. Kimura, T.; Sakamoto, T.; Leveque, J.-M.; Sohmiya, H.; Fujita, M.; Ikeda, S.; Ando, T., "Standardization of ultrasonic power for sonochemical reaction." *Ultrasonics Sonochemistry* **1996,** *3* (3), S157-S161.

4. Son, Y.; Lim, M.; Khim, J., "Investigation of acoustic cavitation energy in a large-scale sonoreactor." *Ultrasonics Sonochemistry* **2009,** *16* (4), 552-6.

5. http://rsb.info.nih.gov/ij/.

6. Matula, T. J., "Inertial cavitation and single-bubble sonoluminescence." *Philosophical Transactions of the Royal Society A: Mathematical, Physical and Engineering Sciences* **1999,** *357*, 225-249.

7. Hopkins, S.; Putterman, S.; Kappus, B.; Suslick, K.; Camara, C., "Dynamics of a Sonoluminescing Bubble in Sulfuric Acid." *Physical Review Letters* **2005,** *95*, 2-5.

8. Barber, B. P. Synchronous Picosecond Sonoluminescence. University of California Los Angeles, 1992.
9. Chen, W.; Chen, X.; Lu, M.; Miao, G.; Wei, R., "Single bubble sonoluminescence driven by non-simple-harmonic ultrasounds." *The Journal of the Acoustical Society of America* **2002,** *111*, 2632.

10. Greenewalt, C., "Partial Pressure of Water Out of Aqueous Solutions of Sulfuric Acid." *Industrial & Engineering Chemistry* **1925,** *17*, 522-523.

11. Rhodes, F. H.; Barbour, C. B., "The Viscosities of Mixtures of Sulfuric Acid and Water." *Industrial & Engineering Chemistry* **1923,** *15*, 850-852.

12. Bobber, R. J., *Underwater Electroacoustic Measurements*. Peninsula Publishing: 1990; p 341.

13. Flannigan, D. 2010. Personal communication.

14. Putterman, S. J., "Sonoluminescence: The Star in a Jar." *Physics World* **1998,** *11*, 38-42.

15. Hopkins, S. D. Exploring the limits of cavitation. University of Illinois at Urbana-Champaign, 2006.

16. Barber, B. P.; Putterman, S. J., "Observation of synchronous picosecond sonoluminescence." *Nature* **1991,** *352* (6333), 318-320.

Chapter 3

Time-resolved single-bubble sonoluminescence in sulfuric acid

This chapter deals with the extraction of time-resolved information about the conditions during sonoluminescence. It includes development of both the production of single-bubble sonoluminescence (SBSL) and streak camera techniques for the detection of SBSL.

3.1 Introduction

The conditions formed inside an acoustically-driven, cavitating bubble during collapse are extreme, reaching temperatures on the order of 15,000 K and pressures of over a thousand atmospheres.[1-3] The chemical consequences of the severe conditions created during cavitation have burgeoned into widespread applications for the synthesis of novel nanomaterials.[4] The mechanism of formation of these extreme conditions during cavitation, however, remains controversial.

The phenomena associated with cavitation have been extensively investigated by spectroscopic observation of light emitted from excited atoms or molecules inside the bubble, integrating over the life of the bubble. To extract information about conditions during cavitation, both atomic emission lines (usually from noble gases[1-2, 5-6]) and the underlying broad continuum[7-8] have been used as spectroscopic thermometers. Unfortunately, these experiments divulge only time-averaged information, whereas the evolution of the conditions created during the collapse of a single bubble has been largely unexplored and the few reports concerning the time evolution of collapsing bubbles are conflicting and problematic.[9-10]

There is strong evidence that an optically opaque plasma is formed under typical single-bubble sonoluminescence (SBSL) conditions.[2, 9, 11-15] The measured emission temperatures during sonoluminescence are not extreme enough to create sufficient ion density for optical opacity in a conventional plasma (e.g., the mean-free path of photons produced inside the plasma is expected to be several hundred microns, which is much larger than the bubble itself[16]). This implies either (1) the plasma has a relatively cool surface surrounding a much hotter opaque plasma core (at least ~35,000 K),[2, 16] or (2) Debye shielding reduces the effective ionization potential of gas atoms in the bubble.[9, 11] In long-lived (~1 μsec) bubbles driven at low frequency (40 Hz), it has been proposed that there is a transition from a dilute plasma at the onset of sonoluminescence to an opaque, blackbody emitter during peak conditions and back to a dilute, optically thin plasma during the bubble's rebound.[9]

There has been some debate, however, over the nature of the continuum emission observed in SBSL and the relative contributions of blackbody vs. bremsstrahlung emission. Some hydrodynamics calculations predict that sonoluminescence emission is at least in part a consequence of bremsstrahlung emission from an optically thin, dilute plasma.[17] This is supported by time-correlated photon counting measurements that show that the bubble emission lifetime has no wavelength dependence.[18-19] A blackbody emitter heating from and cooling to room temperature would be expected to have a longer emission lifetime at visible wavelengths. This may also reflect differences in the parameters controlling cavitation. Putterman has suggested that optical opacity only occurs at lower frequencies: driving at high frequency (1 MHz) in order to reduce the size of the bubble such that the mean free path of photons is longer than the bubble radius results in Bremsstrahlung-type emission.[20] Time resolved spectra from large bubbles shaken at 40 Hz show an apparent transition from Bremsstrahlung to blackbody and back during collapse.[9]

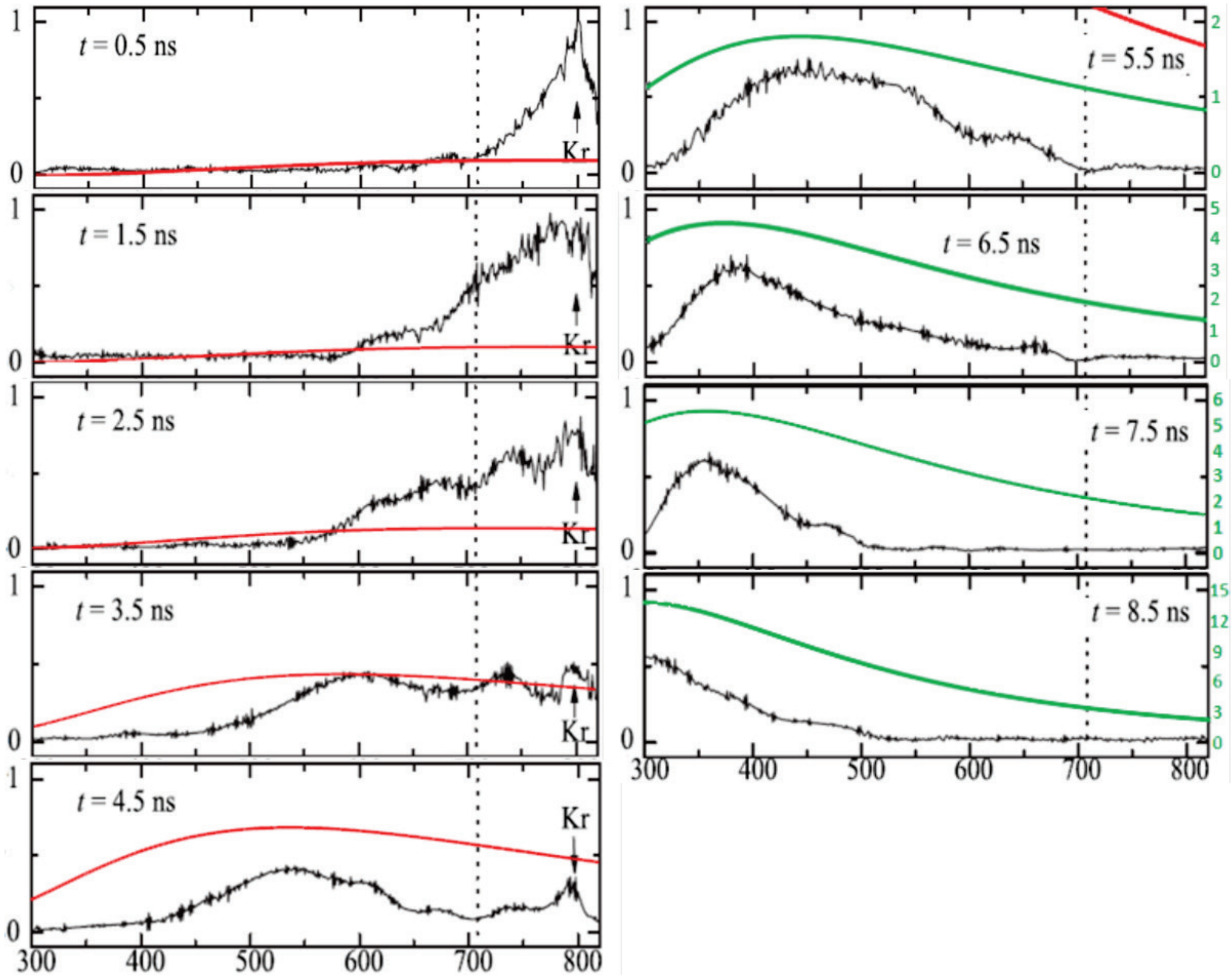

Figure 3.1 Failure of literature spectra to obey Stefan-Boltzmann law. Comparison of literature report[10] of time-resolved SBSL to predicted blackbody emission behavior. Red lines are on-scale with literature values (normalized such that literature and calculated spectra peaks match at 600 nm at t=3.5 ns). Green lines have been scaled to fit in window; note the corresponding green scale indicators on the right of the chart.

The prevailing understanding of bubble behavior, however, was challenged by a recent report by Chen et al.[10] that cannot be reconciled with SBSL as a consequence of compressional heating. Time-resolved spectra indicated a monotonic blue shift (interpreted as heating), but with no observed cooling. For any compressional mechanism, one would expect some approximate temporal symmetry: spectral changes due to heating during bubble compression should be qualitatively similar, but temporally inverted, to cooling during bubble re-expansion. Furthermore, Chen's reported spectral changes and output intensity were entirely inconsistent with the Stefan-Boltzmann law, which dictates that total energy output of a blackbody is directly proportional to the fourth power of the emitter's temperature ($I_{total} \propto T^4$). Surprisingly, the extremely large spectral shifts (>500 nm) over time were accompanied by essentially no change in emission intensity.[10] Figure 3.1 illustrates how grossly Chen's work deviates from the expectation for a blackbody emitter.

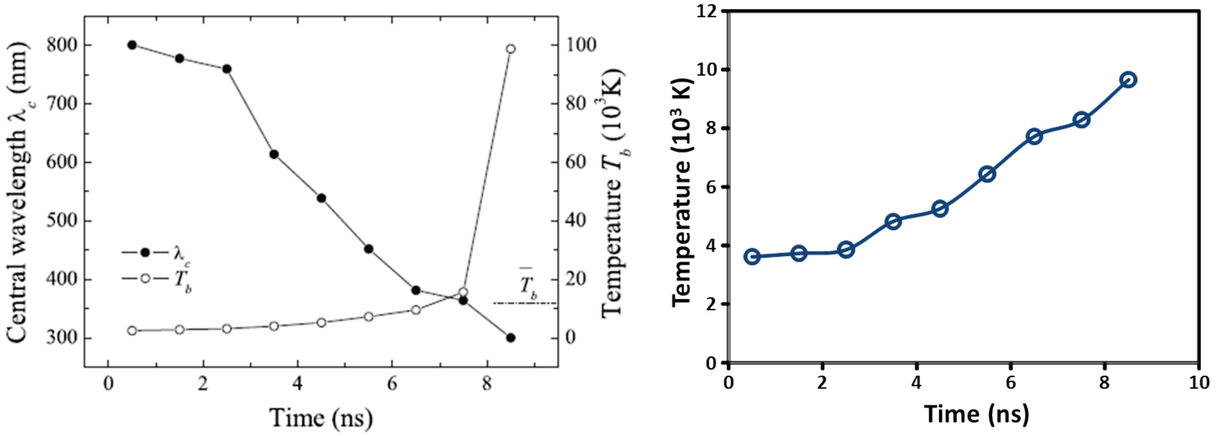

Figure 3.2 Further puzzling literature items. Left: peak wavelengths and extracted temperatures according to Chen.[10] Right: temperatures calculated from Wien's displacement law based on Chen's reported peak wavelengths.

His temperature analysis is also baffling. Figure 3.2 shows his temperature calculations versus what is derived from Wien's law. Wien's law is a consequence of Planck's law and dictates that the blackbody emission temperature is related to the peak wavelength (λ_{max}, wavelength at which the blackbody emitter has the highest intensity) as $T = b/\lambda_{max}$, where b is a constant equal to 2,897,768.5 nm·K. While a maximum temperature of 100,000 K is reported, the corresponding λ_{max} is roughly 300, which indicates an actual temperature of only ~10,000 K. The λ_{max} for a 100,000 K blackbody emitter is expected to occur at 29 nm. Note that the intensities calculated in Figure 3.1 are based on peak wavelength, not reported temperature. If the 8.5 ns time block really corresponded to a 100,000 K blackbody emitter it would be so bright that it would be impossible to resolve the other time blocks in the same measurement. A gain setting that would permit spectral resolution of the 100,000 K blackbody would collect so little light from the lower temperature emission times that they would be indistinguishable.

3.2 Experimental notes

In this work, SBSL was produced in 85 wt% sulfuric acid at 21 kHz in a 250 mL Erlenmeyer flask with the bottom replaced by an optical-grade quartz window affixed by an acid-resistant epoxy (EE-10, ARCOR Epoxy Inc.), which was generously donated by the company. Solutions were degassed overnight and regassed with 50 Torr of noble gas according to the protocol described in Chapter 2. SBSL in sulfuric acid is an attractive system to study due to long emission times (typically several nanoseconds at low ultrasonic frequencies) in comparison to SBSL from water (which can be as short as 50 picoseconds[18-19]). Moreover, the total light emission in sulfuric acid is hundreds to thousands of times more intense than in water.[2]

The acoustic field was applied via a piezoelectric lead zirconate titanate ceramic bonded to the bottom of the resonator with Loctite Quick Set^{TM} epoxy. The ceramic had a large diameter (1.5” inner diameter) to permit light collection through its center. Spectra from cylindrical or spherical cells agreed qualitatively with results from the Erlenmeyer flask.

Time-resolved spectra were acquired with a Hamamatsu C4334-01 streak camera detector attached to an Oriel MS-257 spectrograph. The streak camera was triggered by a delay generator (Stanford Research Systems model DG645), which was in turn triggered by a 0.6 ns PMT (Hamamatsu H10720-01 PMT with a C10065 evaluation board) detecting the previous SL pulse. The pulse-to-pulse synchronicity of bubble events had to be ~10 ns or better in order to collect a sufficient number of usable frames. The trigger rate was low enough to ensure that at most only a single emission event was collected in each frame. The triggering protocol is described in more detail in Chapter 2. Spectra were acquired with 300 picosecond resolution over the range 250 to 700 nm, determined by where the collection optics and photocathode of the streak camera are sensitive.

3.3 Resonator construction and design

Bubbles in sulfuric acid are spatially unstable [21-22] and the region of observation was 200 μm x 50 μm (determined by the spectrograph and streak camera slits, respectively). Bubbles will wander spatially over a radius of a millimeter or two and will therefore frequently not be observed by the detector. It is critical, therefore, that the bubble's motion path be minimized. Considerable effort was expended in an effort to reduce bubble motion for this work. Ultimately, improvements made in this area were small – the most important changes made to permit collection of spectra were in streak camera protocol – but this section will discuss the construction, characterization, and optimization of resonators.

There are several parameters to consider in the production of high-quality SBSL. The most important are solution preparation, choice of PZT ceramic, attachment of the ceramic, and cell geometry. If everything is working well, this last parameter seemed to be the most important, although any of the other factors can cause the system to fail. It is challenging to optimize the system because small changes in any one parameter may ultimately be important, but if one of the other parameters is not close to optimal then that defect will dominate the experiment and the effects of other changes will be obscured.

3.3.1 Metrics for evaluating SBSL quality

Determining whether a parameter change has 'improved' the system can at times be nebulous. There are three vital parameters for collecting time-resolved spectra: synchronicity, longevity, and spatial stability. Synchronicity can be measured concretely, but not easily, by either analyzing many events observed in a PMT or by collecting many events on the streak camera and measuring the temporal width of the integrated events compared to a single event. Figure 3.3 illustrates the importance of high synchronicity. Mie scattering of laser light off a bubble shows the bubble dynamics (bubble radius is proportional to the square of the scattering intensity). The vertical line (and inset) at time 0 is the PMT response to the sonoluminescence event. It is clear that sonoluminescence is a very brief event relative to the acoustic cycle, and capturing that event in such a long time window requires a precise and accurate trigger. The triggering protocol depends on the time interval between sonoluminescence events being highly regular.

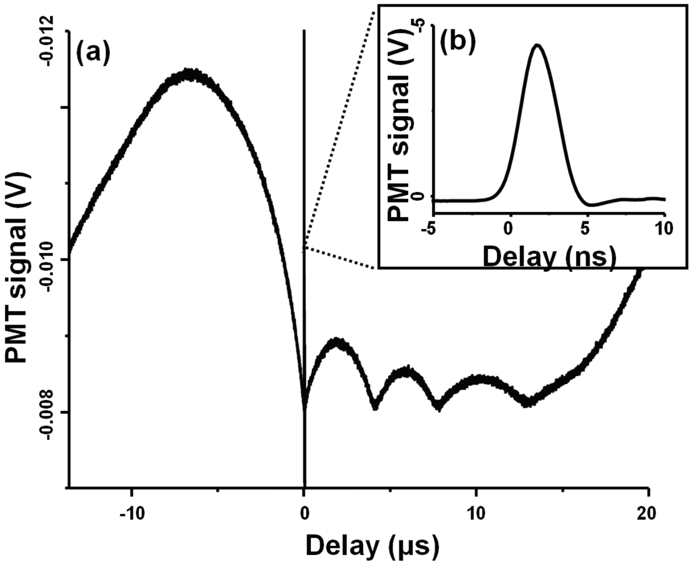

Figure 3.3 Laser scattering off a stably luminescing single bubble. PMT response to 532 nm continuous wave laser scattered off an acoustically-levitated, luminescing bubble. The vertical line at time 0 is sonoluminescence emission (inset).

Spatial stability consists of two subparts: radius of bubble orbit, and reproducibility of bubble position. A wide bubble orbit will result in the bubble not being in the collection window very often and collection efficiency will be correspondingly low. In some cases the bubble will move as the resonance shifts due to temperature fluctuations. In some resonators it is very difficult to get the bubble to return to exactly the same position during retuning. If this occurs it is necessary to realign and refocus the bubble in the optical path. It is vastly preferable to have a bubble that reliably occupies a single position in the cell.

3.3.2 Preparation of solutions for SBSL

Even if a cell has high synchronicity and terrific spatial stability there are limits; the bubble always moves. As a result, only a small number (~10%) of frames captured bubble emission. Due to the low intensity of a single emission event each usable frame consisted of 10-

100 photons, necessitating the collection of tens of thousands of frames in order to produce a spectrum. The resonator typically took about an hour to warm to an equilibrium temperature and a similar amount of time for alignment. A high-quality spectrum could take 6 to 8 hours to acquire in total.

Solutions degenerate over time as atmospheric gasses diffuse in. A water solution exposed to the atmosphere, for example, will become unusable after about an hour. Diluted sulfuric acid solutions will also age relatively rapidly. A 65 wt% sulfuric acid solution, for example, produces extremely spatially stable bubbles, but will decay until it is unusable over the course of about four hours. Concentrated (and consequently viscous) sulfuric acid solutions, however, will typically last for at least four days without any discernible loss of stability or synchronicity. This is contingent on the solution being prepared and transferred properly in the first place; a solution that starts with more air in it will reach an unacceptable concentration of air more quickly. While it would presumably extend the lifespan of the solution by capping the resonator it was generally not done as four days is much longer than needed for a given experiment and there are concerns about the damping of vibrations by the cap. Figure 3.4 shows the reproducibility of SBSL emission over the course of an experiment.

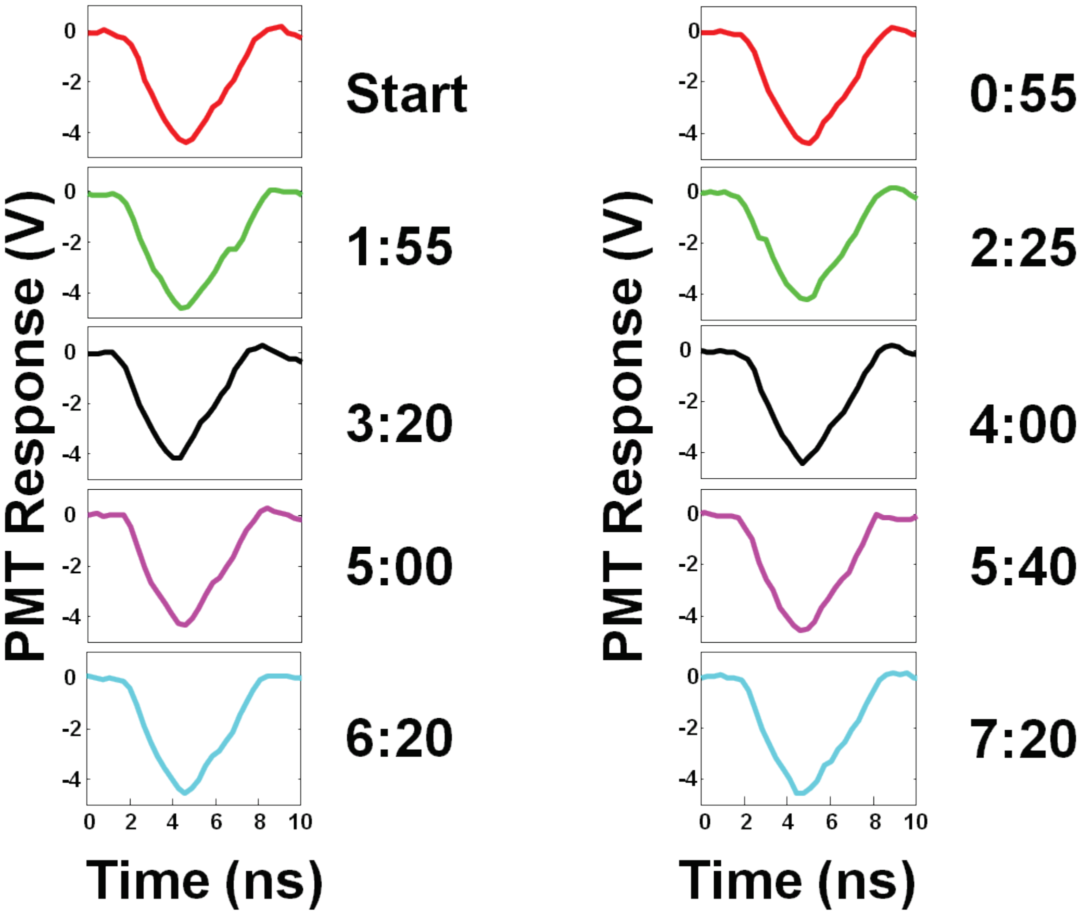

Figure 3.4 SBSL longevity. PMT response to SBSL from a krypton bubble driven at an acoustic pressure of 1.6 bar. Times are listed as hours from the first measurement, which was taken after roughly one hour of warm-up time.

The degassing protocol for producing these solutions was given in Chapter 2. It has been asserted that degassing solutions for very long times, ten to twenty days, will allow for the production of luminescing bubbles as spatially stable as in water.[10, 23-24] Degassing was attempted for many days, including longer than one month. No difference was ever observed between a solution degassed for one day and solutions degassed for longer periods. Other methods to reduce air contamination, such as cannula or syringe transfer rather than pouring, also had no positive effect on bubble behavior. There is also a report of bubble stabilization by introducing a second resonant frequency concurrently with the first harmonic,[25] but work by both the Suslick group and the Putterman group[26] failed to produce similar improvements.

3.3.3 Q measurements

The Q measurement, discussed in detail in Chapter 2, has been proposed as an important factor governing cell performance, with 1,000 cited as a target value.[27] This work made an effort to optimize the Q value, but it was ultimately not clear that it is important. It is certainly true that the Q value depends strongly on solution quality. A solution of 85 wt% sulfuric acid that has not been degassed, for example, might have a Q of under a hundred to a few hundred, whereas it can have a Q value of several thousand in the same cell if properly degassed and regassed. This is presumably because tiny air bubbles scatter and absorb the acoustic field. Water solutions were regularly measured to have Q values of around 2,000 (after degassing) while sulfuric acid solutions (also degassed) in the same resonator could only reach values of ~750. Further, spherical resonators tended to have high Q values, cylinders had moderate Q values, and Erlenmeyer flasks had low Q values. Spatial stability seemed to follow the opposite trend, however, and synchronicity seemed to have no correlation. Q may then be useful for comparing the quality of solution preparations, but does not seem to be useful for comparison of resonators or as an initial diagnostic to see if a cell is expected to be a good resonator. It was speculated, but not confirmed, that a high Q or a low Q would be desirable but an intermediate Q would be problematic. A high Q would result in extremely reproducible bubbles (Barber found that the synchronicity of sonoluminescence was better than that of the function generator producing it, for instance[28]) because it would be dictated by the breathing of the resonator with very little contribution from the driving PZT. A low Q would be the opposite; the resonator would have little influence and the driving ceramics would dictate the bubble behavior, creating synchronicity similar to that of the function generator. An intermediate Q, however, would result in the resonator and the ceramic fighting one another unless they were perfectly in resonance at all times.

3.3.4 Choice and attachment of piezoelectric ceramics

The choice of PZT ceramic is important, but it is not easy to predict what makes a good driver. Some ceramics that had suffered physical damage (e.g., chips and cracks) worked well, while others that appeared pristine produced low-quality bubbles. One uniformly important factor is that ceramics with high piezoelectric constants were easier to work with and generally produced better sonoluminescence. This can be qualitatively determined by simply soldering wires to the ceramic, hooking it up to the sonoluminescence electronics and sweeping an AC voltage through audible frequencies. A ceramic that is working well will produce enough sound to be easily heard at low voltages.

The attachment of ceramics is critical. The Loctite Quick Set^{TM} epoxy makes a strong bond, but the epoxy application must be uniform or else forces will be applied unevenly when the ceramic is driven, potentially activating rocking modes in the ceramic. Similarly, large air bubbles must be avoided to prevent reflection due to the poor acoustic impedance match between air and the glass or epoxy. Small air bubbles cannot be entirely removed from the epoxy mixture, but they can be mostly ejected from between the resonator and the ceramic by applying firm pressure when placing the ceramic. Too much pressure will force most of the epoxy out and create a weak bond; the epoxy process therefore requires some experience to consistently do well. Too little epoxy will make short-lived and possibly uneven unions. Too much epoxy is not an issue as long as excess epoxy is forced out from between the ceramic and the glassware. Although it is possible to hold the ceramic in place until the epoxy has set (at least 15 minutes before it will hold), it was found that the most consistent method was to position the resonator such that the ceramic could be set on top of the resonator. The ceramic was pushed firmly into position and allowed to set under only the force of its own weight. In order to do this without the ceramic being pulled off it was usually required to remove wires. It is vastly preferable to retain short leads attached to the ceramic that can be removed from the rest of the wiring rather than frequently soldering directly to the ceramic, as the heat from the soldering iron will burn away the silver coating on the PZT and eventually render it unusable.

Resonators can be constructed with any number of PZT ceramics. One or two are most popular, with a single ceramic positioned at the bottom of a sphere. Two ceramics are typically position directly opposed to one another on the equator of the cell, although conceivably they could be positioned anywhere, as they are ostensibly activating spherically-symmetric modes. The two ceramics must be a matched set; if their electric impedances differ significantly then they will move out of phase with one another and will not be able to generate a good resonance. It is, of course, also imperative that they be wired in the same way (i.e., the positive terminal should be connected on the same face in both cases). Figure 3.5 shows a matched set of ceramics working in phase and the effect of one ceramic versus two. Two ceramics will approximately double the delivered power, but seem to have no synergistic enhancement; one could achieve the same effect simply by increasing the driving voltage.

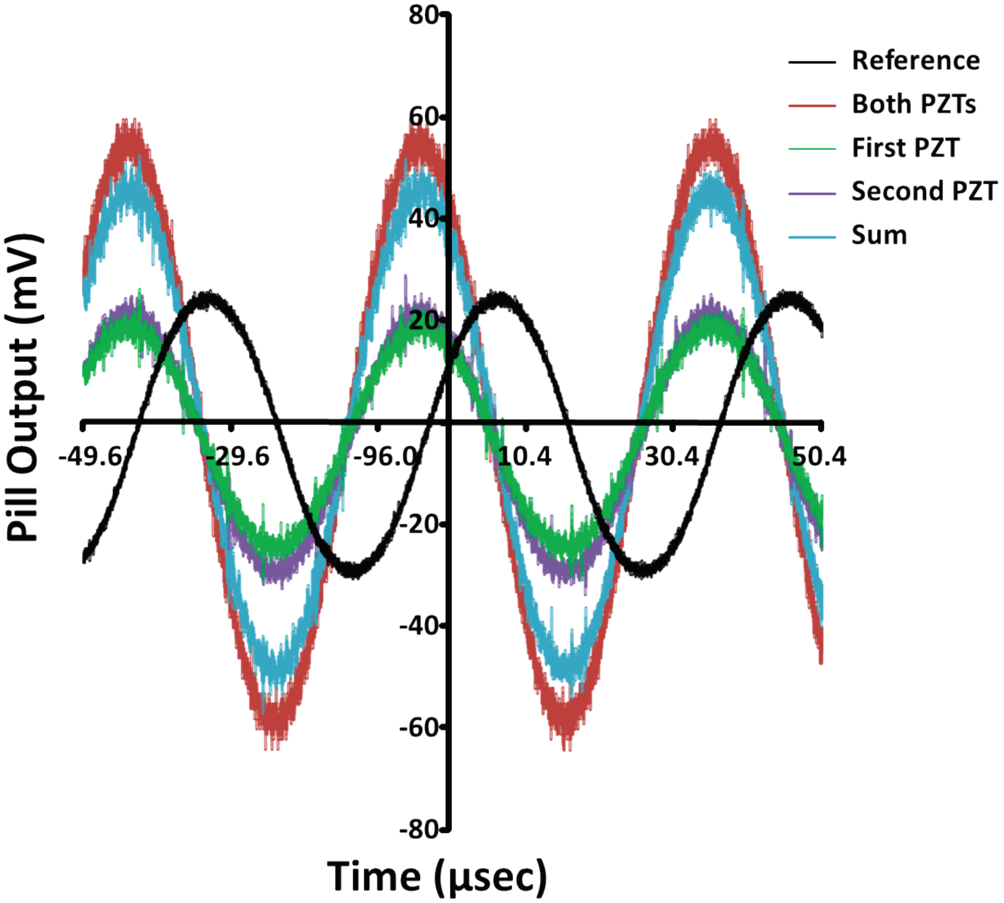

Figure 3.5 Effect of number of driving PZTs. The output of a pill connected to a resonator driven at 25 kHz is shown. Two ceramics made of the same material and with the same dimensions drive the cell independently (green and purple lines). The oscilloscope is triggered on an output from the function generator (black line) so that phases may be compared. The mathematical sum of the green and purple lines is given as the blue line for comparison with both ceramics working in tandem (red line).

Curiously, the response of the resonator to two ceramics made of the same material, with the same geometry, and apparent identical mounting, may be substantially different. Figure 3.6 shows the resonator response to two different driving PZT ceramics or both combined. The resonator response was measured either with a pill or the needle hydrophone. The cell will have a modest response to one ceramic at some frequencies and no response to others. It is also noteworthy that the hydrophone response and the pill response do not entirely agree about which frequency produces the best resonance. The hydrophone measures the acoustic pressure at the bubble's actual position and is the measurement to trust. In this instance the hydrophone gave the strongest response at ~27 kHz, which was where luminescence was produced. Note that the response is convolved with the sensitivity of the detector, so the larger response at higher frequencies cannot be confidently attributed to the achievement of higher acoustic pressure.

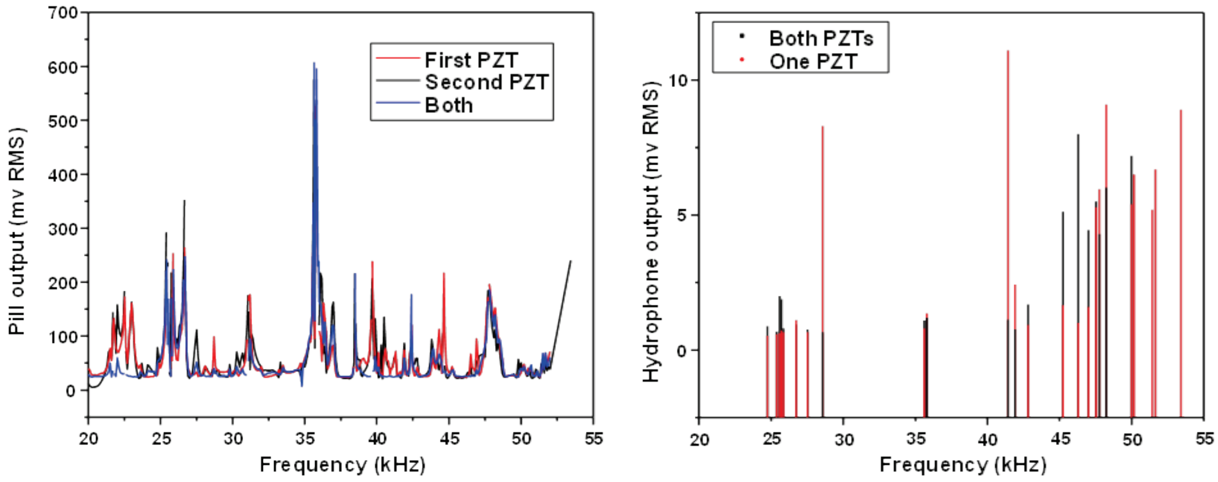

Figure 3.6 Resonances of a quartz sphere under different driving conditions. Left: pill response to two different driving PZT ceramics and both combined. Right: hydrophone response to a single driving PZT ceramic or two ceramics combined.

3.3.5 Choice of Waveform

One of the greatest advances in bubble spatial stability is also one of the greatest mysteries. Essentially all workers in the field use a sinusoidal waveform to drive their cells, although other waveforms are known.[29] It was found in this work, however, that it was much easier to generate sonoluminescence using a square wave, and that bubbles driven with a square wave were brighter and occupied much tighter orbits. Switching between a sine wave and a square wave seemed to have no effect on synchronicity. The other options available on the function generator, a sawtooth or triangular wave form, did not produce sonoluminescence.

It is not quite correct to call the waveform used a "square wave." Although the function generator puts out a well-formed square wave (with a small voltage spike at the start), the amplifier cannot respond rapidly enough and does not have the bandwidth to fully reproduce the waveform. Figure 3.7 shows the function generator output and the amplifier's interpretation of it.

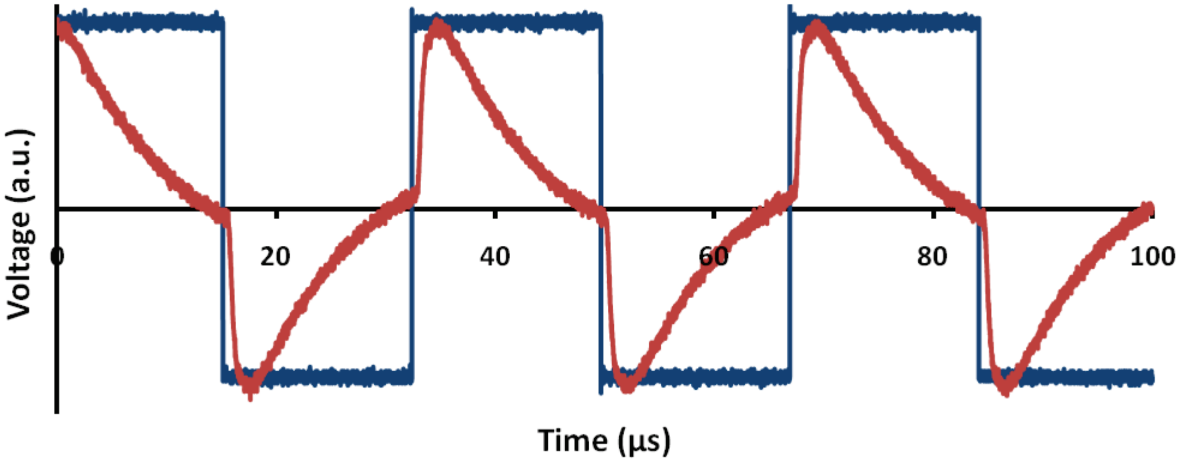

Figure 3.7 The square wave. Blue line: function generator output. Red line: amplifier response to blue line as an input (normalized to function generator output).

The enhancement of bubble behavior was originally thought to be a consequence of the excitation of higher harmonics in the resonator.[25] Curiously, measurement of the actual signal delivered to the bubble's position indicated a pedestrian sine wave (Figure 3.8). A pill detector on the outside of the Erlenmeyer gave a similar, sine-shaped, wave.

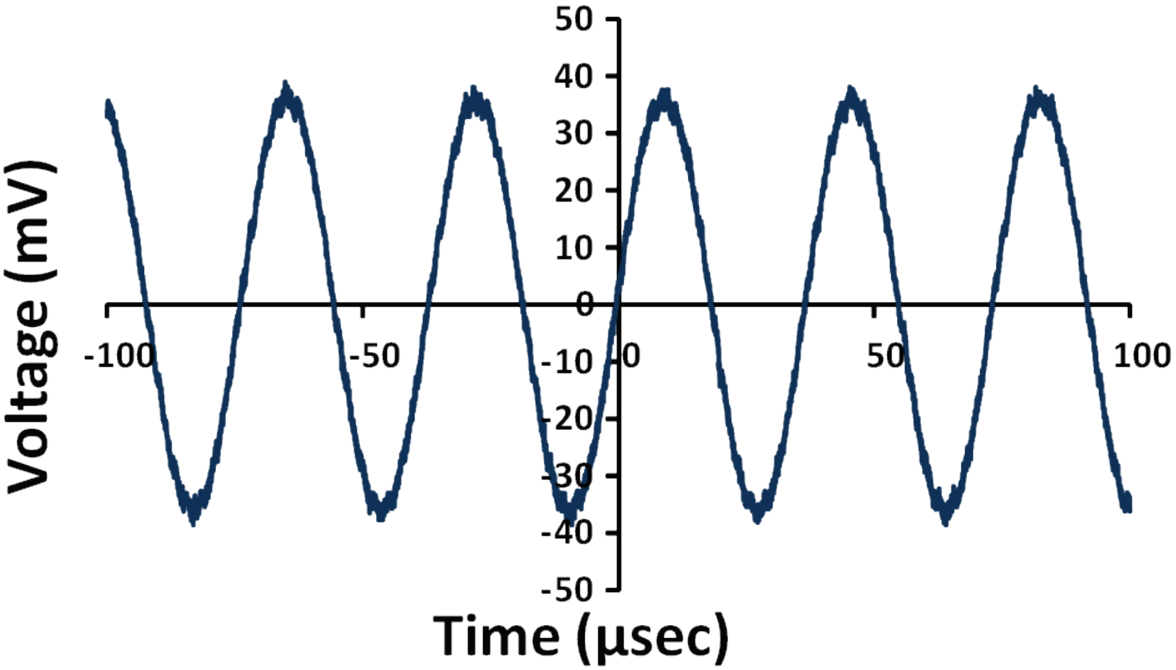

Figure 3.8 The square wave. Hydrophone measurement of acoustic pressure inside an Erlenmeyer flask driven at its resonance with a square waveform.

A Fourier transform of the hydrophone signal did not indicate the activation of any higher harmonics. The pill would detect very strange, nonsimple vibrations in spherical resonators, but hydrophone measurements inside the resonator consistently produced sinusoidal waveforms. Why the square wave produces better SBSL remains mysterious, but it was universally the case that SBSL was enhanced by its use. No dramatic change in the SBSL emission (time dynamics or spectra) was induced by using the square wave compared to the sine wave.

3.3.6 Resonator geometry

The choice of resonator geometry was found to be the single most important parameter that can be easily changed. Figure 3.9 shows SBSL in a number of different geometries: an Erlenmeyer flask, a cylinder, a sphere, and a Klein bottle. Spheres and cylinders have historically been the geometries of choice in the field, based on the poorly-supported assumption that high symmetry is desirable.

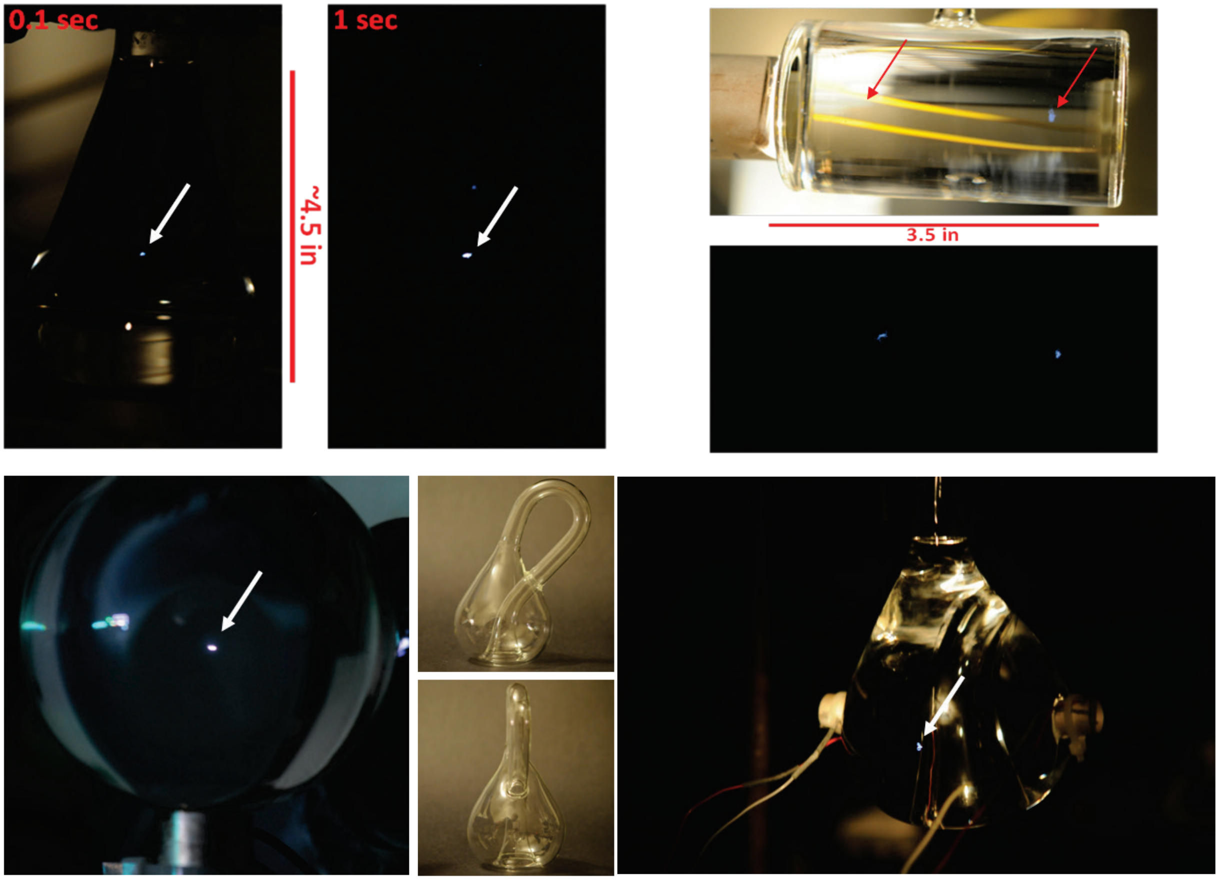

Figure 3.9 Example resonators. SBSL can be generated in a wide variety of cells. As examples: Erlenmeyer flask (top left), cylinders (top right), spheres, (bottom left), and even a Klein bottle (bottom right). An arrow points out the luminescing bubble in cases where it is not obvious. Other bright spots are reflections from either the bubble's luminescence or from external lighting.

Spherical resonators have been used most extensively in the Suslick group, but they have three significant drawbacks. First, the radius of curvature results in imperfect mating between the driving PZT and the glass wall. A flat-flat contact is vastly preferred. The space can (and should) be filled in with epoxy, but this introduces damping and increased chance of air bubbles in the epoxy. Secondly, curves everywhere are optically problematic. This can be ameliorated by cutting the side to introduce a flat window. Lastly, the first spherically-symmetric harmonic of a perfect sphere puts the antinode in the exact center of the resonator. In practice there are no perfect spheres and in most round-bottom flasks used as a resonator there will not be an antinode in the exact center, and because of the approximate symmetry there were be a number of places near the center which are approximately equivalent. In practice it was found that it was rare that a sphere would put the bubble in the exact center, and with small temperature fluctuations the bubble's preferred position would move significantly. From a spectroscopist's point of view this means realigning the bubble onto the collection optics repeatedly.

Cylinders overcome the first two problems of the sphere; PZTs attach to the flat window well and the window is ideal for light collection. The first two harmonics, however, either put the bubble in the center of the cylinder or create two bubbles, one on each end (as in Figure 3.9). If the bubble is in the center the optical pathway is long, requiring optics with long focal lengths and resulting in more absorption of the signal by the liquid medium. Smaller cylinders of course have shorter pathlengths, but the bubble always seems to be less robust (i.e., dies after a few minutes and is less spatially stable) in smaller cells. If there are two bubbles at the ends then there is the potential for light contamination from one bubble while attempting to observe the other, and by definition it is not actually SBSL. Neither of these problems is catastrophic, and cylinders are acceptable resonators for the time-resolved experiment.

The best resonators found, however, were Erlenmeyer flasks. Bubbles produced in these flasks occupied a single position with high reproducibility. The first Erlenmeyer tried, a 125 ml quartz flask, would produce bright and stable luminescence in the same position in the flask at most frequencies between 27 and 60 kHz. Synchronicity was also best and most reliable in Erlenmeyer flasks. Spheres tended to behave unpredictably, with good synchronicity some days and poor synchronicity on others, and cylinders tended to have a bimodal pattern, with the time between shots varying by a large but predictable amount. Further, the bottom of the Erlenmeyer can be replaced with a flat quartz window, making an ideal optical window and an excellent place to mount PZTs. For these reasons the Erlenmeyer flask was the resonator of choice for time-resolved SBSL.

3.4 Applying the streak camera technique to SBSL

The streak camera technique is best applied to applications where adequate data can be collected in a single collection or where events occur in such a precise time window that multiple exposures can be taken in the same frame without jitter. The SBSL experiment does not meet either of these criteria, and there were significant challenges to be overcome as a result. The first deficiency, low light, was overcome by brute force – collecting a large number of frames – which required sulfuric acid solutions that would stably luminesce for many hours. The second problem, temporal jitter, was solved by collecting only a single bubble event in each frame. Correcting the jitter, and adding them together. The actual procedure for this was described in detail in Chapter 2. Although some work of this nature has been described for SBSL in the past it was with water bubbles, where nearly-perfect spatial stability allows for much more efficient collection, and did not resolve spectra by wavelength.[30]

Due to the weak emission from SBSL, there would be few photons (typically ~10 to 100) in a given frame. One fundamental question to be addressed was whether it is possible to jitter-correct a frame with a handful of photons. In the limit of a single photon it is of course impossible; all photons would be centered and added together, eliminating all time information. It was necessary, therefore, to evaluate how many photons should be in a frame in order for it to be useable. To do this, a model was developed in MATLAB. A known, simulated bubble event was generated, as in Figure 3.10.

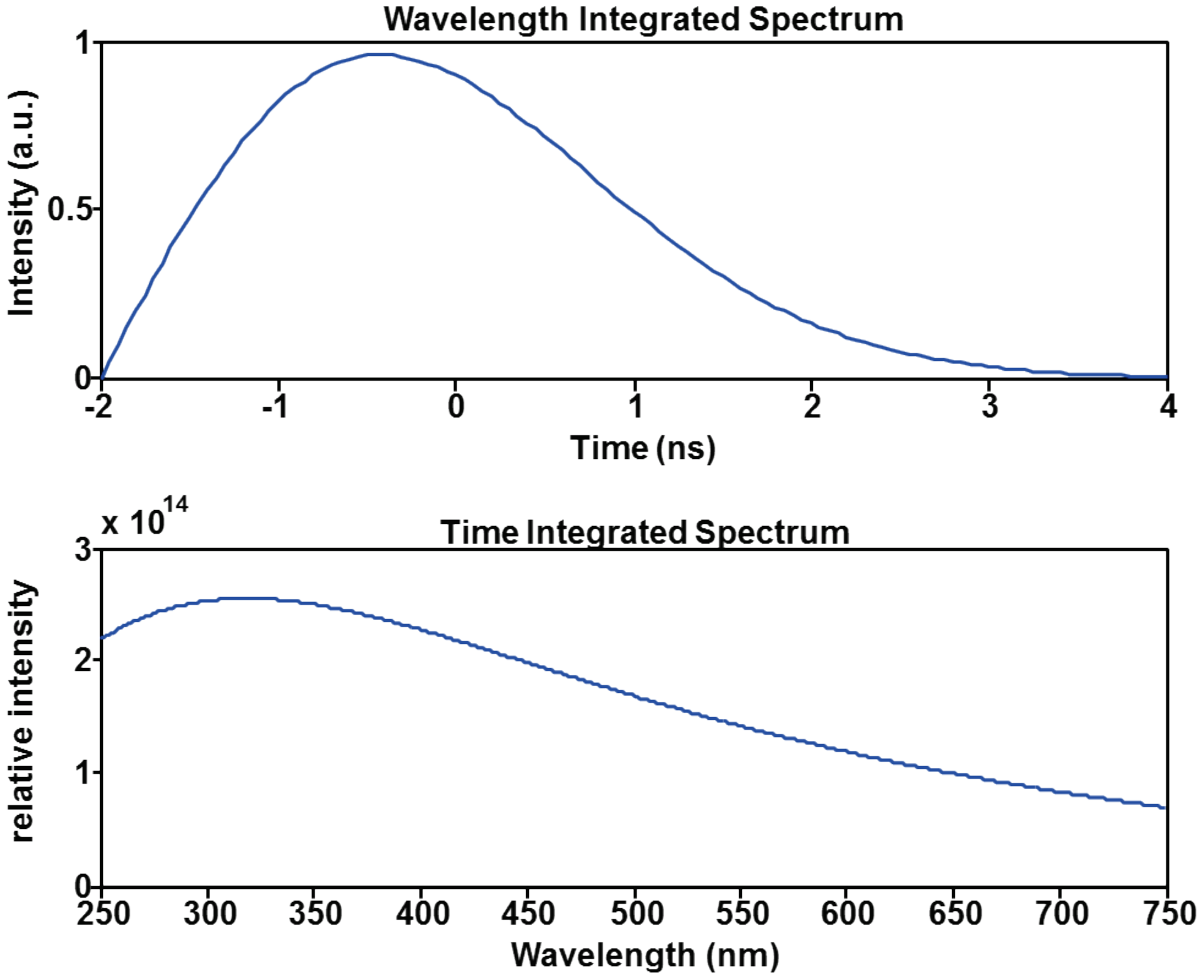

Figure 3.10 Simulated SBSL. Top: time-dependent emission envelope of simulated luminescence event. Bottom: time-integrated emission spectrum corresponding to a 9,000 K blackbody emitter.

The simulator assigns a spectrum to each time step according to Planck's law, with the relative temperatures at each time step distributed according to the Stefan-Boltzmann law. A peak temperature is arbitrarily chosen and each temperature and the spectrum will undergo a red shift and intensity decrease dictated by the initially-defined wavelength-integrated envelope defined. Figure 3.11 shows the blackbody evolution over the entire time range.

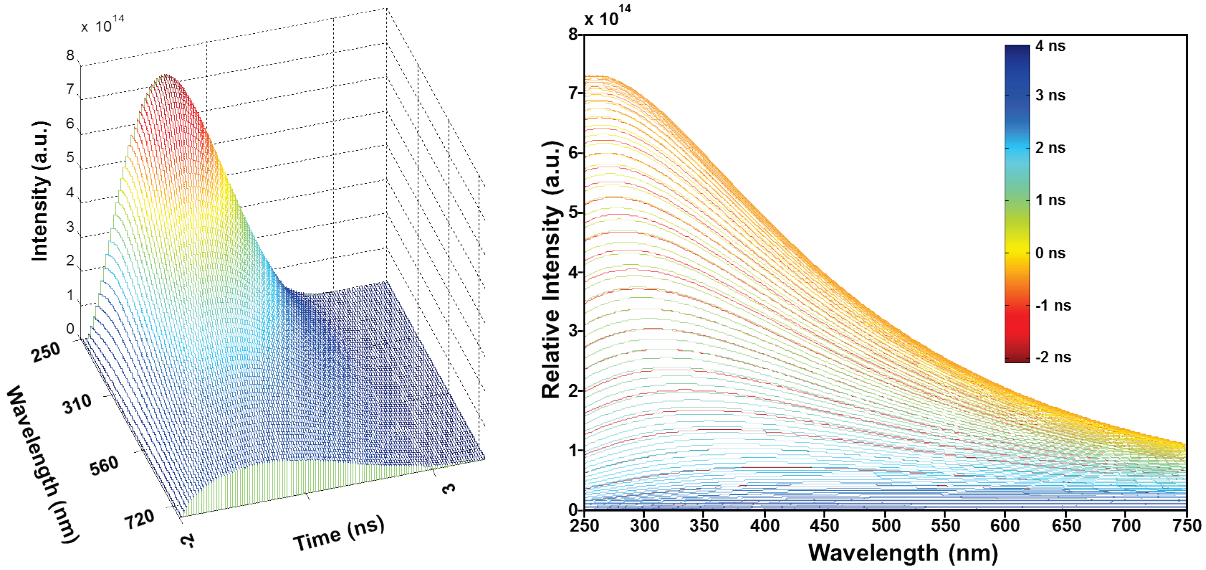

Figure 3.11 Simulated SBSL. Two different views of blackbody spectra simulated for each time step of an SBSL event. In the plot on the left color simply relates to intensity in the *z* axis. In the plot on the right, color relates to the time of emission, corresponding to the color key provided.

A simulated streak camera frame is generated from these data by sampling the spectrum. The probability of selecting a photon at any given position is related to the intensity of emission at that position but all photons have the same value. The spectrum will be reproduced when a large number of frames are integrated because it is more probable to detect a photon at wavelengths where the emission is more intense. This is identical in principle to the single-photon counting technique employed in the actual experiment. Figure 3.12 shows an example of a simulated frame containing five photons.

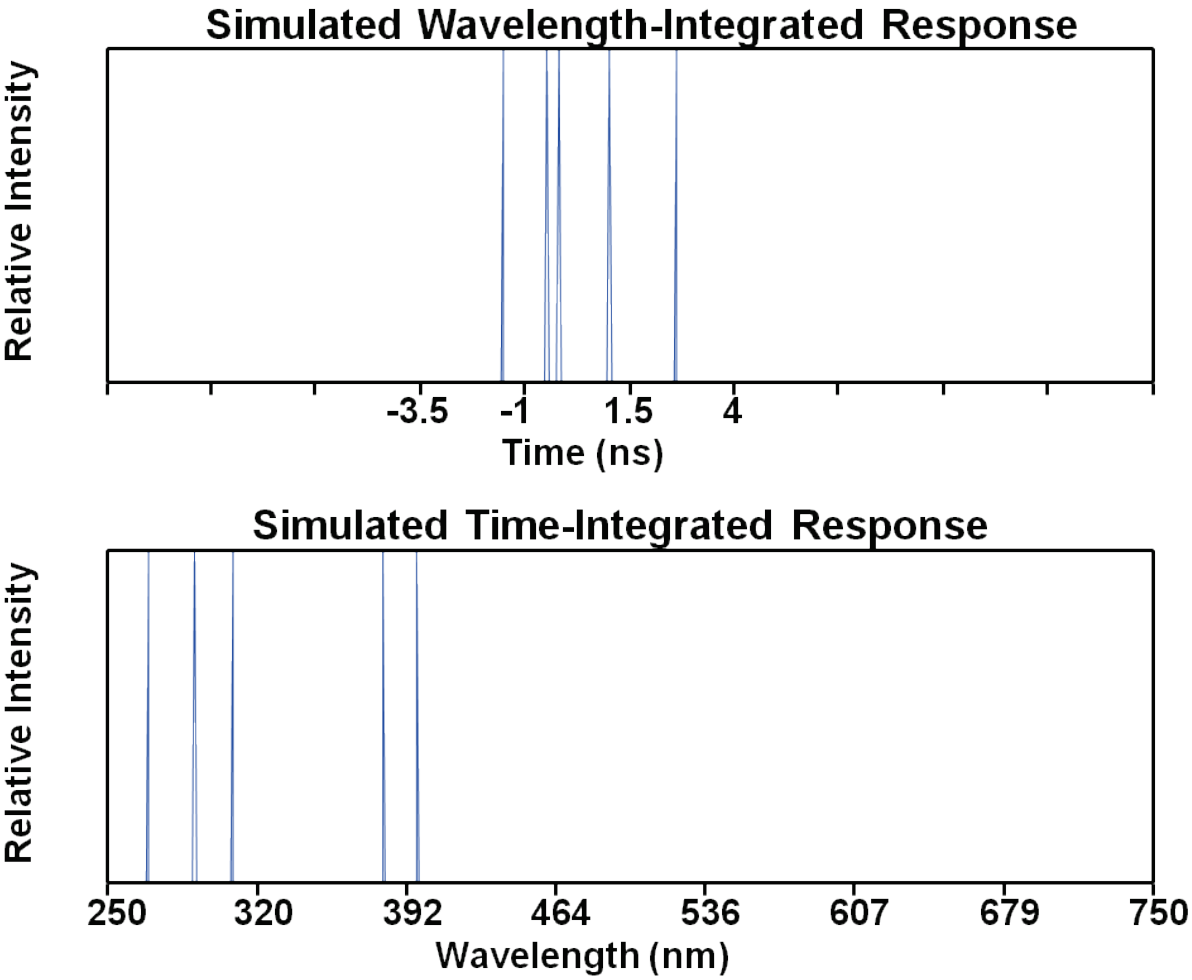

Figure 3.12 Simulated SBSL. Wavelength and time integrated spectra produced from five photons extracted from the initial spectrum.

The model permitted any number of frames to be produced with a given number of photons (a variance in the number of photons was also sometimes employed). If desired, time jitter could also be modeled. These frames were subjected to the same jitter correction algorithm as real data were and added about their centers of mass.

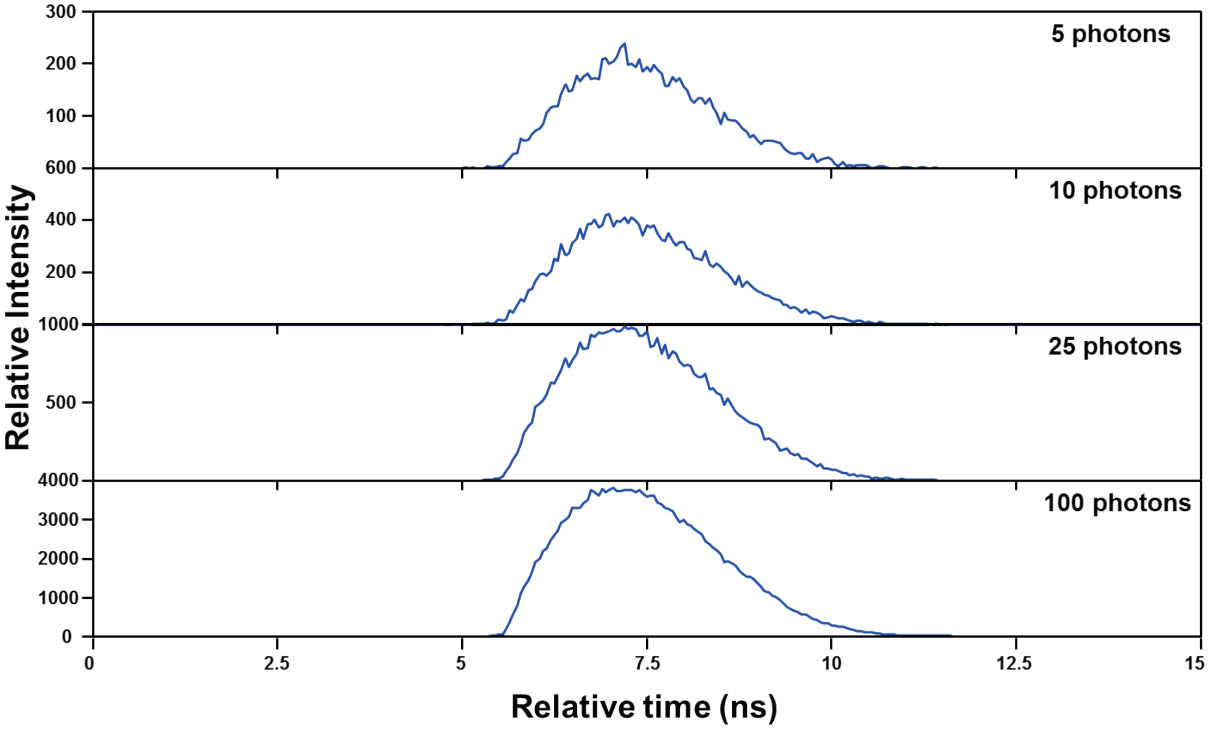

Figure 3.13 Simulated SBSL. Wavelength-integrated spectra from 1000 frames each of (from top to bottom) 5, 10, 25, and 100 photons.

Figure 3.13 shows how well the original pulse shape (introduced in Figure 3.10) is reproduced by frames containing a few (5) to many (100, which is "many" in a practical sense in the context of the SBSL experiment). Although the signal-to-noise is not very attractive, even a frame with as few as five photons approaches acceptable reproduction of the pulse shape. In all cases the pulse width is slightly underestimated, which is both expected and consistent with previous SBSL work.[30]

3.5 Time-resolved SBSL

Iterative improvements to the SBSL set-up and collection protocols eventually permitted the collection of time-resolved spectra. The time evolution of xenon SBSL emission from sulfuric acid is shown in Figure 3.14. The acoustic driving pressure was 1.9 bar, as measured by a DAPCO NP10-3 needle hydrophone. The spectral changes in intensity and the emission spectra are fit well by a blackbody distribution (Planck's law),

$$B_{\lambda}(T) = \frac{A}{\lambda^5}\left(e^{\frac{hc}{\lambda\, \mathrm{k}_B \mathrm{T}}} - 1\right)^{-1}$$

where B_{λ} is the spectral intensity at a given wavelength (λ), h is Planck's constant, c is the speed of light, k_B is Boltzmann's constant, and T is the blackbody temperature. The A value includes several physical constants, the number of frames collected, and the efficiency of light collection. While relative intensities can be compared at different times within an experiment, intensities may not be easily compared across experiments. These blackbody fits assumed the plasma emissivity and emission radius (and consequently the A value) were both constant over the resolvable time range. Figure 3.15 shows the time-averaged spectrum from the same data.

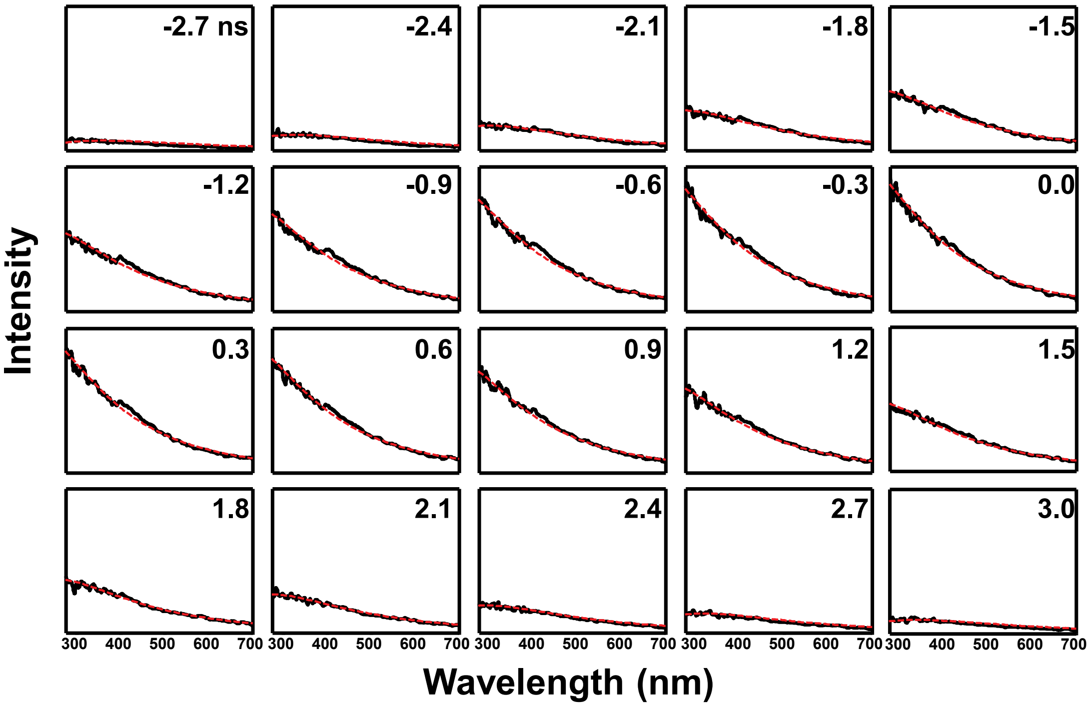

Figure 3.14 Time-resolved xenon emission. Time-resolved emission spectra from a single bubble in 85 wt% sulfuric acid regassed with 50 Torr Xe and driven at 1.9 bar. Solid black lines are experimental data, dashed red lines are blackbody fits. Times are presented with respect to the temporal center of mass.

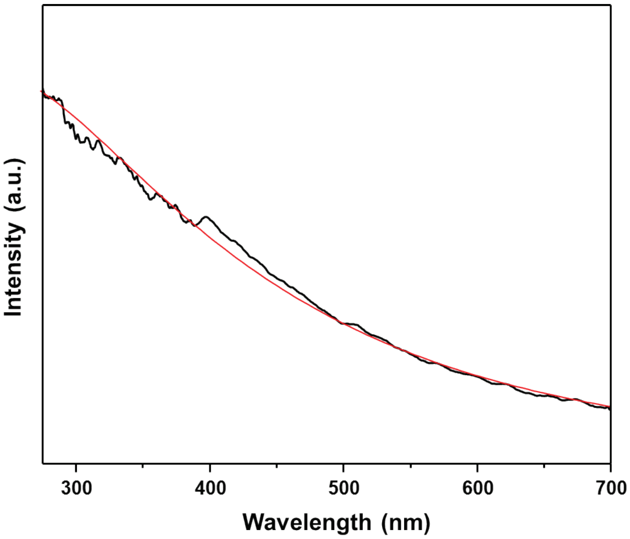

Figure 3.15 Time-averaged Xe spectrum. Black line is Xe emission at 1.9 bar, red line is fit to a 12,100 K blackbody emitter.

Total SBSL emission intensity rises smoothly with slight change in spectral shape, consistent with the Stefan-Boltzmann law for a blackbody. There is also an apparent heating-up time regime and an equivalent (but slightly longer; Figure 3.16 illustrates the difference in rise and fall times) cooling-down period. Both of these observations are consistent with sonoluminescence being the consequence of a compressionally heated gas inside the bubble and with blackbody emission from an optically opaque plasma. Both of these observations are in direct and unambiguous conflict with the previous report of time-resolved SBSL in sulfuric acid discussed earlier.

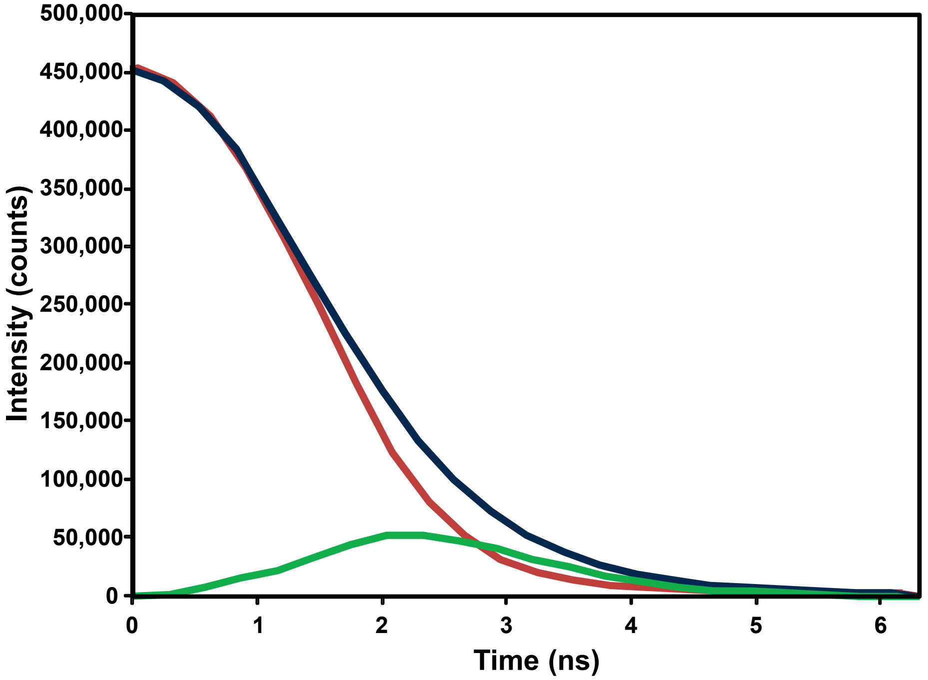

Figure 3.16 Rise and fall times. The rise (red line) and fall (blue line) are shown, illustrating the slight asymmetry in the emission envelope; the times shown are relative to the temporal center of mass in Figure 3.17 (i.e., the absolute values of the time axis in Figure 3.17). The green line is the difference between the two (fall minus rise).

While all spectra presented fit to Planck's law, they do not represent the entire emission event. Figure 3.17 compares the temperature evolution derived from the blackbody fits shown in Figure 3.14 to the complete wavelength-integrated emission profile. There is insufficient light at the beginning and end of the bubble emission to determine the spectral shape. It is consequently not possible to comment on whether it is reasonable to describe the cavitating bubble as a blackbody emitter (and by extension, an opaque plasma) at its earlier and later emission stages.

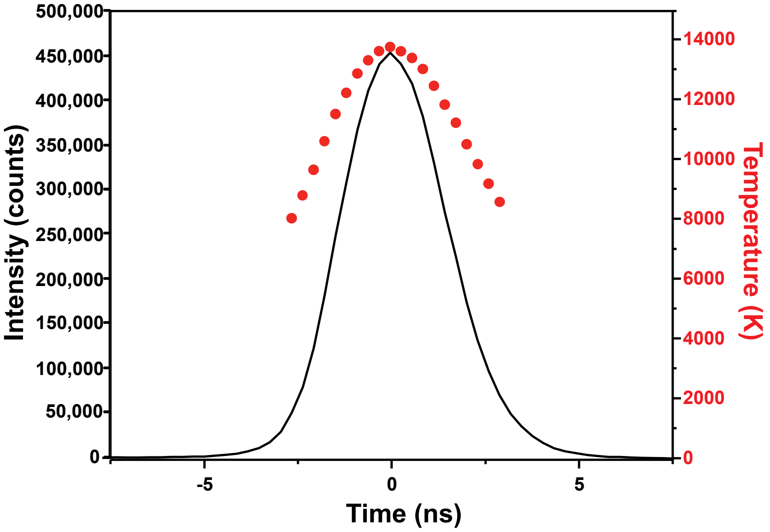

Figure 3.17. Time-resolved temperature profile of Xe emission. Total light output as a function of time as measured by the streak camera (solid line, left axis), and temperatures from blackbody fits to time-resolved spectra of Xe emission at 1.9 bar (red circles, right axis). Temperatures are only calculated for times when there is sufficient signal-to-noise to reliably fit to a blackbody. Uncertainties in temperatures are <±250 K.

One criticism of blackbody emission as an explanation for the continuum in SBSL is that the pulse width of the UV region of the spectrum as measured by time-correlated photon counting was identical to that of the visible region.[18-19] A 3,000 K blackbody, for example, has essentially no intensity below 500 nm, so one might expect that initial heating and final cooling would have no UV component. There is insufficient light emission, however, for us to collect spectra at those temporal extremes. Our observations are consistent with a dilute plasma during initial heating and final cooling stages as proposed by Putterman.[9] An optically opaque blackbody core provides most of the light emission and dominates the time-averaged spectrum.

Sonoluminescence from xenon is long-lived and bright relative to other noble gases, making it the ideal emitter for streak camera collection.[2] Krypton emission, which is nearly as bright, confirms that the phenomena observed are not unique to xenon and allows a direct comparison to the specious literature report. Neon and argon were both also tried, but proved too dim. Krypton emission (Figures 3.18, 3.19, and 3.20) is qualitatively similar to the xenon emission. In both cases total emission intensity rises and falls smoothly with no dramatic change in spectral shape and a blackbody model of the emission during peak output times still fits well. The primary notable difference is the smaller number of time blocks as a consequence of the krypton emission having a shorter lifetime.

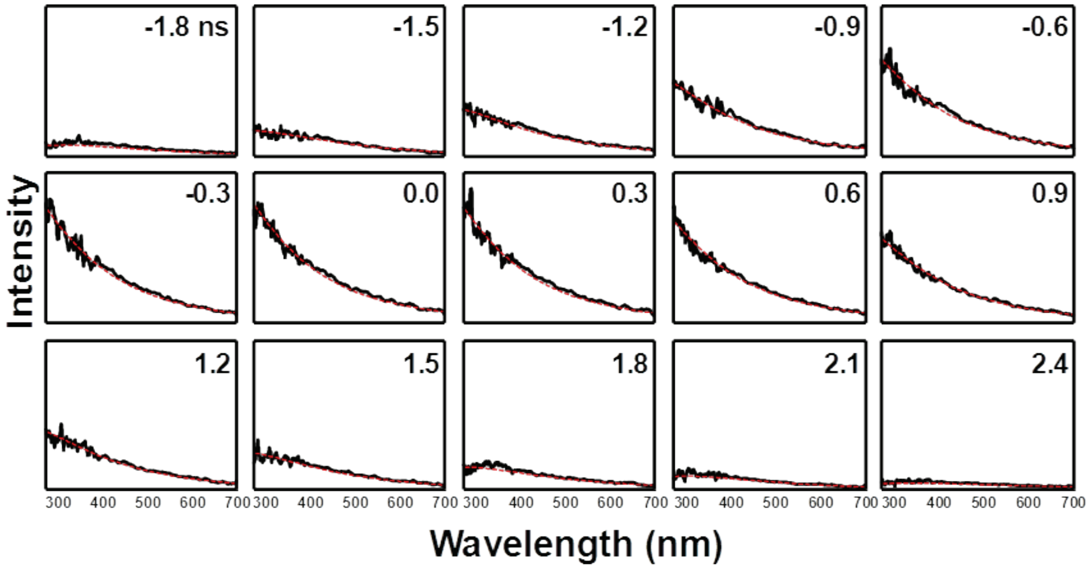

Figure. 3.18 Kr emission. Time-resolved emission spectra from single bubble sonoluminescence in 85 wt% sulfuric acid regassed with 50 Torr Kr and driven at 2.3 bar. Solid black lines are experimental data, dashed red lines are blackbody fits. Times are presented with respect to the temporal center of mass.

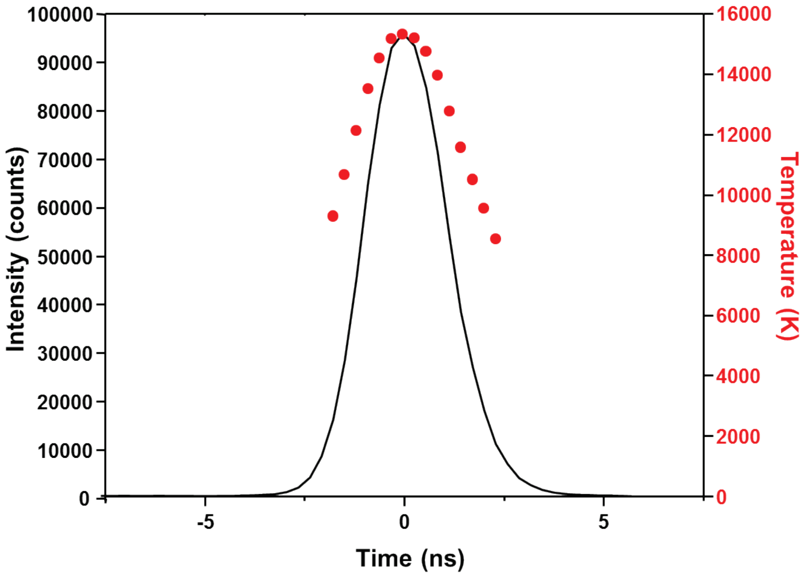

Figure 3.19 Time-resolved temperature profile of Kr emission. Total light output as a function of time as measured by the streak camera (solid line, left axis), and temperatures from blackbody fits to time-resolved spectra of Kr emission at 2.3 bar (red circles, right axis). Temperatures are only calculated for times when there is sufficient signal-to-noise to reliably fit to a blackbody.

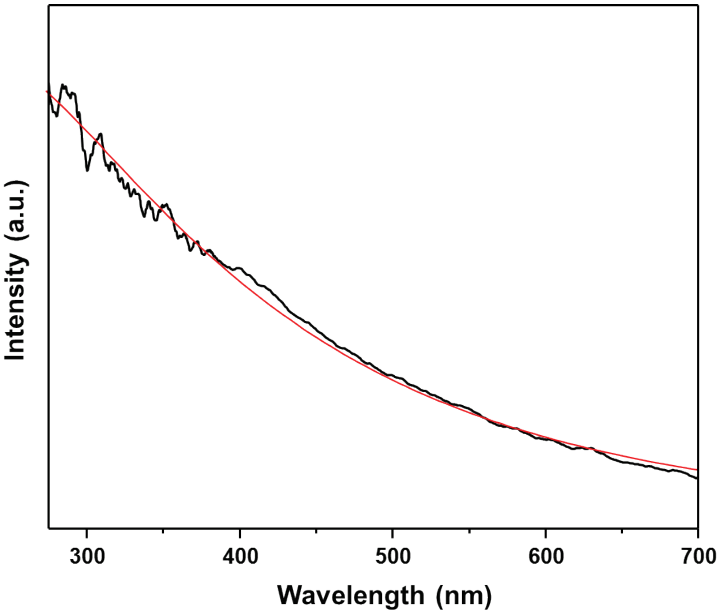

Figure 3.20 Time-averaged Kr spectrum. Black line is Kr emission at 2.3 bar, red line is fit to a 12,100 K blackbody emitter.

A comparison of Kr and Xe temperature dynamics under similar conditions is shown in Figure 3.21. It is not surprising that the xenon emission has a longer duration than the krypton emission; the slightly lower thermal conductivity of the heavier gas (5.65×10^{-3} $W\cdot m^{-1}\cdot K^{-1}$ for Xe versus 9.43×10^{-3} $W\cdot m^{-1}\cdot K^{-1}$ for Kr) means that the bubble will become effectively adiabatic earlier in its collapse and lose adiabaticity later in its rebound. The xenon emission is brighter in aggregate, mostly as a result of being longer-lived, but has lower peak temperatures than the krypton bubbles for a given pressure as a result of ionization cooling, in agreement with time-averaged temperatures derived from blackbody fits.[31-33]

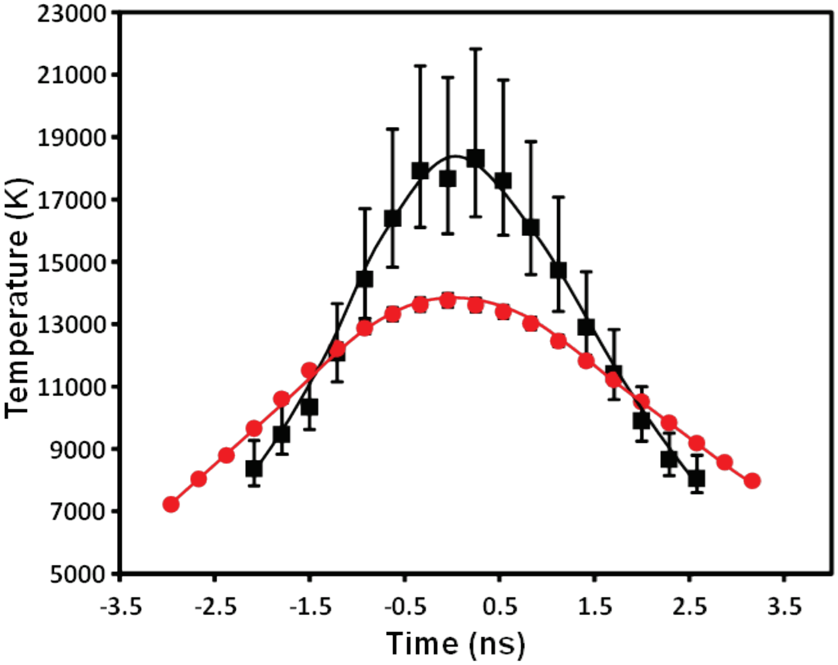

Figure 3.21 Xe/Kr comparison. Temperature evolution of SL with krypton (black squares) or xenon (red circles) at ~2 bar.

It is interesting that thermal conductivity predicts temperature trends for measurements derived from fits to atomic and ionic emission spectra,[2, 6] while blackbody emission is predicted by ionization potential. Thermal conductivity is expected to become less important as ionization occurs because the freed electrons are much more conductive than the heavy nuclei. One might expect, therefore, that atomic emission lines come from a dilute plasma at early and late emission times. It is unfortunate that the streak camera used in this work was not sensitive in the near IR and could not compare the time dynamics of the continuum with the time dynamics of atomic emission. This remains an exciting frontier of the field that will hopefully be achieved as streak camera technology and sonoluminescence techniques evolve.

Peak and time-averaged temperatures are similar to one another (Table I), with the higher peak emission temperatures slightly higher than the average temperatures, as expected, but in further refutation of Chen's report. The total emission intensity of a blackbody has a quartic relationship with temperature, and therefore emission when the bubble is hottest is expected to dominate the time-averaged spectrum. The small change in bubble conditions over the acoustic pressure range measured is consistent with previous observations.[2] Higher pressures could not be probed because bubbles became too unstable to collect spectra.

TABLE I. Peak and average temperatures from Kr SBSL.

Pressure (atm)	Average Temperature (K)	Peak Temperature (K)
1.6	11,970 ± 50	13700 ± 700
2	14,140 ± 150	18,300 ± 2700
2.3	12,840 ± 30	15200 ± 400
2.9	14,180 ± 40	16500 ± 700

3.6 Concluding remarks

In summary, sonoluminescence and streak camera techniques were developed to permit the collection of SBSL spectra with high temporal resolution (300 ps). Time-resolved spectra support the compressional heating description of sonoluminescence. In contrast with a recent problematic report, the time resolved spectra shown here exhibit heating and cooling regimes that are nearly temporally symmetric. Spectra fit well to Planck's law and indicate peak temperatures of ~18,000 K for krypton bubbles and ~14,000 K for xenon bubbles (at ~2 bar acoustic driving pressure), only a few thousand K above time-averaged temperatures.

Our results do not permit us to explain how exactly Chen's experiment went awry, but the differences in results are striking. Figure 3.22 shows Chen's published streak image compared to the streak image corresponding to the Xe data presented above. The literature streak image appears to have somehow been delivered to the detector at a dramatic angle. Since the streak camera interprets spatial information as time information this would explain the spurious result. How this might have occurred is, however, unclear.

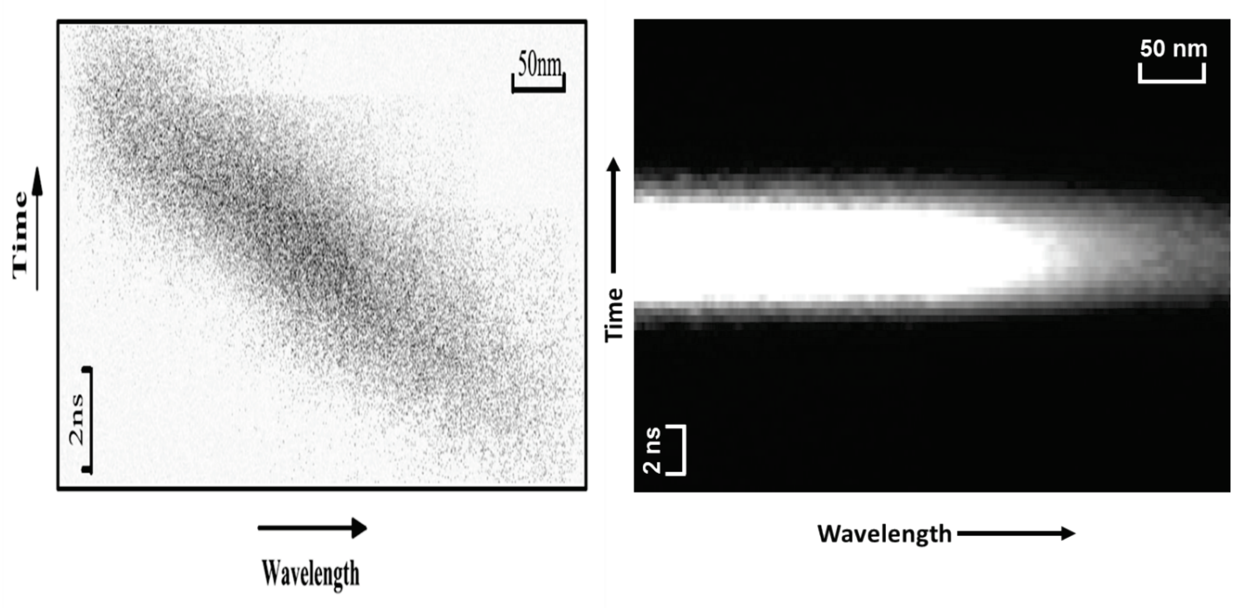

Figure 3.22 Comparison of streak images. Left: literature streak image. Right: streak image from Xe at 1.9 bar.

3.7 References

1. Suslick, K. S.; Flannigan, D. J., "Inside a collapsing bubble: sonoluminescence and the conditions during cavitation." *Annu. Rev. Phys. Chem.* **2008,** *59*, 659-83.

2. Flannigan, D. J.; Suslick, K. S., "Plasma formation and temperature measurement during single-bubble cavitation." *Nature* **2005,** *434*, 52-55.

3. Flannigan, D. J.; Hopkins, S. D.; Camara, C. G.; Putterman, S. J.; Suslick, K. S., "Measurement of Pressure and Density Inside a Single Sonoluminescing Bubble." *Phys. Rev. Lett.* **2006,** *96*, 204301.

4. Bang, J. H.; Suslick, K. S., "Applications of ultrasound to the synthesis of nanostructured materials." *Adv. Mater.* **2010,** *22*, 1039-59.

5. McNamara, W. B.; Didenko, Y. T.; Suslick, K. S., "Sonoluminescence temperatures during multi-bubble cavitation." *Nature* **1999,** *401*, 772-775.

6. Xu, H.; Suslick, K. S., "Molecular Emission and Temperature Measurements from Single-Bubble Sonoluminescence." *Phys. Rev. Lett.* **2010,** *104*, 244301.

7. Matula, T. J., "Inertial cavitation and single-bubble sonoluminescence." *Philos. Trans. R. Soc. London, A* **1999,** *357*, 225-249.

8. Crum, L. A., "Sonoluminescence." *Phys. Today* **1994,** *47* (9), 22.

9. Kappus, B.; Khalid, S.; Chakravarty, A.; Putterman, S., "Phase Transition to an Opaque Plasma in a Sonoluminescing Bubble." *Phys. Rev. Lett.* **2011,** *106*, 234302.

10. Chen, W.; Huang, W.; Liang, Y.; Gao, X.; Cui, W., "Time-resolved spectra of single-bubble sonoluminescence in sulfuric acid with a streak camera." *Phys. Rev. E: Stat., Nonlinear, Soft Matter Phys.* **2008,** *78*, 035031.

11. Khalid, S.; Kappus, B.; Weninger, K.; Putterman, S., "Opacity and Transport Measurements Reveal That Dilute Plasma Models of Sonoluminescence Are Not Valid." *Phys. Rev. Lett.* **2012,** *108*, 104302.

12. Moss, W. C.; Young, D. A.; Harte, J. A.; Levatin, J. L.; Rozsnyai, B. F.; Zimmerman, G. B.; Zimmerman Harold, I., "Computed optical emissions from a sonoluminescing bubble." *Phys. Rev. E: Stat., Nonlinear, Soft Matter Phys.* **1999,** *59*, 2986-2992.

13. Flannigan, D. J.; Suslick, K. S., "Inertially confined plasma in an imploding bubble." *Nat. Phys.* **2010,** *6*, 598-601.

14. Flannigan, D. J.; Suslick, K. S., "Plasma quenching by air during single-bubble sonoluminescence." *J. Phys. Chem. A* **2006,** *110*, 9315-8.

15. Flannigan, D. J.; Suslick, K. S., "Plasma Line Emission during Single-Bubble Cavitation." *Phys. Rev. Lett.* **2005,** *95*, 044301.

16. Hopkins, S. D.; Putterman, S. J.; Kappus, B. A.; Suslick, K. S.; Camara, C. G., "Dynamics of a Sonoluminescing Bubble in Sulfuric Acid." *Phys. Rev. Lett.* **2005,** *95*, 254301.

17. Hilgenfeldt, S.; Grossmann, S.; Lohse, D., "A simple explanation of light emission in sonoluminescence." *Nature* **1999,** *398*, 402-405.

18. Hiller, R. A.; Putterman, S. J.; Weninger, K. R., "Time-Resolved Spectra of Sonoluminescence." *Phys. Rev. Lett.* **1998,** *80*, 1090-1093.

19. Gompf, B.; Günther, R.; Nick, G.; Pecha, R.; Eisenmenger, W., "Resolving Sonoluminescence Pulse Width with Time-Correlated Single Photon Counting." *Phys. Rev. Lett.* **1997,** *79*, 1405-1408.

20. Camara, C.; Putterman, S.; Kirilov, E., "Sonoluminescence from a Single Bubble Driven at 1 Megahertz." *Phys. Rev. Lett.* **2004,** *92*, 124301.

21. Flannigan, D.; Suslick, K., "Emission from Electronically Excited Metal Atoms during Single-Bubble Sonoluminescence." *Phys. Rev. Lett.* **2007,** *99*, 134301.

22. Toegel, R.; Luther, S.; Lohse, D., "Viscosity Destabilizes Sonoluminescing Bubbles." *Phys. Rev. Lett.* **2006,** *96*, 114301.

23. Xu, J.; Chen, W.; Xu, X.; Liang, Y.; Huang, W.; Gao, X., "Composition and its evolution inside a sonoluminescing bubble by line spectra." *Physical Review E* **2007,** *76* (2), 1-6.

24. Huang, W.; Chen, W.; Cui, W., "Resolving the shape of a sonoluminescence pulse in sulfuric acid by the use of streak camera." *The Journal of the Acoustical Society of America* **2009,** *125* (6), 3597-600.

25. Urteaga, R.; Bonetto, F. J., "Trapping an Intensely Bright, Stable Sonoluminescing Bubble." *Phys. Rev. Lett.* **2008,** *100* (7), 074302.

26. Kappus, B. 24 May 2012. Personal Communication.

27. Barber, B. P. Synchronous Picosecond Sonoluminescence. University of California Los Angeles, 1992.

28. Barber, B. P.; Putterman, S. J., "Observation of synchronous picosecond sonoluminescence." *Nature* **1991,** *352* (6333), 318-320.

29. Chen, W.; Chen, X.; Lu, M.; Miao, G.; Wei, R., "Single bubble sonoluminescence driven by non-simple-harmonic ultrasounds." *The Journal of the Acoustical Society of America* **2002,** *111*, 2632.

30. Pecha, R.; Gompf, B.; Nick, G.; Wang, Z. Q.; Eisenmenger, W., "Resolving the Sonoluminescence Pulse Shape with a Streak Camera." *Phys. Rev. Lett.* **1998,** *81*, 717-720.

31. Barber, B. P.; Hiller, R. A.; Löfstedt, R.; Putterman, S. J.; Weninger, K. R., "Defining the unknowns of sonoluminescence." *Phys. Rep.* **1997,** *281*, 65-143.

32. Xavier, C. F.; Clemente, R. A., "Dissociation and ionization in sonoluminescence." *J. Phys. Soc. Jpn.* **2001,** *70*, 387-393.

33. Hammer, D.; Frommhold, L., "Sonoluminescence: How bubbles glow." *J. Mod. Opt.* **2001,** *48*, 239-277.

Chapter 4
Sonocrystallization

The application of ultrasound for the induction of nucleation of drug crystals is presented in this chapter, with aspirin as the primary crystal of choice. The effects of sonocrystallization on particle morphology and size distribution are compared to a number of other nucleation methods. A novel spray sonocrystallization technique is developed and discussed.

4.1 Introduction

Particle size distributions are extremely important in the preparation of pharmaceutical materials. Dissolution profiles of orally-ingested drugs, for instance, strongly depend on available surface area.[1] It is estimated that about 40% of drugs fail in development due to difficulties in pharmacokinetics, most commonly related to their solubility properties. This is perhaps not surprising; in order to be effective a drug typically has to be able to cross cell membranes, requiring a certain degree of lipophilicity. Solubility in the body, on the other hand, requires hydrophilicity.[2] Controlling the surface area of particles in order to expedite the solvation of partly hydrophobic particles is one way to help combat the solubility problem.

There are many other reasons why controlling particle size is important to the pharmaceutical industry. Aerosol drugs, for example, are often delivered as suspensions of particles (metered-dose inhalers) or as dry powders (dry powder inhalers). Large particles are unable to "make the turn" and lodge in the back of the throat rather than continue on to the lungs. Particles hitting the throat in this way are more likely to be responsible for undesirable side effects than deliver therapeutic benefit. If the particles are too small they do not settle in the lungs before exhalation and are simply expelled from the body. There is a narrow size distribution, therefore, that is considered acceptable for aerosol drug materials, usually reported as an aerodynamic diameter of 0.5 to 5 μm, although some authors will indicate even stricter requirements within that range.[3-7]

Particles above ~3 μm experience significant inertial impaction and do not make it to the lungs. Particles below ~1 μm experience little gravitational settling; air friction keeps them suspended for the same reason that clouds do not fall out of the sky (friction is directly proportional to radius per Stokes' law while the force of gravity increases with the cube of radius, resulting in small particles experiencing more braking). Particles around 0.5 μm and larger are also not significantly influenced by Brownian motion and there is therefore no force to induce deposition before the next exhalation ejects them from the body. Figure 4.1 shows the deposition distribution of inhaled particles as a function of aerodynamic diameter.[4] Particles in the 10-100 nm size range are predicted to perform acceptably by Figure 4.1 also. Practical considerations in delivery and stability, difficulty in formulation, and complications with agglomeration have prevented any nanoparticle pulmonary drugs from meeting FDA approval so far, but some successful clinical trials have been conducted.[8]

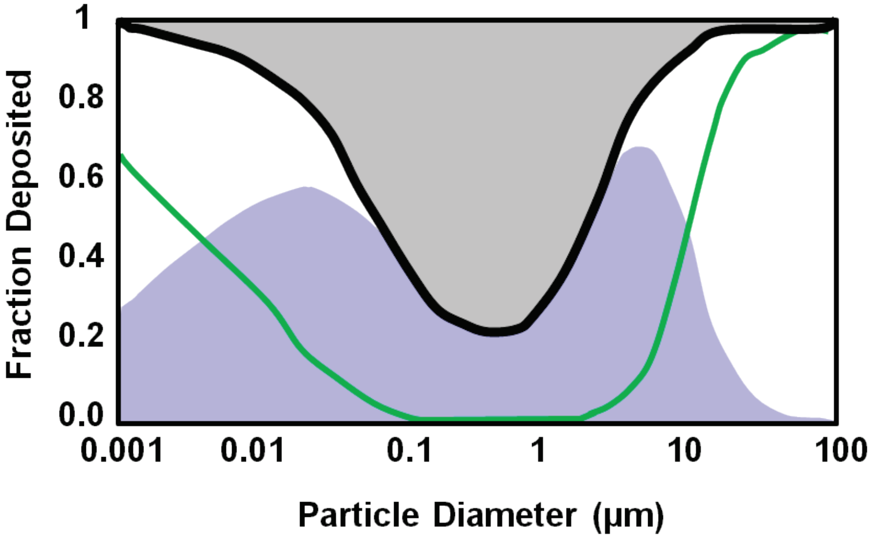

Figure 4.1 Deposition of inhaled particles. Gray shaded region: particles exhaled. Green line: extrathoracic delivery (particles caught in throat). Shaded blue region: intrathoracic delivery (good delivery). Thick black line: total deposition in the body (sum of green and blue). Adapted from Scheuch, G.; Siekmeier, R. *J. Physiol. Pharmacol.* **2007**, *58*, 615-25.

Parenteral drugs delivered by intravenous, subcutaneous, or intramuscular injection can also be slurries of particles or emulsions rather than solutions. Particle size is again important for controlling the rate of release, and in the case of intravenous injection it is critical that particles are not larger than ~5 μm else the patient suffers a potentially fatal pulmonary embolism.[9] Additionally, the choice of a slurry over a solution is often a practical one: it is sometimes not possible to dissolve the drug in a reasonable volume of solvent. In addition to the kinetic benefit of increasing surface area, reducing the particle size to the nanoscale will dramatically increase the surface energy to volume energy ratio. Surface energy effects will influence intrinsic solubility according to the Ostwald-Freundlich equation:[10]

$$\ln\frac{S}{S_0} = \frac{2M\gamma}{\rho rRT}$$

where S is the particle solubility, S_0 is the solubility of a flat, solid sheet of the drug material, M is the molecular weight, γ is the interfacial tension, ρ is the particle density, r is particle radius, R is the gas constant, and T is temperature. Typically it is necessary to be below 200 nm, and sometimes well below, for increases in intrinsic solubility to be important. Figure 4.2 illustrates the effect of particle size on solubility for a model particle with a molecular weight of 708 and a density of 1 g/ml. The increase in surface area can also have deleterious effects, such as particle agglomeration and faster Ostwald ripening, and may shorten shelf-life or require stabilizing agents.

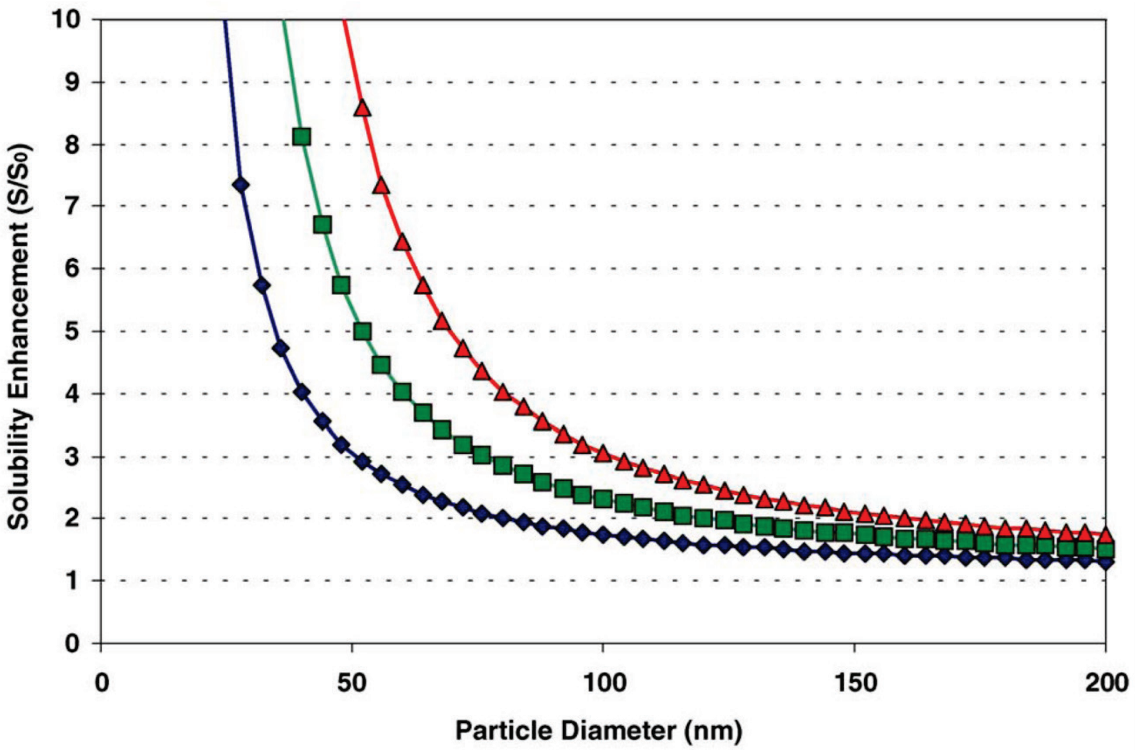

Figure 4.2 Solubility enhancement by nanosizing. The effects of size and surface tension are demonstrated for a hypothetical particle of molecular weight 708 and density of 1 g/ml. Blue lines and diamonds correspond to a surface tension of 50 dynes/cm, the green line and squares represent 75 dynes/cm, and the red line and triangles represent 100 dynes/cm.[10]

There are other, more exotic, delivery methods where particle size is important also (e.g., buccal delivery[11] or suppositories[12]). In spite of the importance of controlling particle size distributions, industrial-scale solutions to the problem are often remarkably poor. It is common to micronize large crystals mechanically (common examples include liquid or air jet milling, wet or dry milling, rotor-stator milling, and high-pressure homogenization[13]). These techniques tend to produce broad crystal size distributions with non-uniform morphologies, can introduce defects (which influences shelf life and solubility profile), can induce phase change among polymorphs, tends to produce amorphous materials, and can cause electrostatic charging and agglomeration.[14] These drug materials are commonly waxy solids that reagglomerate badly after milling.[15]

It is vastly preferable to crystallize particles in the desired distribution and avoid post-crystallization modification as much as possible. This chapter aims to give a sampling of the power of ultrasound for preparing pharmaceutical crystals. Ultrasound can have dramatic influences on particle size and morphology, on ease of preparation, and on reproducibility. Figure 4.3 compares sonocrystallized aspirin to aspirin from the manufacturer and to aspirin crystallized without any induction of nucleation. This chapter will make comparisons among a variety of techniques and apply ultrasound to generate particles covering a broad range of size regimes.

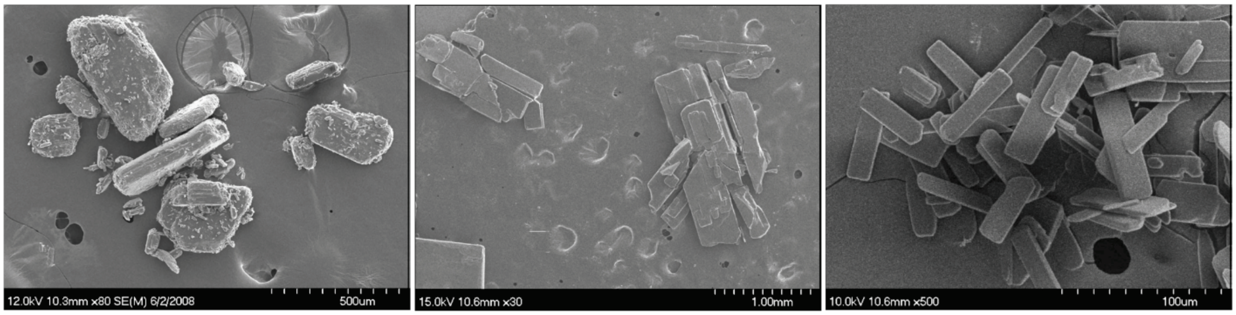

Figure 4.3 Scanning electron micrographs of aspirin crystals. Left: aspirin directly from Sigma-Aldrich. Middle: Aspirin crystallized from acetic acid with no intentionally-induced nucleation. Right: aspirin from solution identical to preparation in middle panel, but nucleation induced by sonicating at 10 W for 15 seconds.

4.2 Experimental notes

Materials and equipment Acetylsalicylic acid (Aldrich, 99%), ethanol (200 proof), and glacial acetic acid (Fisher Scientific) were used as-received. Nanopure water was prepared using a Barnstead NANOpure® ultrapure water purification system, scrubbing for organics, particles larger than 450 nm, and deionized to a resistance greater than 18 MΩ·cm.

Sonication was performed at 20 kHz with a Sonics and Materials horn (VCX750) with a 1 cm^2 tip under temperature control by an Isotemp 1006S water bath. Horn intensities were calibrated by calorimetry with water.

Particles were imaged using a Canon PC1015 digital camera attached to a Zeiss Axioskop optical/fluorescence microscope with polarization analyzer or with a Hitachi 4700 SEM.

Cooling crystallization of aspirin In a typical experiment 6.7 g of aspirin were dissolved with stirring in 40.0 ml of acetic acid at 45 °C. The stir bar was removed and the solution was supersaturated by cooling to 20 °C. Nucleation was induced by one of various methods to be detailed in the discussion section. Crystals were allowed to ripen for 24 hours and isolated by filtration and vacuum drying.

Measurement of particle size distributions Particle size distributions were estimated gravimetrically with the aid of an ultrasonic sifter (ATM Corporation). The sifter consists of successively smaller meshes. Vibration encourages particles to move to the bin with the largest mesh that will not allow them to egress through to the next bin. Each mesh was weighed before and after sifting and the relative masses were used to compare particle size distributions.

4.3 Cooling crystallization of aspirin

The sonocrystallization procedure was adapted from a previous report.[16] Aspirin was dissolved in acetic acid at elevated temperature and supersaturated by cooling. Stirring can induce nucleation, so the solution was allowed to rest in the thermal bath to equilibrate for 45 minutes after thermometry indicated it had achieved the desired temperature. Nucleation was induced by sonication at 10 W for 15 seconds. Figure 4.4 shows the rapid nucleation progression; the solution proceeds from a completely homogeneous, supersaturated solution, to an opaque mixture of aspirin crystals and mother liquor. It would be possible to modify average crystal size and crystal size distribution by adjusting the sonication parameters.[16-17]

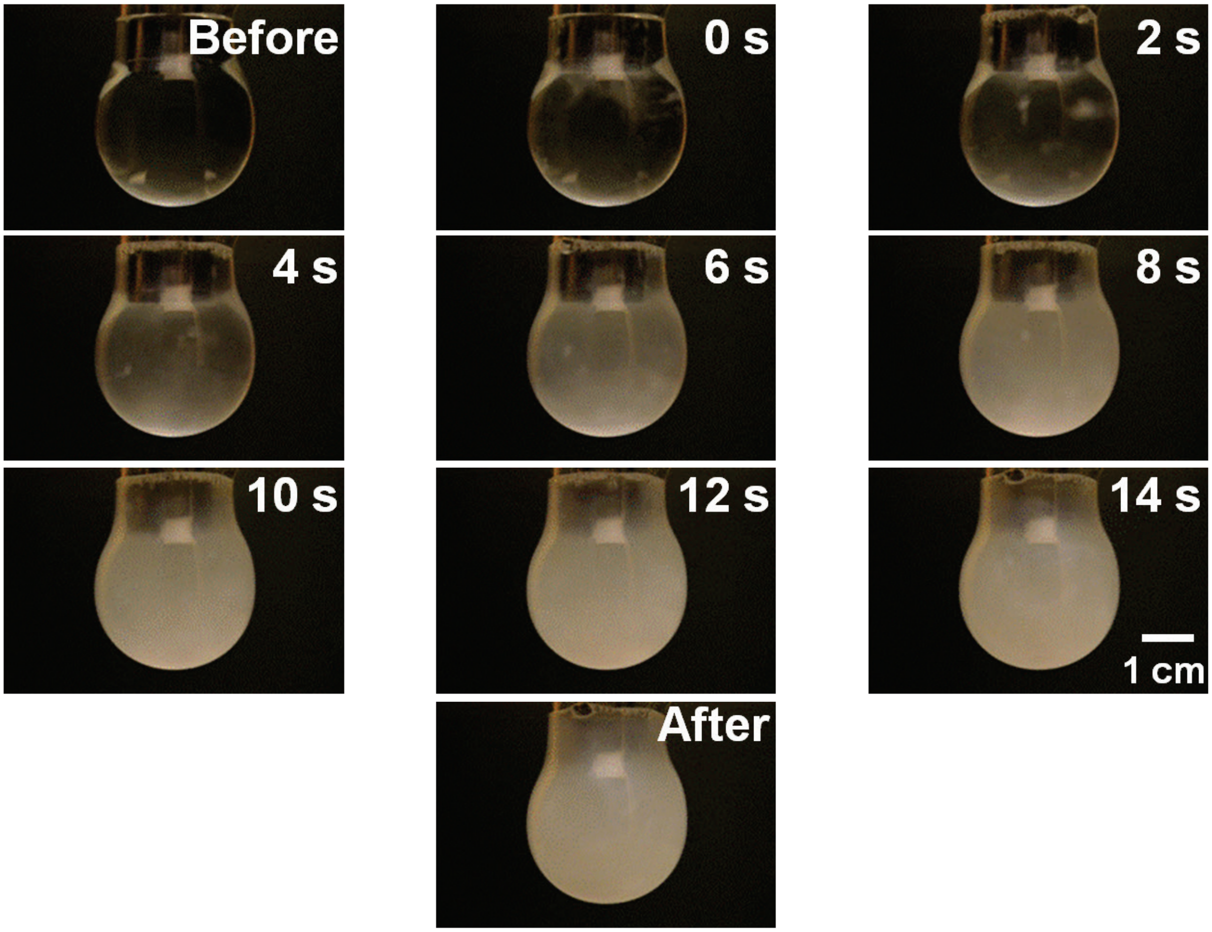

Figure 4.4 Sonocrystallization of aspirin. Aspirin dissolved in acetic acid and supersaturated by cooling. Nucleation was induced by sonication for 15 seconds at 10 W. Frames were extracted from video every 2 seconds. Initial solution exhibits minor sweating from cooling, but solution is completely homogeneous.

Aspirin does not typically exhibit polymorphism. Aspirin was first prepared in 1853[18] (and its predecessor, salicylic acid has been in use since at least 400 BC). It was believed until the 1960s that only one polymorph of aspirin existed, and it was not until 2005 that the second form of aspirin was actually prepared.[19] Form II is only stable below 100 K and will spontaneously convert to form I under ambient conditions. This lack of polymorphism makes aspirin a relatively simple crystal to study. Powder XRD confirmed that no surprising crystal structure is produced by sonocrystallization (Figure 4.5).

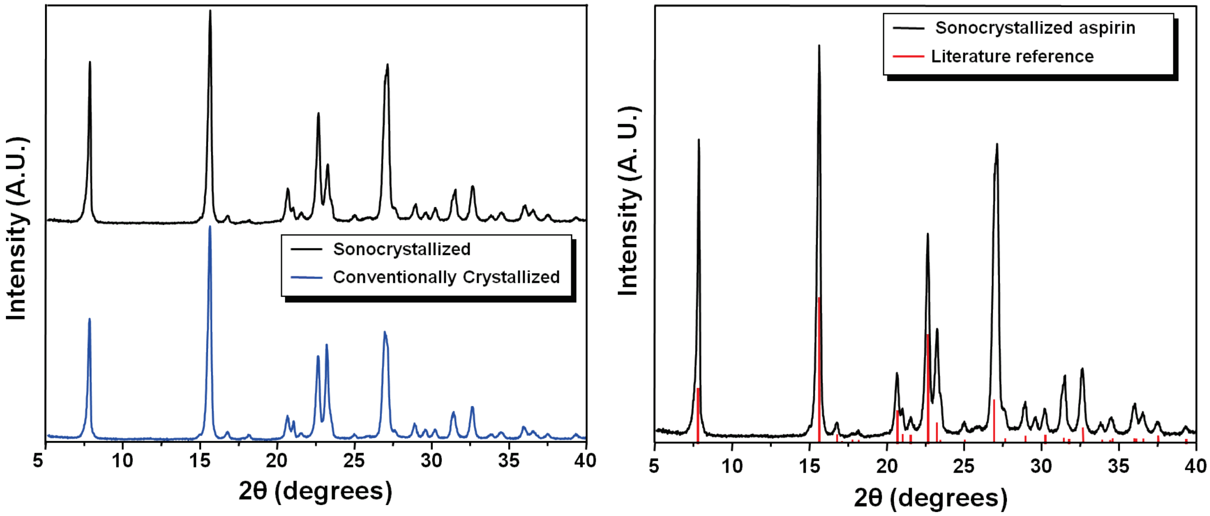

Figure 4.5 Powder XRD. Left: comparison of sonocrystallized aspirin to aspirin crystallized with no induced nucleation. Right: comparison of sonocrystallized aspirin to reference card.

The effects of ultrasound on crystallization processes were highlighted in Chapter 1, Section 1.3. While there is a considerable body of work empirically showing the effects of sonocrystallization, no broad comparison of sonocrystallization with other techniques has been assayed. It is indeed a non-trivial task; for truly fair comparison each technique should be optimized for a given application, as conditions that work well for one method may not be advantageous to another. Presented here is a simplistic approach: a comparison of various nucleation methods under similar conditions. Crystals are presented for comparison in terms of crystal size distribution and optically-observable differences in size and morphology.

Figure 4.6 shows aspirin crystals prepared by eight different methods. All crystals were precipitated from a supersaturated solution of aspirin in acetic acid except for the "as-received" crystals, which were taken directly from the bottle provided by Sigma-Aldrich, and the "hand-ground" crystals. The latter were prepared by vigorously using a mortar and pestle on the "no induction" crystals for 5 minutes. The degree of supersaturation (defined as the ratio of aspirin in solution to the thermodynamic solubility limit) was ~1.5, determined gravimetrically by weighing the product isolated and comparing to the mass of aspirin originally dissolved.

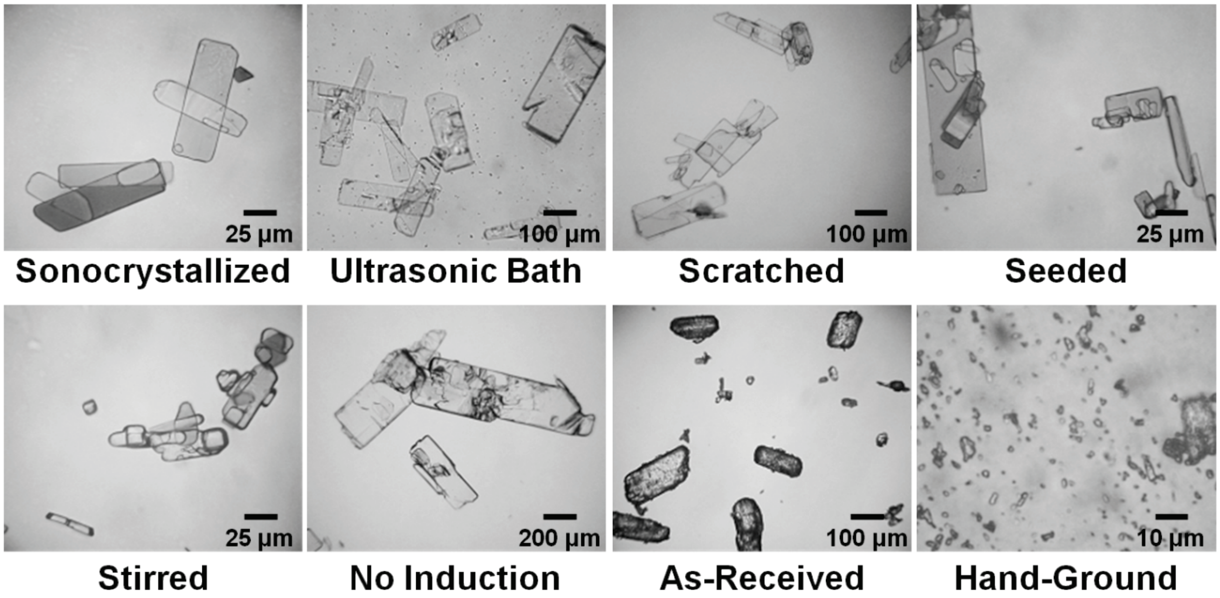

Figure 4.6 Optical micrographs of aspirin. Aspirin particles crystallized from supersaturated acetic acid solution by different nucleation methods.

The mechanism of nucleation during sonocrystallization is discussed in detail in Chapter 1. Scratching the side of the crystallization vessel with a glass stir rod is a common laboratory technique, but the mechanism of action is not fully agreed upon. Creating defects or fresh surfaces on the glassware or introducing seeds (evaporation of solvent on the stir rod forming tiny crystals when the rod is pulled out of the solution, and then pushed into the vessel during the next downstroke of the scratching) are both viable mechanisms. Amusingly, it has been proposed that crystallization induced by scratching glassware with a glass stirring rod is caused by cavitation.[20-21]

Seeding is a standard industrial technique because it can be very effective. It can also be extremely difficult, however; seeding must be done at precisely the right time in a supersaturation procedure. Premature seeding will result in the seeds simply dissolving while tardy seeding can result in catastrophic crashing out of the material or competitive spontaneous nucleation.[22-23] It is also difficult to produce small particles with a seeding technique.[24]

Stirring was done using a magnetic “football”. The pressure underneath the stir bar favors the denser phase and therefore locally increases the degree of supersaturation per the Clausius-Clapeyron relation. Crystals nucleated in this way are ejected by the stirring motion and a large number of seeds are rapidly produced and distributed in solution.

Crystals labeled “no induction” were allowed to come out of solution without any intentional stimulus. It is not really correct to say that nucleation was not induced; in practice it is certain that nucleation occurred on microbubbles in solution, defects in the glassware used, particulate impurities in the solvent, or the incidence of a cosmic ray. It would therefore be more precise (but less wieldy) to say that the nucleation technique in this case is unknown rather than nonexistent. Particles prepared in this way were vigorously ground by hand with a mortar and pestle for 5 minutes to create the particles presented in the “hand-ground” micrograph. The particles prepared by grinding were then used to seed nucleation for the “seeded” sample. “As-received” particles are shown as they appear when taken directly from product provided by Sigma-Aldrich.

Particle size distributions were estimated gravimetrically with the aid of a sonic sifter as described in Section 4.2. The bins measured in this way are presented in Figure 4.7. Some preparation techniques exhibit significant clumping, which manifests as apparent large particles.

This problem is most readily apparent in the “seeded” and “stirred” samples, where the largest bin has a larger population than one might expect based on the trend of the other bins. This problem is significantly less in the horn sonocrystallized sample compared to the seeded and stirred samples.

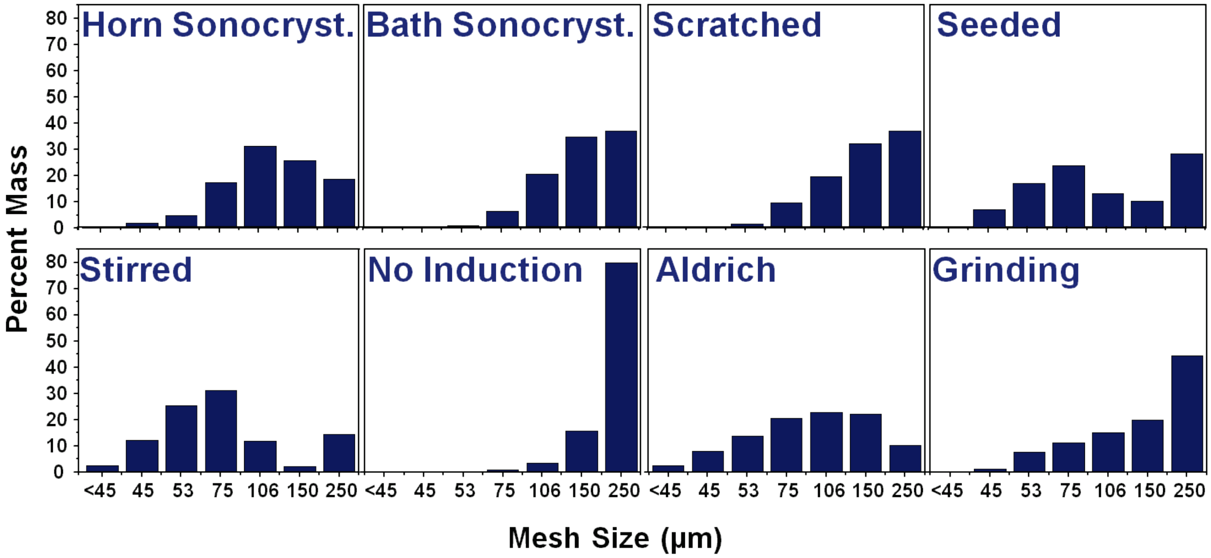

Figure 4.7 Particle size distributions. Comparison of crystal size distributions as measured gravimetrically with the aid of an ATM Corporation sonic sifter.

As discussed earlier, the ideal case would be to compare each crystallization technique after each has been optimized for a specific application. Even then it is not clear that the comparison would have greater value, as it would not be rigorously generalizable to other crystallization systems or other applications. Comparisons of this nature will always suffer from these limitations. What is presented here should give a flavor for sonocrystallization in the context of the field, and shows that ultrasound can be a competitive technique, but the reader should be careful not to overinterpret the results.

4.4 Spray sonocrystallization

There are many ways to incorporate ultrasound into a more sophisticated scheme. Section 1.3 in the introductory chapter discussed some of these. Discussed here is a new technique using ultrasound in antisolvent sonocrystallization. The technical details of the technique were introduced in Section 2.1.4 of the materials and methods chapter. Briefly, a drug solution (it is not necessarily restricted to pharmaceutical materials, but for simplicity discussion will be presented in that context) flows through a hole drilled in an ultrasonic horn, exiting the bottom (an acoustic antinode of the horn). The horn is immersed in an antisolvent and the solvent is dispersed via momentum transfer from the horn. Ideally each droplet acts as an individual crystallization chamber. The antisolvent can be in a fixed-volume reservoir or be constantly refreshed in a continuous flow cell. Presented here is a sampling of the (surprisingly diverse) possible products prepared in this way.

4.4.1 Spray sonocrystallization of aspirin

Aspirin was still used as a model material because of familiarity, wide-spread real-world use, and because it is extremely cheap. Early experiments were performed with the specific aim of producing crystals of an appropriate size for inhalation (0.5 to 5 μm). High concentrations of aspirin in ethanol (saturated solutions, ~400 mg/ml) injected at high flow rates (at least 4.6 ml/min) into a 40 ml reservoir of nanopure water (the solubility of aspirin in water is ~3 g/ml at room temperature) resulted in uniform crystals of promising dimensions. Figure 4.8 shows crystals made in this way sonicated at several power settings.

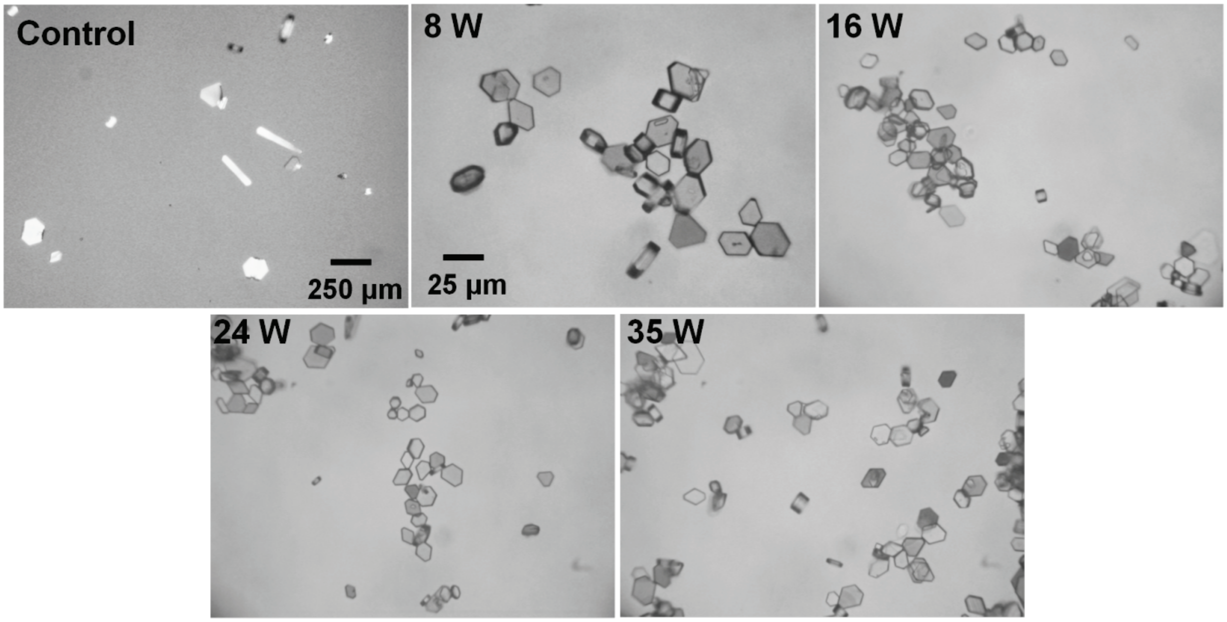

Figure 4.8 Effect of power. Antisolvent sonocrystallization of saturated aspirin in ethanol injected into a 40 ml water reservoir at 9 ml/min for 15 seconds while sonicating at different acoustic powers. All images are the same scale except the control (no sonication).

Crystals formed in the absence of ultrasound in this case were much larger than those formed with sonication, and exhibited nonuniform morphologies. Generally, the absence of ultrasound results in clumps of material rather than well-defined crystals and clogging of the solvent inlet, or else no nucleation, depending on the experimental conditions (most importantly, drug concentration and drug/solvent/antisolvent formulation). At higher horn intensities particles get smaller, although the change is only dramatic when going from no sonication to 8 W and from 8 W to 16 W; at higher intensities the changes are slight. There are several interpretations for this. One is that greater momentum transfer leads to smaller droplets dispersed in the antisolvent (probably not the case here, as discussed later in this section, although generally viable). The second possibility is that the higher intensity ultrasound creates more nucleation sites and the crystals are smaller because the available drug is distributed over a larger number of crystals. Related to this, it is also possible that nascent crystals are broken and then ripen. There is greater breakage at higher power (see Chapter 5) so these crystals end up smaller.

One initial concern is that differences in particle size could be the result of slightly different ripening times (taking longer to get the sample to the microscope). These particles are reasonably stable, however, with very little observable change in size or habit over several days, although the first observation is not until several minutes after nucleation. A more compelling concern arises as a result of using a fixed reservoir of antisolvent. This initially seemed necessary as a practical concession to the constraints of operating on the laboratory scale. The obvious problem arises that running experiments for different times or at different flow rates will create a different solvent/antisolvent profile and make comparisons challenging. It is also a problem for reproducibility, as running two experiments for identical time periods requires great care. Figure 4.9 illustrates this problem.

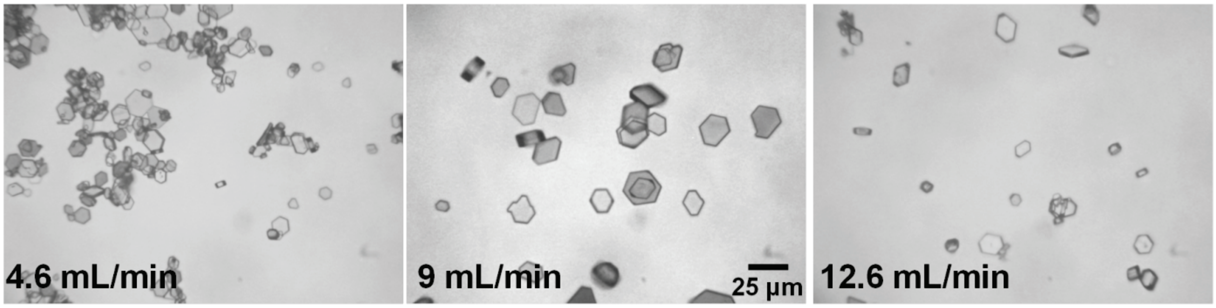

Figure 4.9 Effect of flow rate. Antisolvent sonocrystallization of saturated aspirin in ethanol injected into a 40 ml water reservoir at different flow rates. Crystals nucleated with sonication at 8 W and an experiment time of 15 seconds. All images are the same scale.

It seems that the flow rate of 9 ml/min produced larger particles than both the higher flow rate and the lower flow rate, which is surprising. All three experiments were run for 15 seconds, resulting in a different solubility profile in each case in addition to the different flow rate. It is nontrivial to control the solvent/antisolvent admixture in an experiment such as this. It was briefly attempted, but it proved simpler to modify the experimental apparatus to bypass the issue.

It was also observed that at solvent flow rates lower than 4.6 ml/min, or using slightly lower concentrations of aspirin, that no product would form that could be observed by optical microscopy. The mixture would take on an opaque or translucent milky quality, indicating the presence of sub-optical crystals. It was additionally noticed that filtration of large crystals prepared in this way would leave a milky filtrate. Dynamic light scattering indicated particles of a few hundred nanometers. The production of monodisperse micron-scale crystals and also nanocrystals (each with reasonably tight particle size distributions that do not overlap) is unexpected. It is proposed that this indicates two distinct nucleation mechanisms. The first nucleation mechanism, leading to nanocrystals, is speculated to be due to the dispersion of droplets, each acting as an individual crystallization vessel. The second mechanism would be a bulk sonocrystallization due to poor dispersion at high flow rates. It could also be that nucleation is slow compared to diffusion of the solvent into the antisolvent, and the drug dissolves into the antisolvent as a metastable solution that then nucleates and grows crystals in a classical fashion. This does not seem likely in the specific instance of aspirin, as the nanocrystals would make excellent nucleation sites for the growth of the larger crystals, but could be the case when all crystals formed are micron-scale (for example, the crystallization of acetaminophen that will be mentioned in Section 4.4.2).

The experimental set-up was significantly revised in order to overcome problems related to the changing solvent/antisolvent profile. Instead of a fixed reservoir a continuous flow tube was used. The nanocrystals were targeted rather than the micron-sized crystals, in part because they are more interesting, and in part because conditions that would lead to micron-sized particles would also tend to clog the crystallization tube. Figure 4.10 shows an example of the sonocrystallization of aspirin with a continuous-flow crystallization tube.

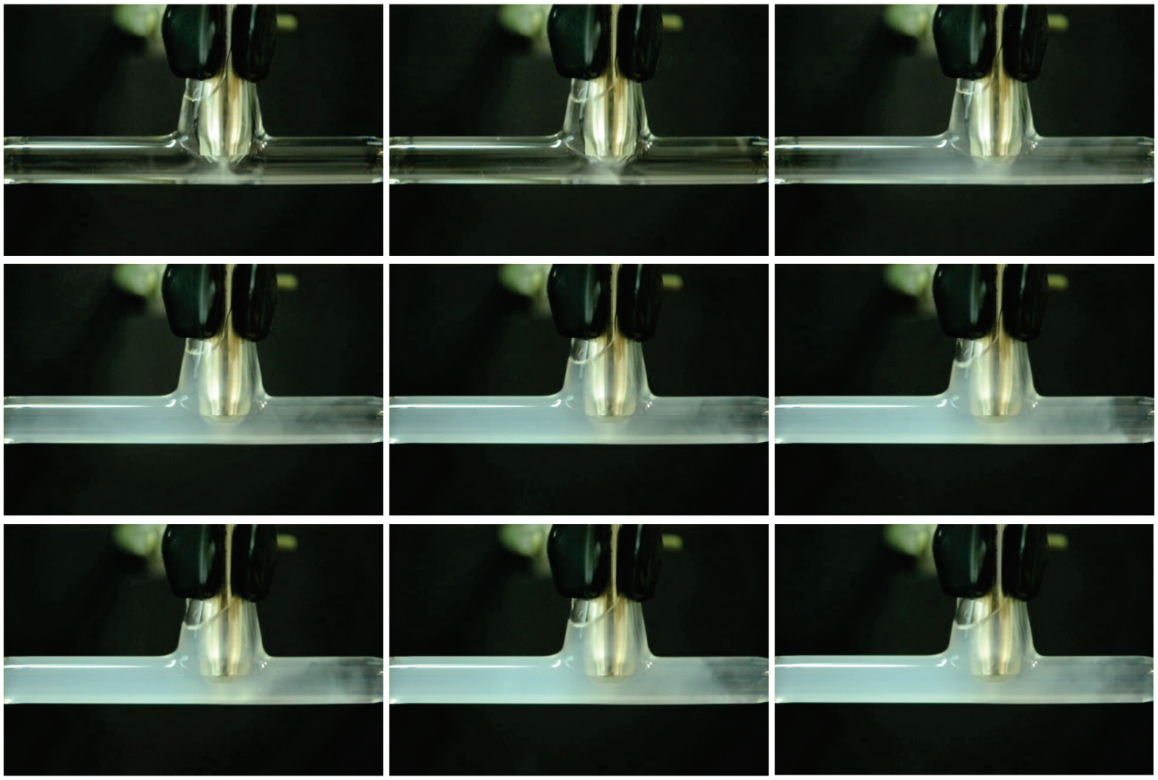

Figure 4.10 Spray sonocrystallization. Antisolvent sonocrystallization of aspirin. A saturated solution of aspirin in ethanol is ultrasonically dispersed in a continuous flow of water (flowing right to left). Images are extracted from a video, each frame is separated by 3 seconds. In the first two frames the horn is on but no solvent has reached the antisolvent yet; the slight cloudiness is solely from cavitating bubbles. Crystallization begins in the third frame.

The solvent/antisolvent profile, as well as the temperature profile, in this instance are also not constant, but it reaches equilibrium within a reasonable period of time. This was monitored by collecting aliquots at fixed intervals to determine how long it took for the sample particle size distribution to stabilize. Figure 4.11 shows that this would occur in under a minute for a saturated solution of aspirin in ethanol flowing at 2 ml/min into nanopure water flowing at 65 ml/min.

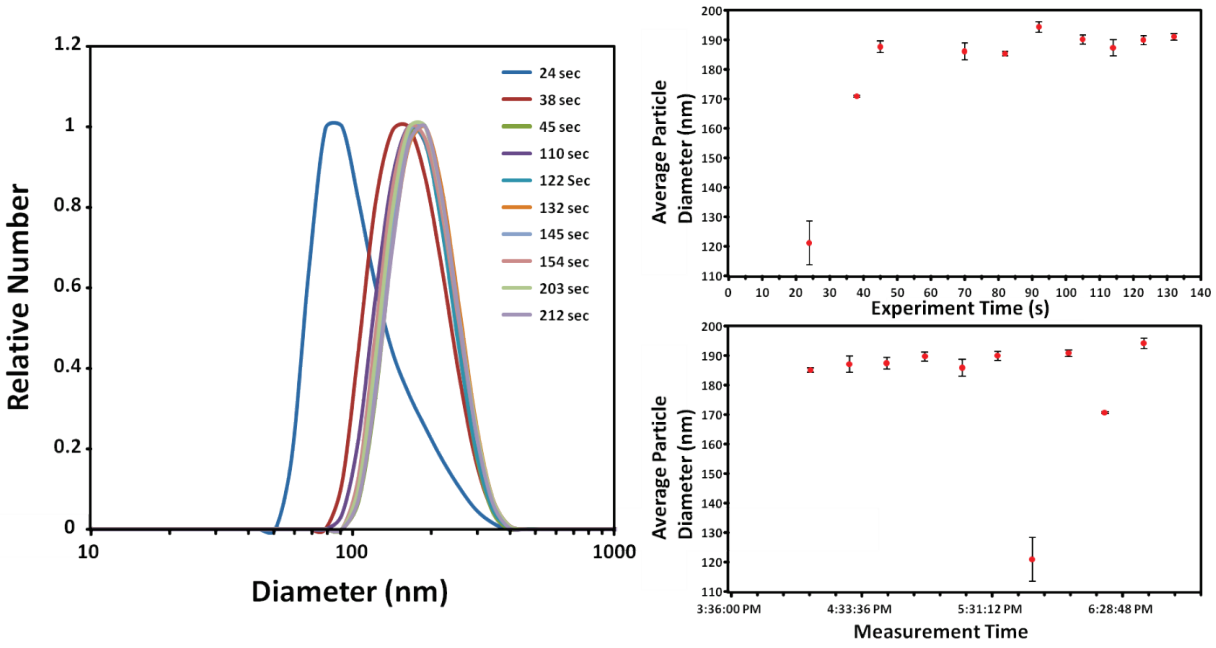

Figure 4.11 Equilibration of spray sonocrystallization. Aliquots collected from antisolvent sonocrystallization of aspirin and evaluated by dynamic light scattering. Left: particle size distributions for each collection; legend indicates how long the experiment ran before the aliquot was collected. Right top: average particle size as a function of crystallization experiment time. Bottom right: average particle size as a function of dynamic light scattering measurement time, intended to give a sense of ripening.

The plot in the bottom right of Figure 4.11 highlights a difficult problem. Particle sizes are plotted against measurement time and there is a clear, although small, trend in particle size. Although water is a decent antisolvent, ripening still occurs. The two outliers are from early experiment times and the sonication parameters dominated the ripening. This problem is not terminal: the change in particle size is only a few percent over several hours, so one can be confident that ripening is a minor effect if samples are analyzed promptly. It does create insurmountable issues with attempts to otherwise characterize the particles, however. It is not possible to prepare SEM samples when the nanoparticles retain some solubility in the host liquid; additional precipitation on the SEM stage makes micrographs unusable. Attempts to solve this problem by using a 'harder' antisolvent generally results in clumping of particles (making dynamic light scattering unreliable). Furthermore, even very poor solvents can evince some solubilization of the drug material, especially when the drug is in nanoparticle form. Section 4.4.2 explores several solvent/antisolvent/drug sonocrystallization systems.

4.4.2 Spray sonocrystallization of other materials

Several other drug materials were tested with the spray sonocrystallization technique. Cromolyn (a non-steroidal asthma treatment typically delivered as an aerosol), acetaminophen (also called paracetamol, the active ingredient in Tylenol, which is a common analgesic), and folic acid (vitamin B_9) were all attempted. Each has different solubility characteristics and consequently their own solvent/antisolvent system. Cromolyn crystals prepared in this way were mostly small than 1 μm in diameter. Cromolyn was only attempted with a static antisolvent system rather than the continuous flow tube and will consequently not be discussed further here.

Acetaminophen generally seemed to crystallize slowly, even using antisolvents in which it had extremely low solubility. This is an undesirable trait; ideally crystallization will occur before dispersed droplets have opportunity to combine with other droplets or diffuse uniformly into the antisolvent. Even with antisolvents that were expected[20] to be very good, such as methylene chloride or toluene, it would not nucleate at all in the time frame of the experiment. Only when using hexanes as the antisolvent were crystals obtained, and they were relatively large (Figure 4.12) and clumped into large aggregates.

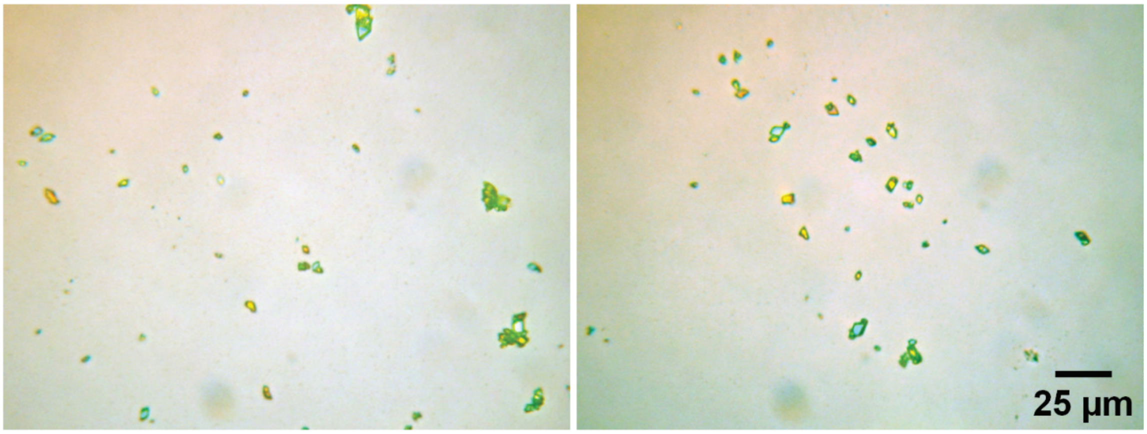

Figure 4.12 Spray sonocrystallized acetaminophen. Micron-scale particles isolated from spray sonocrystallization of acetaminophen dissolved in ethanol (1.4 M) injected into a continuous flow of hexanes.

Folic acid was a more versatile option, crystallizing readily under a number of solvent/antisolvent schemes, and exhibiting a diversity of possible size distributions and morphologies. Folic acid is very nearly insoluble in neutral to moderately acidic water (it will become quite soluble at very low pH), but dissolves readily in base (as the folate ion). A saturated sodium bicarbonate solution is a more than adequate solvent (it is possible to clog the crystallization tube even at low flow rates with high concentrations of folic acid), and acidic water makes a good antisolvent. The choice of acid made a surprisingly large difference in particle characteristics; HCl creates particles too small to resolve optically, while H_2SO_4 forms large needles (Figure 4.13). This may again be the result of crystallization kinetics compared to the rate of droplet aggregation or solvent-antisolvent interdiffusion.

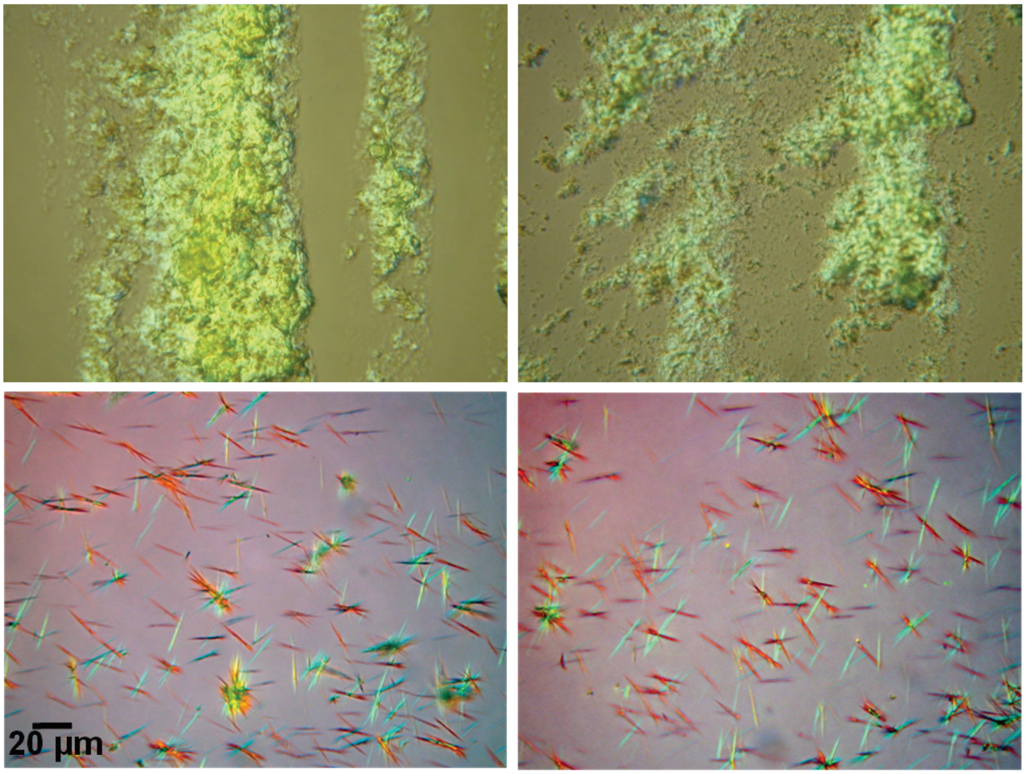

Figure 4.13 Spray sonocrystallized folic acid. 0.3 M folic acid dissolved in saturated sodium bicarbonate solution and spray sonocrystallized in 1 M acid (top: HCl, bottom: H_2SO_4). Solvent injected at a flow rate of 4.5 ml/min and antisolvent flow at 65 ml/min. All images on the same scale.

Unfortunately it was prohibitively challenging to adequately characterize the suboptical crystals produced in this way due to their slight solubility in even acidic aqueous media. While optical microscopy can give a sense of their characteristics, there is no way to prepare a dynamic light scattering sample without causing them to dissolve or ripen. Similarly, any attempt to prepare an SEM sample would lead to precipitation of residual folic acid from the mother liquor.

In an effort to overcome these obstacles, the solvent/antisolvent system was changed to acetone (in which folic acid had no solubility that could be detected by UV-vis spectrophotometry) as the antisolvent and a 20% aqueous ammonium hydroxide solution as the solvent. Product was collected in a large reservoir of antisolvent to dilute any residual solvent to irrelevance. Crystals could be isolated by repeated centrifugation and rinsing.

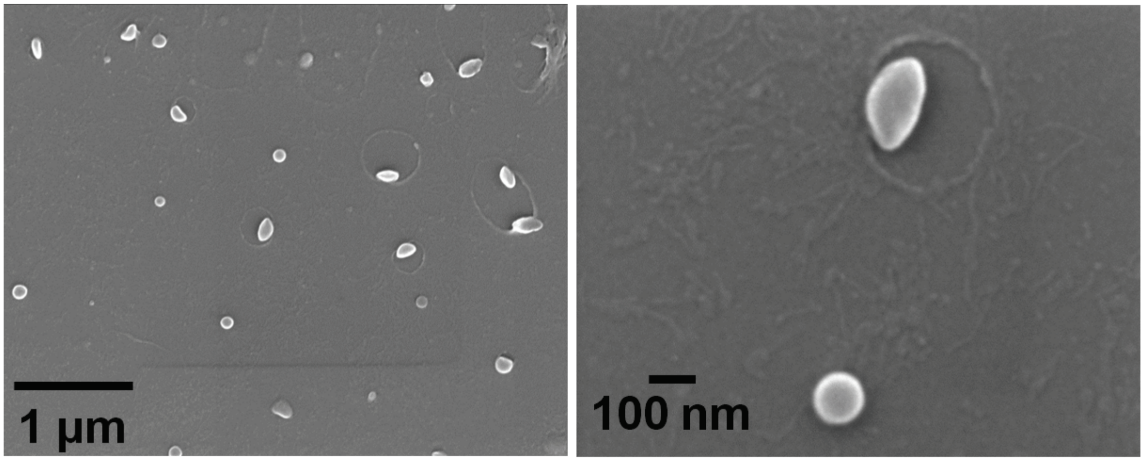

Figure 4.14 SEM of folic acid. 0.3 M folic acid dissolved in aqueous ammonium hydroxide solution and spray sonocrystallized with acetone as the antisolvent. The solvent flow rate was 0.6 ml/min and the antisolvent flow rate was 65 ml/min.

This formulation yielded nanocrystals (Figure 4.14), but even then there was some evidence of residue left after the evaporation of the acetone. Sadly, these crystals were too polydisperse for characterization by dynamic light scattering unless they were allowed to ripen for several days (possibly due to aggregation). The addition of a surfactant (Tween 20) had little effect other than to further obfuscate SEM micrographs.

4.5 Concluding remarks

Sonocrystallization is a powerful and versatile technique that has not yet reached maturity. While it is almost certainly not the technique of choice for all specific applications, in a general sense it is competitive with many industrial and laboratory standards, as demonstrated by the comparative work in this chapter. In addition to having a competitive particle size distribution and producing well-formed crystals, the sonocrystallization procedure can be extremely simple and facile.

More sophisticated designs are also possible, as shown by the invention and development of the spray sonocrystallization technique. Although all experiments presented here are naturally on the laboratory scale, it is not hard to imagine that an array of similar devices in a continuous-production operation could permit industrial scale operation. The ability to produce a variety of different crystals with this technique has been demonstrated, including nanoscale crystals without the need for any surfactant or other templating method. Although the foundation of this technique has been laid there is still a significant space to investigate and effective ways to isolate and characterize spray sonocrystallized particles remains challenging.

4.6 References

1. Johnson, K. C.; Swindell, A. C., "Guidance in the setting of drug particle size specifications to minimize variability in absorption." *Pharm. Res.* **1996,** *13*, 1795-1798.

2. Merisko-Liversidge, E. M.; Liversidge, G. G., "Drug nanoparticles: formulating poorly water-soluble compounds." *Toxicologic pathology* **2008,** *36* (1), 43-8.

3. Finlay, W. H., *The mechanics of inhaled pharmaceutical aerosols: An introduction*. Academic Press: 2001.

4. Scheuch, G.; Siekmeier, R., "Novel approaches to enhance pulmonary delivery of proteins and peptides." *Journal of physiology and pharmacology : an official journal of the Polish Physiological Society* **2007,** *58 Suppl 5* (Pt 2), 615-25.

5. Abbas, A.; Srour, M.; Tang, P.; Chiou, H.; Chan, H.; Romagnoli, J., "Sonocrystallisation of sodium chloride particles for inhalation." *Chem. Eng. Sci.* **2007,** *62* (9), 2445-2453.

6. Dhumal, R. S.; Biradar, S. V.; Paradkar, A. R.; York, P., "Particle engineering using sonocrystallization: salbutamol sulphate for pulmonary delivery." *Int. J. Pharm.* **2009,** *368* (1-2), 129-37.

7. Kaerger, J. S.; Price, R., "Processing of spherical crystalline particles via a novel solution atomization and crystallization by sonication (SAXS) technique." *Pharm. Res.* **2004,** *21* (2), 372-81.

8. Watts, A. B.; Williams, R. O., *Controlled Pulmonary Drug Delivery*. Springer New York: New York, NY, 2011; p 335-366.

9. Cuellar, I.; Bullon, J.; Forgarini, A.; Cardenas, A.; Briceno, M., "More efficient preparation of parenteral emulsions or how to improve a pharmaceutical recipe by formulation engineering." *Chem. Eng. Sci.* **2005,** *60* (8-9), 2127-2134.

10. Kipp, J. E., "The role of solid nanoparticle technology in the parenteral delivery of poorly water-soluble drugs." *Int. J. Pharm.* **2004,** *284* (1–2), 109-122.

11. Rao, S.; Song, Y.; Peddie, F.; Evans, A. M., "Particle size reduction to the nanometer range: a promising approach to improve buccal absorption of poorly water-soluble drugs." *International journal of nanomedicine* **2011,** *6*, 1245-51.

12. Parrott, E. L., "Influence of particle size on rectal absorption of aspirin." *J. Pharm. Sci.* **1975,** *64* (5), 878-880.

13. Thorat, A. A.; Dalvi, S. V., "Liquid antisolvent precipitation and stabilization of nanoparticles of poorly water soluble drugs in aqueous suspensions: Recent developments and future perspective." *Chem. Eng. J. (Lausanne)* **2012,** *181-182*, 1-34.

14. Rogueda, P. Production of drug microparticles in presence of ultrasonic energy using antisolvent. WO 004847, 2005.

15. Begon, D.; Pfefer, G.; Kohl, M. Process for producing fine medicinal substance. US 0049321, 2003.

16. Miyasaka, E.; Ebihara, S.; Hirasawa, I., "Investigation of primary nucleation phenomena of acetylsalicylic acid crystals induced by ultrasonic irradiation--ultrasonic energy needed to activate primary nucleation." *J. Cryst. Growth* **2006,** *295*, 97-101.

17. Miyasaka, E.; Kato, Y.; Hagisawa, M.; Hirasawa, I., "Effect of ultrasonic irradiation on the number of acetylsalicylic acid crystals produced under the supersaturated condition and the

ability of controlling the final crystal size via primary nucleation." *J. Cryst. Growth* **2006,** *289* (1), 324-330.

18. Gerhardt, C., "Untersuchungen über die wasserfreien organischen Säuren." *Justus Liebigs Annalen der Chemie* **1853,** *87* (1), 57-84.

19. Vishweshwar, P.; McMahon, J. A.; Oliveira, M.; Peterson, M. L.; Zaworotko, M. J., "The Predictably Elusive Form II of Aspirin." *J. Am. Chem. Soc.* **2005,** *127* (48), 16802-16803.

20. Mullin, J. W., *Crystallization*. 4th ed.; Butterworth–Heinemann: Woburn, MA, 2001.

21. Hunt, J. D.; Jackson, K. A., "Nucleation of solid in an undercooled liquid by cavitation." *J. Appl. Phys.* **1966**.

22. Tung, H.-H.; Paul, E. L.; Midler, M.; McCauley, J. A., *Crystallization of Organic Compounds*. John Wiley & Sons, Inc.: Hoboken, NJ, USA, 2009.

23. Luque de Castro, M. D.; Priego-Capote, F., "Ultrasound-assisted crystallization (sonocrystallization)." *Ultrason. Sonochem.* **2007,** *14*, 717-724.

24. Dennehy, R. D., "Particle Engineering Using Power Ultrasound." *Org. Process Res. Dev.* **2003,** *7* (6), 1002-1006.

Chapter 5
Sonofragmentation of Aspirin

This chapter discusses the effects of ultrasound on molecular crystals after they have already been formed and isolated. The effects of ultrasonic parameters and liquid properties in particular are explored. Ultrasonic dosimetry in viscous media and a population balance model were applied in an effort to quantify how each parameter influences particle breakage.

5.1 Introduction

The application of ultrasound for inducing nucleation (sonocrystallization) of pharmaceutically active ingredients (APIs) is a topic of interest due to its influence on crystal size distributions[1] and polymorphism,[2-3] improved reproducibility,[4] and the reduction or elimination of adding foreign materials such as seed crystals.[5]

While sonocrystallization has received considerable recent attention due to its ability to influence crystal properties for pharmaceutical applications, [6-13] reports on the effects of ultrasound on particles post-crystallization are relatively modest in number,[14] limited in scope, or empirical in nature.[15-18]

The physical and chemical effects of ultrasound are primarily consequences of acoustic cavitation: the formation, growth, and collapse of bubbles driven by an acoustic wave. The compressional heating caused by the rapid bubble collapse results in intense local temperatures and pressures, on the order of 5000 K and 1000 bar.[19-21] The bubble can rebound from its nadir and emit a shockwave that can cause interparticle collisions[22-28] or break friable crystals (sonofragmentation).[29] Figure 5.1 shows an example of sonofragmentation.

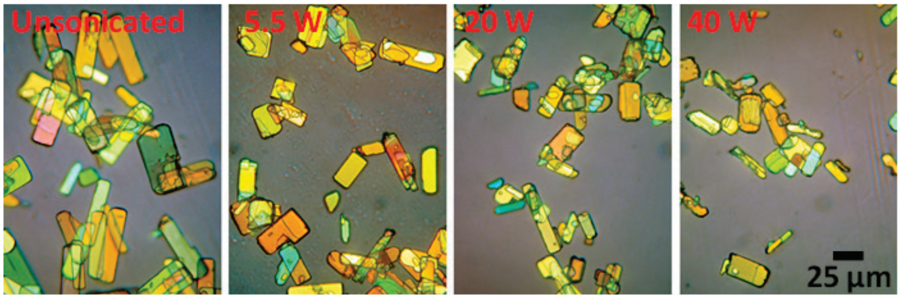

Figure 5.1 Sonofragmentation. Optical micrographs of aspirin crystals sonicated in dodecane at 20 kHz for 1 minute at different ultrasonic intensities.

5.2 Experimental

Materials and equipment Acetylsalicylic acid (Aldrich, 99%), dodecane (Reagent Plus, ≥99%), and glacial acetic acid (Fisher Scientific) were used as-received. Poly(dimethyl)siloxane silicone oils (Dow-Corning 200 fluid) were used as-received for viscosities of 100 cSt and below or 250 cSt and above. Oils of intermediate viscosities were prepared by mixing 100 cSt and 250 cSt oils in different proportions and their viscosities were measured with a Bohlin CS 10 rheometer.

Sonication was performed at 20 kHz with a Sonics and Materials horn (VCX750 for experiments at 10 W or above, VCX600 for experiments below 10 W) with a 1 cm^2 tip under temperature control by an Isotemp 1006S water bath. Horn intensities were calibrated by calorimetry with water.

Particles were imaged using a Canon PC1015 digital camera attached to a Zeiss Axioskop optical/fluorescence microscope with polarization analyzer and manually sized by image analysis using ImageJ (available through NIH). Approximately 200 particles were measured for each data set.

Sonocrystallization of aspirin The sonocrystallization procedure was adapted from a previous report.[30] In a typical experiment 6.7 g of aspirin were dissolved with stirring in 40.0 ml of acetic acid at 45 °C. The solution was supersaturated by cooling to 20 °C and the solution was sonicated at 10 W for 15 seconds to induce crystallization. Crystals were allowed to ripen for 24 hours and isolated by filtration and vacuum drying. Sonocrystallization procedures are discussed in detail in Chapter 4.

Sonofragmentation of aspirin Sonocrystallized aspirin (typically 0.1 g) was mixed with 5.0 ml of liquid (saturated aqueous solution of aspirin, dodecane, or silicone oil) and allowed to thermally equilibrate to 23 °C (at least 30 minutes) in a temperature-controlled water bath. This mixture was sonicated at different intensities and times. All sonication experiments apart from the initial crystallization were performed under a 2 second on, 8 second off pulse cycle to reduce temperature variation. Sonication times are reported as the total time exposed to ultrasound. An aliquot was removed by disposable pipette for analysis by optical microscopy.

5.3 Results and discussion

Sonocrystallized aspirin was used as a model material as it is easy to prepare and the crystals are relatively uniform and of sufficient size for facile characterization by optical microscopy. The choice of liquid used in the slurry is extremely important. The goal of this experiment was to isolate breakage events from other effects, such as crystal growth, ripening, and dissolution. Sonication under conditions where these other processes can be occurring is also presented for reference.

5.3.1 Sonication of aspirin in aqueous media

The first liquid employed as a medium for sonication was deionized water saturated with aspirin prior to slurry loading. It was hoped that the low solubility of aspirin in water (~3 mg/ml at room temperature)[31] combined with the presaturation would eliminate any extraneous phenomena, but it was generally found that temperature fluctuations during sonication would result in non-simple changes in crystal morphology, with sometimes interesting results.

Sonication at moderate times and ultrasonic power settings appears to break particles in a straightforward fashion. Figure 5.2 shows the effects of ultrasound on aspirin particles sonicated for a few minutes at low power in a saturated aqueous solution. They appear to break apart without any obvious evidence of more complicated processes.

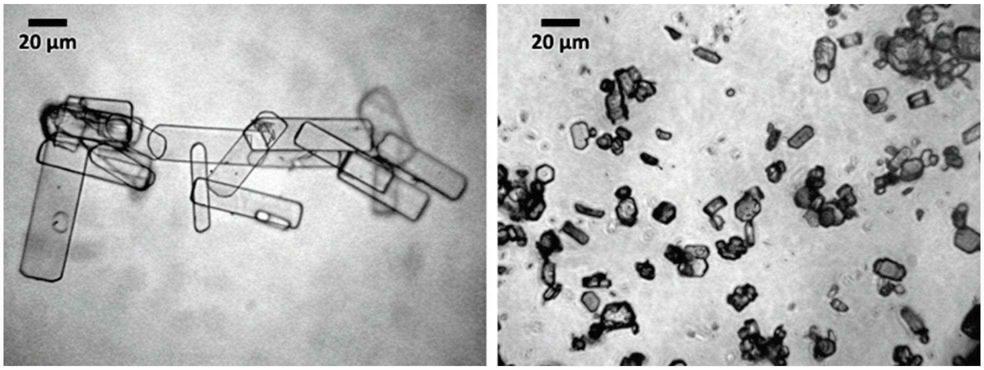

Figure 5.2 Sonication of aspirin in aqueous solution. Left: unbroken aspirin particles prepared by sonocrystallization. Right: aspirin after 5 min sonication at 10 W in saturated aqueous solution.

Sonication for longer times, however, makes it evident that breakage is not cleanly decoupled from other processes. Figure 5.3 shows significant changes in crystal morphology, including crystal growth in (at least) the smallest dimension. Hexagons with low aspect ratios become evident. Whether this is Ostwald ripening or a distinct dissolution/recrystallization effect is not obvious. The hexagonal crystal morphology is the predicted ground state form for aspirin in water.[32]

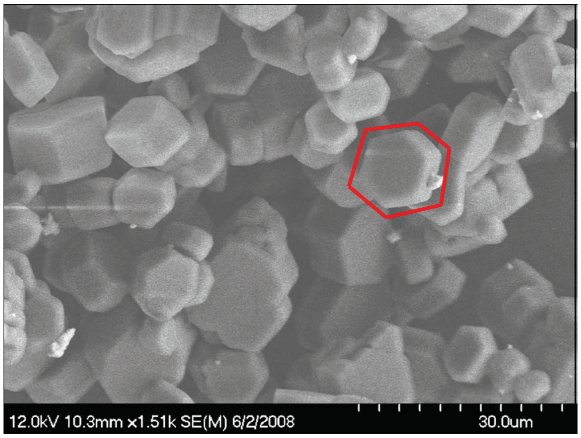

Figure 5.3 Sonorecrystallization. Formation of hexagonal morphologies after sonication of sonocrystallized aspirin in saturated aqueous solution at 10 W for 60 minutes.

The recrystallization or ripening process was strongly dependent on initial morphology, possibly indicating that fragmentation enhances the kinetics of the process due to the increase in available surface area. A comparison of the sonication of sonocrystallized aspirin to aspirin as-received from Sigma-Aldrich and aspirin crystallized without the induction of nucleation is shown in Figure 5.4. While the sonocrystallized aspirin forms mostly uniform hexagons, the other aspirin crystals exhibit much less significant changes in morphology and the changes observed are more consistent with breakage than with recrystallization. The as-received crystals show the least change in morphology, possibly because their initial aspect ratios are high and consequently there is less breakage and also less formation of small, easily dissolvable crystals to reform into the expected ground-state hexagons. The crystals in Figure 5.4D are perhaps better described as circular than hexagonal, possibly due to rounding of the edges during the high-intensity sonication.

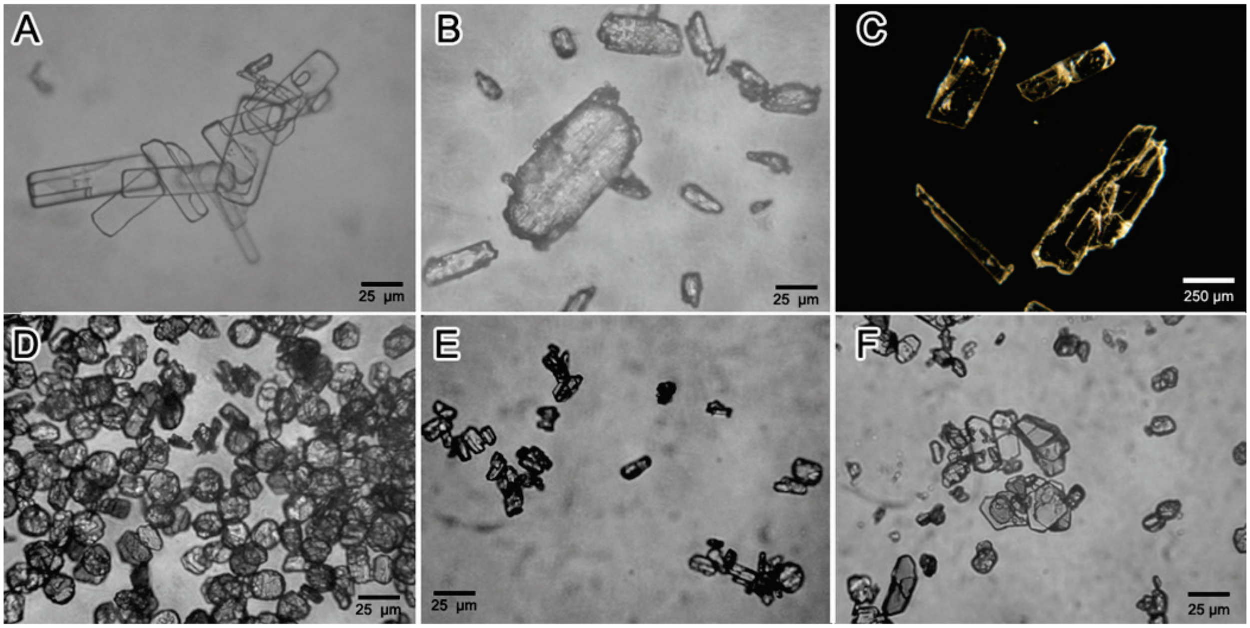

Figure 5.4 Sonorecrystallization. Sonication of aspirin in saturated aqueous solution. A, B, C: sonocrystallized aspirin, aspirin as-received, aspirin crystallized with no induction of nucleation. D, E, F: same samples after 1 hour of sonication at 50 W.

Although the recrystallization or ripening under sonication appeared interesting at first blush, it is probably strictly due to local heating and ultrasound provides only a modest rate enhancement. Sonication was performed in a thermostatted bath held at 23 °C and pulsed such that the horn was only on half the time, but heating still occurs. The temperature at the end of one experiment where significant recrystallization occurred was measured to be 37 °C after one hour. Stirring a solution of sonocrystallized aspirin at that temperature for two hours did not produce comparable recrystallization, but stirring at 60 °C did. This seems to indicate that local heating around cavitation events, along with the reduction in particle size, is response for local dissolution followed by ripening of other crystals or recrystallization.

5.3.2 Sonication of aspirin in hydrocarbons

The ripening or recrystallization processes occurring simultaneously with particle breakage in the aqueous medium created too complex of a system. It was preferred instead to work in a hydrocarbon, in which aspirin has negligible solubility. Dodecane was the primary liquid of choice as it provided a good balance of low vapor pressure (compared, for example, to hexane) and low cost (compared primarily to hexadecane, another common choice of solvent in sonochemistry). Other hydrocarbons were tried solely to determine the significance of vapor pressure on particle breakage.

Preliminary experiments were done qualitatively to optimize experimental parameters. Flat bottom cells were compared to round-bottom cells, as there was concern that particles would be able to “hide” in the junction of the cell base and a straight wall. It was indeed observed that round-bottomed cells appeared to produce more homogeneous samples after sonication. The time scale of interest was also estimated qualitatively, with a sample of aspirin in dodecane sonicated for varying times. Figure 5.5 shows that although breakage is probably still occurring between one hour and two hours of sonication, the rate is obviously very low. Most of the breakage has already occurred within 5 minutes and for subsequent experiments investigations focused on what was happening in the first few minutes.

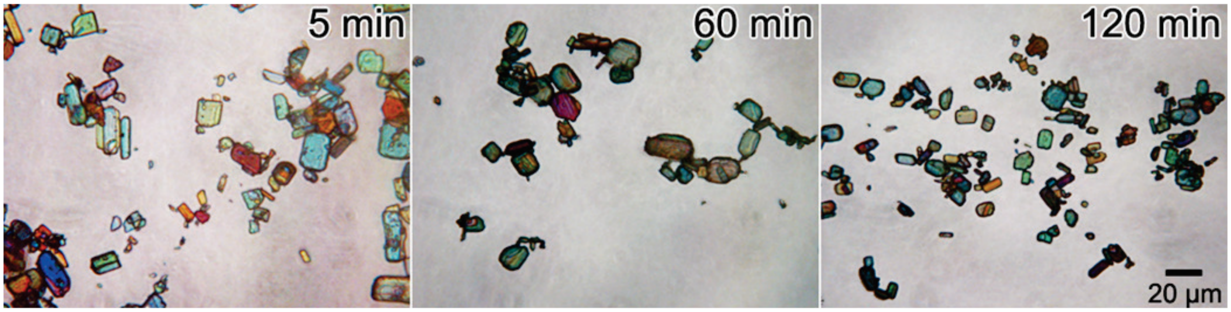

Figure 5.5 Sonofragmentation. Breakage of sonocrystallized aspirin particles at 10 W and variable exposure time. Sonication performed with a 50% duty cycle (10 sec on, 10 sec off). Times are listed as total time exposed to ultrasound (i.e., a "5 minute" experiment takes 10 minutes but the horn was energized for only five of those minutes). All images are on the same scale.

Breakage was quantified by image analysis using ImageJ, as discussed in Chapter 2. Particle sizes are expressed as volumes, which are approximated from optical micrographs (Figure 5.6). Crystals were characterized in terms of circularity and surface area as measured via optical microscopy. The circularity (c) is defined as

$$c = \frac{4\pi a}{p^2}$$

where a is the surface area and p is the perimeter of the two-dimensional image of the crystal. The crystal depth d, defined as the shortest dimension, is estimated from the surface area and perimeter using a proportionality constant obtained from the scanning electron microscope (SEM) images assuming the particles have a similar shape.

$$d \approx \frac{a}{2.06\,p}$$

The mass for each particle was calculated from

$$m = \rho a d$$

where ρ is the density of aspirin (1.40 g/cm^3).

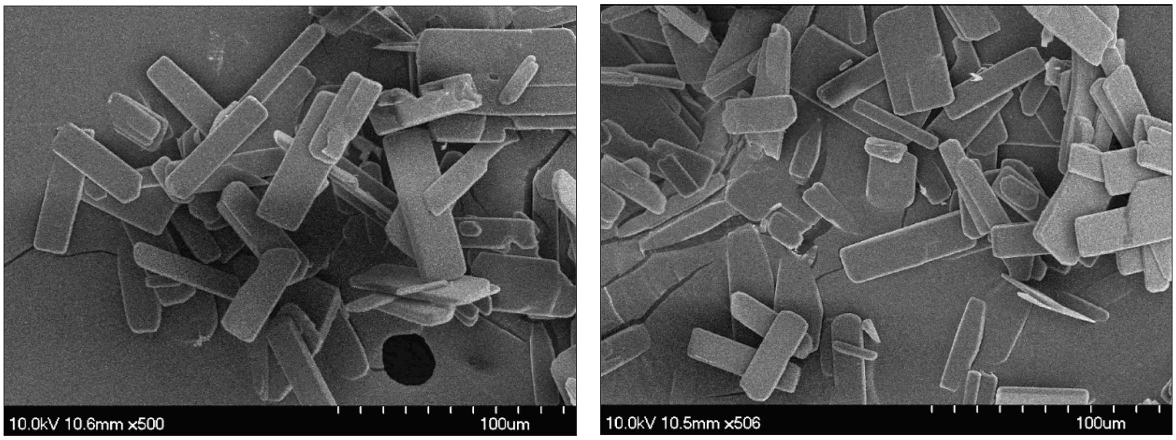

Figure 5.6 Sonocrystallized aspirin. Optical micrographs used for estimating relative crystal dimensions.

Figure 5.7 shows that particle breakage as a function of time is well-behaved and that significant particle breakage occurs even at short sonication times. Breakage efficiency drops sharply with as the particle size is reduced because of the reduced torque applied by a given force as the typical crystal length becomes smaller. The number of cavitation events per second is dependent on the applied acoustic power and consequently breakage occurs less rapidly at lower power.

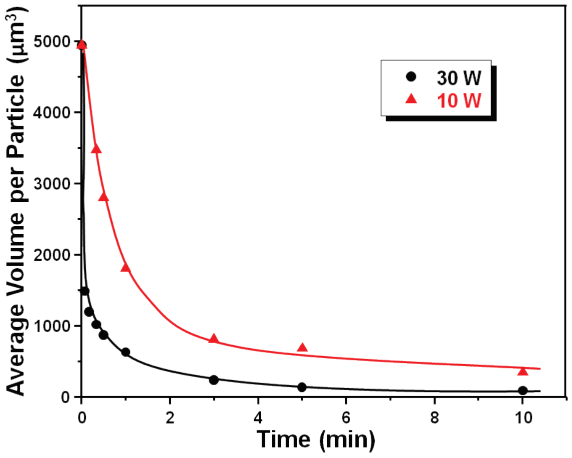

Figure 5.7 Effect of sonication time on particle size. Aspirin particles were sonicated for 1 min in dodecane. Leftmost point represents unbroken particles.

The effects of power can be seen more clearly in Figure 5.8. The change in particle size is strongly dependent on applied power at lower powers. At higher powers it is again evident that particles break relatively slowly as they become smaller and the effect of power is less pronounced.

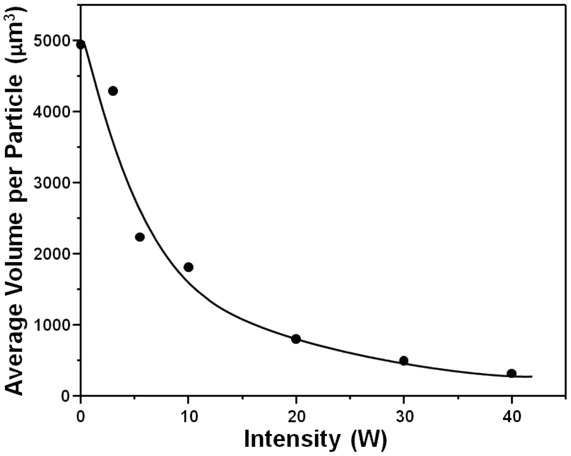

Figure 5.8 Effect of sonication power on particle size. Aspirin particles were sonicated for 1 min in dodecane. Leftmost point represents unbroken particles.

Vapor pressure is known to have significant effects on the conditions inside a sonoluminescing bubble.[33-35] The energy concentrated by collapsing bubbles is distributed among the molecules inside the bubble. A larger number of molecules will consequently dilute the energy, resulting in less extreme conditions. This is especially true if the gas is a polyatomic, which can distribute the energy into molecular rotations, bond vibrations, and bond dissociation. One might therefore expect that vapor pressure will also strongly influence the physical effects of ultrasound, but this is not necessarily the case.[28] Figure 5.9 shows that the effect of vapor pressure on particle breakage is small or negligible over the range probed (the vapor pressure varies by more than 6 orders of magnitude).

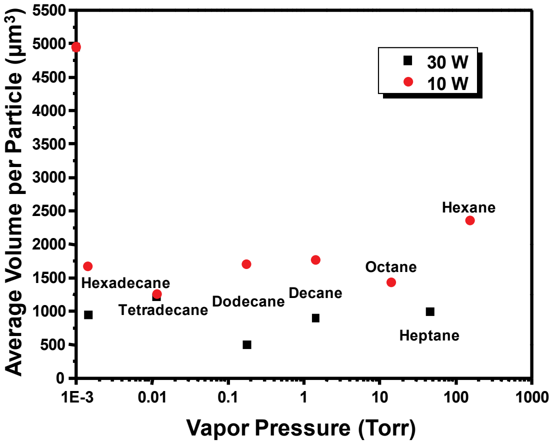

Figure 5.9 Effect of vapor pressure. Sonication of aspirin for 1 minute in different hydrocarbons at varying powers. Leftmost point (intersecting the ordinate axis) represents unbroken particles.

The bubble's rebound is rapid, and the process reconverts most of the energy that was concentrated as thermal energy back into mechanical energy. As a result the shockwave emitted appears to be essentially independent of the vapor pressure of the solvent.

5.3.3 Sonication of aspirin in silicone oils

Viscosity is expected to have a significant impact on the rate of particle breakage. It will influence a large number of relevant parameters, including the number of cavitating bubbles, bubble dynamics, drag on moving particles, and distance of propagation of shockwaves. It is not immediately obvious which of these, if not all, will influence rates of particle breakage or how large their respective impacts will be.

Sound propagating through a liquid medium from a point source is attenuated by absorptive losses, which depend on viscosity. The intensity (*I*) of the sonic field at a given distance (*d*) from a source emitting a wave of intensity I_0 can be described as

$$I = I_0 e^{-\alpha d}$$

where α is the attenuation coefficient.[36] The value of α depends on the frequency (f) of the sound wave, the speed of sound in the liquid (C), the density of the liquid (ρ), and the viscosity of the liquid (μ):

$$\alpha = \frac{8\,\mu\,\pi^2\,f^2}{3\,\rho\,C^3}$$

The number of cavitation events is expected to correlate with the intensity distribution of the ultrasonic field (i.e., a rapid die off of the ultrasonic field will result in the sonication of a much smaller cavitation zone).

The effect of viscosity was probed using Dow Corning 200 fluid®, which is polydimethylsiloxane, also referred to as PDMS or silicone oil. The viscosity of these silicone oils is related to the polymer chain length distribution. Silicone oil is a Newtonian fluid and can be readily purchased at viscosities ranging from 5 cSt to 60,000 cSt.

For this experiment silicone oils could be purchased with viscosities of 20, 50, 100, 350, 500, and 1000 cSt. For the gap between 100 and 350 cSt is was necessary to make mixtures of 350 and 100 cSt oils to achieve intermediate viscosities. Four binary mixtures were prepared, with compositions of 20%, 40%, 60%, and 80% (by volume) of 350 cSt silicone oil with the remaining volume 100 cSt silicone oil. These were mixed well and their actual viscosities were measured with Bohlin CS 10 rheometer (Figure 5.10) with the generous help of the Zukoski group.

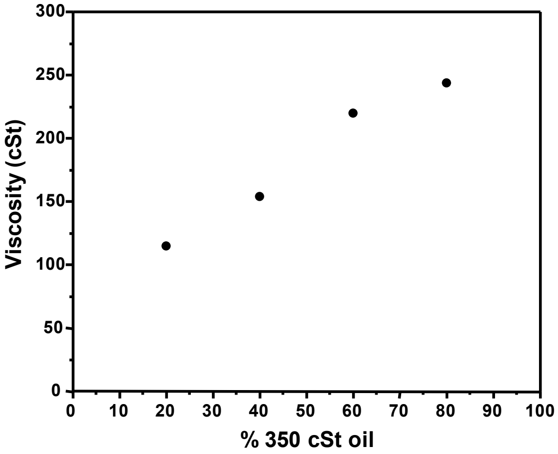

Figure 5.10 Viscosities of mixtures of silicone oils. Mixtures of 350 cSt and 100 cSt silicone oils, as measured by a rotary rheometer calibrated to the stock solutions.

The dependency of particle breakage on viscosity, shown in Figure 5.11, exhibits a strong viscosity effect and threshold behavior: no measurable particle breakage occurs in silicone oils more viscous than ~300 cSt under the experimental parameters used due to the suppression of cavitation at high viscosity. Although particle breakage clearly depends strongly on viscosity, it only becomes evident with large changes in viscosity, implying that small changes in viscosity due to thermal fluctuations in a typical crystallization experiment should not be a concern.

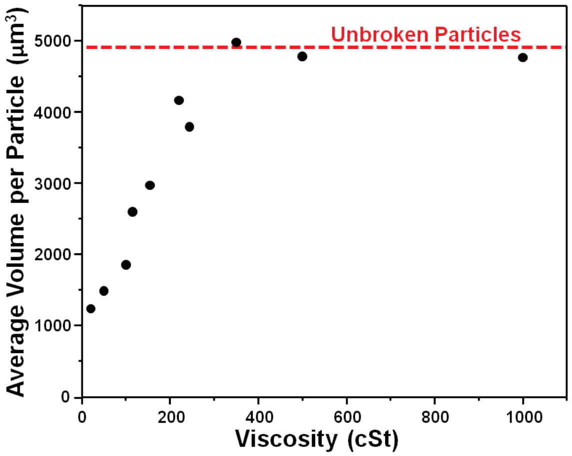

Figure 5.11 Effect of liquid viscosity. Average particle sizes of aspirin sonicated at 30 W for 1 minute in silicone oils of different viscosities.

One pertinent question is whether viscosity is really the only parameter being probed in this experiment. Changing the chain length distribution of the polymer does indeed change other physical properties of the liquid. Figure 5.12 show how surface tension and density vary over the range of silicone oils probed.

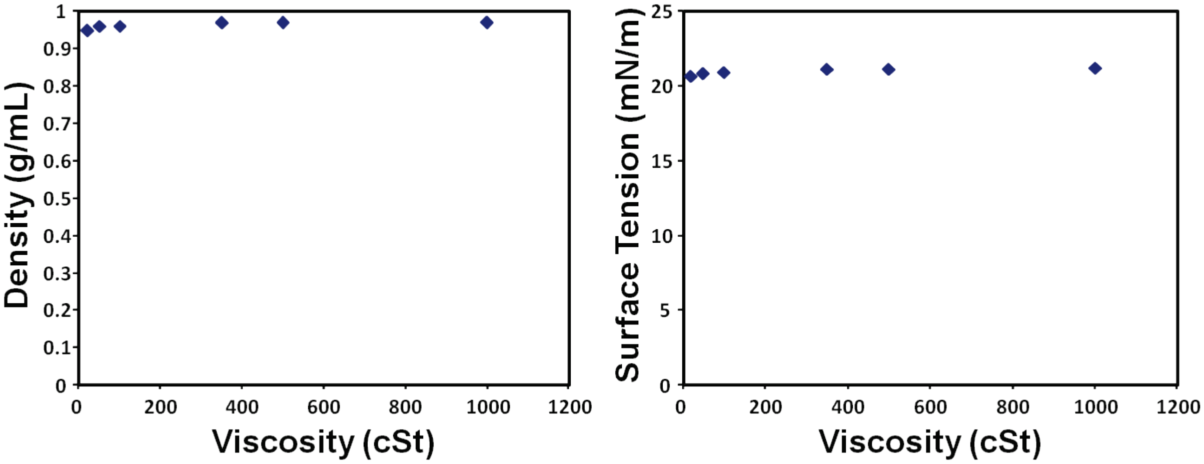

Figure 5.12 Physical properties of silicone oils. Densities and surface tensions of silicone oils are plotted versus viscosity. Data taken from distributor's specifications.[37]

Density varies by less than 2.5% between 20 cSt and 1000 cSt oils. Surface tension varies by less than 3% over this range. Density might be expected to affect how long it takes aspirin particles to settle during idle parts of the duty cycle, which could have a small impact on the experiment. Surface tension could also affect the quality of the suspension, and more importantly, influence bubble dynamics and the number of bubbles formed. Fortunately, the differences in these physical properties are trivially small in this instance.

5.3.4 Ultrasonic dosimetry in viscous media

As mentioned in section 5.2.3, it is unclear which effects of viscosity are dominant in determining rates of particle breakage. Some of the possible effects are not easy to probe empirically. One effect that can be investigated readily is the relative number of cavitating bubbles in different silicone oils. The relative number of events can be estimated using dosimetry to provide a quantitative comparison of the sonochemical yield. The sonochemical oxidation of iodide to triiodide (the Weissler reaction)[38-39] in aqueous solution is the most common example of sonochemical dosimetry. The decomposition of iron pentacarbonyl and radical trapping by diphenylpicrylhydrazyl have been used in organic media.[33, 40] Another common technique for ultrasonic dosimetry is observation of physical damage to a metal target.[41-42] Although these techniques are standard methods in the field, they have never been applied properly to study the effects of viscosity on ultrasound. The latter method, observation of physical damage to a metal target, was performed in order to see if there was a correlation between particle breakage and the suppression of cavitation by high viscosity.

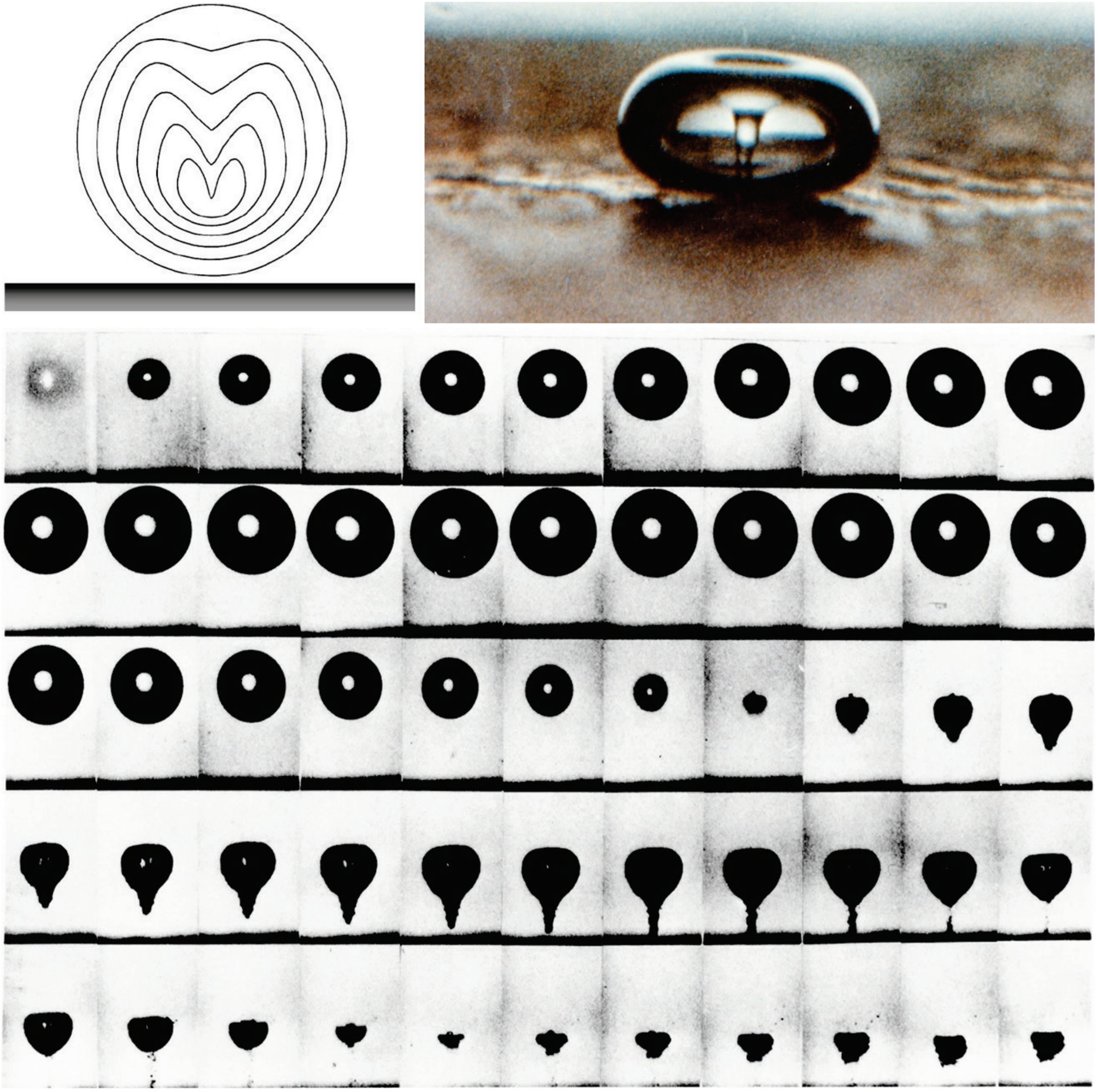

Figure 5.13 Asymmetric bubble collapse. Bubble collapsing at an extended surface. Top left: cartoon of bubble collapse, each line representing a successive time. Top right: photograph of microjet impinging on a surface. Bottom: evolution of asymmetric collapse captured at 75,000 frames per second.[43]

At extended surfaces (several times the bubble radius, ~200 µm at 20 kHz[27]) bubbles collapse asymmetrically, forming microjets that impinge on the surface.[44] This is the primary mechanism of action for ultrasonic cleaning of window blinds and a significant mechanism by which depth charges breach the hull of a submarine.[45] Figure 5.13 shows some photographs of asymmetric bubble collapse.

The microjet ejected from this asymmetric bubble collapse is responsible for surface damage and is the basis for the dosimetry presented here. Heavy duty aluminum foil (0.7 mil thick) supported on a stainless steel ring was used as the target. The target was attached to the support by epoxy and the support was fixed during sonication by a magnet. Silicone oils were sonicated for 1 minute in an ultrasonic bath before use to remove dissolved gasses. The relative number of cavitation events was estimated by counting the number of dimples observed on the foil target after sonication. Figure 5.14 shows the experimental configuration.

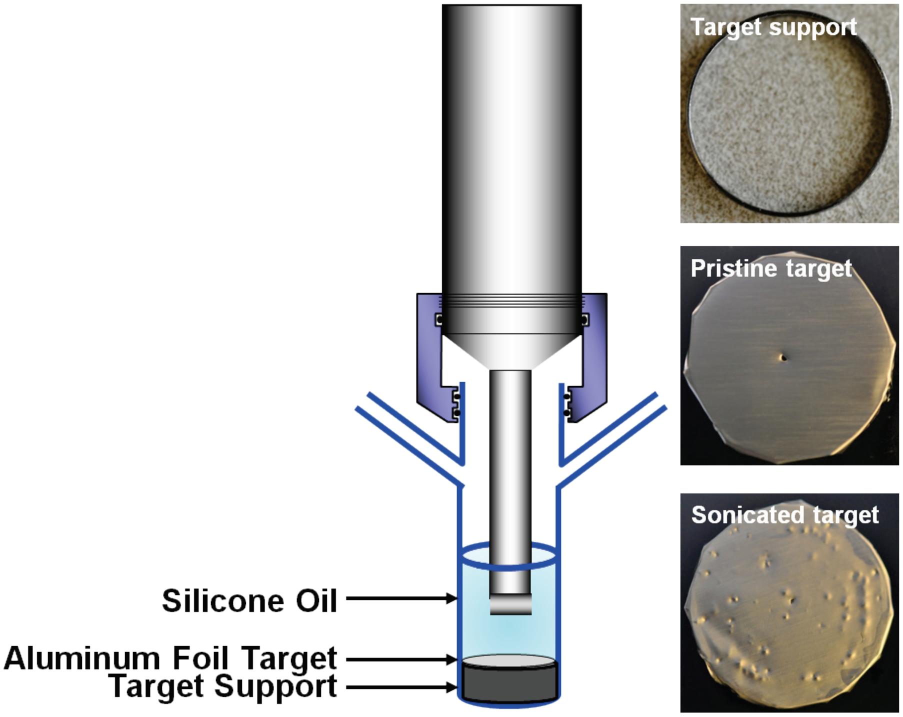

Figure 5.14 Experimental setup. Left: experimental schematic. The target support height can be varied by changing the number of support rings (which can stack). The support is fixed in place by a magnet below the cell. Right from top to bottom: stainless steel target support, pristine target, target after sonication. The hole in the center of the pristine target is introduced using a needle and allows air to escape so that there is no gas pocket under the foil.

Some optimization of this system was required before use. Some conditions can lead to complete destruction of the target and other conditions will lead to no detectable foil damage. Viscosity has a huge impact on which conditions cause which effects, so conditions that work well for one viscosity may be unworkable for others. The most important parameter is the distance between the horn and the target. The number of cavitation events is linear with time for short sonication times, but this is not expected to be true for longer sonication periods. The viscosity of silicone oils are extremely stable with respect to temperature compared to other liquids, but the effect is still non-trivial. It was preferred to use sonication parameters similar to those used for sonofragmentation experiments so that the temperature profile would be similar. Figure 5.15 illustrates the significance of temperature. Note that the linear relationship is on a logarithmic scale, corresponding to an exponential dependence.

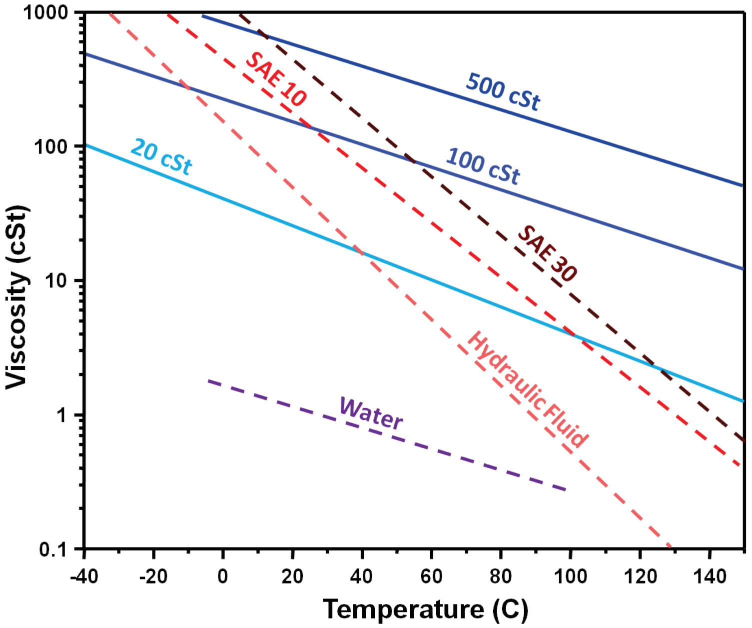

Figure 5.15 Effect of temperature on viscosity. Several silicone oils are compared to water, hydraulic fluid, and several motor oils. Data adapted from manufacturer's literature.[46]

Targets were sonicated at 30 W for 30 seconds. In this time frame the temperature of the more viscous silicone oils would increase by roughly 20 ºC. The target was held 2 cm from the horn tip, which was found to be a good distance for all viscosities of oil. The effect of changing the distance between the horn tip and the target was found to be small when varied between 8 and 18 mm at a sonication power of 30 W in dodecane. The shape of the cavitation zone is assumed to be roughly constant as the oil viscosity changes. It is known that this is dramatically not the case when changing intensity, so comparisons of intensity are not trivial.[35] Indeed, an attempt to compare the number of cavitation events at different intensities produced strange results.

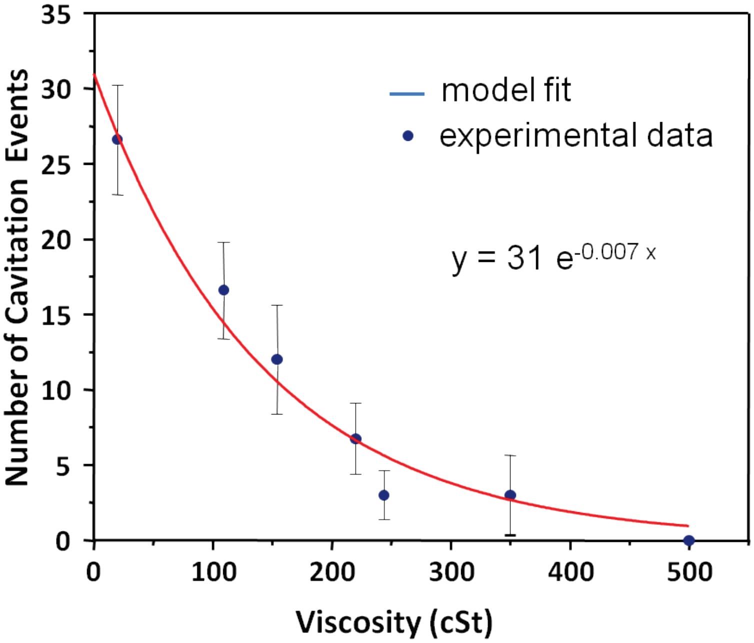

Figure 5.16 Effect of viscosity on cavitation. The number of cavitation events is shown as a function of silicone oil viscosity and fit to an exponential decay.

The number of cavitation events as a function of viscosity is shown in Figure 5.16. The cavitation damage drops off dramatically, until no cavitation at all is observed in 500 cSt silicone oil. The suppression of cavitation is described well as an exponential decay. This relationship was used in the population-balance modeling discussed in Section 5.3.5 in an effort to correlate it with rates of particle breakage.

5.3.5 Population-balance modeling

One desideratum was to begin to develop a quantitative understanding of the effects of high-intensity ultrasound on particle breakage. To this end a quantitative model was applied. Early attempts at modeling tried to simply predict the average particle size using Excel. Particles were broken in discrete time steps based on the simplistic assumptions that all particle breakage events resulted in the production of two particles of equal size and that particles broke as the result of interparticle collisions. Particles were binned based on size (all initial particles were placed in a bin corresponding to the average particle size and each successive bin was half the radius of the previous bin) and at each time step the probability of breakage was described by a recursive function:

$$X_t = X_{t-1} - k[(X_{t-1}\, r_x^2 f(x) + r_{x-1}^2\, X_{t-1}) - 2((X-1)_{t-1}\, r_{x-1}^2 f(x) + r_{x-1}^2\, (X-1)_{t-1})]/f(g)^2$$

where

$$f(x) = \Sigma(X_{t-1}\, r_x^2)$$

and

$$f(g) = \Sigma X_{t-1}$$

Here X_t was the population of a given size bin at a given time (and so X-1 is the next largest bin and X_{t-1} is the same bin in the time step before). The rate constant, or probability of a particle breaking, was k and assumed to be constant for a first approximation. The probability of breakage was assumed to depend on the probability of particle collision, which was acknowledged by the inclusion of an area term, r_x^2, where r_x indicates the radius of particles in bin X. The function $f(x)$ creates cross terms – the odds of a particle in a given bin colliding with particles in any other bin (based on population and cross sectional area).

The red part represents the destructive term: particles leaving the bin and moving into the next smallest bin. The odds of a particle in a bin colliding with other particles in the same bin is double counted, once in the $f(x)$ component and also explicitly because it could cause both particles to break. The green bit is the constructive term and comes from particles in the larger bin breaking to form two particles in the next smallest bin. Again, there is double counting to include the possibility of two particles in the same bin colliding and returning up to four particles. The very smallest bin does not have the terms in red text as those particles cannot break in the model and the very largest bin does not have the green text as there are no larger particles from which to populate the maximum bin.

The discrete time steps employed introduce a complication: the population of a bin does not change until the time step advances. This means that when a particle interacts with particles in one bin and breaks the model has no memory of this and allows the same particle to interact with particles in other bins and break more times. To address this overcounting problem the recursive function was divided by $f(g)^2$. This essentially makes it so only a fraction of available particles have a chance to interact with a fraction of each other bin. As a simplistic example, if there were ten bins each with one particle, each bin would have a 10% chance of interacting with any other specific bin. The term is squared because both the bin interacting and the bin being interacted with must be fractionated to allow realistic interaction with each other bin.

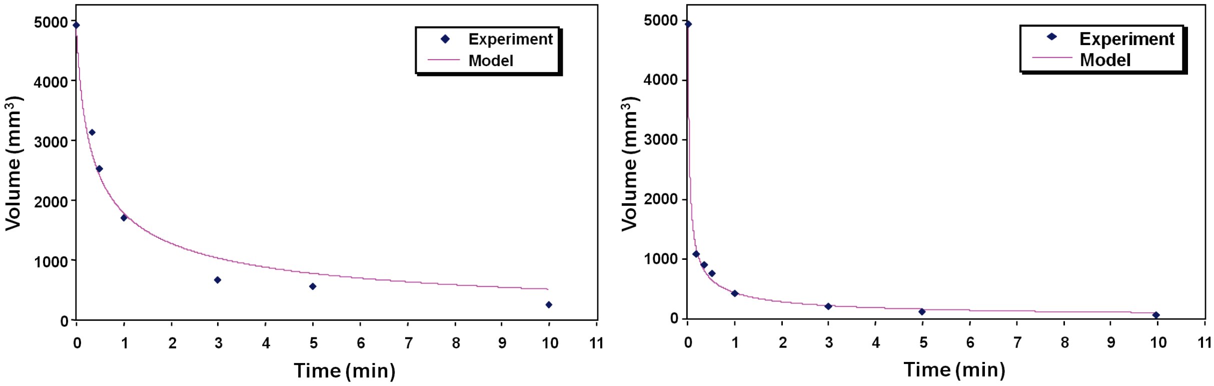

Figure 5.17 Modeling of sonofragmentation. Left: model applied to sonofragmentation at 10 W. Right: model applied to sonofragmentation at 30 W.

The rate constant, *k*, was optimized using the solver function in Excel. Figure 5.17 shows that the model fit remarkably well to the data at 30 W and moderately well to the data at 10 W. There are several significant problems with this model; however, mass is not conserved, and only average particle sizes are matched rather than particle size distributions. To overcome these observations a population balance model was applied, working in collaboration with the Braatz group. The bulk of mature versions of the population balance modeling was done by Michael Rasche in the Braatz group. Only an overview, therefore, will be given here with the aim of providing context to the empirical work presented earlier. The interested reader can find additional details elsewhere.[47]

Modeling was done using a quantitative 2-parameter model to describe the breakage behavior with the population balance equation (PBE) for binary breakage events,[48]

$$\frac{\partial}{\partial t}[n(t,m)] = \int_m^\infty S(u)b(m,u)n(t,u)du - S(m)n(t,m) \qquad (1)$$

where n is the number density function, *b* is the breakage function, *m* is the mass or the bin designation, *u* is the designation for bins larger than *m*, and *t* is the time. The dependency of the breakage rate, *S*, on crystal mass, *m*, ultrasonic intensity, *Π*, and viscosity, *η*, is assumed to be related to the number of cavitating bubbles and follow power-law,[48] proportionality,[49-50] and exponential (Figure 5.16) dependencies, respectively:

$$S(m) = S_0 \Pi \exp(-0.0069\eta) m^q, \qquad q \geq 0, \tag{2}$$

S_0 and q are used as fitting parameters, representing everything unknown about or not modeled in the system (effect of surface tension, vapor pressure, density, etc.), and the importance of particle mass, respectively. The simplifying assumption that crystals break in half is made,[51] yielding the breakage kernel, b:

$$b(m,u) = \begin{cases} 2, & u = 2m \\ 1, & u = 2m+1 \\ 1, & u = 2m-1 \\ 0, & \text{otherwise} \end{cases} \tag{3}$$

using a matrix method for the breakage update[52]

$$n(t_{j+1}) = n(t_j) A \tag{4}$$

Where A is a lower diagonal square matrix and $n(t_j)$ is a row vector.

Model parameters for trials using dodecane varying applied power and time were found to have values of $S_{0,opt} = 1.5 \times 10^{-4}$, and $q_{opt} = 0.52$. Confidence regions for these parameters indicate an uncertainty of <14% for q, and slightly larger for S_0.

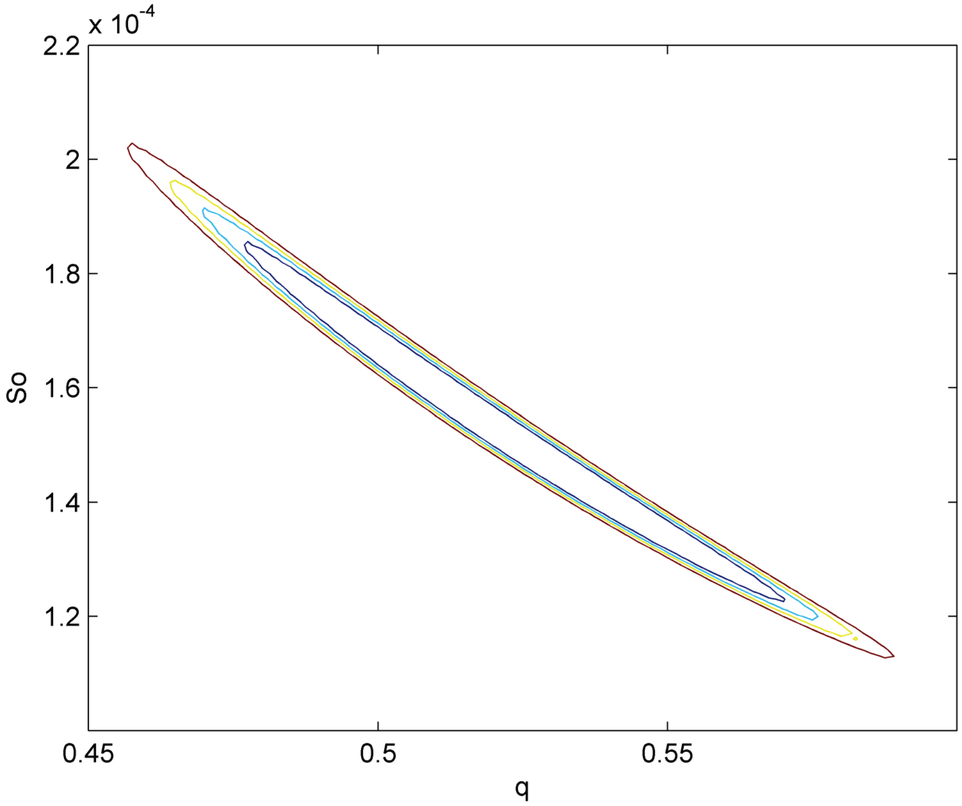

Figure 5.18. Confidence regions for parameters S_0 and q for the combined power and time trials.

The model with optimized parameters demonstrates reasonable agreement with experimental data (Figure 5.19), but in almost all cases overestimate the amount of breakage (the exception occurs at the shorter times for higher levels of intensity). In many cases the model fit is not stunning. There are a number of reasons for this. One is that the breakage assumption of binary events producing two identical smaller particles is simplistic, although that is probably a minor contributor. The limited size of the data set (~200 particles each) is fundamentally challenging for modeling. Further, the assumption that the number of cavitation events is linear with ultrasonic intensity probably breaks down badly at low and high ultrasonic power (near the cavitation threshold and where acoustic shielding become important, respectively), and may skew the optimization of model parameters.

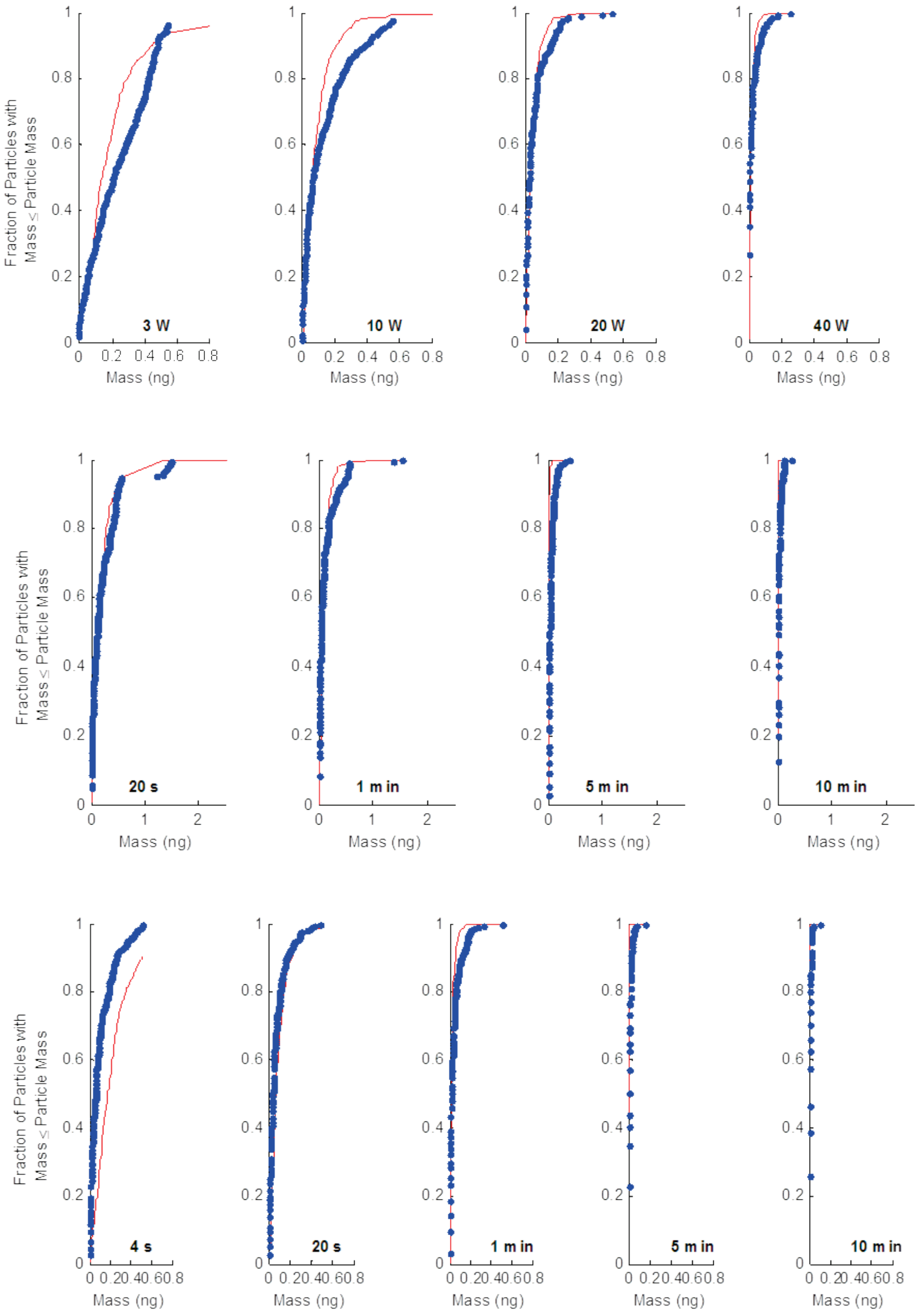

Figure 5.19 Population balance modeling. Experimental data (•) and simulation results (—) for trials of one minute for different ultrasonic intensity (top), trials of varying time for 10W intensity (middle), and trials of varying time for 30W intensity, (bottom).

Model parameters for the trials using silicone oils are found to be $S_{0,\text{opt}} = 8.8\times10^{-4}$, and $q_{\text{opt}} = 2.68\times10^{-12}$. Confidence regions show <1.5% uncertainty in the value of S_0 and imply that the optimal value for q is zero; i.e. for the viscosity trials, the breakage rate was not affected by the crystal mass.

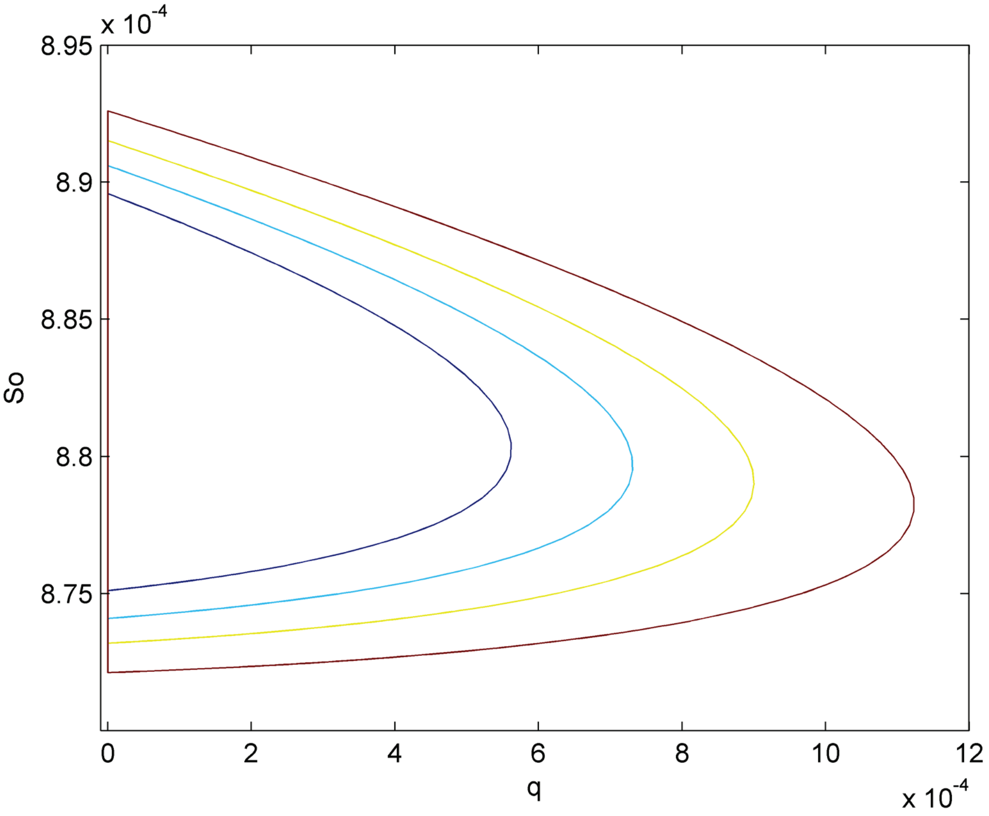

Figure 5.20. Confidence regions for parameters S_0 and q in the viscosity trials.

The model is in close agreement with the experimental data over the range of viscosities investigated. As expected, a larger viscosity inhibits cavitation and the breakage rate decreases. At the lowest viscosity, no crystals of mass greater than 1 ng were evident after 1 minute.

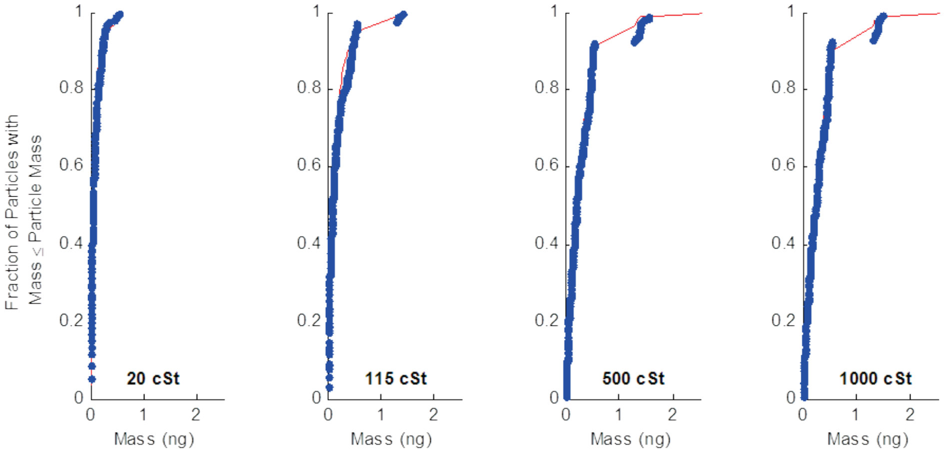

Figure 5.21. Experimental data (•) and simulation results (—) for trials of one minute using silicone oils of different viscosities.

5.4 Conclusions

In summary, ultrasonically-induced particle breakage exhibits strong dependences on sonication time, sonication power, and the viscosity of the liquid medium. At high viscosities (~300 cSt for aspirin sonicated at 30 W) particle breakage can be inhibited almost completely. Breakage rates decrease dramatically as particles get smaller. A 2-parameter population balance model can describe the breakage process and the influences of sonication time, sonication power, and liquid viscosity can be quantitatively extracted.

5.5 References

1. Li, H.; Wang, J.; Bao, Y.; Guo, Z.; Zhang, M., "Rapid sonocrystallization in the salting-out process." *J. Cryst. Growth* **2003,** *247*, 192.

2. Price, G. J.; Mahon, M. F.; Shannon, J.; Cooper, C., "Composition of Calcium Carbonate Polymorphs Precipitated Using Ultrasound." *Cryst. Growth Des.* **2010,** *11* (1), 39-44.

3. Gracin, S.; Uusi-penttila, M.; Rasmuson, Å. C., "Influence of Ultrasound on the Nucleation of Polymorphs of p-Aminobenzoic Acid." *Cryst. Growth Des.* **2005,** *5*, 1787-1794.

4. Ruecroft, G.; Hipkiss, D.; Ly, T.; Maxted, N.; Cains, P. W., "Sonocrystallization: The Use of Ultrasound for Improved Industrial Crystallization." *Org. Process Res. Dev.* **2005,** *9* (6), 923-932.

5. McCausland, L. J.; Cains, P. W.; Martin, P. D., "Use the power of sonocrystallization for improved properties." *Chem. Eng. Prog.* **2001,** *97* (7), 56-61.

6. Kordylla, A.; Koch, S.; Tumakaka, F.; Schembecker, G., "Towards an optimized crystallization with ultrasound: Effect of solvent properties and ultrasonic process parameters." *J. Cryst. Growth* **2008,** *310*, 4177-4184.

7. Guo, Z.; Jones, a. G.; Li, N.; Germana, S., "High-speed observation of the effects of ultrasound on liquid mixing and agglomerated crystal breakage processes." *Powder Technol.* **2007,** *171*, 146-153.

8. Devarakonda, S.; Evans, J. M. B.; Myerson, A. S., "Impact of Ultrasonic Energy on the Flow Crystallization of Dextrose Monohydrate." *Growth (Lakeland)* **2004,** *4*.

9. Abbas, A.; Srour, M.; Tang, P.; Chiou, H.; Chan, H.-K.; Romagnoli, J. A., "Sonocrystallisation of sodium chloride particles for inhalation." *Chem. Eng. Sci.* **2007,** *62*, 2445-2453.

10. Miyasaka, E.; Kato, Y.; Hagisawa, M.; Hirasawa, I., "Effect of ultrasonic irradiation on the number of acetylsalicylic acid crystals produced under the supersaturated condition and the ability of controlling the final crystal size via primary nucleation." *J. Cryst. Growth* **2006,** *289* (1), 324-330.

11. Dennehy, R. D., "Particle Engineering Using Power Ultrasound." *Org. Process Res. Dev.* **2003,** *7* (6), 1002-1006.

12. Wohlgemuth, K.; Kordylla, A.; Ruether, F.; Schembecker, G., "Experimental study of the effect of bubbles on nucleation during batch cooling crystallization." *Chem. Eng. Sci.* **2009,** *64*, 4155-4163.

13. Wohlgemuth, K.; Ruether, F.; Schembecker, G., "Sonocrystallization and crystallization with gassing of adipic acid." *Chem. Eng. Sci.* **2010,** *65*, 1016-1027.

14. Raman, V.; Abbas, A.; Zhu, W., "Particle grinding by high-intensity ultrasound: Kinetic modeling and identification of breakage mechanisms." *AIChE J.* **2011,** *57*, 2025-2035.

15. Raman, V.; Abbas, A., "Experimental investigations on ultrasound mediated particle breakage." *Ultrason. Sonochem.* **2008,** *15*, 55-64.

16. Teipel, U.; Leisinger, K.; Mikonsaari, I., "Comminution of crystalline material by ultrasonics." *Int. J. Miner. Process.* **2004,** *74*, S183-S190.

17. Teipel, U.; Mikonsaari, I., "Size Reduction of Particulate Energetic Material." *Propellants, Explos., Pyrotech.* **2002,** *27*, 168.

18. Wagterveld, R. M.; Boels, L.; Mayer, M. J.; Witkamp, G. J., "Visualization of acoustic cavitation effects on suspended calcite crystals." *Ultrason. Sonochem.* **2011,** *18*, 216-25.

19. Suslick, K. S.; Flannigan, D. J., "Inside a collapsing bubble: sonoluminescence and the conditions during cavitation." *Annu. Rev. Phys. Chem.* **2008,** *59*, 659-83.

20. McNamara, W. B.; Didenko, Y. T.; Suslick, K. S., "Pressure during Sonoluminescence." *J. Phys. Chem. B* **2003,** *107* (30), 7303-7306.

21. McNamara III, W. B.; Didenko, Y. T., "Sonoluminescence temperatures during multi-bubble cavitation." *Nature* **1999,** *401* (6755), 772.

22. Suslick, K. S.; Casadonte, D. J.; Doktycz, S. J., "Ultrasonic irradiation of copper powder." *Chem. Mater.* **1989,** *1* (1), 6-8.

23. Suslick, K. S.; Casadonte, D. J.; Green, M. L. H.; Thompson, M. E., "Effects of high intensity ultrasound on inorganic solids." *Ultrasonics* **1987,** *25* (1), 56-59.

24. Doktycz, S. J.; Suslick, K. S., "Interparticle collisions driven by ultrasound." *Science* **1990,** *247* (4946), 1067.

25. Suslick, K. S.; Doktycz, S. J., "The sonochemistry of zinc powder." *J. Am. Chem. Soc.* **2002,** *111* (6), 2342-2344.

26. Suslick, K. S.; Casadonte, D. J., "Heterogeneous sonocatalysis with nickel powder." *J. Am. Chem. Soc.* **1987,** *109* (11), 3459-3461.

27. Suslick, K. S.; Price, G. J., "Applications of ultrasound to materials chemistry." *Annual Review of Materials Science* **1999,** *29* (1), 295.

28. Prozorov, T.; Prozorov, R.; Suslick, K. S., "High Velocity Interparticle Collisions Driven by Ultrasound." *J. Am. Chem. Soc.* **2004,** *126* (43), 13890-13891.

29. Zeiger, B. W.; Suslick, K. S., "Sonofragmentation of Molecular Crystals." *J. Am. Chem. Soc.* **2011,** *133*, 14530-3.

30. Miyasaka, E.; Ebihara, S.; Hirasawa, I., "Investigation of primary nucleation phenomena of acetylsalicylic acid crystals induced by ultrasonic irradiation--ultrasonic energy needed to activate primary nucleation." *J. Cryst. Growth* **2006,** *295*, 97-101.

31. Hammond, R. B.; Pencheva, K.; Roberts, K. J.; Auffret, T., "Quantifying solubility enhancement due to particle size reduction and crystal habit modification: Case study of acetyl salicylic acid." *J. Pharm. Sci.* **2007,** *96* (8), 1967-1973.

32. Hammond, R. B.; Pencheva, K.; Roberts, K. J., "A Structural−Kinetic Approach to Model Face-Specific Solution/Crystal Surface Energy Associated with the Crystallization of Acetyl Salicylic Acid from Supersaturated Aqueous/Ethanol Solution." *Cryst. Growth Des.* **2006,** *6* (6), 1324-1334.

33. Suslick, K. S.; Gawienowski, J. J.; Schubert, P. F.; Wang, H. H., "Sonochemistry in non-aqueous liquids." *Ultrasonics* **1984,** *22* (1), 33-36.

34. Suslick, K. S.; Hammerton, D. A.; Cline, R. E., "Sonochemical hot spot." *J. Am. Chem. Soc.* **1986,** *108* (18), 5641-5642.

35. Hopkins, S.; Putterman, S.; Kappus, B.; Suslick, K.; Camara, C., "Dynamics of a Sonoluminescing Bubble in Sulfuric Acid." *Phys. Rev. Lett.* **2005,** *95* (25), 2-5.

36. Majumdar, S.; Kumar, P. S.; Pandit, a. B., "Effect of liquid-phase properties on ultrasound intensity and cavitational activity." *Ultrason. Sonochem.* **1998,** *5* (3), 113-8.

37. http://www.univarusa.com/vwr-inc/tools.nsf/bb56593a79a8632f88256e36002aa68b!OpenView&Start=130.

38. Gutierrez, M.; Henglein, A.; Ibanez, F., "Radical scavenging in the sonolysis of aqueous solutions of iodide, bromide, and azide." *The Journal of Physical Chemistry* **1991,** *95* (15), 6044-6047.

39. Morison, K. R.; Hutchinson, C. A., "Limitations of the Weissler reaction as a model reaction for measuring the efficiency of hydrodynamic cavitation." *Ultrason. Sonochem.* **2009,** *16* (1), 176-183.

40. Suslick, K. S.; Gawienowski, J. J.; Schubert, P. F.; Wang, H. H., "Alkane sonochemistry." *The Journal of Physical Chemistry* **1983,** *87* (13), 2299-2301.

41. Kanthale, P., "Cavity cluster approach for quantification of cavitational intensity in sonochemical reactors." *Ultrason. Sonochem.* **2003,** *10* (4-5), 181-189.

42. Virone, C.; Kramer, H. J. M.; Rosmalen, G. M. V.; Stoop, A. H.; Bakker, T. W., "Primary nucleation induced by ultrasonic cavitation." *J. Cryst. Growth* **2006,** *294*, 9-15.

43. Lauterborn, W.; Hentschel, W., "Cavitation bubble dynamics studied by high speed photography and holography: part one." *Ultrasonics* **1985,** *23* (6), 260-268.

44. Blake, J. R.; Keen, G. S.; Tong, R. P.; Wilson, M., "Acoustic cavitation: the fluid dynamics of non-spherical bubbles." *Philosophical Transactions of the Royal Society A: Mathematical, Physical and Engineering Sciences* **1999,** *357* (1751), 251-267.

45. Brennen, C. E., *Cavitation and bubble dynamics*. Oxford University Press: New York, NY, 1995; p 74.

46. Dow Corning technical support. 2010. Personal Communication.

47. Rasche, M. Masters thesis, University of Illinois at Urbana-Champaign, 2010.

48. Tan, H. S.; Salman, A. D.; Hounslow, M. J., "Kinetics of fluidised bed melt granulation IV . Selecting the breakage model." *Powder Technol.* **2004,** *144*, 65 - 83.

49. Colussi, a. J.; Hung, H.-M.; Hoffmann, M. R., "Sonochemical Degradation Rates of Volatile Solutes." *J. Phys. Chem. A* **1999,** *103*, 2696-2699.

50. Son, Y.; Lim, M.; Khim, J., "Investigation of acoustic cavitation energy in a large-scale sonoreactor." *Ultrason. Sonochem.* **2009,** *16*, 552-6.

51. Rasche, M.; Zeiger, B. W.; Suslick, K. S.; Braatz, R. D., "“Mathematical Modelling of the Evolution of the Particle Size Distribution during Ultrasound-Induced Breakage.” " *Chem. Eng. Sci.* (submitted).

52. Broadbent, S. R.; Callcott, T. G., "A Matrix Analysis of Processes Involving Particle Assemblies." *Philosophical Transactions of the Royal Society A: Mathematical, Physical and Engineering Sciences* **1956,** *249*, 99-123.

Chapter 6
Mechanisms of Sonofragmentation

The effects of high-intensity ultrasound on molecular crystals were examined in detail in Chapter 5, including an effort to quantify the importance of various parameters. The mechanism of action, however, was not explored, although some assumptions about the mechanism were made for the purposes of modeling. This chapter explores mechanisms of sonofragmentation and justifies the assumption of first-order kinetics made during modeling.

6.1 Introduction

Developing processes for the production of active pharmaceutical ingredients (APIs) with a specific crystal size or polymorph distribution is critical for improved drug delivery by aerosolization, injection, or ingestion, for control of bioavailability, and for economy of preparation.[1-2] The use of ultrasound for the crystallization of APIs has attracted substantial recent attention[3-6] due to (1) its influence on particle size and size distribution,[7] (2) reduction of metastable zone-width, induction time, and supersaturation levels required for nucleation,[8-10] (3) improved reproducibility of crystallization,[11] (4) control of polymorphism,[12] and (5) reduction or elimination of the need for seed crystals or other foreign materials.[13]

Particle size distributions are very important in the preparation of APIs, as they are directly related to dissolution rate and bioavailability. Adjustment of particle size after crystallization by techniques such as grinding are often ineffective, are time and energy intensive, and can introduce impurities or defects.[14] Alternatively, particle size can be influenced during crystallization by adjusting the number of nuclei formed in the initial stages of crystal growth: the more nuclei, the smaller the final crystals.[15-16] Ultrasound provides a facile method to control the number of nucleation sites created during crystallization.[17] The size distribution of the final crystals is a function both of the primary nucleation rate of the system (from disparity in ripening times among particles) and of the rate of crystal fragmentation from sonication. An example of such sonofragmentation is shown in Figure 6.1.

The effects of ultrasound arise from acoustic cavitation: the formation, growth, and implosive collapse of bubbles coupled to the ultrasonic field. The rapid, nearly adiabatic implosion of a bubble results in intense local heating and high pressures — on the order of 5000 K and 1000 bar for multi-bubble cavitation — with heating and cooling rates $>10^{10}$ K/sec.[18-20] The collapsing bubble emits a shockwave that, in water, has pressures up to 60 kbar and velocities on the order of 4000 m/sec.[21] At extended surfaces bubbles collapse asymmetrically, creating microjets that can cause pitting or generate shear forces.[22] Enhanced mass transport, emulsification, and bulk heating also result with often interesting chemical consequences.[23-27]

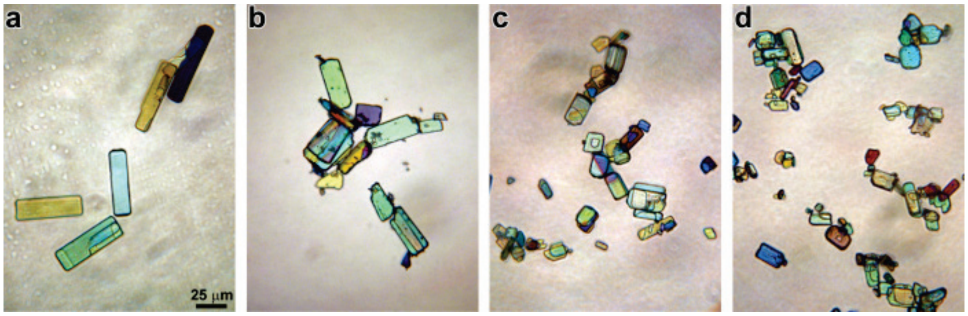

Figure 6.1 Cross-polarized optical micrographs showing the sonofragmentation of aspirin crystals. (a) before sonication, (b) after 1 min sonication, (c) after 3 min sonication, and (d) after 10 min sonication. Sonication using a 1 cm^2 titanium horn immersed in a 2 wt% slurry in dodecane at 10 W, 20 kHz. All images at the same magnification.

Although there have been a variety of empirical investigations into the phenomenon of sonocrystallization, the nucleation mechanism remains poorly understood and experimental reports have offered contradictory results. For example, high-speed photography has suggested that ice sonocrystallized from supercooled water is the result of pressure changes associated with emitted shockwaves,[28-29] whereas other work shows that bubbles can act as nucleation sites.[30] It has also been proposed that crystallization is expedited by increased supersaturation from diffusion of the API into heated liquid regions surrounding the collapsing bubble followed by rapid heat dissipation.[31]

Particle breakage after the initial crystallization event affects average particle sizes and size distributions both through reducing the size of existing crystals and by creating secondary nucleation sites. There is a thorough body of work on the effects of ultrasound on heterogeneous mixtures involving inorganic solids. Experiments with metal particles conclusively show the effects of interparticle collisions, resulting in particle agglomeration, smoothing of surfaces, and removal of surface-passivating oxide coatings.[26, 32-39] In contrast, the literature on the effects of ultrasound on molecular crystals is modest.

Fragmentation of molecular crystals during ultrasonic irradiation plays a central role in the process of sonocrystallization, and interparticle collisions are generally emphasized as the origin of sonofragmentation.[40-43] The markedly different properties of molecular crystals compared to metallic particles (e.g., friability vs. malleability, density, tensile strength, melting point), however, should lead one to closer examination of alternative possible mechanisms of fragmentation for molecular crystals. In fact, very early work in this area suggested that interparticle collisions *were not* important in the rates of particle breakage of ceramic particles[44] or of dispersion of aggregates,[45] although no effort was made to distinguish among other possible breakage mechanisms and these results received no notice in the field of sonochemistry.

There are four proposed classes of possible mechanisms for sonofragmentation: interparticle collisions, horn-particle collisions, particle-wall collisions, or particle-shockwave interactions. Microjets from asymmetric bubble collapse are not expected at the surface of particles below ~200 μm,[26] but they could be significant contributors to the particle-shockwave mechanism for systems involving larger particles. The experiments described in this chapter indicate that interparticle collisions, in fact, are not a major contributor to particle breakage and that direct particle-shockwave interactions are implicated as the primary pathway.

6.2 Experimental

Materials and equipment. Dodecane (Reagent Plus, ≥99%), 1,10-dibromodecane (Fluka, >95%), and glacial acetic acid (Fisher Scientific) were used as-received. Aspirin (acetylsalicylic acid, Aldrich, 99%) was recrystallized from acetic acid.

Sonications were performed at 20 kHz with a Sonics and Materials horn (VCX-750 for experiments at 10W or above, VCX-600 for experiments below 10W) with a 1 cm^2 diameter titanium horn. The sonicated solutions were thermostated with an Isotemp 1006S water bath. Ultrasonic intensities were calibrated by calorimetry with water.

Imaging and Analysis. Particles were imaged using a Canon PC1015 digital camera attached to a Zeiss Axioskop optical/fluorescence microscope with polarization analyzer and manually sized with the aid of a public-domain image processing program, ImageJ (available through NIH). The graphs are expressed in terms of particle volumes (with the assumption of an average spherical radius based on measured area of the micrograph projection). Each data point represents the average of approximately 200 particles. Comparisons of particle volume emphasize the larger particles which are of greater interest because they represent the majority of the mass of the API.

Sonocrystallization of aspirin. The sonocrystallization procedure was described in Chapter 4. In a typical experiment 6.71 g of aspirin were dissolved with stirring in 40.0 ml of acetic acid at 45 °C. The solution was supersaturated by cooling to 20 °C and the solution was sonicated at 10 W for 15 seconds to induce crystallization. Crystals were allowed to ripen for 24 hours and isolated by filtration and vacuum drying.

Sonofragmentation of aspirin. All sonication experiments apart from the initial crystallization were performed under a 20% duty cycle (a repeating cycle of 2 seconds ultrasound on, 8 seconds ultrasound off) in order to reduce temperature variation, although viscosity and vapor pressure experiments shown in Chapter 5 indicate that temperature variation is probably not a significant factor. After sonication, aliquots were removed by disposable pipette for analysis by optical microscopy. In all cases, sonications were done at low power and for short times to ensure that fragmentation was not taken beyond easily measured sizes during the times of the experiments and that no threshold behavior in the particle breakage was occurring (i.e., particles becoming so small that significant breakage ceased).

Loading experiments were performed by suspending varying amounts of aspirin crystals in 5 ml dodecane followed by ultrasound treatment for 10 seconds total ultrasonic exposure at 5.5 W.

Particle-horn decoupling experiments were achieved by placing a slurry (0.08 g in 4 ml) in a 4 ml vial held directly below the horn with a flexible membrane. The base of the vial was cut off and replaced with a nitrile latex membrane to allow better penetration of the ultrasonic field while at the same time isolating the aspirin crystals from direct contact with the ultrasonic horn. Ethylene glycol was used as the coupling fluid outside the vial to provide for transmission of the ultrasound from the horn into the vial contents with minimal energy loss to cavitation in the transmission medium. 1,10-dibromodecane was used as the suspending liquid in place of dodecane: the aspirin crystals were insoluble in both liquids, but due to its density 1,10-dibromodecane provided a much better suspension of the aspirin crystals without settling. These experiments were performed at 27 °C, slightly above the melting point of the 1,10-dibromodecane.

Particle-wall decoupling experiments used a latex membrane (Trojan™ non-lubricated condom, washed with water and ethanol and air-dried) placed around the slurry to protect particles from hitting the glass reactor wall (Figure 6.5). A total of 8.0 ml of dodecane was required in order to adequately fill the membrane and the surrounding reaction cell; 3.0 ml filled the area between the membrane and the horn, the other 5.0 ml was outside the membrane. 0.030 g aspirin was loaded into the membrane and compared to an experiment with 0.080 g aspirin in 8.0 ml of dodecane with no membrane.

The contributions of particle-wall and particle-horn collisions were additionally explored by employing sonication reactors of varying volumes, while holding the particle concentration constant at 0.01 g/ml and the horn immersion depth constant at 0.8 cm. Reactor cells with radii of 1, 1.5, 2, and 2.3 cm were used with corresponding liquid volumes of 5, 13, 27, and 30.5 ml of dodecane. Sonications were performed at 10 W for 30 seconds total ultrasonic exposure time.

6.3 Discussion

Sonocrystallized aspirin suspended in dodecane (in which aspirin has no solubility) was used as a model system. Particle sizes were measured by direct image analysis of optical micrographs and are expressed in terms of volumes of an equivalent sphere. The particle volume measurement emphasizes the larger particles, which are measurable with higher precision and are of greater interest because they represent the majority of the mass of the API.

There are four possible mechanisms for sonofragmentation that must be addressed: particle-horn collisions, particle-wall collisions, particle-particle collisions, and direct particle-shockwave interactions. High-speed photography has shown that particles can break through direct contact with the horn[30] and also that agglomerates can be dispersed directly by clouds of cavitating bubbles.[46] In order to determine which of these four proposed mechanisms dominates, experiments were performed to protect the particles from the wall or from the horn and to differentiate particle-particle and particle-shockwave interactions.

6.3.1 Particle-horn decoupling

Particle-horn collisions were eliminated as a possibility by sequestering the slurry in a 4-ml vial with a thin membrane to separate the slurry of aspirin from direct contact with the ultrasonic horn (Figure 6.2). 1,10-dibromodecane was used to slurry the aspirin powder both because it does not dissolve aspirin and because it has a good density match with aspirin (1.40 g/cm^3 for aspirin, 1.34 g/cm^3 for 1,10-dibromodecane versus 0.75 g/cm^3 for dodecane). The horn was positioned 1 mm above the membrane and the horn surface and the membrane surface were parallel with one another. Direct contact between the horn and the membrane would lead to rupture of the membrane.

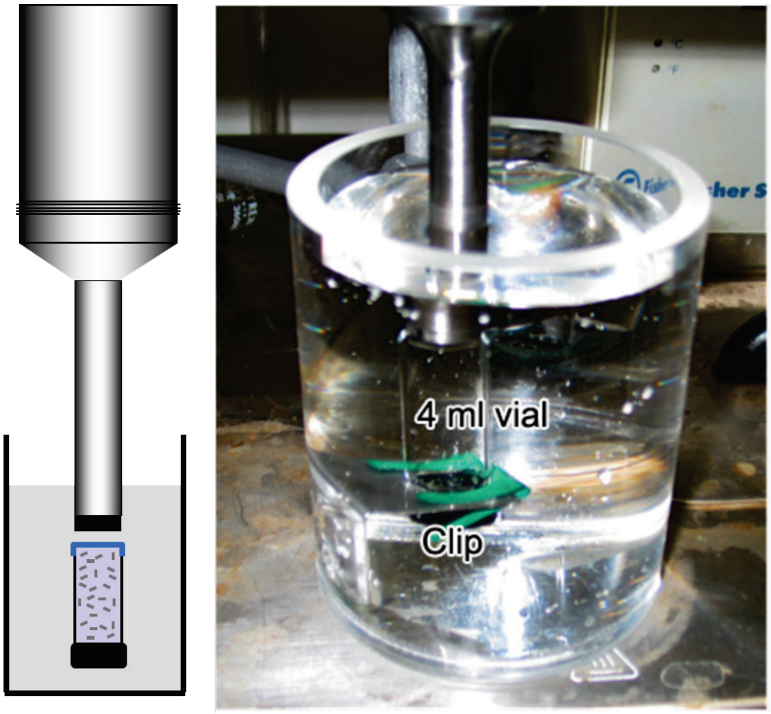

Figure 6.2 Particle-horn decoupling. Vial contains a slurry of 1,10-dibromodecane and aspirin. Outside of the vial ethylene glycol serves as the carrier medium for the ultrasonic field, and a nitrile latex membrane (blue) separates the slurry from the carrier medium. Left: cartoon of entire setup. Right: photograph of experimental setup except that the vial contains only liquid (no particles) and has a solid glass bottom instead of a membrane.

It was necessary to use 1,10-dibromodecane in place of dodecane because of the attenuation of ultrasonic power by the membrane and because the average distance between the horn and particles was greater. Sonicating aspirin particles in dodecane would result in the particles setting, unperturbed, in the vial cap. It was necessary to evaluate several membranes prior to the experiment to ensure that the ultrasonic wave was penetrating into the slurry. This was accomplished by chemical dosimetry using the Weissler reaction. The vial was filled with a 0.10 M solution of sodium iodide and sonicated. The following chemical reactions occur in an aqueous iodide solution:[47-48]

$$H_2O \xrightarrow{)))} H\cdot + \cdot OH$$

$$I^- + \cdot OH \longrightarrow I + {}^-OH$$

$$I^- + I \longrightarrow I_2^-$$

$$2I_2^- \longrightarrow I_2 + 2I^-$$

$$I_2 + I^- \longrightarrow I_3^-$$

The formation of triiodide is accompanied by a change in absorption spectrum and can be used to quantify the sonochemical yield. There are additional reactions occurring simultaneously; most relevant is the reduction of triiodide to iodide by hydrogen peroxide in neutral or basic media.

$$2\,\cdot OH \longrightarrow H_2O_2$$

$$H_2O_2 + I_3^- \rightleftharpoons O_2 + 2H^+ + 3I^-$$

This back reaction was inhibited by working in a slightly acidic phosphate buffer solution (0.10 M, pH 5.8).

It was observed that the bottom of the glass vial would reflect the ultrasonic wave so much that no cavitation could be detected by this dosimetric method. Even thinning the glass was insufficient and also led to the bottom of the vial frequently breaking. It was necessary to completely remove the bottom of the vial and replace it with a thin membrane. A variety of membranes were tried, with nitrile latex being the most effective. Figure 6.3 compares the sonochemical yield through the nitrile latex membrane to the sonochemical yield under direct horn immersion. Significant attenuation of the ultrasonic field is evident, but there is readily measurable cavitation. This membrane scheme was used for sonofragmentation, with the aspirin/1,10-dibromodecane slurry replacing the iodide solution.

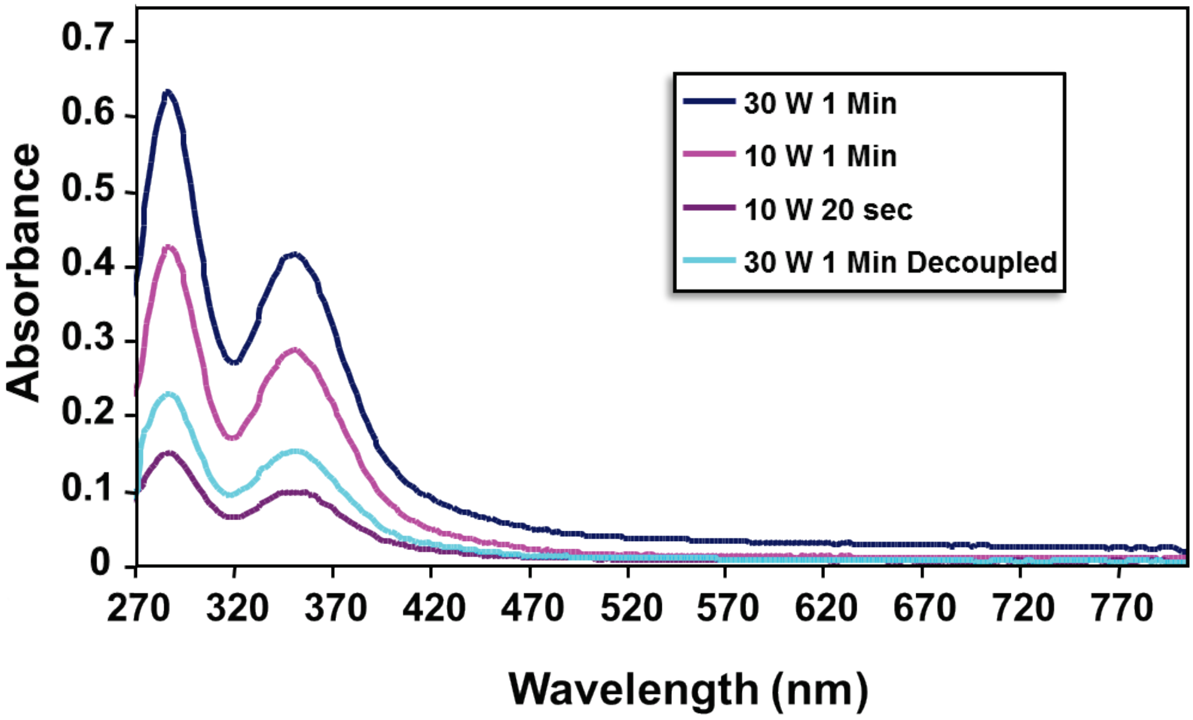

Figure 6.3 Oxidation of sodium iodide. Triiodide absorbance from sonication of aqueous NaI, 0.10 M NaI, and 0.10 M Phospate buffer (pH 5.8). Teal line is iodide oxidized through membrane, other lines are from oxidation while the horn is directly immersed in the solution.

As can be seen in Figure 6.4, aspirin particles broke readily, even in the absence of direct contact between the aspirin slurry and the ultrasonic horn. The comparable experiment of sonicating aspirin in 1,10-dibromodecane in a standard reactor is shown for reference, but making a quantitative comparison has limited value because the membrane significantly attenuates the ultrasonic intensity and because there is a greater average distance between the slurry particles and the horn in the vial compared to direct horn immersion. Regardless, Figure 6.4 shows that particle-horn collisions are not the dominant mechanism of particle breakage.

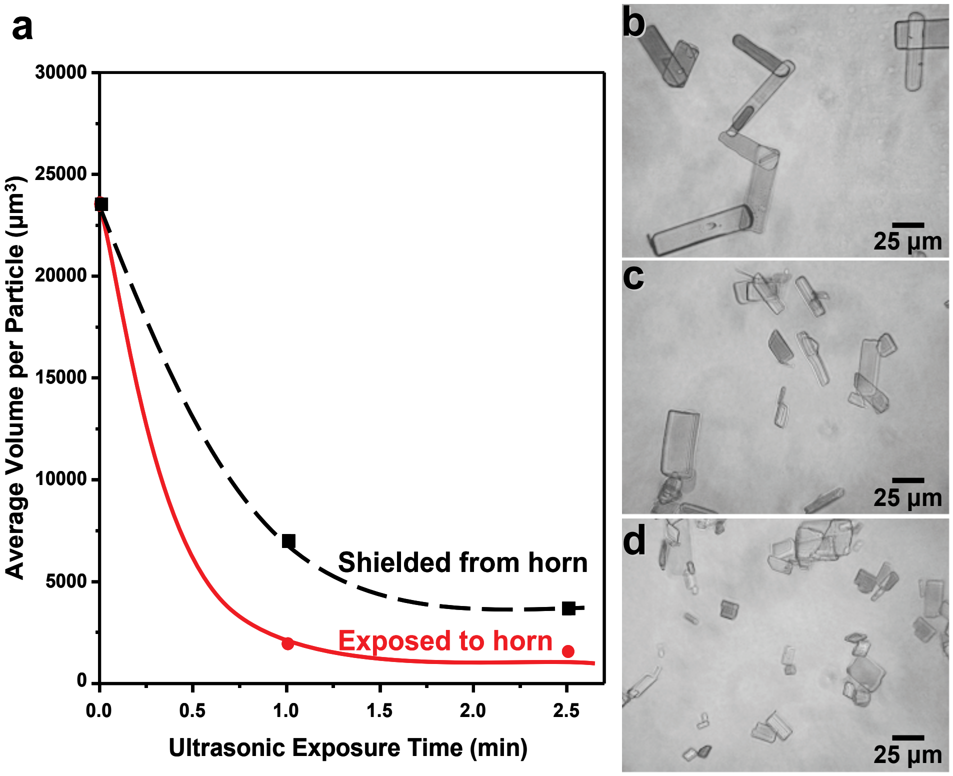

Figure 6.4 Particle-horn decoupling. (a) Comparison of particle breakage between particles able to collide directly with the ultrasonic horn (solid red line) vs. particles exposed to ultrasound but shielded from direct contact with the horn (dashed black line). Horn output is 30 W. (b) Optical micrograph of particles before sonication. (c) Particles isolated from direct horn contact after 1 minute of sonication. (d) Particles exposed to horn after 1 minute of sonication.

6.3.2 Particle-wall decoupling

It is similarly demonstrable that particle-wall collisions are not the primary breakage mechanism by using a flexible latex membrane to contain the slurry without direct contact with the outer rigid glass reactor wall. This flexible cell was immersed in dodecane inside a glass container, as diagrammed in Figure 6.5, so that acoustic reflection off the glass wall would still occur and the system would be perturbed as little as possible.

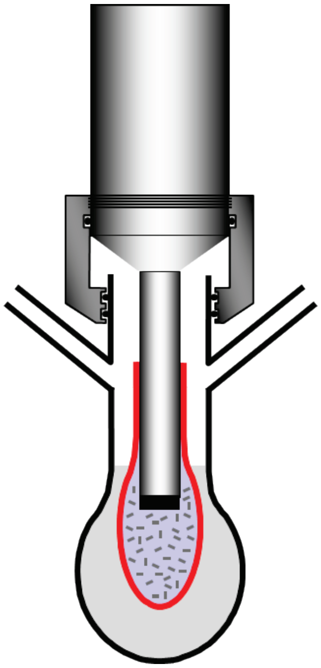

Figure 6.5. Particle-cell decoupling. A latex barrier (red) prevents particles from hitting the glass cell wall. The slurry is suspended in dodecane, and the space between the membrane and the reactor is filled with dodecane.

The difference between particle breakage in a flexible cell versus a rigid walled container is shown in Figure 6.6. The higher rate of breakage observed in the flexible cell is due to the closer proximity to the horn (and hence the cavitation zone) of the aspirin suspension within the membrane. It was necessary to keep sonication times short in this experiment because the horn had a tendency to tear the membrane and shorter experiment times caused this to occur less frequently. The fact that particles are held in closer proximity to the horn during particle-cell decoupling means that it is again unfeasible to make a quantitative assertion about the contribution of particle-cell interactions. It can be stated that particle-cell interactions do not dominate the kinetics of particle breakage.

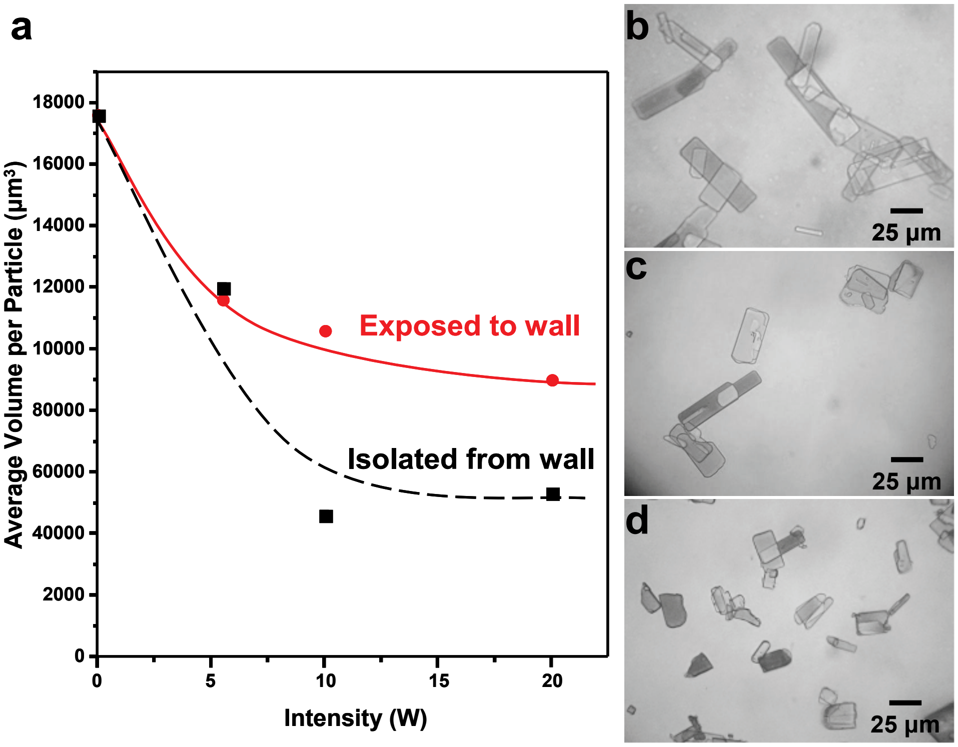

Figure 6.6 Particle-cell decoupling. (a) Comparison of particle breakage between particles in a rigid container (solid red line) and in a flexible cell (dashed black line) for an ultrasonic exposure of 30 s. (b) Optical micrograph of particles before sonication. (c) Particles in rigid container sonicated at 20 W for 30 s. (d) Particles in flexible cell sonicated at 20 W for 30 s.

6.3.3 Effect of reactor size

The insignificance of particle-wall and particle-horn collisions is further supported by varying the size of the reactor (Figure 6.7). Figure 6.8 shows that increasing the reactor size has only a modest effect (~30%) on the final particle size even though the ratio of slurry volume to horn area increases by more than 6-fold and the distance from the horn to the reactor wall more than doubles. The minor change in final particle size is primarily due to dilution, since the size of the cavitation zone is constant.

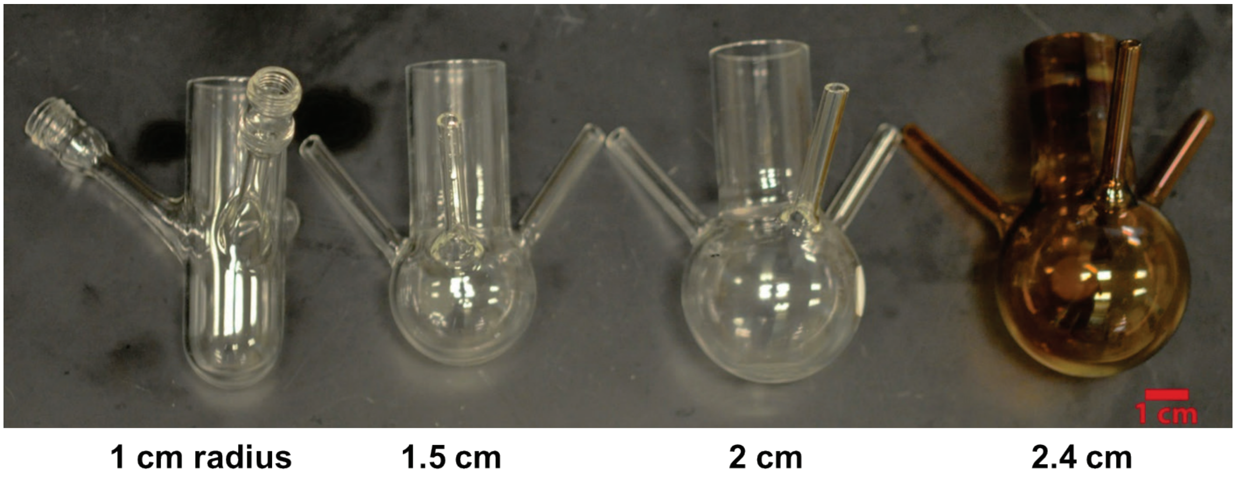

Figure 6.7 Different sonication vessels used.

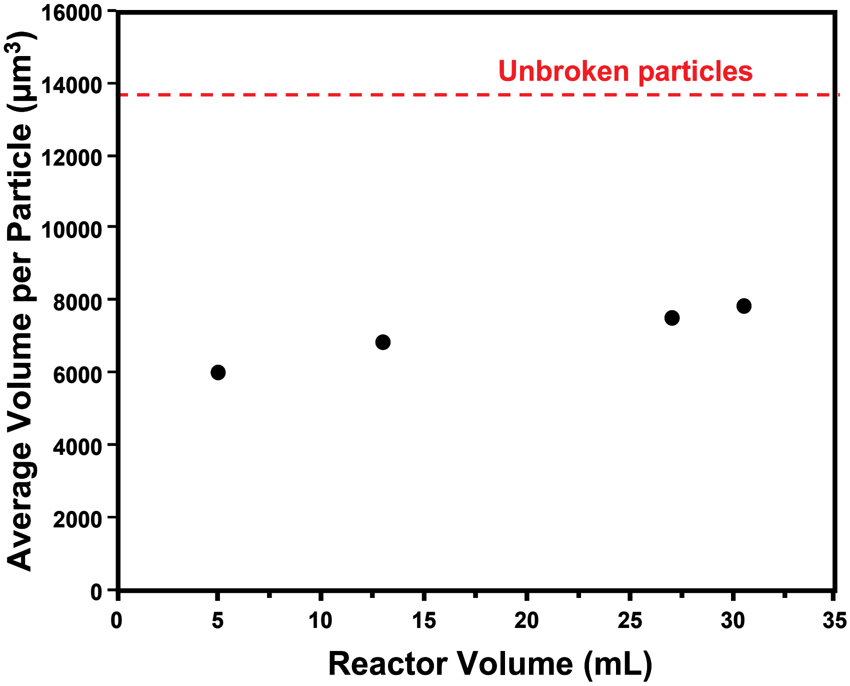

Figure 6.8 Effect of changing reactor size on particle size after sonication. The reactor volume increases over a six-fold range and the ultrasonic horn to reactor wall distance changes from 1.0 to 2.4 cm. Particles were suspended in dodecane with a loading of 0.01 g/ml and sonicated for 30 seconds at 10 W.

6.3.4 Particle-particle versus shockwave-particle interactions

The importance of interparticle collisions versus particle-shockwave interactions was evaluated by observing the effect of particle concentration on final particle size. It is not easy to decouple these mechanisms in the same way as the particle-horn or particle-cell interactions. Instead, a kinetics experiment was performed.

If the rate of particle fragmentation (dN/dt) were strictly first order in particle concentration (that is, dependent solely on particle-shockwave interactions with no contribution from particle-particle collisions), then the average particle size after a given ultrasonic exposure time (τ) would be zero order in concentration of particles (i.e., N, the "loading" of the slurry). In contrast, if the rate of fragmentation were dominated by interparticle collisions, $\mathrm{d}N/\mathrm{d}t$ would be second order in N, and the particle size would be linearly related to N. Figure 6.9 illustrates the two proposed mechanisms being compared here and justification for the assertions made in this paragraph follow.

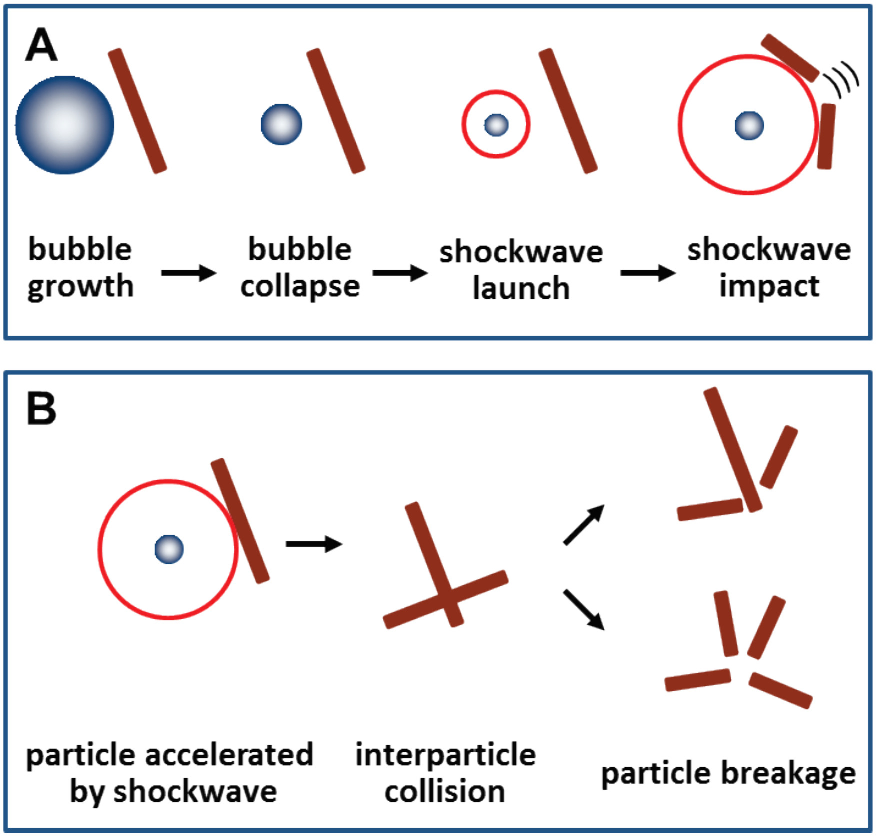

Figure 6.9 Particle-shockwave mechanism versus particle-particle collision mechanism. A: particle-shockwave interaction. Particles interact exclusively with shockwave events (although not necessarily only one particle broken per shockwave). The pressure front creates a differential acceleration that overcomes cohesive forces and breaks the particle. B: Particles are accelerated by the shockwave but are not broken until they collide with another particle. Collisions can cause one, both, or neither particle to break. The probabilities of 0, 1, or 2 breakage events will be reflected in the rate constant of the process.

The average particle volume or size (*S*) is the total particle volume (*V*) divided by the total number of particles (N):

$$S = \frac{V}{N} \tag{1}$$

The total particle volume is conserved while the total number of particles is the initial number of particles plus the number of additional particles formed by fragmentation (a binary breakage event creating 2 pieces out of 1 original particle is considered to have formed 1 new particle):

$$N_{total} = N_{initial} + N_{formed} \tag{2}$$

The rate of particle breakage depends on the breakage mechanism. There are two cases to consider: **(A)**, the assumption that the rate of particle breakage is dependent only on shockwave formation and therefore does not depend on interparticle collisions versus **(B)**, the assumption that the rate of particle breakage is dominated by interparticle collisions and is therefore second order in particle concentration. Both cases assume a fixed number of cavitation events and that mixing is equally efficient in all cases.

(A) Fragmentation model independent of interparticle collisions. If the particle breakage rate does not depend on interparticle collisions, then the particle formation rate (*dN*) can be described as a function of ultrasonic exposure time (*dt*) and a rate constant, k_1, by a first-order differential equation.

$$dN = k_1 \cdot N \cdot dt \tag{3}$$

When integrated there is a linear relationship between the initial and final numbers of particles for a given ultrasonic exposure time (τ).

$$N_{final} = N_{initial} \cdot e^{k_1 \tau} \tag{4}$$

Because V (the total volume of all particles) is constant, it can be expressed as $S_{initial} \cdot N_{initial}$, so combining equation 4 with equation 1 gives a function for the average particle size (S) that is independent of loading:

$$S = S_{initial} \cdot e^{-k_1 \tau} \tag{5}$$

(B) Fragmentation model dominated by interparticle collisions. If the rate of particle breakage is dominated by interparticle collisions as the source of fragmentation, then it will be second order in particle concentration, and the rate equation depends on a different rate constant, k_2, and integrates to equation 6.

$$\frac{1}{N_{initial}} - \frac{1}{N_{final}} = k_2 \cdot \tau \tag{6}$$

Solving for N_{final} and inserting it into equation 1 to express the relation in terms of particle size gives equation 7.

$$S = S_{initial}\big(1 - (N_{initial} \cdot k_2 \cdot \tau)\big) \tag{7}$$

Equation 7 is not quite correct because it assumes that the rate of breakage is independent of the particle size. In reality the breakage rate at higher loadings (i.e., larger N) would increase less dramatically than predicted because breakage efficiency decreases as fragmentation occurs. We should, however, still expect a strong fragmentation-rate dependence on loading, especially for lower loadings. The observed effect of varying the number of initial particles, shown in Figure 6.10, clearly shows essentially no dependence of average particle size on loading: *interparticle collisions do not dominate the mechanism of sonofragmentation.*

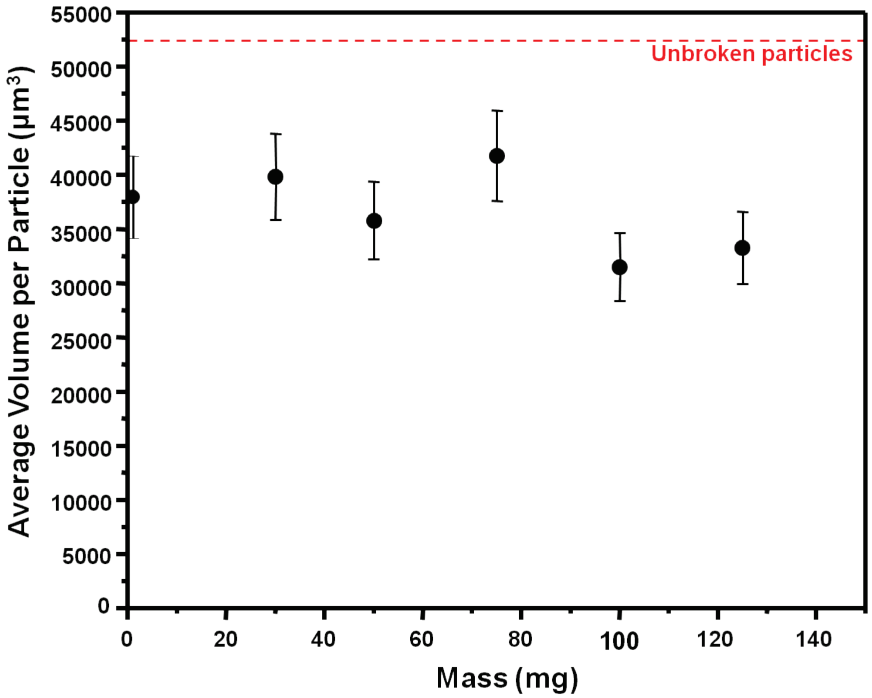

Figure 6.10 Effect of particle loading on final particle size. After sonication for 10 seconds at 5.5 W. All masses are suspended in 5 ml of dodecane. Errors estimated as 10% of particle size based on standard deviation of similar measurements.

6.4 Conclusions and caveats

In summary, particle loading studies of molecular crystals demonstrate that sonofragmentation is independent of slurry concentration, which rules out particle-particle collisions as an important breakage mechanism. This result is in stark contrast with metal powder slurries, where particle-particle collisions are predominantly responsible for the chemical and physical effects of sonication.[38-39] The shift in dominant mechanisms between sonication of metal powders vs. aspirin slurries highlights the differences in properties between malleable metallic particles and friable molecular crystals.

Of the remaining possible breakage mechanisms (particle-wall collisions, particle-horn collisions, and direct particle-shockwave interactions), decoupling experiments show that the first two possibilities are, at best, minor contributors to the total fragmentation rate. The dominance of direct particle-shockwave interactions has important implications for the design of sonocrystallization processes and for ultrasonic processing of friable materials such as active pharmaceutical ingredients (e.g., particle concentration is not very important, vessel materials and sizes are not especially important from a particle breakage standpoint, and an external sonication source compared to an immersion horn is not critical).

It is important to emphasize, however, that this work operates under the assumption that one mechanism dominates. This seems like a reasonable assumption based on the data shown here, but is not conclusively demonstrated. Further, even granting that assumption, a dominant mechanism is distinct from an exclusive mechanism. It is probable that all these mechanisms have some contribution under most experimental conditions, and it is possible that under other conditions other mechanisms would become more important. As discussed early, metal particles unambiguously undergo high-speed interparticle collisions. The relatively large crystals in this work are simply destroyed by the initial impact of the shockwave, but if one were to systematically vary the physical properties of the crystals to be more like metal particles one would expect that interparticle collisions would become more and more important. The results here should be taken as an extreme (although likely common among molecular crystals) case rather than an exclusive general rule.

6.5 References

1. Woo, X. Y.; Nagy, Z. K.; Tan, R. B. H.; Braatz, R. D., "Adaptive concentration control of cooling and antisolvent crystallization with laser backscattering measurement." *Crystal Growth and Design* **2008,** *9*, 182-191.

2. Eder, R. J. P.; Radl, S.; Schmitt, E.; Innerhofer, S.; Maier, M.; Gruber-Woelfler, H.; Khinast, J. G., "Continuously Seeded, Continuously Operated Tubular Crystallizer for the Production of Active Pharmaceutical Ingredients." *Cryst. Growth Des.* **2010,** *10*, 2247-2257.

3. Ambrus, R.; Amirzadi, N.; Sipos, P.; P, "Effect of Sonocrystallization on the Habit and Structure of Gemfibrozil Crystals." *Chem. Eng. Technol.* **2010,** *33* (5), 827-832.

4. Ruecroft, G., "Sonocrystallisation to the rescue." *Innovations in Pharmaceutical Technology* **2007,** (22), 74-76.

5. Wohlgemuth, K.; Kordylla, A.; Ruether, F.; Schembecker, G., "Experimental study of the effect of bubbles on nucleation during batch cooling crystallization." *Chem. Eng. Sci.* **2009,** *64*, 4155-4163.

6. Dejan-Krešimir Bučar, D.-K.; Macgillivray, L. R., "Preparation and reactivity of nanocrystalline cocrystals formed via sonocrystallization. Supporting information." *J. Am. Chem. Soc.* **2007,** *129*, 32-3.

7. Li, H.; Wang, J.; Bao, Y.; Guo, Z.; Zhang, M., "Rapid sonocrystallization in the salting-out process." *J. Cryst. Growth* **2003,** *247*, 192.

8. Guo, Z.; Zhang, M.; Li, H.; Wang, J.; Kougoulos, E., "Effect of ultrasound on anti-solvent crystallization process." *J. Cryst. Growth* **2005,** *273* (3-4), 555-563.

9. Luque de Castro, M. D.; Priego-Capote, F., "Ultrasound-assisted crystallization (sonocrystallization)." *Ultrason. Sonochem.* **2007,** *14*, 717-724.

10. Lyczko, N.; Espitalier, F.; Louisnard, O.; Schwartzentruber, J., "Effect of ultrasound on the induction time and the metastable zone widths of potassium sulphate." *Chem. Eng. J. (Lausanne)* **2002,** *86*, 233.

11. Ruecroft, G.; Hipkiss, D.; Ly, T.; Maxted, N.; Cains, P. W., "Sonocrystallization: The Use of Ultrasound for Improved Industrial Crystallization." *Org. Process Res. Dev.* **2005,** *9* (6), 923-932.

12. Gracin, S.; Uusi-Penttila, M.; Rasmuson, Å. C., "Influence of Ultrasound on the Nucleation of Polymorphs of p-Aminobenzoic Acid." *Cryst. Growth Des.* **2005,** *5*, 1787-1794.

13. McCausland, L. J.; Cains, P. W.; Martin, P. D., "Use the power of sonocrystallization for improved properties." *Chem. Eng. Prog.* **2001,** *97* (7), 56-61.

14. Abbas, A.; Srour, M.; Tang, P.; Chiou, H.; Chan, H.-K.; Romagnoli, J. A., "Sonocrystallisation of sodium chloride particles for inhalation." *Chem. Eng. Sci.* **2007,** *62*, 2445-2453.

15. Miyasaka, E.; Ebihara, S.; Hirasawa, I., "Investigation of primary nucleation phenomena of acetylsalicylic acid crystals induced by ultrasonic irradiation--ultrasonic energy needed to activate primary nucleation." *J. Cryst. Growth* **2006,** *295*, 97-101.

16. Miyasaka, E.; Kato, Y.; Hagisawa, M.; Hirasawa, I., "Effect of ultrasonic irradiation on the number of acetylsalicylic acid crystals produced under the supersaturated condition and the ability of controlling the final crystal size via primary nucleation." *J. Cryst. Growth* **2006,** *289* (1), 324-330.

17. Dennehy, R. D., "Particle Engineering Using Power Ultrasound." *Org. Process Res. Dev.* **2003,** *7* (6), 1002-1006.

18. Suslick, K. S.; Flannigan, D. J., "Inside a collapsing bubble: sonoluminescence and the conditions during cavitation." *Annu. Rev. Phys. Chem.* **2008,** *59* (December), 659-683.

19. McNamara III, W. B.; Didenko, Y. T., "Sonoluminescence temperatures during multi-bubble cavitation." *Nature* **1999,** *401* (6755), 772.

20. McNamara, W. B.; Didenko, Y. T.; Suslick, K. S., "Pressure during Sonoluminescenceâ€ " *The Journal of Physical Chemistry B* **2003,** *107* (30), 7303-7306.

21. Pecha, R.; Gompf, B., "Microimplosions: cavitation collapse and shock wave emission on a nanosecond time scale." *Phys. Rev. Lett.* **2000,** *84*, 1328-30.

22. Blake, J. R.; Keen, G. S.; Tong, R. P.; Wilson, M., "Acoustic cavitation: the fluid dynamics of non-spherical bubbles." *Philosophical Transactions of the Royal Society A: Mathematical, Physical and Engineering Sciences* **1999,** *357* (1751), 251-267.

23. Suslick, K. S., *Ultrasound : Its Chemical, Physical, and Biological Effects* VCH Publishers: New York, N.Y., 1988.

24. Suslick, K. S., "Sonochemistry." *Science* **1990,** *247* (4949), 1439-1445.

25. Mason, T. J.; Lorimer, J. P., *Applied Sonochemistry* Wiley-VCH: Weinheim, 2002.

26. Suslick, K. S.; Price, G. J., "Applications of ultrasound to materials chemistry." *Annual Review of Materials Science* **1999,** *29* (1), 295.

27. Bang, J. H.; Suslick, K. S., "Applications of ultrasound to the synthesis of nanostructured materials." *Adv. Mater. (Weinheim, Ger.)* **2010,** *22* (10), 1039-59.

28. Ohsaka, K.; Trinh, E. H., "Dynamic nucleation of ice induced by a single stable cavitation bubble." *Appl. Phys. Lett.* **1998,** *73*, 129.

29. Chow, R.; Mettin, R.; Lindinger, B.; Kurz, T.; Lauterborn, W., "The importance of acoustic cavitation in the sonocrystallisation of ice-high speed observations of a single acoustic bubble." *Ultrasonics, 2003 IEEE Symposium on Ultrasonics* **2003**, 1447-1450 Vol.2.

30. Wohlgemuth, K.; Ruether, F.; Schembecker, G., "Sonocrystallization and crystallization with gassing of adipic acid." *Chem. Eng. Sci.* **2010,** *65*, 1016-1027.

31. Thompson, L. H.; Doraiswamy, L. K., "The rate enhancing effect of ultrasound by inducing supersaturation in a solid-liquid system." *Chem. Eng. Sci.* **2000,** *55*, 3085-3090.

32. Suslick, K. S.; Doktycz, S. J., *"The Effects of Ultrasound on Solids" in Advances in Sonochemistry*. JAI Press: New York, NY, 1990.

33. Chatakondu, K.; Green, M. L. H.; Thompson, M. E.; Suslick, K. S., "The enhancement of intercalation reactions by ultrasound." *J. Chem. Soc., Chem. ...* **1987**, 900-900.

34. Suslick, K. S.; Casadonte, D. J.; Green, M. L. H.; Thompson, M. E., "Effects of high intensity ultrasound on inorganic solids." *Ultrasonics* **1987,** *25* (1), 56-59.

35. Suslick, K. S.; Casadonte, D. J., "Heterogeneous sonocatalysis with nickel powder." *J. Am. Chem. Soc.* **1987,** *109* (11), 3459-3461.

36. Suslick, K. S.; Casadonte, D. J.; Doktycz, S. J., "Ultrasonic irradiation of copper powder." *Chem. Mater.* **1989,** *1* (1), 6-8.

37. Suslick, K. S.; Doktycz, S. J., "The sonochemistry of zinc powder." *J. Am. Chem. Soc.* **2002,** *111* (6), 2342-2344.

38. Doktycz, S. J.; Suslick, K. S., "Interparticle collisions driven by ultrasound." *Science* **1990,** *247* (4946), 1067.

39. Prozorov, T.; Prozorov, R.; Suslick, K. S., "High Velocity Interparticle Collisions Driven by Ultrasound." *J. Am. Chem. Soc.* **2004,** *126* (43), 13890-13891.

40. Kass, M., "Ultrasonically induced fragmentation and strain in alumina particles." *Mater. Lett.* **2000,** *42* (4), 246-250.

41. Chu, S. H.; Choi, S. H.; Kim, J. W.; King, G. C.; Elliott, J. R. In *Ultrasonication of bismuth telluride nanocrystals fabricated by solvothermal method*, 2006; Spie: pp 61720A-61720A.

42. Raman, V.; Abbas, A., "Experimental investigations on ultrasound mediated particle breakage." *Ultrason. Sonochem.* **2008,** *15* (1), 55-64.

43. Price, G. J.; Mahon, M. F.; Shannon, J.; Cooper, C., "Composition of Calcium Carbonate Polymorphs Precipitated Using Ultrasound." *Cryst. Growth Des.* **2011,** *11* (1), 39-44.

44. Klink, A.; Midler, M.; Allegreti, J., "A Study of Crystal Cleavage by Sonifier Action." *Chemical Engineering Progress Symposium Series* **1971,** *67*, 74-80.

45. Aoki, M.; Ring, T. A.; Haggerty, J. S., "Analysis and modeling of the ultrasonic dispersion technique." *Advanced Ceramic Materials;(USA)* **1987,** *2*.

46. Wagterveld, R. M.; Boels, L.; Mayer, M. J.; Witkamp, G. J., "Visualization of acoustic cavitation effects on suspended calcite crystals." *Ultrason. Sonochem.* **2011,** *18*, 216-25.

47. Morison, K. R.; Hutchinson, C. A., "Limitations of the Weissler reaction as a model reaction for measuring the efficiency of hydrodynamic cavitation." *Ultrason. Sonochem.* **2009,** *16* (1), 176-183.

48. Gutierrez, M.; Henglein, A.; Ibanez, F., "Radical scavenging in the sonolysis of aqueous solutions of iodide, bromide, and azide." *The Journal of Physical Chemistry* **1991,** *95* (15), 6044-6047.